

Solid-State Li–Metal Batteries: Challenges and Horizons of Oxide and Sulfide Solid Electrolytes and Their Interfaces

Kun Joong Kim, Moran Balaish, Masaki Wadaguchi, Lingping Kong, and Jennifer L. M. Rupp*

The introduction of new, safe, and reliable solid-electrolyte chemistries and technologies can potentially overcome the challenges facing their liquid counterparts while widening the breadth of possible applications. Through tech-historic evolution and rationally analyzing the transition from liquid-based Li-ion batteries (LIBs) to all-solid-state Li-metal batteries (ASSLBs), a roadmap for the development of a successful oxide and sulfide-based ASSLB focusing on interfacial challenges is introduced, while accounting for five parameters: energy density, power density, longterm stability, processing, and safety. First taking a strategic approach, this review dismantles the ASSLB into its three major components and discusses the most promising solid electrolytes and their most advantageous pairing options with oxide cathode materials and the Li metal anode. A thorough analysis of the chemical, electrochemical, and mechanical properties of the two most promising and investigated classes of inorganic solid electrolytes, namely oxides and sulfides, is presented. Next, the overriding challenges associated with the pairing of the solid electrolyte with oxide-based cathodes and a Li-metal anode, leading to limited performance for solid-state batteries are extensively addressed and possible strategies to mitigate these issues are presented. Finally, future perspectives, guidelines, and selective interface engineering strategies toward the resolution of these challenges are analyzed and discussed.

1. Introduction

The realization of portable electronic devices and electric vehicles has been enabled in major part by the development of rechargeable batteries, including lead-acid, Ni–Cd, Ni–MH, and Li-ion batteries (LIBs). Batteries are expected to be flexible,

lightweight, and compact and allow for versatile device geometries. They must also be scalable and offer high energy density to provide improved packing efficiency and longer device operation. Although both Ni–MH batteries and LIBs have been commercialized since the 1990s,^[1] LIBs possess twice the gravimetric/volumetric energy density (250 Wh kg⁻¹/700 Wh L⁻¹ vs 170 Wh kg⁻¹/350 Wh L⁻¹),^[2] higher battery voltage (3.7 V vs 1.2 V), and longer cycle life with lower self-discharge,^[3] contributing tremendously to the proliferation of portable electronic devices (e.g., mobile phones, laptops, cameras, tablets) as well as emerging new technologies such as wearable electronic devices (e.g., smart watches and sport-related tracking devices). Their high gravimetric/volumetric energy density,^[2] excellent cycle life (thousands of cycles), and lack of the memory effect have positioned LIBs as state-of-the-art power sources and one of the greatest successes of modern electrochemistry, revolutionizing the way we acquire, process, transmit, and share information globally. Nevertheless, advances in battery energy density, safety, costs, and

flexibility in shape and size are still needed to keep up with the rapidly growing demand for devices with even longer runtime as well as real-time data collection and transmission capabilities in addition to increasingly energy-demanding applications such as electric vehicles (EVs) and electricity grid storage. Even though LIBs were first commercialized in all electric vehicles (EVs) in 2010 and also emerged for grid application in the same time frame, the low energy density (\approx 250 Wh kg⁻¹) and high average cost (\approx \$156 kWh⁻¹ in 2019) of conventional LIBs do not meet the requirements for advanced EVs and grid-scale energy storage.^[4–6] Specifically, the driving range per charge (miles), which is related to the energy density of each cell, and the cost are important parameters for EVs. For example, one 85 kWh battery pack in a Tesla Model S requires 7104 LIB cells, with an energy density of 265 Wh kg⁻¹, providing an average range of 250 miles, which is ahead of the range of other EVs but still behind the target of 375 miles.^[4] In grid-scale applications, LIBs can be used for various tasks: frequency regulation, peak shaving, load leveling, and large-scale integration of renewable energies, with specific properties generally required for each task. For frequency regulation, LIBs need to provide a fast response, high rate performance, and high-power capability,

Dr. K. J. Kim, Dr. M. Balaish, Dr. L. Kong, Prof. J. L. M. Rupp
Department of Materials Science and Engineering

Massachusetts Institute of Technology
Cambridge, MA 02139, USA
E-mail: jrupp@mit.edu

M. Wadaguchi
NGK SPARK PLUG CO., LTD
2808 Iwasaki, Komaki-shi, Aichi 485-8510, Japan

Prof. J. L. M. Rupp
Department of Electrical Engineering and Computer Science
Massachusetts Institute of Technology
Cambridge, MA 02139, USA

 The ORCID identification number(s) for the author(s) of this article can be found under <https://doi.org/10.1002/aenm.202002689>.

DOI: 10.1002/aenm.202002689

which is challenging for current LIBs. For peak shaving and load leveling in wind farms and solar-power-connected energy storage systems, Mitsubishi Heavy Industries has installed a 1 MW/400 kWh battery using a combination of nickel, manganese, and cobalt as the cathode, a natural-graphite-based anode, an electrolyte, and electrolyte additives.^[5] Toshiba launched a project in 2013 to install a 40 MW/20 MWh LIB system to promote the integration of renewable energy into the grid.^[6] The main challenge for the integration of LIBs with renewable energies is that LIBs require high power density that provides a few kW within a few minutes, up to MW within hours,^[7] which is beyond the power density limit (<300 W kg⁻¹) of current LIB technology.^[8] To put this down in numbers, LIBs for EVs require capacities that are 10 000× greater than those for portable electronics, and LIBs for the electricity grid require 1000× greater capacity than that for EVs.^[9] JCESR (Joint Center for Energy Storage Research) prioritized an energy density of 400 Wh kg⁻¹ and cost of \$100 kWh⁻¹ at the pack level for transportation and grid batteries.^[9] However, there is limited room for further capacity improvement of conventional LIBs, as we rapidly approach the practical limit of their chemistries (e.g., LiCoO₂, graphite).^[10] Moreover, large-scale applications of LIBs for EVs and grid-scale energy storages face unprecedented challenges in terms of safety requirements.^[11,12] Thus, the introduction of new chemistries and battery technologies with higher energy and power density and lower cost is currently of great scientific and industrial interest. Li–sulfur (\approx 650 Wh kg⁻¹)^[13] and Li–oxygen (\approx 950 Wh kg⁻¹)^[14,15] chemistries are only two examples of battery systems that have been intensively pursued in recent years owing to their higher practical energy density compared with that of state-of-the-art LIBs (\approx 250 Wh kg⁻¹).^[16]

1.1. Possible Turn Around from Liquid- to Solid-State Batteries

The chemistry of the electrode affects the energy density, which is simply the product of the capacity and voltage. Consequently, an increase of the energy density can potentially be achieved through i) optimization of the active materials (anode and cathode) over inactive components (separator, binders, current collectors, electrolyte) in the battery and ii) introduction of high-capacity and high-voltage materials, which can deliver more energy per ion transferred, and iii) improvement of manufacturing techniques (e.g., processing at lower temperatures, use of scalable fabrication processes). Focusing on the second criterion, the typical state-of-the-art commercial LIB consists of a carbonaceous negative electrode (anode), such as natural and/or synthetic graphite or a mixture of both (or, to a lesser extent, amorphous carbon).^[17] Graphite is a highly stable material with excellent conductivity; however, its theoretical capacity is limited to 372 mAh g⁻¹. Replacement of the classic graphite anode with high-capacity anode materials such as Si, Sn, SnO₂, MnO₂, or NiO has been explored for LIBs; however, such technologies remain in their infancy mainly because of their poor initial coulombic efficiency and cycle stability.^[18] Extensive research efforts have focused on reviving Li metal as the ultimate anode material for often name-tagged “beyond LIBs” owing to its outstanding theoretical specific capacity (3860 mA h g⁻¹), low electrochemical potential (−3.04 V vs SHE), and low density (0.53 g cm⁻³ at

room temperature). Replacing the conventional graphite anode with a lithium–metal (Li) electrode should in principle provide a feasible path for increasing the specific energy (volumetric energy density) by 35% (50%)^[19] from 150 Wh kg⁻¹ (250 Wh L⁻¹) to 250 Wh kg⁻¹ (750 Wh L⁻¹) at the pack level, fulfilling the US Department of Energy (DOE) requirements for electric propulsion applications.^[20,21] Nevertheless, the positive electrode (cathode) is known to be the bottleneck for improving specific capacities in conventional LIBs,^[22] as it contains inactive components including conductive additives (carbon) and a polymer binder in addition to the active material. Common cathode materials include metal oxides such as Li cobalt oxide (LiCoO₂, LCO), Li iron phosphate (LiFePO₄, LFO), and Li manganese oxide (LiMn₂O₄, LMO). High-voltage (polyanion, spinel) and large-capacity (Ni- and Li-rich layered oxide) cathode materials have also been explored as possible replacements for traditional cathode materials.

The third main battery component in a conventional LIB, the ion-conducting medium, consists of a lithium salt (e.g., LiPF₆, LiClO₄, LiBF₄) dissolved in a mixture of organic solvents (e.g., ethylene carbonate (EC), ethyl methyl carbonate (EMC), dimethyl carbonate (DMC)). Electrolytes should possess the following properties: low volatility, safety (incombustibility), high ionic conductivity, transference number (t_{Li^+}) close to unity, large electrochemical window, good thermal stability, low electrode/electrolyte charge-transfer resistance, low cost, and ease of processability. Liquid electrolytes possess high ionic conductivity (10^{-2} – 10^{-1} S cm⁻¹) and excellent electrode wettability at ambient, but a low $t_{\text{Li}^+} < 0.5$ and suffer from limited electrochemical and thermal stability.^[23,24] This includes limited capacity and cycle life at temperatures over 30 °C, as well as safety issues (e.g., leakage, flammability, combustibility).^[25] Worst-case scenarios related to these limitations such as fires and explosions of batteries in mobile phones, electric cars, and laptops have received worldwide attention. The common origin of these LIB safety issues is thermal runaway events that occur when the battery is overheated above \approx 80 °C.^[26,27] Once overheated, the temperature rises exponentially, leading to decomposition of the solid-electrolyte interphase (SEI), melting of the separator, and reaction between the anode (lithium metal or intercalated anode) with the organic solvent; in addition, the decomposition of the cathode material releases flammable gases and oxygen. Once enough oxygen and heat accumulate, the flammable organic electrolyte starts to combust, causing a fire or explosion. The traditional liquid electrolyte consists almost exclusively of a combination of cyclic and linear alkyl carbonates (i.e., EC+DMC in a 1:1 ratio by weight), a highly volatile and flammable solvent, and inorganic LiPF₆. This compromised salt decomposes into LiF and PF₅ (which further decompose into HF and PF₃O), with the surface reaction between these highly reactive species and the electrodes limiting the performance and cycle life. The thermal decomposition of the liquid electrolyte, reduction of the electrolyte by the anode, and oxidation of the electrolyte by the cathode are all possible exothermic reactions that can initiate thermal runaway in the battery, which are often caused by thermal (overheating), electrical (overcharge), or mechanical abuse.^[26,28] The safety issues associated with the liquid electrolyte will become more pronounced if a Li-metal anode is used to boost the energy

density of the battery. Li metal is thermodynamically unstable in any traditional nonaqueous organic electrolytes, instantly forming a SEI, which consists of insoluble organic (polyolefins) and inorganic products from the reduction of the electrolyte solution on the lithium-metal surface.^[29,30] The SEI is a key component for the operation of Li-metal batteries, serving as a solid electrolyte that allows the conduction of Li ions while blocking the passage of electrons. Nonetheless, it is also one of the most vulnerable areas in a Li-metal-based battery; decomposition of the SEI at cell temperatures exceeding 70 °C and dendrite growth during regenerative breaking of the SEI can both lead to thermal runaway.^[31] Several additional factors hindering the practical and successful commercialization of secondary Li-metal batteries include i) their low coulombic efficiency and poor cycle stability due to lithium peel-off during cycling, ii) safety issues due to possible dendrite growth during metal electrodeposition, and iii) low lithium passage (relative to lithium present) per cycle,^[19] which are not acceptable for commercial high-energy-density battery design (US DOE targets at least 80% of lithium present to pass per cycle).^[32] Several strategies have been established to suppress dendrite growth, including decreasing the current density, encapsulating the Li metal in a rigid host and stabilizing the Li-metal surface with buffer layers.^[33]

1.2. A Roadmap for the Development of a Successful Battery: Boosting Performance While Minding Safety and Costs

In a roadmap for the development of a successful battery with specific targets for energy density, power density, long-term stability, and processing, an additional prerequisite for widespread adoption is safety.^[10,26–28,34] Battery safety can be improved by implementing external protection devices, such as current-limiting devices (external electronic devices)^[28] and temperature and pressure sensors, or through internal protection approaches. On the material level, such internal approaches include favoring reliable cathode materials with higher thermal stability (LiFePO₄ is stable up to 400 °C, whereas LCO decomposes at 250 °C), using flame-retardant additives (e.g., fluorinated and organophosphorus compounds),^[35,36] stabilizing the SEI (e.g., LiI, fluoroethylene carbonate) and improving its uniformity to achieve even local current distributions,^[37,38] and incorporating thermal-shutdown separators.^[26] However, such external and internal protection measures generally increase manufacturing costs and reduce energy density.^[28]

The drive toward a safer alternative to conventional liquid-based batteries has motivated academic and industrial pursuits toward high-energy-density solid-state batteries, and in particular all-solid-state Li metal batteries (ASSLBs), which are believed to be one of the most promising candidates to attain the desired energy densities (>500 Wh kg⁻¹, >700 Wh L⁻¹)^[39] and power densities (>10 kW kg⁻¹).^[40] The high energy density is achieved through the adoption of high-capacity (1000 mA h g⁻¹)^[41] and high-voltage (5 V)^[42] cathode materials and the optimal anode material, lithium (Li) metal. Solid electrolytes are incombustible, nonvolatile, nonflammable, and stable at elevated temperatures; they also exhibit for some solid-Li conductors higher transference number (t_{Li^+}) close to unity when compared to their liquid counterparts, high elastic modulus, and wide

electrochemical stability without any leakage problems. In addition, solid electrolytes i) have a negligible self-discharge due to their low electronic conductivity; ii) allow high current densities without concentration polarization due to the immobility of the anionic framework, potentially leading to higher power density and energy density (via coupling with thick electrodes); iii) possess larger thermal conductivity than liquids, thereby mitigating to some extent heat-dissipation issues linked to batteries; iv) may prevent unwanted electrode “cross-talk” due to immiscibility of the decomposition products in the solid electrolyte; and v) are less prone to aging mechanisms and are expected to support longer lifetime devices owing to the slower reactivity of solids compared to liquids. The incorporation of solid electrolytes in LIBs, either Li⁺-conductive polymers (e.g., ethylene oxide (PEO), polyacrylonitrile (PAN), polymethyl methacrylate (PMMA), polyvinylidene fluoride (PVDF)) or inorganic conductive ceramics (e.g., amorphous lithium phosphorus oxynitride (LiPON), perovskite $\text{Li}_x\text{La}_{(2-x)/3}\text{TiO}_3$ (LLTO), NASICON-type $\text{Li}_{1.3}\text{Al}_{0.3}\text{Ti}_{1.7}(\text{PO}_4)_3$ (LATP), LISICON-type $\text{Li}_{14}\text{Zn}(\text{GeO}_4)_4$, garnet-type $\text{Li}_7\text{La}_3\text{Zr}_2\text{O}_{12}$ (LLZO), and sulfides (thio-LISICON $\text{Li}_2\text{S}-\text{P}_2\text{S}_5$ types)), began for many of these materials in the 1980s and 1990s, respectively.^[43] Replacing the liquid and/or gel electrolyte and separator with an intrinsically nonflammable, nonvolatile solid electrolyte shows great promise and is perhaps the ultimate solution toward safer high-energy-density all-solid-state Li metal batteries (ASSLBs). Moreover, the high density of solid electrolytes compared to liquid electrolytes necessitates the use of lithium metal as the anode material in an ASSLB configuration to increase the volumetric and gravimetric energy density by roughly 70% and 40%, respectively, as opposed to the 10% decrease in gravimetric energy density if the traditional graphite anode were used (Figure 1).^[10] On the cathode side, the wider electrochemical stability of solid electrolytes should support an increase in the cell voltage from 4.2 to 5 V (with the adoption of high-voltage cathodes), without significant electrolyte decomposition, resulting in a potential increase of more than 20% in energy density.^[10]

Nonetheless, commercialization of solid electrolytes, especially for electric propulsion and load-leveling applications, requires the resolution of the following critical issues: i) interfaces: reduction of active surface area for reactions and decrease of charge-transfer resistance at electrode/electrolyte interfaces, ii) safety: overall safety and possibly that with lithium metal, and iii) manufacturing costs. Continuous efforts have been focused on the realization of high-energy-density ASSLBs. Recently, a sulfide-based bulk-type cell with minimalistic configuration consisting of a Li-metal anode, $\beta\text{-Li}_3\text{PS}_4$ solid electrolyte, and $\text{Li}(\text{Ni}_{0.6}\text{Co}_{0.2}\text{Mn}_{0.2})\text{O}_2$ cathode active material exhibited a total cell resistance (summation of ohmic and polarization resistances) of 350–450 Ω cm² at room temperature cycling at 0.16–0.19 C.^[44] In addition, the state-of-the-art garnet-based ASSLB with Li_2CO_3 -coated LCO, $(\text{Li},\text{C})\text{B}_{0.3}\text{O}_{0.3}$, and LLZO as a cathode composite, LLZO as the solid electrolyte, and a Li-metal anode exhibited a total interfacial resistance of ~270 5Ω cm² tested at 100 °C under 0.05 C, which predominantly originated from the cathode interface.^[45] Overall, the total cell resistances for both cases were still much higher than that of commercial LIBs (10–20 Ω cm²) and low current density (<0.2 C) still to be overcome.^[40,46] Similarly, a recent holistic analysis of

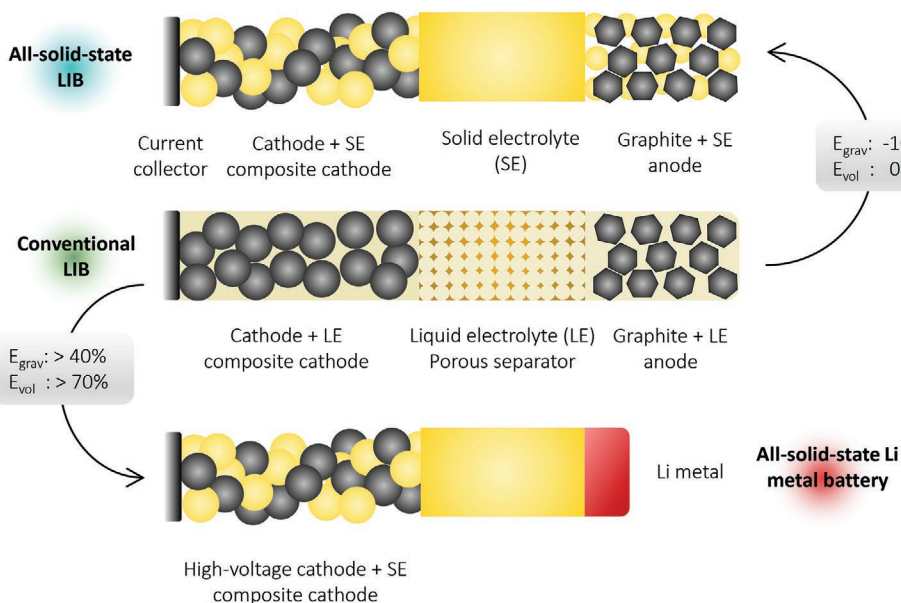


Figure 1. Change in energy density upon replacing liquid electrolyte in conventional LIB with solid electrolyte (all-solid-state LIB) and Li metal anode (all-solid-state Li metal batteries). The volumetric and gravimetric energy densities are represented by E_{vol} and E_{grav} , respectively. Reproduced with permission.^[10] Copyright 2016, The Nature Publishing Group.

state-of-the-art solid state battery performance suggests that a practical and high-specific-energy ASSLB cell requires internal resistance of less than $\approx 40 \Omega \text{ cm}^2$ to allow cycling at 1C with more than 90% energy efficiency,^[44] implying that further efforts are needed to reduce the cell impedance. Generally, the high impedance originates from both thick-electrolyte's with lowered conductivity and limited electrochemical reaction at the electrolyte/electrode interfaces. Therefore, reduction of the solid-electrolyte thickness and interfacial resistances are important tasks. Moreover, severe capacity loss with continued cycling has often been observed in sulfide electrolytes, especially because of the increasing interfacial impedance resulting from their poor oxidation limit. The interfacial degradation mechanisms reported thus far include interfacial decomposition/reaction or mechanical/chemical bonding issues during cell fabrication and operation. As the key redox reactions during battery operation occur at the interfaces, controlling the interface quality is imperative, lending further credence to the significant efforts being placed on engineering cathode and cathode/electrolyte architectures.

This review brings to the forefront the predominant interfacial challenges facing high-energy-density Li-metal solid-state batteries by highlighting the most promising inorganic solid electrolytes. First, we dismantle the solid-state battery into its three main components: the anode, cathode, and electrolyte. We discuss the two most investigated classes of solid electrolytes, oxides with focus on garnet-type oxides and sulfides, with chemical, mechanical, and electrochemical considerations. Next, the origins of one of the paramount issues leading to poor performance of solid-state batteries, the interfacial resistance at the electrolyte/anode and electrolyte/cathode interfaces, are addressed and possible strategies to mitigate these issues are presented. Finally, future perspectives, guidelines, and selective interface engineering strategies toward the resolution of these interfacial challenges are outlined.

1.3. The Origin of Cell Voltage and Battery Polarization

In a rechargeable battery, upon discharge (charge), Li ions deintercalate from the low (high)-potential Li insertion anode (cathode), migrate through the electrolyte, and intercalate into the cathode (anode) in a “rocking-chair” fashion while electrons flow through the external circuit, generating an electric current.^[47] When Li ions migrate out of the active material and travel to the anode through a solid electrolyte, valence changes of the transition-metal oxide (active material) occur to achieve charge neutrality, necessitating a sufficient amount of electronic and ionic conduction at the electrolyte/electrode interfaces to prevent degradation of the specific capacity and cycle life.^[48,49] A deeper understanding of the critical issues associated with battery deterioration, especially interfacial challenges, requires a short overview of the basics, with emphasis on the origins of cell voltage and typical battery polarizations. Here, we present such overview based on simplified schematics of solid-state battery with Li metal anode (Figure 2).

First, the thermodynamically driven open-circuit voltage (V_{oc}) between the anode and cathode is related to the chemical potential of the cell components determined by the difference in Gibbs energy at zero current. Generally, the overall voltage (V) of the cell is lower than the open-circuit voltage attributed to the applied current flowing through the cell, resulting in voltage drops due to several physical phenomena (Figure 2) as follows^[50]

$$V = V_{\text{oc}} - iR_{\text{Ohm}} - [(\eta_{p,k})a + (\eta_{p,k})c] - [(\eta_{p,t})a + (\eta_{p,t})c] \quad (1)$$

Here, V_{oc} is the standard cell potential; i is the applied current; R_{Ohm} is the ohmic resistance of the cell; $(\eta_{p,k})a$ and $(\eta_{p,k})c$ refer to kinetic polarization at the anode or cathode, respectively; and $(\eta_{p,t})a$ and $(\eta_{p,t})c$ are the transport polarizations relating to the

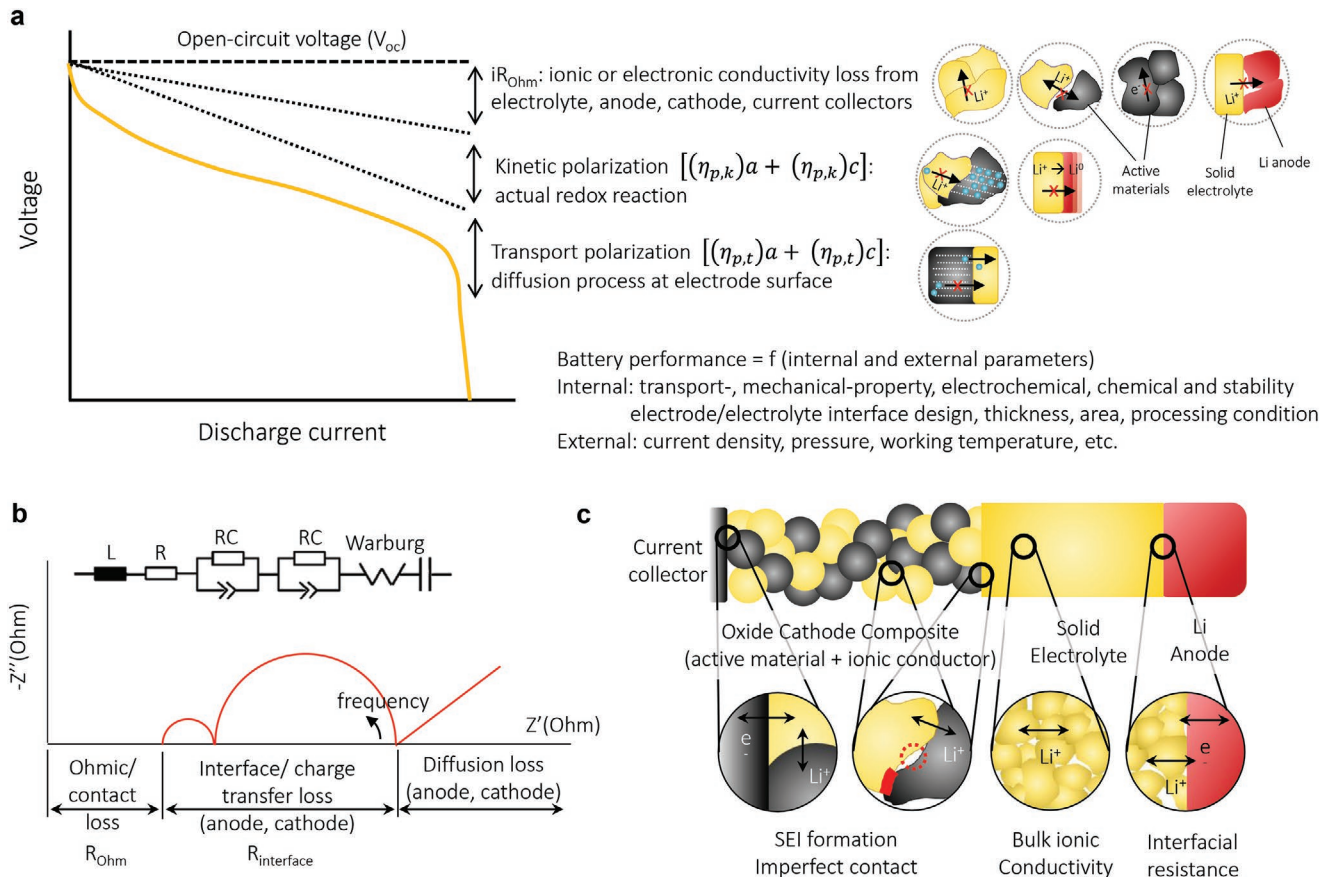


Figure 2. a) Typical discharge curve of a battery, showing the influence of the various types of polarization. Overall voltage (V) of the cell is lower than the open-circuit voltage (V_{oc}) ascribed to the applied current flowing through the cell, which result in voltage drops due to several physical phenomena. b–c) classic impedance spectra with frequency and associated components of solid state batteries. Simple battery circuit diagram, where the electrolyte and cell internal connections (inductance L , resistance R) in series with two constant phase elements parallel to two corresponding resistances ($R1//C1$ and $R2//C2$). Warburg impedance for diffusion processes, R_{Ohm} is the internal resistance, and two $R_{interface}$ are the impedances of the electrode reactions (c), which influenced by SEI formation, imperfect contact, and interfacial cracking.

charge-transfer at the anode and cathode interfaces, respectively. These represent nonlinear contributions in the voltage-discharge curve. The ohmic resistance overpotential iR_{Ohm} arises from charge-carrier motion and represents a linear contribution in accordance with Ohm's law. Typically, the ohmic resistance overpotential is the summation of the electronic conduction properties (mainly from the electrode) and ionic conduction properties (mainly from the electrolyte) of all the internal cell components, including interfaces and contact resistances. In general, polarization, also known as overpotential, is the voltage drop as a function of applied current density. Kinetic (activation) polarization, usually dominant at low current density, acts on the electrochemical energy of activation and is the change of potential across the interface. Transport (concentration) polarization originates from mass-transport limitation determined by the surface concentration of active species and thus by the rate of supply and removal of charge carriers. The concentration polarization is dominant at high current densities when the transport of charge carriers to the electrolyte/electrode interface becomes a limiting factor for the cell reaction. It is important to note that the equilibrium electrochemical potentials only consider the initial and final potentials of the materials in the

reaction, without kinetic considerations of the reactions themselves. Thus, electrochemical reaction kinetics play an important role, where one sluggish reaction can lead to significant deterioration of the overall battery cell performance. Analysis of the quantitative contribution of each resistant factor, which can be probed by in parts by equivalent circuit models via frequency-dependent electrochemical impedance spectroscopy (see schematic in Figure 2b,c), can provide significant insight for optimization of the overall performance of the battery in electrochemical cells.^[51,52] Nonetheless, all three overpotential contributions are interrelated; thus, their contributions cannot always be easily separated as the magnitude of all the ohmic and polarization resistances are a strong function of how the components of the cell are designed and their properties. These include the internal parameters such as desired transport-, mechanical-property, chemical, and electrochemical stability of selected single materials (electrolyte) or multiple components (composite cathode). Next, choice of materials for each component (electrode and solid electrolyte) and its architecture (e.g., electrode/electrolyte interface design, thickness, cell area) still could be considered as advanced internal parameters. For example, limited bulk ionic conductivity in solid electrolyte

(Figure 2c) increase Ohmic loss (high-frequency semicircle in Figure 2b). As results, energy density and rate-performance is decreased. The resistive interfaces due to imperfection of interfacial contact or solid electrolyte interphase (SEI) formation are responsible for both Ohmic and interfacial charge-transfer resistance (kinetic and transport polarization, mid- and low-frequency in semicircle in Figure 2b) during open-circuit and operation. Different cell architectures require different processing routes, meaning that introduction of additional parameter, e.g. processing temperature, which will determine the quality of electrolyte (microstructural density) and interfacial contact during fabrication of oxide-based solid-state cathode. Externally, characterization condition including current densities, pressure, and temperature affects the battery performance (Figure 2).^[53–56]

2. Solid Electrolytes: Sulfides and Oxides

The realization of solid electrolytes is a critical step toward an intrinsically safe ASSLB, which with improved packing density through polar stacking^[57] could, in principle, result in high-energy-density solid-state batteries by coupling with a lithium-metal anode and high-voltage cathode. Key properties of solid electrolytes include high ionic conductivity, which has recently been linked to the critical current density (CCD) for Li dendrite initiation at the Li/electrolyte interface,^[58] negligible electronic conductivity, wide electrochemical stability window, and chemical compatibility with the cathode (and anode) material. The last requirement implies that the highest occupied molecular orbital (HOMO) of the electrolyte must be below the cathode potential to prevent oxidation of the electrolyte by the cathode (unless a passivation layer is present). The electrolyte should not participate in the lithium insertion/extraction process and should only act as an ion-conducting solid. Other stringent requirements for battery design and engineering include wide thermal stability, adequate mechanical properties, good electrode/electrolyte adhesion, and capability of being manufactured into ideally thin electrolytes (10–25 μm) with lowered area-specific resistance (ASR). First-principles calculation^[59] has shown that the wide electrochemical window observed in many experiments (0–5 V) is not thermodynamically intrinsic to the solid material but is the result of sluggish kinetics of the decomposition reaction leading to the formation of a passivation layer (interphase), similar to the SEI, which inhibits further decomposition of the bulk material. Currently, only one solid electrolyte, i.e., a LiPON thin-film electrolyte, has exhibited excellent stability for 10 000 cycles when paired with a high-voltage cathode of LiMn_{1.5}Ni_{0.5}O₄ and others are still to be proven.^[42] Sulfide electrolytes^[60] and several other classes of oxide electrolytes with outstanding electrochemical stability (e.g., NASICON-type Li_{1.3}Al_xTi_{2-x}(PO₄)₃ (LATP) and Li_{1.5}Al_xGe_{2-x}(PO₄)₃ (LAGP) with high oxidation stability; garnet-type LLZO)^[59] also present opportunities for pairing with high-voltage cathode materials^[61] including Li₂NiMn₃O₈, Li₂FeMn₃O₈, and LiCoMnO₄ toward a high-energy-density battery beyond traditional graphite-based LIBs. Nonetheless, physicochemical (mechanical, chemical, thermal) stability issues accompanied by interfacial challenges at the cathode/electrolyte

and anode/electrolyte interfaces require the implementation of interface engineering strategies including compositional tuning,^[62,63] coating and buffer layers,^[64–66] polymer interlayers,^[67,68] and alloying.^[69,70]

One major prerequisite for solid electrolytes, i.e., satisfactory room-temperature ionic conductivity, has been achieved for several material classes of solid Li-ion conductors including various types of oxides, sulfides, and nitrides. Owing to their remarkable features, the two most explored material classes of solid electrolytes for power source applications^[11] are oxides and sulfides. Oxides (i.e., garnet LLZO, LiPON) are best known for their high chemical stability against Li metal due to kinetic stabilization,^[57] and sulfides (reduced at ≈1.6 V and oxidized at ≈2.3 V)^[59] are best known for their high Li-ionic conductivity, which is attributed to the large size and polarizability of the sulfide ion.^[71–75] Sulfides exhibit high room-temperature ionic conductivity up to 25 mS cm⁻¹,^[40] low grain-boundary resistance, and mechanical softness, enabling room-temperature densification via cold pressing and resulting in improved electrode/electrolyte physical contact.^[76–78] Conversely, oxide solid electrolytes (e.g., the perovskite Li_{3.3}La_{0.56}TiO₃, NASICON-type LiTi₂(PO₄)₃, LISICON-type Li₁₄Zn(GeO₄)₄, and garnet-type Li₇La₃Zr₂O₁₂) exhibit generally better resistance to oxidation than sulfides. They have higher oxidation potential, with the NASICON-type oxides LATP, Li_xLa_{2/3-x}TiO₃ and LAGP being thermodynamically stable up to ≈4.2 V.^[59] The garnet Li₇La₃Zr₂O₁₂ (cubic phase) shows the highest resistance to lithium reduction (theoretical reduction potential of 0.05 V vs Li⁺/Li), showing potential for future solid-state battery applications.^[57,59,76,79–84] In the following section we present an extensive survey and analysis of several major properties of sulfides and oxides solid electrolytes, including but not limited to: Li⁺ ion conductivity, activation energy, pre-exponential, transference number, electrochemical stability window, mechanical properties and processing temperature, also overviewed in Figure 3 (Table 1, Supporting Information).

2.1. Structure and Ion-Transport Properties

2.1.1. Oxides

Among oxide solid electrolytes, there are only a few known fast ion conductors. Bulk ionic conductivity greater than 1 or even 10 mS cm⁻¹ has been achieved at room temperature for perovskite, NASICON, and garnet-type oxide electrolytes with activation energy of 0.2eV–0.3eV (Figure 3). However, room-temperature conductivity greater than 1 mS cm⁻¹ has only been exhibited by a handful of lithium-conducting oxides, including LLTO, LATP, LLZO, and the recently discovered LiTa₂PO₈.^[85,86] Moreover, among these materials, only LLZO has demonstrated total conductivity greater than 1 mS cm⁻¹ with good stability against Li metal; that of the others is hindered by high resistance at grain boundaries or instability against Li-metal anodes.

The ideal perovskite structure with the general formula ABO₃ and cubic Pm3m symmetry consists of A-site ions (typically alkaline-earth or rare-earth elements) at the corners of a cube, B ions (typically transition-metal ions) at the center, and oxygen atoms at the face-center positions. The A-site La³⁺, Li⁺,

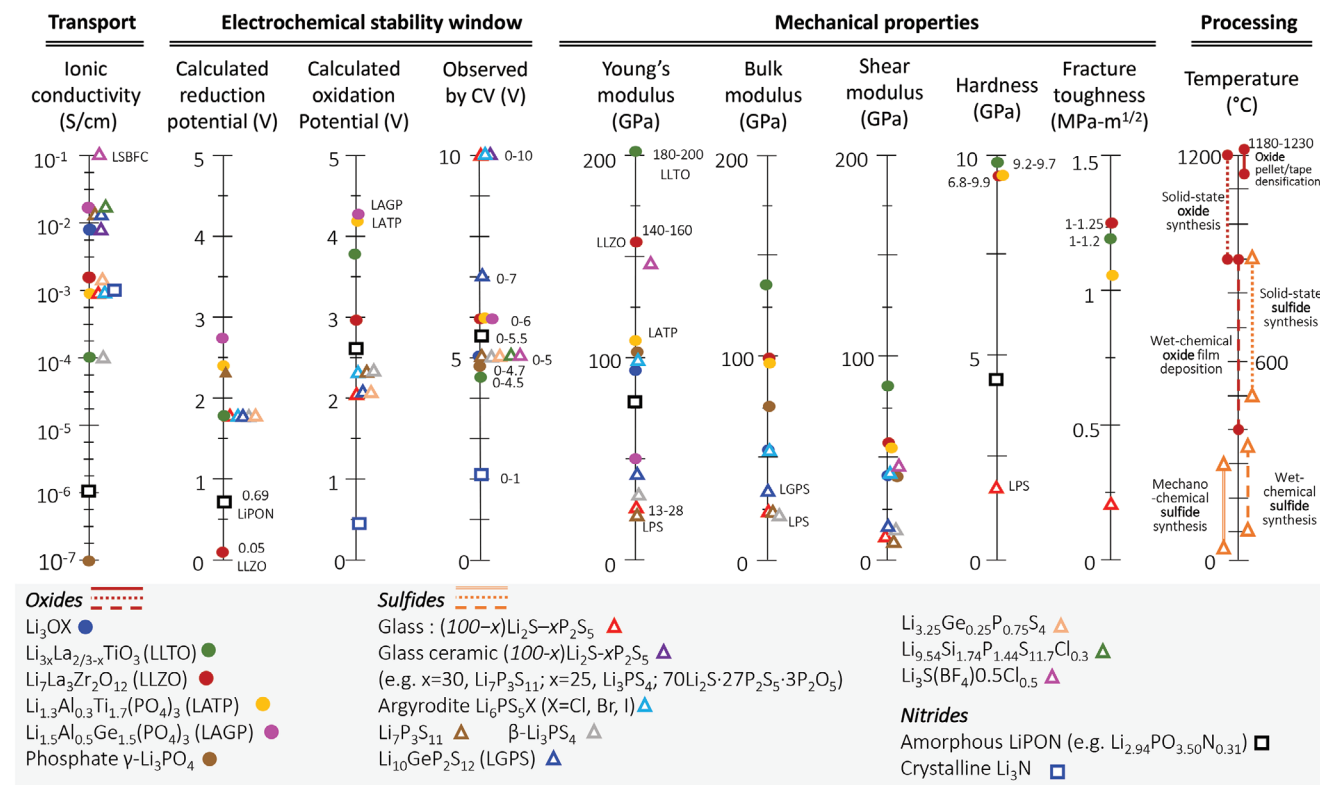


Figure 3. Overview of transport, electrochemical, mechanical stabilities, and processing temperature of oxides and sulfide solid electrolyte. Corresponding data including Li^+ ion conductivity, activation energy, pre-exponential, transference number, electrochemical stability window, mechanical properties, and processing temperature are available in Table S1 (Supporting Information).

and vacancies are equally distributed to allow the conduction of Li ions, which can be introduced into the perovskite at the A site through aliovalent doping.^[87,88] Lithium lanthanum titanate ($\text{Li}_x\text{La}_{(2-x)/3}\text{TiO}_3$, LLTO) exhibits a maximum bulk ionic conductivity of $1 \times 10^{-3} \text{ S cm}^{-1}$ at room temperature at x near 0.3 (corresponding to an A-site vacancy concentration of 8–10%), with a decrease in the conductivity observed for higher lithium content.^[89–91] Because of the difference in the ionic radii of Li^+ (0.92 Å) and La^{3+} (1.36 Å), the higher lithium concentration causes local distortion in A-site ordering that results in slow diffusion and ion conduction.^[92,93] Despite the high bulk “grain” conductivity, the magnitude of the grain-boundary conductivity of $\text{Li}_{0.34}\text{La}_{0.51}\text{TiO}_{2.94}$ has been reported to be on the order of $10^{-5} \text{ S cm}^{-1}$ at room temperature, resulting in low total ionic conductivity for a classic polycrystalline microstructure.^[89] Enhancement of the grain-boundary conductivity has been achieved by introducing an amorphous-silicate boundary layer^[94] or by optimizing the Li content in LLTO or sintering temperature.^[95,96] The grain conductivity was shown to be nearly independent of the sintering temperature between 1200 and 1350 °C (for average grain sizes of 1–5 mm and a relative theoretical density >95%), whereas the grain-boundary conductivity increased with sintering temperature through reduction of the grain-boundary length.^[96] Very recently, 30 mol% Li-excess LLTO ($\text{Li}_{0.22}\text{La}_{0.60}\text{TiO}_3$) sintered at 1400 °C exhibited a total ionic conductivity of $4.8 \times 10^{-4} \text{ S cm}^{-1}$ at room temperature, the highest reported value achieved for a bulk pellet so far.^[97] However, fundamentally understanding of grain

boundary chemistry and the transport properties still remain unclear. In LLTO, the ion transport in the grain-boundary region is greatly hindered, and the transport of Li ions is readily blocked in the boundary regions, which can potentially limit the overall cell performance owing to the high resistance or become the most susceptible points for metallic lithium precipitation and dendritic propagation,^[98] limiting its application as a battery electrolyte. The resistivity of the grain boundaries has two potential fundamental origins: 1) a charged grain-boundary core, arising from the differences in defect segregation energies between the bulk and grain boundary, resulting in the formation of space-charge potentials and ion-depletion zones in the adjacent grain, hindering ion transport,^[99] or 2) the formation of an insulating secondary phase at grain boundaries. However, distinguishing between these phenomena can be challenging as the grain-boundary core widths are extremely small on the order of 2–3 unit cells.^[100] Developing tools to distinguish between these effects are important for designing better perovskite Li -ionic conductors that do not suffer from poor grain-boundary transport characteristics.

The general molecular formula of NASICON-framework conductors is $\text{L}_{1+6x}\text{M}^{4+}_{2-x}\text{M}'^{3+}_x(\text{PO}_4)_3$, where L is Li or Na; M is Ti, Ge, Sn, Hf, or Zr; and M' is Cr, Al, Ga, Sc, Y, In, or La. The phase is generally stabilized with a rhombohedral unit cell and space group $\bar{R}\bar{3}c$, which forms 3D network structures. The framework consists of isolated MO_6 octahedra interconnected via corner sharing with PO_4 tetrahedra in alternating sequences along the c-axis direction.^[101–106] In rhombohedral phases, Li

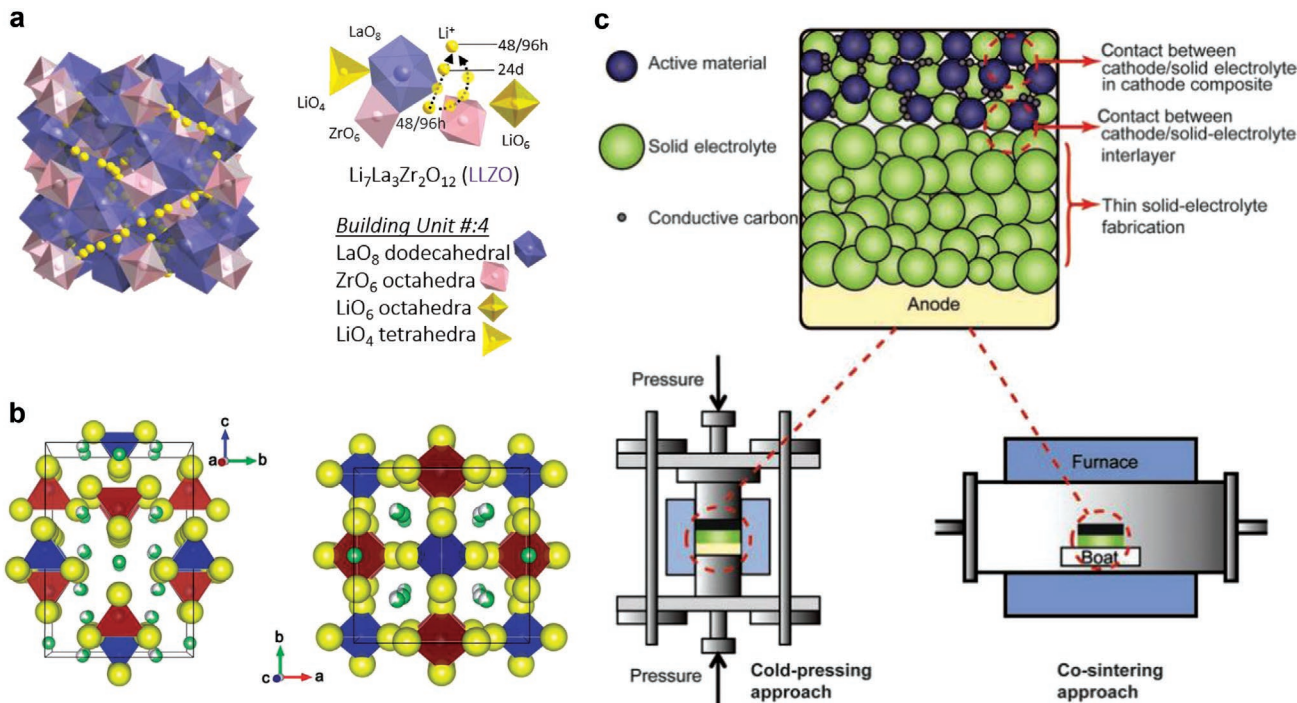


Figure 4. Li ion transport pathways for a) $\text{Li}_7\text{La}_3\text{Zr}_2\text{O}_{12}$ and b) $\text{Li}_{10}\text{GeP}_2\text{S}_{12}$. c) Processing approaches for sulfide (left) and oxide solid electrolyte (right). a) Reproduced with permission.^[507] Copyright 2020, the Nature Publishing Group. b) Reproduced with permission.^[169] Copyright 2013, the Royal Society of Chemistry. c) Reproduced with permission.^[342] Copyright 2018, Cambridge University Press.

ions conduct through two different interstitial sites in M' and M'' by hopping from one site to another, with octahedral symmetry (6-fold coordinated) directly between two adjacent MO_6 octahedra (M'), whereas the M'' sites are 8-fold coordinated and located between two columns of MO_6 octahedra. Partial occupancies of these two sites with Li ions has been shown to be crucial for fast lithium-ion conduction with low activation energy.^[107] Li-ion diffusion can be slowed down depending on the nature of the framework, the size of the bottlenecks along the pathways, and the concentration of Li ions at interstitial sites. Thus, it is important to select an appropriate framework skeleton according to mobile ion's radius to improve the ion diffusion and ionic conductivity.^[108] In the NASICON family, $\text{LiTi}_2(\text{PO}_4)_3$ (LTP), and $\text{LiGe}_2(\text{PO}_4)_3$ (LGP) are the most studied host compounds, and the ionic conductivity has been shown to be greatly enhanced upon partial substitution of $\text{Ti}^{4+}/\text{Ge}^{4+}$ ions by trivalent and divalent cations, such as Al, Ga, Sc, In, Y, La, Fe, Cr, Zn, and Ca in LTP/LGP systems.^[109,110] In the polycrystalline NASICON system in general, achieving highly dense samples has been difficult because of their poor sintering behavior. The highest room-temperature conductivity on the order of $10^{-3} \text{ S cm}^{-1}$ in the LTP system was observed for a polycrystalline $\text{Li}_{1.3}\text{Al}_{0.3}\text{Ti}_{1.7}(\text{PO}_4)_3$ pellet prepared by field-assisted sintering.^[111] In the LGP system, a glass-ceramic $\text{Li}_{1.5}\text{Al}_{0.4}\text{Cr}_{0.1}\text{Ge}_{1.5}(\text{PO}_4)_3$ pellet sample exhibited so far the highest ion conductivity of $6.65 \times 10^{-3} \text{ S cm}^{-1}$.^[112]

One of the most promising Li-ion conducting oxides is the garnet-type oxide electrolyte with the nominal formula $\text{Li}_7\text{La}_3\text{Zr}_2\text{O}_{12}$ (LLZO) because of its fast Li-ion conductivity with wide electrochemical window and high stability against Li metal.

The pristine LLZO phase exists in two polymorphs: tetragonal (space group $I4_1/acd$) and cubic ($Ia\bar{3}d$). Tetragonal LLZO is stable up to $100\text{--}150^\circ\text{C}$ ^[113] with poor room-temperature ionic conductivity on the order of $10^{-7} \text{ S cm}^{-1}$, whereas the higher-temperature stable cubic LLZO exhibits roughly three-orders-of-magnitude higher ionic conductivities on the order of $10^{-4}\text{--}10^{-3} \text{ S cm}^{-1}$.^[114] The general framework of the garnet structure consists of 8-fold coordinated LaO_8 dodecahedra (24c), 6-fold coordinated ZrO_6 octahedra (16a), and Li ions partially occupying the tetrahedra sites [LiO_4] bridged by a single octahedron [LiO_6] and forming a 3D network with superior lithium conduction pathways (Figure 4a).^[115,116] Various chemical compositions have been investigated by applying aliovalent doping at different structural sites to identify highly conductive compositions in the garnet-type structure. Generally, the ionic conductivity increases with the amount of Li per formula unit from Li3- ($\text{Li}_3\text{Ln}_3\text{Te}_2\text{O}_{12}$, Ln = Y, Pr, Nd, Sm-Lu), Li5- ($\text{Li}_5\text{La}_3\text{M}_2\text{O}_{12}$, M = Nb, Ta), and Li6- ($\text{Li}_6\text{ALa}_2\text{M}_2\text{O}_{12}$, A = Mg, Ca, Sr).^[117] The Li7 phase is obtained by replacing M with Zr in $\text{Li}_5\text{La}_3\text{M}_2\text{O}_{12}$ (LLZO) along with excess Li stuffing for charge neutrality. The highest conductivities have been observed between Li6.1 and Li6.8.^[118] Nevertheless, the effect of dopants in LLZO on the phase stabilization and electrical properties has been the subject of intense research.^[119\text{--}126] It has been shown that the dopants can increase the cubic over tetragonal phase ratio, grain size, relative theoretical density and overall ionic conductivity of undoped cubic $\text{Li}_7\text{La}_3\text{Zr}_2\text{O}_{12}$ by up to 4 orders of magnitude (especially for Ta compared with Al).^[84,119,123,126\text{--}142] When aliovalent cations of Al^{3+} or Ga^{3+} are substituted on the Li site or Ta^{5+} , Nb^{5+} , or Sb^{5+} are substituted on the Zr site, vacancy

disorder within the Li sublattice is increased, and highly conductive cubic structure can be stabilized. Density functional theory and molecular dynamics calculations have suggested that doping-induced Li vacancy concentrations greater than 0.4–0.5 per LLZO formula unit are required for the phase transition.^[14] Experimentally, substitution of 0.2–0.24 mol of Al for the Li site creates 0.4–0.48 mol of lithium vacancies in the LLZO framework, resulting in a room-temperature ionic conductivity of 0.4 mS cm⁻¹ in a hot-pressed polycrystalline LLZO pellet. LaAlO₃ appears as a second phase when the Al concentration exceeds its solubility limit of ≈0.389 mol,^[120] which certainly leads to deterioration of the ionic conduction. The highest conductivity of close to 1–2 mS cm⁻¹ was observed for both Ta- and Ga-stabilized LLZO:Li_{6.75}La₃Zr_{1.75}Ta_{0.25}O₁₂,^[143] Li_{6.55}Ga_{0.15}La₃Zr_{2.5}O₁₂.^[144] The detailed structure and transport mechanism have been presented in several recent reviews.^[145–148]

2.1.2. Sulfides

Sulfide solid electrolytes can be classified as glasses, glass-ceramics (via crystallization of/from glass electrolytes), and ceramic solid electrolytes, having ionic conductivities (10⁻⁶–10⁻¹ S cm⁻¹) with low activation energy (0.15eV–0.35eV) (Figure 3). Glassy sulfides of the binary system (100 – x)Li₂S-xP₂S₅ (LPS) with Li₂S and P₂S₅ serving as network modifiers and formers, respectively, have attracted much attention owing to their isotropic structure and conduction. The isotropic nature of the glassy structure enriches the tuning possibilities and chemo-mechanical properties via the diverse composition range available.^[149–151] These materials exhibit conductivities on the order of ≈10⁻⁴ S cm⁻¹ (at room temperature), significantly higher than that of thin-film LiPON glass, around 10⁻⁶ S cm⁻¹ (at room temperature).^[42,152] Further improvement of the ionic conductivity can be achieved by reducing the presence of voids and grain boundaries in glassy sulfides through cold-pressing, stemming from the isotropic structure and free volume of the glass.^[149] Moreover, the addition of oxides (e.g., P₂O₅, Li₃OBr)^[63,153] or lithium salt^[154–156] has been shown to increase the ionic conductivity of glassy electrolytes by an order of magnitude to ≈10⁻³ S cm⁻¹ at room temperature acting as network former coordinating the polyhedra.^[155,156] However, this improvement is often accompanied by narrowing of the electrochemical window due to the decomposition of halides.^[157] Finally, glassy sulfides offer ease of fabrication and cost-attractive scalability, which are required for ASSLB assemblies overall.^[156,157]

The so-called sulfide “glass-ceramics,” formed by the partial crystallization of glassy sulfides to reduce the grain-boundary resistance, may exhibit higher ionic conductivities on the order of ≈10⁻³ S cm⁻¹, which is attributed to a simple room-temperature cold-press densification process (for x ≤ 30). Specifically, an ionic conductivity of 2.2 × 10⁻³ S cm⁻¹ at room temperature has been achieved for Li₇P₃S₁₁ⁱ for x = 30, and an ionic conductivity of 1.3 × 10⁻³ S cm⁻¹ has been achieved for Li₃PS₄ for x = 25.^[158,159] The boosted conductivity compared with that of glassy sulfides is attributed to the arrangements of the pyro-thiophosphate anion P₂S₇⁴⁻, which plays an important role

in the fast Li⁺ diffusion through a network of neighboring Li⁺ cations composed of Li-Li chains.^[156,158,160–162] Heat treatment may further increase the ionic conductivity of glassy sulfides up to 1.7 × 10⁻² S cm⁻¹ at room temperature due to the precipitation of superionic metastable crystals embedded in a glassy matrix, such as Li₇P₃S₁₁ for the treatment of 70Li₂S–30P₂S₅ at 280 °C.^[158,163]

Crystalline sulfides, such as the argyrodite Li₆PS₅X (X = Cl, Br, I) and thio-lithium superionic conductor (LISICON) family, expressed by the general formula Li_xM_{1-y}M'_yS₄ (M = Si, Ge, Sn, Zr; M' = P, Al, Zn, Ga, Sb 0 < x < 1), are derived from the Li₂S-P₂S₅-LiX and Li₂S-M'₂S₅-MS₂ systems, respectively.^[164,165] The argyrodite Li₆PS₅I is comprised of fully ordered S²⁻ and I⁻, Li₆PS₅Cl is comprised of fully disordered S²⁻ and Cl⁻, while Li₆PS₅Br is comprised of a mixture of ordered and disordered structures and thus exhibit the fastest Li⁺ mobility.^[164] The thio-LISICON family related to the γLi₃PO₄ framework exhibits higher ionic conductivity than its oxide counterpart because of the large and polarizable nonmetal sulfide ions serving as network formers (supporting faster Li⁺ mobility) or the interstitial-vacancy feature via substitutions (2.2 × 10⁻³ S cm⁻¹ for Li_{3.25}Ge_{0.25}P_{0.75}S₄)^[165] compared to 1.0 × 10⁻⁷ S cm⁻¹ at room temperature for the oxide LISICON Li₁₄Zn(GeO₄)₄.^[166,167] The most notable ceramic sulfides are Li₁₀GeP₂S₁₂ (LGPS)^[78] and Li₁₀SiP₂S₁₂ (LSPS)^[40] Superionic Li-ion conductors such as Li₁₀GeP₂S₁₂ (12 mS cm⁻¹ at 27 °C and 1.0 mS cm⁻¹ at –30 °C)^[78] and Li_{9.54}Si_{1.74}P_{1.44}S_{11.7}Cl_{0.3} (25 mS cm⁻¹ at room temperature)^[40] have been theoretically^[168] and experimentally^[40,78] shown to follow the structural guidelines for superior Li⁺ ionic conductivity with the underlying body-centered cubic-like anionic framework allowing for direct conductance of Li ions between interconnected tetrahedral sites with lower activation barrier than those in close-packed frameworks. The size of S²⁻ in the Li₁₀GeP₂S₁₂ structural framework is considered ideal in terms of the channel size created for Li⁺ conduction.^[169] The LGPS structure, composed of a framework of (Ge_{0.5}P_{0.5})S₄, PS₄, and LiS₄ tetrahedra and LiS₆ octahedra, was initially suggested to have a purely 1D lithium conduction pathway along the crystallographic c-axis at room temperature. It was suggested that the Li atoms in LiS₄ tetrahedra were mobile and enabled the fast diffusion along the c-axis, whereas the Li atoms in LiS₆ octahedra were immobile and did not contribute to Li transport/diffusion (Figure 4b). Nonetheless, it was later determined that although Li ions are predominantly along the c-axis direction in LGPS, cross-channel diffusion in the a–b plane is also significant.^[169–172] Recently, neutron powder diffraction in combination with nuclear density map analysis was used to clarify the diffusion pathways in LGPS, and it was concluded that the material contains a combination of 1D diffusion channels crossing two diffusion planes.^[171] The 3D conduction was also confirmed computationally.^[172] However, Kuhn et al.^[173] suggested weak anisotropic Li diffusion in LGPS, and Bhattacharya et al.^[170] suggested that all the Li ions are equally mobile without any “framework” Li, leaving the ion diffusivity dimensionality in LGPS a matter of debate.^[78,169–173] In general, 1D diffusion, as opposed to cross-channel diffusion, in solids may pose a challenge for electrolyte adoption, as it may significantly hamper ionic conductivity in the presence of certain crystal defects.^[174]

2.2. Processing of the Solid Electrolytes

Densification of the solid electrolyte is a key processing step, whether oxides or sulfides are considered, and can affect the electrochemical performance (Ohmic, polarization resistance) of the solid-state battery. Glass and glass–ceramic sulfides offer almost endless opportunities for tuning of their properties through the selection of particular network modifiers and formers. The chemical and mechanical properties of glass and glass–ceramic sulfides enable low-temperature sintering and ease of achieving intimate contact with the electrode material (formability). The oxide-type SSB electrolytes such as selected garnet LLZO possesses tremendous potential merits as a solid electrolyte; however, achieving strong interfacial bonding at both the electrolyte/electrode (oxide cathode, Li metal) interfaces without ion-blocking SEI formation during processing has been considered a large bottleneck for developing LLZO-based ASSLBs. It remains unclear how to process a LLZO-based full-cell architecture with reliable and competitive performance; however, collective efforts suggest that developing cost-effective, nonequilibrium and low-temperature processing is of prime importance to produce a reliable full-cell architecture to be tested by avoiding interfacial reaction. For example, the emerging extremely low-temperature processing route ($400\text{ }^{\circ}\text{C}$)^[175] is a promising seed technology that can be combined with a novel cell-fabrication strategy as a new standard.^[43] Such alternative low-temperature processing routes and insights can guide the next steps toward the development of a standard architecture for garnet-based ASSLBs and improved performance. Importantly, this is believed to be an important step forward toward potentially demonstrating the many currently veiled advantages of garnet-based ASSLBs (Li metal compatibility, chemical compatibility during cycling, and air stability) compared with those of sulfide-based ones.

Before diving in the complex task of solid electrolyte/electrode processing (or multiple components of electrode composites), we focus on the challenges associated with the fabrication of mechanically stable, thin-, and dense layer of sulfide or oxide solid electrolytes, while the compatibility and processing issues with either the cathode or Li metal anode was discussed in later sections.

2.2.1. Oxides

Processing for various oxide-type solid electrolytes including perovskite (LLTO), NASICON (LATP, LAGP), and garnet-type (LLZO) has been mainly performed using solid-state synthesis routes. Several processing attempts have been made for LLZO solid electrolytes. Conventionally, synthesized or commercial crystalline powders are cold-pressed followed by high-temperature sintering ($>1100\text{ }^{\circ}\text{C}$)^[119,137,178–181] to obtain highly dense electrolyte pellets (Figure 4c). Li evaporation during processing reduces both the phase purity and relative density of the sample. Other techniques such as hot-pressing and field-assisted or spark plasma sintering minimize Li evaporation by accelerating the sintering force in a limited amount of time at high temperature.^[137,178–180,182,183] However, the addition of an excess lithium reservoir such as LiOH, Li₂CO₃, or mother powder is essential

to diminish partial conversion to the Li-deficient pyrochlore phase La₂Zr₂O₇ during oxide processing. With increasing temperature, all metal precursors are decomposed, the high-conducting cubic LLZO formation occurs at temperatures $\approx 750\text{ }^{\circ}\text{C}$; however, temperatures in the range of 900–1230 °C are required to fully stabilize and densify the LLZO electrolyte (Figure 3).^[177] Densification of LLZO solid-electrolyte powders with low porosity is of utmost importance for optimization and unification of the mechanical and electrical properties.^[119,178] Nevertheless, achieving a dense electrolyte with the right phase is crucial to improve the ionic conductivity. For example, the total ionic conductivity of cubic LLZO (Li_{6.19}Al_{0.27}La₃Zr₂O₁₂) can change by more than an order of magnitude from 0.009 to $0.34 \times 10^{-3}\text{ S cm}^{-1}$, changing the relative theoretical density from 85% to 98%, respectively.^[178] Other than classical solid-state sintering approach, several nonequilibrium densification processes that use artificial or chemically induced pressure as alternative sinter driving force to the temperature. These processes can overcome thermodynamic instability, second-phase formation and Li loss, including high-pressure field assisted sintering technique (FAST), also known as spark plasma sintering (SPS),^[184] flash sintering and aerosol deposition methods for thin-film (1–10 μm) fabrication. For example, highly dense oxide electrolytes,^[185,186] electrolyte–electrode composite^[187] can be prepared with significantly lowered the sintering temperature and time. In flash sintering, a commercial LLZO powders (particle size ≈1μm) were used for sintering LLZO green body at 850 °C for a few seconds to form over 96% dense LLZO pellet, showing room temperature conductivity of 0.5 mS cm^{-1} . A half-cell of LCO–LLZO as cathode composite and LLZO as electrolyte were prepared by SPS at 675 °C for 10 min, demonstrating 95% theoretical density. More recently, even further an additional low-temperature sintering process has been reported via namely “cold sintering”^[188,189] that uses a combination of external pressure together with a chemically activated pressure. A reasonable ionic conductivity over 10^{-4} S cm^{-1} is shown as exemplified in cold-sintered LATP, LAGP^[190] and LLZO^[191] pellets at less than 200 °C of sinter temperature with 85–90% of theoretical density, and densification of binder-free LIB composite electrode (Li₄Ti₅O₁₂,^[192] LiFePO₄)^[193] have been shown, which is remarkable.

Although conventional and alternative solid-state processing is used to produce millimeter-thick bulky electrolytes, practical design principles of battery electrolytes require solid electrolytes that are thinner than a pellet for enhanced battery performance and as high of an energy density as possible.^[194] The electrolyte thickness increases the internal resistance of the device, which can be a limiting factor in the overall cell performance. In commercialized Li-ion batteries with a 25 μm thick porous separator soaked with liquid electrolyte (LiPF₆ in EC/DMC), the solid-electrolyte resistance should not contribute more than $3.75\text{ }\Omega\text{ cm}^2$ to the total resistance.^[40] Using the reported ionic-conductivity of LLZO, the target thickness can be simply determined; for LLZO films with an ionic conductivity of $0.5\text{--}1\text{ mS cm}^{-1}$, a film thickness of 18.7–37 μm is required. Encouragingly, in recent years, significant advances in thinning LLZO electrolytes have been achieved. Successful fabrication of 25 μm thick, dense, free-standing LLZO electrolytes with ionic conductivities as high as 1 mS cm^{-1} have been successfully prepared using tape

casting.^[195–197] However, the often poor mechanical strength of such thin ceramics may cause difficulties for other processing steps during cathode preparation (usually high temperatures >700 °C are required) or the application of external pressure. A trilayer LLZO electrolyte composed of a 20 μm thick dense LLZO film sandwiched by two 50 μm thick porous LLZO films was shown to enhance the mechanical strength (breaking force) by 10 times higher compared with that of a 20 μm thick free-standing LLZO film.^[198] Tape-cased thin LLZO electrolytes have shown great promise for liquid–solid hybrid batteries, where organic-based electrolytes are used as the cathode electrolyte (catholyte).^[197,198] For application of free-standing oxide electrolytes in all-solid-state batteries, however, serious consideration of mechanical and chemical compatibility issues upon assembly with a solid-state cathode composite, which involves screen printing and high-temperature (700–1050 °C) firing, is necessary.^[45,199,200] Furthermore, without supporting parts that are mechanically strong enough in the entire unit cell architecture, the battery components will be vulnerable with increasing cell size when scaled up, highlighting the importance of establishing suitable solid-state battery architecture and processing routes. Perhaps, one can prepare an oxide electrolyte by film deposition on top of a supporting substrate. The substrate can be either an internal component (cathode, anode, or current collector) or external component (artificial substrate such as a thin stainless plate). By considering the target thickness, potential scalability, and properties of the resultant LLZO film (conductivity, stability), various deposition methods including vacuum-based techniques (CVD,^[201] PLD^[133,202–205]), wet-chemical routes (sol-gel^[206–208] route or spray pyrolysis^[209]) and aerosol deposition methods^[210,211] have been investigated. Another merit of these techniques is lowered processing temperature down to 400–900 °C or down to room temperature^[212] for thin-film electrolyte synthesis, phase formation and densification (Figure 3). Current work to improve the ionic conduction of thin-film LLZO electrolytes has been covered in recent reviews.^[147,194] In summary, the ionic conductivity has been shown to be generally lowered when solid electrolytes are prepared as thin films and managing Li-loss to phase stabilize is more challenging when compared to sintered bulk pellet or tape processed samples, see refs. [43,206] for discussion. However, if the resistance of the electrolyte satisfies the target value discussed above, a conductivity slightly lower than that of the bulk will not be a critical limiting factor to the overall performance. More importantly, processing of the electrode/electrolyte interface requires significant attention. For example, current cathode/electrolyte processing techniques generally require high-temperature deposition or postannealing steps that potentially instigate interfacial side reactions, increasing the resistance at the electrolyte/electrode interface. More in-depth consideration of currently available full-cell architectures and oxide processing and deposition technologies is needed to inspire further advances of reliable and high-performance oxide-based batteries based on thin oxide electrolytes.

2.2.2. Sulfides

Since 1980s and for two decades, sulfides have been synthesized solely via solid-state reaction. The mechanochemical and

wet-chemical synthesis routes of the binary system Li₂S–P₂S₅ were demonstrated only two and three decades afterward, respectively, maintaining their popularity since then. The fast ion diffusion in sulfides (e.g., Li⁺, PS₄³⁻, and I⁻ in the Li₂S–P₂S₅–LiI system)^[155] at the particle boundaries at low temperatures and the large free volume, especially in glassy structures, facilitate densification and create good particle-to-particle contact simply with the application of cold pressing at room temperature (e.g., 90% density at 350 MPa in Li₂S–P₂S₅)^[150] or relatively low temperature (close to the glass transition temperature ≈200 °C).^[150] The origin of the outstanding Li⁺-ion mobility and ionic conductivity of sulfides at room temperature is the low bond-energy and relatively covalent bonding character between Li and S compared with that between Li and O in oxides.^[213] Replacing the high-temperature (>1000 °C) sintering normally associated with oxide-based solid electrolyte manufacturing and deteriorated interfaces with cold-pressing sulfide electrolytes at room temperature or hot-pressing of these materials near their glass-transition temperatures^[151] is a clear advantage for the commercial production of solid-state batteries to reduce costs (Figure 4c).

Several processing techniques are available for the synthesis of sulfide solid electrolytes (Figure 3), namely: i) high-temperature solid-state reaction;^[214] ii) room-temperature mechanochemical milling using a high-energy planetary ball mill apparatus,^[150,156] and iii) wet-chemical synthesis routes.^[215,216,217,218] In the solid-state reaction route, high temperature (≈500–900 °C)^[157,163,219,220,221,222] is required for the thermodynamics and/or to enhance the kinetics of the reaction.^[214] The high vapor pressure of common sulfide precursors (e.g., P₂S₅, Li₂S) necessitates their vacuum (or inert environment)-sealing in a carbon-coated quartz tube during heat treatment,^[157,163] which poses a critical issue for scale-up. The last is followed by a cooling step, either slow cooling (to ensure crystallization) or quenching step in ice water (to obtain amorphous material).^[157,163] In the mechanochemical method, glass, glass–ceramic, and ceramic sulfides are typically synthesized under nonequilibrium conditions using a high-energy planetary ball mill apparatus at room temperature,^[150,156,223] which obviates the need for high temperatures and cooling steps. Explicit guidelines and ball-milling parameters (material and geometry of the ball milling jar and balls, rotation speed, milling cycling program, the respective volumetric/weight ration of the milling jar, balls, and the powders)^[224] can be widely found in the literature. Nonetheless, fundamental understanding of their effect on the crystallization temperature of the glasses, Li⁺ transport properties and activation energies has yet been reported. The ionic conductivities of glassy sulfides prepared via ball-milling can be enhanced by improving densification via a subsequent heating annealing step (120–300 °C),^[225,226] or by operating the ball-milling at low temperature (55 °C).^[227] Although a relatively time-consuming process with small throughput, ball milling method provide a reliable technique to produce homogeneous sulfide solid electrolytes with reproducible phases and transport properties. Recently, the wet-chemical technique, a simple, microstructure-controllable (nanometer–micrometer scale compared to micrometer scale in solid-state synthesis), and cost-effective process toward mass production, has been reported for sulfide

solid electrolytes of $\beta\text{-Li}_3\text{PS}_4$,^[215] $\text{Li}_7\text{P}_3\text{S}_{11}$,^[216,217] and Li_4SnS_4 .^[218] The wet-chemical synthesis includes either: i) liquid-phase synthesis: the reaction of precursor (e.g., Li_2S and P_2S_5) in an aprotic solvent (typically polar, e.g., tetrahydrofuran, acetonitrile, and ethyl acetate) to avoid the protonation of sulfides and formation of the toxic H_2S gas, or ii) solution-based synthesis: the dissolution of the sulfide solid electrolyte (rather than the precursors) in the solvent to assure homogeneous solution. In both cases, the following step includes a drying step preferably under vacuum to assure complete evaporation of the organic solvent (80–250 °C) and a subsequent heat-treatment step for crystallization (140–300 °C).^[216,215]

Compared to solid-state reaction and the mechanochemical method, wet-chemical synthesis benefits from reduced processing time and temperature (Figure 3) and from diverse tunable parameter (e.g., solvent, additives, precursors-to-solvent ratio, purity of chemicals, mixing and drying procedures)^[224] providing an additional nob to control the phase, size, and morphology of the sulfide particles in addition to unlocking access routes for new metastable phases and affecting the transport properties of the sulfide solid electrolytes. For instance, a nanocrystalline porous microstructure was enabled by the evaporation of the solvent medium via wet-chemical synthesis of $\beta\text{-Li}_3\text{PS}_4$.^[215] The nanocrystalline structure boosted the ionic conductivity by 3 orders of magnitude (e.g., $\beta\text{-Li}_3\text{PS}_4$:^[215] $1.6 \times 10^{-4} \text{ S cm}^{-1}$ and $\text{Li}_7\text{P}_3\text{S}_{11}$:^[217] $9.7 \times 10^{-4} \text{ S cm}^{-1}$ at room temperature) compared to that for solid-state synthesis through the surface conduction mechanism without compromising electrochemical stability (e.g., $\beta\text{-Li}_3\text{PS}_4$:^[215] 0.22–5 V vs Li^+/Li) or compatibility with Li metal (Figure 3).^[215] Nonetheless, fundamental understanding of the relation between multiple processing parameters and the reaction mechanism of the binary system $\text{Li}_2\text{S}-\text{P}_2\text{S}_5$ in liquid media is scarce and despite the considerable progress in liquid-phase chemistries of sulfides, mechanisms and guidelines still need to be elucidated. More efforts should be devoted to the developing and understanding of wet-chemical solution-based synthesis methods, where reduced processing costs, scalability, high throughput and improved production efficiency is expected. For the manufacturing of sulfide solid electrolyte for ASSLBs, the possibility to form an intimate contact between the electrodes and the solid electrolyte by deposition (or precipitation) of the solid electrolyte directly on the electrode material (through solution-based synthesis) is a huge advantage that should be further explored for ASSLBs based on current and new chemistries of sulfide solid electrolytes.^[228] This promising scalable method to deposit sulfide solid electrolyte directly on the electrode material is contingent upon cost-effective, chemically compatible, nontoxic, preferably low boiling point solvents that can be chemically combined with both the sulfide solid electrolyte and the cathode active material.

2.3. Chemical Stability in Ambient Air and its Effect on Electrolyte Performance

The stability of solid electrolytes in ambient air is imperative for ease of preparation during manufacturing and the cell-assembly process to reduce production costs. Moreover, poor

air stability can lead to chemical^[136,229–231] and mechanical degradation,^[232,233] resulting in a decrease of ionic conductivity, high interfacial resistances, and limited electrochemical device performance.^[230,234]

2.3.1. Oxide

Generally speaking, the air-stability of oxide solid electrolytes (e.g., LATP, LLTO and LLZO) is superior to sulfides. In particular, LATP and LLTO are intrinsically stable in ambient condition, providing tremendous advantage for battery processing and manufacturing, while LLZO readily forms a carbonaceous layer on the surface once exposed to humidity and carbon dioxide in air, increasing interfacial resistance during processing and operation. Among the different oxide solid electrolytes, garnet-structured LLZO is considered one of the most promising (and most explored) solid electrolyte with the combination of fast Li-ion conduction pathways, a wide electrochemical window, and excellent stability against Li metal demonstrated at the low reduction potential of 0.05 V versus Li^+/Li ,^[57,59,76,82–84] and is thus the focus of this section. The instabilities of garnet-type electrolytes upon moisture exposure have been broadly investigated and linked to i) synthesis and sintering conditions,^[136,229] ii) material properties (chemical composition, grain size, grain boundaries, relative density),^[136,231,233–235] iii) postprocessing conditions, and vi) electrochemical properties such as the ionic conductivity and interfacial resistance.^[136,230,234,236] Although garnet-type oxides were initially thought to be chemically stable under ambient atmosphere, the susceptibility of the lithium-garnet structure to the atmosphere (moisture, CO_2) has been confirmed both experimentally^[229,232,237] and computationally^[229,231,235,238] over the last decade.^[239] The results indicate that lithium garnet-type structures do not corrode in protonated environments, though a spontaneous reversible Li^+/H^+ ion exchange typically occurs.^[234,235,237,239,240] Early on, an aqueous treatment revealed partial replacement of Li^+ in the garnet structure by H^+ from aqueous environments when $\text{Li}_5\text{La}_3\text{Nb}_2\text{O}_{12}$,^[239] Ba-doped $\text{Li}_5\text{La}_3\text{Nb}_2\text{O}_{12}$ (HCl and water),^[241] $\text{Li}_5\text{La}_3\text{Ta}_2\text{O}_{12}$,^[239] $\text{Li}_5\text{La}_3\text{Sn}_2\text{O}_{12}$ (benzoic acid and ethanol solution),^[242] and Al-doped^[234] and Nb-doped^[240] $\text{Li}_7\text{La}_3\text{Zr}_2\text{O}_{12}$ (water and LiOH)^[235] powders were placed in water, leading to a rapid increase in pH^[235,239] Studies have shown that different lithium garnet compositions may experience different Li^+/H^+ exchange mechanisms, leaving the role of various metal ions in the ion-exchange mechanism unclear.^[235,240,242,243] For the preferable fast conducting cubic $\text{Li}_7\text{La}_3\text{Zr}_2\text{O}_{12}$, a spontaneous and rapidly reversible Li^+/H^+ exchange in water was observed without structure degradation, confirmed by a decrease in the lattice parameter due to the partial Li^+/H^+ exchange while the original cubic $Ia\bar{3}d$ structure was preserved.^[235,240]

After the Li^+/H^+ ion exchange upon exposure to aqueous solutions was observed in lithium-garnet-type powders, the effect of air exposure (mainly moisture and CO_2) was investigated for dense $\text{Li}_7\text{La}_3\text{Zr}_2\text{O}_{12}$,^[231] and Al-,^[136,229,230,233] Ta-,^[232] Ga-,^[244] Nb-,^[245] and Nb/Y^[246]-doped LLZO pellets. The garnet-type LLZO structure is thermodynamically unstable when exposed to ambient (dry to humid) air, leading to the formation

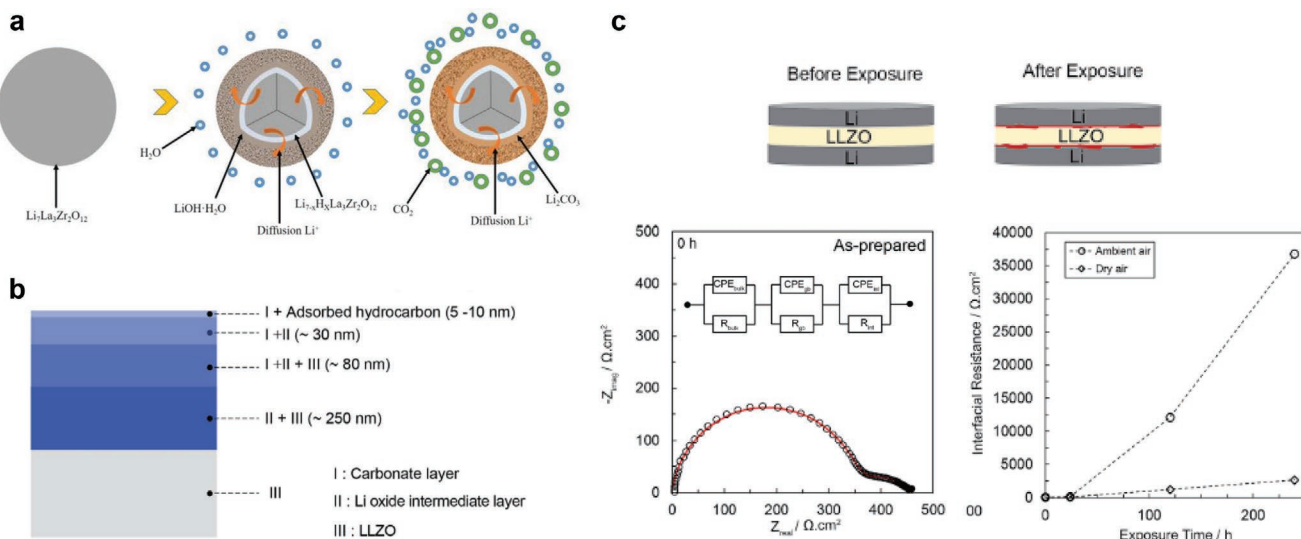


Figure 5. Effect of chemical stability of $\text{Li}_7\text{La}_3\text{Zr}_2\text{O}_{12}$ on a,b) Li_2CO_3 formation steps, and c) interfacial resistance. a) Reproduced with permission.^[508] Copyright 2016, Wiley-VCH. b) Reproduced with permission.^[229] Copyright 2017, the Royal Society of Chemistry.

of a lithium carbonate (Li_2CO_3) contamination layer and higher interfacial resistance at the Li/LLZO interface.^[136,229–231] At low-to-moderate temperatures ($25^\circ\text{C} < T < 200^\circ\text{C}$), the reaction is thought to consist of several sequential steps, including the Li^+/H^+ exchange and protonation of LLZO and the formation of a lithium hydroxide (LiOH) intermediate accompanied by Li and presumably O loss in LLZO, followed by LiOH reaction with CO_2 (carbonation) to form lithium carbonate (Li_2CO_3) (Figure 5a). Interestingly, Gibbs free energy considerations indicate that upon heating to $\approx 320^\circ\text{C}$, decomposition of Li_2CO_3 and deprotonation of LLZO occurs.^[229] Some minor differences in the estimation of the reaction layer thickness and constituents have been reported.^[229–231] A layer of Li_2CO_3 with a thickness of <100 nm, confirmed via X-ray photoelectron spectroscopy (XPS) and soft X-ray absorption spectroscopy (XAS), was reported for Al-doped LLZO samples (92% relative density) exposed to ambient moist air for several days (%RH not specified).^[230] In contrast, a thicker Li_2CO_3 layer (125–130 nm thick) was determined by XPS when Al-doped LLZO (97% relative density) was exposed to 50% RH; the Li_2CO_3 was accompanied by lithium oxide/hydroxide components after the first 5–10 nm for the next ≈ 360 nm until reaching the Li-deficient LLZO layer and then pristine LLZO bulk (Figure 5b).^[229] After 1.5–6 months of ambient and humid exposure ($\approx 50\%$ –80% RH), a micrometer-thick Li_2CO_3 reaction layer was observed,^[231,232] whereas ambient exposure of an Al-doped $\text{Li}_7\text{La}_3\text{Zr}_2\text{O}_{12}$ pellet for 1 year revealed its friable nature after prolonged exposure.^[234] The effect of moisture exposure on the charge-carrier transport properties has also been explored (Figure 5c).^[229] Although reports indicate that the bulk ionic conductivity of LLZO is only slightly affected by Li^+/H^+ exchange,^[229,242,243] a difference of almost one order of magnitude in the interfacial resistance (960 vs $109 \Omega \cdot \text{cm}^2$) was measured due to the formation of a nanometric thick (<100 nm) Li_2CO_3 reaction layer, which dramatically affected the overpotential for Li stripping plating and cycle life.^[230] When a LLZO pellet was controllably exposed to 0.5% and 50% RH for 10 days, the Li/LLZO interfacial

resistance unacceptably increased from $54 \Omega \cdot \text{cm}^2$ (polished under inert atmosphere) to ≈ 3000 and $\approx 37000 \Omega \cdot \text{cm}^2$, respectively. For context, in a typical LIB, the interfacial resistance is lower than tens of $\Omega \cdot \text{cm}^2$.^[40,46,47]

The effect of processing and resulting average grain size and grain boundary chemistry on the air stability of LLZO remains under debate.^[136,231,234,235,244] Reducing the grain size by one order of magnitude (from 200 to $20 \mu\text{m}$) was found to be effective in improving the air stability of LLZO pellets, with the interfacial resistance only doubling from 38 to $64 \Omega \cdot \text{cm}^2$ upon 24 h exposure to ambient air (%RH was not reported).^[231] Grain size was found to indirectly affect the stability of LLZO ($\approx 92\%$ relative theoretical density) under ambient air conditions through different sintering mechanisms, leading to enrichment of Al dopants mainly at grain boundaries compared to the pellet surface for large grains.^[231] Gibbs free energy analysis indicated that for higher Al and lower Li concentration at the surface, as observed for small-grain-sized LLZO, Al-doped LLZO was most likely form Li_2CO_3 via the kinetically slower direct reaction route with CO_2 in air rather than with moisture.^[231] However, the model was drafted without accounting for Li^+/H^+ exchange, which is critical to the understanding of the effect of dopants in LLZO on the air stability. Conversely, when Al-doped LLZO pellets with higher relative density (96% relative theoretical density) were investigated, the opposite trend was observed, indicating that larger grains and fewer grain boundaries offer fewer high-interfacial-energy regions for reaction and prolonged air stability, with a modestly high ionic conductivity of $\approx 10^{-4} \text{ S cm}^{-1}$ maintained for 3 months.^[136] This claim was also confirmed very recently for Ga-doped LLZO with an average grain size of $\approx 460 \mu\text{m}$ and relative theoretical density of 98%, with a negligible effect on the ionic conductivity after 12 days exposure at $\approx 30\%$ RH.^[244] It is important to note that the LLZO pellet was coated with 15 nm Pd during the air-storage period, which may have protected the pellet from reacting with moisture and CO_2 . In addition, the interfacial resistance values were not reported explicitly.^[244] Grain boundaries may also affect the air stability

of LLZO. On the one hand, grain-boundary susceptibility to moisture was clearly evident when a cleaved Al-doped LLZO pellet was exposed to ambient atmosphere for one week.^[234] It appears that Li_2CO_3 particles arranged around the grain boundaries, which was attributed to the susceptibility of the high-interfacial-energy regions.^[234] On the other hand, an HRTEM study of undoped-LLZO powder before and after exposure to water revealed no change in the grain-boundary features; the LLZO powder also did not contain any impurities or amorphous phases along the boundary.^[235] These discrepancies regarding the effect of materials properties on the air stability of LLZO necessitates further exploration to establish strategies to eliminate chemical degradation and high interfacial resistances.

A thorough investigation concluded that as-prepared LLZO powder readily reacts with moisture.^[229] One of the clearest parameter to decrease the reaction between LLZO and moisture is to densify and sinter the LLZO powder-compact into dense LLZO pellets. Whereas the cubic garnet structure of a dense pellet with 96% relative theoretical density was preserved after 6 weeks of exposure to 80% RH, forming a 25 μm thick Li_2CO_3 layer followed by a reduction in ionic conductivity ($6.45\text{--}3.61 \times 10^{-4} \text{ S cm}^{-1}$),^[232] a pellet with 83% relative density exposed to humid atmosphere ($\approx 75\text{--}85\%$ RH) spontaneously cracked and was pulverized after merely 3 weeks of exposure, mainly due to the formation of the pyrochlore phase $\text{La}_2\text{Zr}_2\text{O}_7$.^[233] As such, the introduction of a sintering agent (Al_2O_3 , Y_2O_3) can greatly reduce the susceptibility of LLZO to moisture and CO_2 by increasing the relative density.^[231,246] Recently, the microstructure of air-sintered LLZO was modified by controlling the powder size and eliminating powder agglomeration with freeze drying, achieving 98% relative theoretical density in addition to abnormal grain growth ($\approx 460 \mu\text{m}$) and minimal grain boundaries.^[244]

In conclusion, fast-conducting “cubic” LLZO can be synthesized, stabilized and densified at ambient atmosphere via classic sintering routes over 1000 °C, which is a tremendous advantage for manufacturing as compare to the processing for sulfide solid electrolyte. However, the postprocessing of LLZO dense pellets is more sensitive, restricting the exposure of LLZO pellets to up to 24 h under ambient air ($\approx 50\%$ RH) to limit the interfacial resistance below $\approx 150 \Omega \text{ cm}^2$.^[229] These issues may be overcome by surface polishing under an inert environment,^[230,232] which has been proven to effectively reduce the resistance of the Li/LLZO interface.^[230] However, the impracticality of this approach for mass adoption has shifted efforts toward suppressing the formation of Li_2CO_3 upon air exposure.^[231] As an alternative a codoping strategy of Nb and Y in the Zr sites was developed and implemented for LLZO, with improved air stability and resulted in only a small decrease in the ionic conductivity from 8.26 to $6.91 \times 10^{-4} \text{ S cm}^{-1}$ after 6 weeks exposure to air.^[246] It was hypothesized that both the i) high relative density of the codoped LLZO pellet considering Y_2O_3 is a well-known sintering agent and ii) lower valance of Y (+3) compared to Zr (+4) compensating for the lithium loss, that serves as sites for Li^+/H^+ exchange, due to the introduction of Nb^{5+} and thus improve the air stability. Also, lithium fluoride, LiF, has been used as an additive to form a protective layer covering Ta-doped LLZO grains, suppressing reactions with moist air.^[247] The additive suppressed the presence of surface absorbents species by 75% and decreased the Li/LLZO

interfacial resistance by $\approx 70\%$.^[247] Additionally, LLZO pellets with LiF were aged in air for two weeks without any Raman indication of lithium carbonate formation.^[247] The introduction of an optimal amount of the additive Li_3BO_3 also led to reduction of the total resistance of a Li/LLZO/Li cell after LLZO was exposed to ambient air for different time periods.^[248]

2.3.2. Sulfides

Despite the generally higher ionic conductivity of sulfides relative to oxides, their Achilles heel is their extremely poor air stability,^[214,249,250] as they undergo an hydrolysis reaction with water molecules, generating also toxic H_2S .^[214] The poor chemical stability requires tedious handling procedures under a dry inert gas atmosphere,^[150,78] increasing processing costs to maintain safety standards, and moving sulfide solid electrolytes further away from widespread commercialization. The poor chemical stability attributed to glassy sulfides is related to their structure, chemical bonding, and nonbridging sulfur (NBS) units in the glass network.^[250] Glasses with a lower concentration of Li-modifier units are more chemically stable because of the smaller number of NBS bonds, which are susceptible to chemical degradation. Lithium ions form an ionic bond with sulfur, which is generally weaker than the other covalent bonds of the glass network, making lithium ions prone to leach out due to reaction with water.^[250] The addition of the trivalent glass modifier Ga_2S_3 has been proven to improve the chemical stability of $\text{Li}_2\text{S}\text{--}\text{Ge}_2\text{S}_5$ glassy sulfides by eliminating NBS units.^[250] Structural units such as S^{2-} (in Li_2S) and *pyro*-thiophosphate ($\text{P}_2\text{S}_7^{4-}$) have been found to be more susceptible to structural changes and chemical degradation, whereas *ortho*-thiophosphate (PS_4^{3-}) Li_3PS_4 ($75\text{Li}_2\text{S}:25\text{P}_2\text{S}_5$) glass and glass-ceramic exhibit improved tolerance for hydrolysis because of the isolated nature of the PS_4^{3-} anion^[214] and the low reactivity of the PS_4^{3-} ion with water molecules in the atmosphere.^[214] The low chemical stability of sulfides may be addressed by compositional tuning (e.g., phosphorous-free or oxy-sulfide systems).^[71-73,251] Phosphorous-free, tin-based sulfides such as Li_4SnS_4 ($0.11 \times 10^{-3} \text{ S cm}^{-1}$ at room temperature),^[252] $\text{Li}_4\text{SnS}_4\text{--LiI}$,^[253] Sb-substituted Li_4SnS_4 , ($0.85 \times 10^{-3} \text{ S cm}^{-1}$ at 30 °C),^[71] and As-substituted Li_4SnS_4 ($1.39 \times 10^{-3} \text{ S cm}^{-1}$ at 25 °C)^[73] are a promising class of thio-LISICON solid electrolytes that possess high ionic conductivity and improved air stability, as explained by the hard–soft acid–base (HSAB) theory.^[73] According to the HSAB theory, small hard acids (Li, P > Ge) tend to react with hard bases (O), whereas large and polarizable soft acids (Sn, As) react with soft bases (S). As such, substitution of the hard acid (small and nonpolarizable P) with soft acids (large, polarizable Sn and As), which are less reactive toward the hard base O, is expected to increase the chemical stability toward moisture.^[73] Another approach to maintain high ionic conductivities in sulfides while improving the chemical and electrochemical stability is by partially substituting sulfur with oxygen by introducing oxides during the solid-state synthesis.^[251] For example, in $\text{Li}_{10}\text{GeP}_2\text{S}_{12}$ (LGPS), the introduced oxygen atoms are prone to form O–P bonds (better than O–Ge bonds), which are stronger than S–P bonds, thereby enhancing the thermodynamic stability and widening the electrochemical window ($\approx 0\text{--}10 \text{ V}$) while maintaining an exceptionally high ionic conductivity of $1.03 \times 10^{-2} \text{ S cm}^{-1}$ at

25 °C for $\text{Li}_{10}\text{GeP}_2\text{S}_{11.7}\text{O}_{0.3}$ (compared to $1.2 \times 10^{-2} \text{ S cm}^{-1}$ at 25 °C for $\text{Li}_{10}\text{GeP}_2\text{S}_{12}$).^[251] Importantly, the partial substitution of the soft base S with a hard base O is expected to improve the chemical stability even further in Sn/As-substituted LGPS as the soft acid Sn is less prone to be attacked by the hard base O than the soft base S. The strategy of using solid-electrolyte composites of sulfides with metal oxides such as $\text{ZnO}/\text{Fe}_2\text{O}_3/\text{Bi}_2\text{O}_3$, which favorably react with H_2S and act as absorbents,^[11,254] has shown promise with H_2S reduction upon air exposure, yet normally at the expense of electrochemical performance. Further clarification of the air stability of glass, glass-ceramic, and crystalline sulfides is urgently needed alongside out-of-the-box approaches to address the acute degradation of sulfides.

2.4. Mechanical Stability and Processability

Determination of the mechanical properties of solid electrolytes has become an increasingly pressing challenge, attracting considerable attention as key properties for the processing and assembling of solid-state battery architectures with improved electrochemical performance.^[150] The last is especially evident when the ionic conductivity and electrochemical properties of numerous solid electrolytes (e.g., $\text{Li}_{10}\text{GeP}_2\text{S}_{12}$, $\text{Li}_{9.54}\text{Si}_{1.74}\text{P}_{1.44}\text{S}_{11.7}\text{Cl}_{0.3}$, $\text{Li}_3\text{S}(\text{BF}_4)_{0.5}\text{Cl}_{0.5}$, etc.) have already equated or surpassed those of their liquid counterparts ($\approx 10^{-2}$ – $10^{-1} \text{ S cm}^{-1}$).^[40,78,255] Currently, only scarce literature data is available on the mechanical integrity of garnet-type LLZO^[119,137,178–181,256–258] and sulfide-type LPS^[149–151,155,259] and LGPS^[77,171,260,261] (Figure 3). During the operation of a solid-state battery, the contraction and expansion of the active material of the electrode during intercalation and deintercalation of Li^+ ions induces the formation of internal stress within the electrode structure and may lead to volume changes,^[262–265] poor interfacial contact toward the electrolyte being a solid, and fewer percolation pathways for Li diffusion due to fragmentation of the electrodes.^[150] Inorganic solid electrolytes are not only expected to relentlessly maintain intimate contact with both electrodes despite volume changes by compensating for stress through elastic deformation but are also expected to resist micro-crack formation and Li dendrite propagation. The mechanical properties of solid electrolytes can be divided into elastic, plastic, and fracture properties. The room temperature elastic moduli is of key importance characterized by entities such as the Young's modulus E , shear modulus G , bulk modulus B , and formability. These are traditionally evaluated from the molding pressure dependence on the relative density of compacted powders (Figure 3).^[149,266] Also, the hardness H (plastic behavior) and fracture toughness K_{IC} (fracture behavior) are also important mechanical properties, we will refer to these quantities throughout the following for oxides and sulfides.

2.4.1. Oxides

The Young's modulus is an intrinsic property determined by the crystal structure and chemical bonding of a solid material indicating stiffness.^[257] Although solid electrolytes generally exhibit a high Young's moduli, these are hard and brittle by

nature, and may crack or fracture upon applied pressure, their mechanical properties can significantly change depending on the type of solid ceramic used and its chemical composition. Oxides are brittle ceramics (low Pugh's^[267] B/G ratio) with high Young's modulus on the order of 100–200 GPa,^[257] normally measured using nanoindentation or acoustic impulsive excitation.^[119,137,178,180,256,257] Specifically, the Young's moduli of LLTO ($\text{Li}_{0.33}\text{La}_{0.57}\text{TiO}_3$), LATP ($\text{Li}_{1.3}\text{Al}_{0.3}\text{Ti}_{1.7}(\text{PO}_4)_3$), and LLZO have been reported to be ≈ 183 –200 GPa (nanoindentation),^[268–270] 115 GPa (stress-strain curves),^[271] and ≈ 140 –160 GPa,^[119,137,178,180,256,257] with significantly lower values for amorphous oxides such as $50\text{Li}_2\text{O}\cdot 50\text{P}_2\text{O}_5$, LiPON and $\gamma\text{Li}_3\text{PO}_4$ of 50 GPa,^[150] 77 GPa (nanoindentation),^[272] and 103.4 GPa^[273] (Figure 3). The relatively high elastic modulus of undoped LLZO (resp. tetragonal phase) measured by dynamic nanoindentation (i.e., the true material property) was determined to be $E = 156 \pm 9 \text{ GPa}$, indicating low elasticity, which can in turn translate into fracture and battery failure. By doping (e.g., Al, Ta) garnet-type LLZO and turning to its cubic phase, the elastic modulus can be further tuned (reduced) by 5%–20% through interatomic bonding (lattice parameter) and structural changes, considering the lower Young's modulus of the cubic LLZO phase relative to the tetragonal one.^[119] Although the grain size has been proven not to affect the Young's modulus in polycrystalline ceramics with micro-sized grains significantly,^[274] the experimental Young's modulus may be determined more by the chemistry itself and obviously by its porosity, flaws, and grain boundaries.^[119] Once the polycrystalline microstructural features of Al/Ta-LLZO (porosity 2%–8%) were taken into account via loads and indentation depths, even lower experimental and simulated values of the Young's modulus in the range of ≈ 82 –127 GPa^[119] and 140–146 GPa,^[137] respectively, were observed for cubic Al and Ta-doped LLZO.^[119] The large variation in the Young's modulus, even at high relative densities of LLZO, is a manufacturing limitation, especially as it can echo fracture toughness values and unforeseen battery failure.^[119]

Doped LLZO has been established as a material with isotropic elastic properties, as indicated by the Zener anisotropy ratio A of ≈ 1.3 for the cubic crystal (note that, $A = 1$ refers to an isotropic material).^[137] In isotropic elastic solids, the bulk modulus B and shear modulus G are correlated to the Young's modulus by the Poisson ratio ν ^[275] ($\nu_{\text{Ta}} = 0.24$ and $\nu_{\text{Al}} = 0.26$ for Ta- and Al-doped LLZO, respectively).^[137,276] The measured/estimated bulk modulus B (indicator of compressibility) and shear modulus G of LLZO are $\approx 100 \text{ GPa}$ ^[256] and ≈ 56 –61 GPa,^[137,256,257] respectively. Pugh's ratio B/G ^[267] is an estimation of the ductile/brittle nature of a solid material,^[77] with values higher than 1.75 indicating a transition from brittle to ductile behavior. Achieving good contact between the brittle electrolyte and composite electrodes is difficult and requires buffer layers. Thus, selecting solid electrolytes with decreased stiffness and gaining some degree of ductility is important to secure improved interfacial contact. According to Pugh's ratio (1.75 and 1.59 for Al-doped and Ta-doped LLZO, respectively),^[137] LLZO is an intrinsically brittle material, as also manifested by its low fracture toughness of $0.99 \text{ MPa m}^{1/2}$.^[181,137] For context, the typical fracture toughness of brittle soda glass is $0.7 \text{ MPa m}^{1/2}$, and that of ductile pure aluminum is 100 – $350 \text{ MPa m}^{1/2}$.^[277]

The Young's and shear moduli have been found to be closely related to dendrite penetration in LLZO, where a decrease in stiffness is consistent with crack propagation.^[257,278,279] Monroe and Newman^[279] employed linear elasticity theory to compute the effect of bulk mechanical forces on the formation of Li dendrites at the Li/solid electrolyte interface. They concluded that an electrolyte with a shear modulus greater than twice that of Li metal (i.e., $> \approx 2 \times 3.4\text{--}4.25$ GPa according to DFT calculation)^[137] should be theoretically sufficient to prevent dendrite propagation in the solid electrolyte. Undeniably, Li dendrite nucleation and propagation have been observed in different types of inorganic solid electrolytes (with the only exception being LiPON)^[42,280] despite fulfilling Monroe's shear modulus criterion.^[70,76,179,257,280\text{--}287] The model, developed for polymer electrolytes assuming an ideal system with a homogeneous Li/polymer electrolyte contact, was determined necessary but not sufficient, as dendrite propagation also depends on the integrity of the Li/electrolyte interface rather than only the elastic properties of the solid electrolyte.^[137] Wolfenstine et al.^[257] interpreted the criterion differently and suggested that it may be more appropriate to consider the shear modulus of the grain boundary (12–36 GPa for LLZO)^[257] instead of the bulk, bearing in mind that lithium dendrites preferably propagate at grain boundaries.^[286] The corrected Monroe–Newman criterion predicted lithium dendrite growth in the case of LLZO; however, additional work is required for further verification.

Although knowledge of the elastic constants is important to secure good contact in particular for composite electrodes and at the electrode/electrolyte interface for improved battery performance, the Young's modulus can also be used to estimate the fracture strength based on Griffith theory^[275] with DFT calculations accounting for crack lengths.^[275,276] The ability of a material containing cracks to resist fracture (fracture toughness) and to resist plastic deformation (hardness) is a pressing challenge for battery cell assembly and battery failure.^[288,178] Although some studies have found no obvious connection between the maximum CCD and fracture toughness but a strong dependence on the grain size,^[179] others have found a link between the mechanical properties and CCD in dense LLZO.^[180,288] Fractures are known to be initiated in ceramics at high current densities, leading to dendrite formation and propagation through the solid electrolyte.^[288] The CCD at which fracture initiates is a function of the fracture toughness to the fourth power, meaning that the smallest improvement in fracture toughness will lead to a substantial improvement in the critical current density.^[180,288] Fracture strength and toughness largely depend on flaws, cracks, and voids; thus, variability in solid-electrolyte manufacturing can have a catastrophic effect.^[275,289,70,76,179,257,280\text{--}287] Polycrystalline ceramic oxides typically exhibit hardness and fracture toughness in the range of 0.8–26 GPa and $\approx 1.5\text{--}15$ MPa m^{1/2}, respectively.^[276,290,291] The garnet LLZO, perovskite LLTO, and NASICON-type oxide LATP are stiff ($E \approx 100\text{--}200$ GPa) with hardness values of 6.8–9.9 GPa (depending on the grain size and porosity) with a single-crystal hardness of ≈ 9.1 ,^[178,179] ≈ 9.5 ,^[268,292] and 7.1 GPa,^[268] respectively, and an average fracture toughness of ≈ 1.25 , ≈ 0.92 , and ≈ 1.1 MPa m^{1/2}, respectively (relative density $> 97\%$) (Figure 3).^[180] Hardness is a global property depending not only on the crystal structure and

bonding^[293] but also on the microstructure, i.e., the porosity, grain size, defects, flaws, cracks, voids, grain boundaries, inhomogeneity, and secondary phases (as well as probe size).^[178,257,275,289] Cubic Ta-doped LLZO (relative density 92%–98%) exhibited large scatter in the single-crystal hardness, ranging from $\approx 9\text{--}12$ GPa (the large scatter was related to surface roughness); however, once considering microstructure features, the effective hardness was unified at $\approx 5\text{--}6$ GPa.^[119] Recently, the microscopic/local hardness of LLZO was assessed using the micro-pillar indentation splitting method and was determined to be ≈ 8.5 GPa (with a fracture toughness of 0.99 MPa m^{1/2}).^[181] The hardness values of LLZO, LLTO, and LATP indicate reduced plastic deformation in all three types of Li oxides, which in turn leads to extremely brittle behavior. The macroscopic fracture toughness for the transgranular fraction in LLZO ranges from 0.6–1.6 MPa m^{1/2} depending on the analytical equation, relative density, and technique used.^[178\text{--}180,268] An inverse correlation was observed between the relative density and fracture toughness of polycrystalline LLZO (Li_{6.19}Al_{0.27}La₃Zr₂O₁₂), attributed to the crack-deflection toughening mechanism along grain boundaries.^[178,294] The transgranular (viz. intragranular) fracture mode observed for high-relative-density (>97%) LLZO specimens implied stronger grain boundaries and good grain-to-grain contact and Li-ion transport.^[180] However, as the fracture toughness increased in low-relative-density LLZO specimens, the ionic conductivity decreased due to grain boundary resistance.^[178,180] Sakamoto et al.^[178] added partially stabilized ZrO₂ particles to the LLZO matrix to increase the fracture toughness without compromising the ionic conductivity. However, the high chemical reactivity of LLZO with different types of oxides (ZrO₂, Al₂O₃) during high-temperature treatments led to the evolution of the pyrochlore phase La₂Zr₂O₇, which moved that solution further away.^[257] The addition of a second glassy phase along LLZO grain boundaries was also suggested to maintain high ionic conductivity at the grain boundaries without compromising the mechanical strength.^[178]

2.4.2. Sulfides

Stiff solid electrolytes with high Young's modulus are subjected to larger stresses during volume changes, which can result in fracture and loss of contact between the electrolyte and electrode components. In contrast, glassy electrolytes with low Young's modulus can better accommodate large stresses via strain accommodation and favor electrode/electrolyte contact, which can lead to prolonged cycle life. Sulfides are regarded as ductile materials (larger Pugh's ratio B/G ; $\approx 1.75\text{--}2.5$)^[149] with high relative density and an intermediate Young's modulus of $\approx 10\text{--}20$ GPa,^[150] with glassy sulfides being "softer" than their glass-ceramic and crystalline counterparts (20–30 GPa).^[77] The Young's modulus of glass oxides can be estimated from its Coulomb forces (bond dissociation energies per mole per unit volume) and the packing factor (estimated from the mean atomic volume).^[151,295] The low melting and glass-transition temperatures, lower bond energy, lower ion packing density, large anions such as PS₄³⁻ and P₂S₇⁴⁻, and large free volume support the lower Young's modulus of glassy sulfides relative

to that of glassy/stiff oxides.^[151] [more Ref] The determination of the mechanical properties (e.g., Young's modulus, fracture toughness) of sulfides is challenging because of rapid surface degradation in air; the properties are generally measured using compression tests (for cold-pressed pellets),^[155] ultrasonic sound velocity measurements (for hot-pressed pellets),^[149] or special instrumented indentation measurements.^[259]

The mechanical properties of glass and glass–ceramic sulfides based on the $\text{Li}_2\text{S}-\text{P}_2\text{S}_5$ system can be tuned by replacing the Li_2S glass modifier, the glass former cation in the P_2S_5 former (e.g., SiS_2 , GeS_2), and/or by totally or partially replacing S with O via the introduction of oxides (e.g., P_2O_5 , Li_2O).^[149,151,296] The increase in alkali content, Li_2S (50–80 mol%),^[149] in LPS glassy sulfide systems results in a higher Young's modulus, increasing from 18 to 25 GPa,^[150] and up to one-order-of-magnitude higher ionic conductivity.^[297] In general, glass and glass–ceramic sulfides of the parent system LPS hot pressed with ≈99% relative density exhibit Young's, bulk, and shear moduli in the range of ≈13–28, ≈10–25, and ≈5–12 GPa, respectively with a Poisson ratio of $\nu = 0.26–0.32$.^[149,151,296,150] The large Pugh's ratio B/G in the range of ≈1.75–2.5^[149] indicates that sulfides are ductile materials, which can better accommodate elastic mismatch with adjacent electrodes. An exemplary glassy sulfide is 50 Li_2S –50 P_2S_5 (or 70:30 mol%) with a Pugh's ratio of 1.8, Young's modulus of ≈18 GPa,^[150,259] bulk modulus of 12.5 GPa, and shear modulus of ≈7 GPa,^[149,259] which is barely compliant with the Monroe–Newman criterion for dendrite propagation.^[279] The glassy sulfide 67 Li_2S –33 GeS_2 with a Pugh's ratio of 2.3 and slightly higher Young's modulus of 27.8 GPa, bulk modulus of 23.1 GPa, and shear modulus of 10.7 GPa may better satisfy the Monroe–Newman criterion.^[149] Moreover, glassy sulfides with modifier-rich compositions have been shown to improve densification and Young's modulus via structural changes from PS_3^- (*meta*-) to $\text{P}_2\text{S}_7^{4-}$ (*pyro*-) and the isolated structure of PS_4^{3-} (*ortho*-) with improved compacting capabilities (higher ion packing factor).^[149] The ability of sulfide to undergo elastic deformation without being damaged, i.e., formability,^[149] is higher for glasses than for crystals because of the isotropic nature and free volume of the structures. High formability is a clear advantage for powder compacting (densification) and for achieving intimate contact between the electrolyte and electrode, especially when employed as composites, via cold-pressing sintering and for compensating for volume changes associated with high discharge/charge capacity during battery operation.^[155] The hardness of amorphous LPS (70:30) was measured to be ≈1.9 GPa.^[259] For LPS, a fracture toughness K_{IC} of $0.23 \pm 0.04 \text{ MPa m}^{1/2}$ was measured by crack-length analysis; this value is comparable to that of the delithiated LCO cathode.^[298] Recently, a clear line was drawn between the CCD and the fracture strength (30–100 MPa for functional ceramics) of solid electrolytes, where lower fracture stress increases the probability of dendrite nucleation and low fracture toughness decreases the dendrite growth rate.^[58] The ≈80% lower fracture toughness of glassy LPS sulfides compared to garnet-type LLZO^[181] imply their low resistance to fracture and higher probability of dendrite formation (nucleation).^[259]

Glassy sulfides exhibit relatively low ionic conductivity unless Li halides are used.^[155] The pursuit of sulfide electrolytes with conductivities comparable to liquid electrolytes has focused

the search on crystalline sulfide electrolytes such as LGPS and LSPS.^[40,78] First-principles calculations were used to estimate the elastic properties of the ultrafast Li-ion conductor LGPS.^[77] The Young's modulus, bulk modulus, and shear modulus were calculated to be 37.19, ≈30.36, and 14.35 GPa, respectively, with a Poisson ratio of $\nu = 0.296$. LGPS exhibited ductility with a high calculated B/G ratio (2.12), indicating favorable processing of full-battery assemblies.^[77] The strong chemical bonding in LGPS (B) compared to its resistance to plastic deformation (G) indicates that stress-induced fracture will not easily occur.^[77] One major concern regarding solid electrolytes is their mechanical and electrochemical stability when part of the composite electrode or the adjacent electrode is under strain (the Young's modulus of sulfides is low compared to other electrode components). Ceramic sulfides may undergo mechanical deformation and decomposition during oxidation, which can substantially affect their electrochemical stability and require confined electrode architectures.^[261,299] Within this family of compounds, higher modulus is evident for compounds with excess Si content (e.g., $\text{Li}_{9.54}\text{Si}_{1.74}\text{P}_{1.44}\text{S}_{11.7}\text{Cl}_{0.3}$)^[40] and lower S and P content.^[299] The chemical potential is fundamentally coupled to volume changes via the Gibbs–Duhem relationship.^[300] Thus, volume changes and consequently evolution of strain could in principle lead to changes in the electrochemical stability. The electrochemical window of LGPS improved from 1.7–2.1 to 0.7–3.1 V by applying a controlled core and high-modulus rigid shell (e.g., amorphous Si; ≈140 GPa) microstructure, which hindered decomposition associated with expansion of the electrolyte. It was suggested that the microstructure of crystalline sulfide electrolytes (e.g., the existence of amorphous phases, controlled by synthesis) may govern the electrochemical stability and chemical compatibility at the interface.^[299]

Ultimately, mechanical consideration necessitates a solid electrolyte with high fracture toughness to prevent cracks and lithium dendrite propagation but moderate elastic modulus to prevent stress concentration at the interface. The rather low values of the elastic modulus and hardness of high-density LLZO specimens compared to those of other types of Li oxides, usually reflected in the fracture toughness, can be advantageous in terms of manufacturing, yet the large scattering needs to be addressed.^[119] A mixing of the electrolyte with one or two of the electrodes is considered vital to maintain intimate contact and minimize ohmic resistance during prolonged battery operation.

2.5. Electrochemical Stability

Along with high ionic conductivity, good electrochemical stability is an additional important benchmark toward the widespread commercial adoption of solid electrolytes. The operation of a battery, i.e., the operation of the main components with different chemical potential under applied voltage, requires estimation of the electrochemical stability of the solid electrolyte with consideration of the i) predefined potential range, ii) chemical compatibility between the electrolyte and electrodes, and iii) electrochemical stability at the electrolyte/electrode interface under battery operation (cycling). In the following section, we will address the first issue, and the chemical

and electrochemical reactions occurring at the interfaces will be addressed in later sections.

Research attention is aimed at improving the chemical compatibility and improving the effective electrochemical stability of the solid electrolyte at the electrolyte/electrode interfaces.^[59,82,83,135,301,302] The voltage stability window indicates the voltage range in which the solid electrolyte is stable and beyond which the material starts to insert or extract Li ions. In other words, the electrolyte can be reduced at the anode side by lithium metal with the uptake of Li ions and oxidized at the cathode side by the extraction of Li ions. Although a utopian ideal, a chemically stable solid electrolyte with a voltage stability window of $\approx(-0.5)$ –5.0 V is desired to be paired with a lithium-metal anode and high-voltage cathode, leading to minimal parasitic reactions during battery operation. A limited electrochemical stability window of the solid electrolyte may lead to its decomposition and the subsequent formation of an interphase layer, which, depending on its electronic and ion-transport properties, may impair the electrode/electrolyte interface integrity, significantly increasing the interfacial resistance. This in turn will limit the coulombic efficiency, leading to capacity fading and poor cycle performance in solid-state batteries. On the other hand, if Li binary decomposition products (LiF, Li₂O, Li₂S, Li₃P, Li₃N) of the solid electrolyte (e.g., LiI, LiCl, Li₂O, and Li₂S) formed during the low-voltage reduction of Li₇P₂S₈I, Li₆PS₅Cl, LIPON, Li₄GeS₄, Li₃PS₄, which are good electronic insulators and ionic conductors and thermodynamically stable against lithium metal, the interphase layer can effectively extend its electrochemical stability.^[59] As a general rule, the chemical composition and ion/electron transport properties, and thus the stability, of the SEI layer crucially affect the ability of the electrolyte to control self-limiting degradation and hence are imperative to the successful operation of solid-state batteries.^[59,60,76,82,83,135,238,301–303]

Initially, the experimental electrochemical stability windows of common solid electrolytes, such as LLZO and Li₁₀GeP₂S₁₂,^[304] Li_{3.25}Ge_{0.25}P_{0.75}S₄, Li_{9.54}Si_{1.74}P_{1.44}S_{11.7}Cl_{0.3},^[305] and Li₆PS₅X (X = Cl, Br, I)^[306] were greatly overestimated at \approx 0–9 V^[307,84] and \approx 0–5/7 V (and in some cases \approx 0–10 V),^[40,60,165,78,251,304–306] respectively. First-principles calculation confirmed that such thermodynamically stable electrolytes do not exist and that their instabilities result in a strong driving force for decomposition beyond their electrochemical stability window.^[59,82,83,135,238,301–303] For instance, the thermodynamically predicted electrochemical stability window of Li₁₀GeP₂S₁₂ and Li_{3.25}Ge_{0.25}P_{0.75}S₄ was \approx 1.7–2.1 V,^[76,82,302,303] in contrast to the wider experimentally measured voltage window of \approx 0–7 V (Figure 3, Figure 6a).^[40,60,165,78,251,304–306] Theoretical studies are a powerful tool to determine the intrinsic thermodynamic electrochemical stability window, defining the potential range where no reduction or oxidation of the solid electrolyte occurs.^[76,172,82,303,170] This is especially relevant to electrode/electrolyte stability studies, where arduous efforts are required to investigate interface reactions, further clarifying the need for chemical and electrochemical predictive modeling.^[302] The foremost computational methods used for estimation of the solid-electrolyte stability window include: i) the HOMO–LUMO method,^[172,303] which is the upper bound limit of the electrochemical stability window assuming inert electrodes, ii) the stoichiometry stability method applied to compute the insertion/extraction reaction of

a single Li atom into/from the solid-electrolyte structure,^[83,303] and iii) the phase stability (grand canonical phase diagram) method,^[172,303,82,59,302] which identifies equilibrium potentials of possible decomposition reactions and generally produces narrower stability windows than the aforementioned computation methods. Recently, an indirect thermodynamic pathway was hypothesized where indirect, kinetically favored decomposition mechanism was suggested via (de)lithiation of the solid electrolyte followed by further decomposition into the thermodynamically stable decomposition products.^[308] The redox activity of solid electrolytes was used to rationalize the larger electrochemical stability windows than those previously reported for direct decomposition routes for Li₆PS₅Cl, garnet LLZO, and NASICON LAGP.^[172,303,82,59,302] Nonetheless, the aforementioned modeling is associated with bulk thermodynamics; considering the sluggish kinetics of the electrolyte decomposition products and the formation of a passivating interphase layer that inhibits continuous decomposition, a wider effective electrochemical stability window has been attributed to and observed for most solid electrolytes.

2.5.1. Oxides

Oxides generally exhibit better oxidation stability than sulfides with the oxidation potential of most oxides being higher than \approx 3 V, including LLZO (2.9 V), LLTO (3.7 V), and LATP/LAGP (\approx 4.2 V) accompanied by the evolution of oxygen gas at high oxidation potentials and significant overpotential associated with poor kinetics.^[76,82,59,303] The high oxidation potential situates LLTO and LATP as solid electrolytes with the best electrochemical stability against cathode materials such as LCO. For LATP, there are some conflicting reports about the electrochemical stability window. According to the stoichiometry stability method, LATP is stable in the voltage window of 0.66–3.13 V (Figure 6b),^[303] whereas the phase stability methods declare a stability window with significantly higher reduction and oxidation potentials of \approx 2.2–4.3 V.^[59,82] Unfortunately, this discrepancy cannot currently be resolved as few experimental studies have been performed on the topic.^[309] Nonetheless, most oxidation decomposition products of oxides (but also sulfides) are Li-deficient and electronically insulating, which contribute to the stability and desired properties of the passivation layer.^[59]

Garnet-type LLZO not only exhibits high ionic conductivity at room temperature on the order of 10^{-3} S cm⁻¹ and a Li-ion transference number of unity but also possesses excellent stability toward Li metal (Figure 3). This material has one of the lowest reduction potentials of 0.05 V versus Li⁺/Li and thus a small thermodynamic driving force and the best resistance to be reduced (by Li metal) at 0 V, as confirmed both theoretically and experimentally.^[57,59,76,82,83,84] First-principles computation based on a Li grand potential phase diagram indicate that the thermodynamic electrochemical stability window of LLZO ranges between 0.05 and 2.91 V,^[76,82] which is considerably smaller than the experimentally reported window of \approx 0–6 V.^[84,307] At voltages higher than 2.91 V, oxidation of LLZO was presumed with the formation of Li₂O₂, Li₆Zr₂O₇, and La₂O₃ and the formation of La₂Zr₂O₇ accompanied by the evolution of O₂ due to the decomposition of Li₂O₂ at voltages higher than

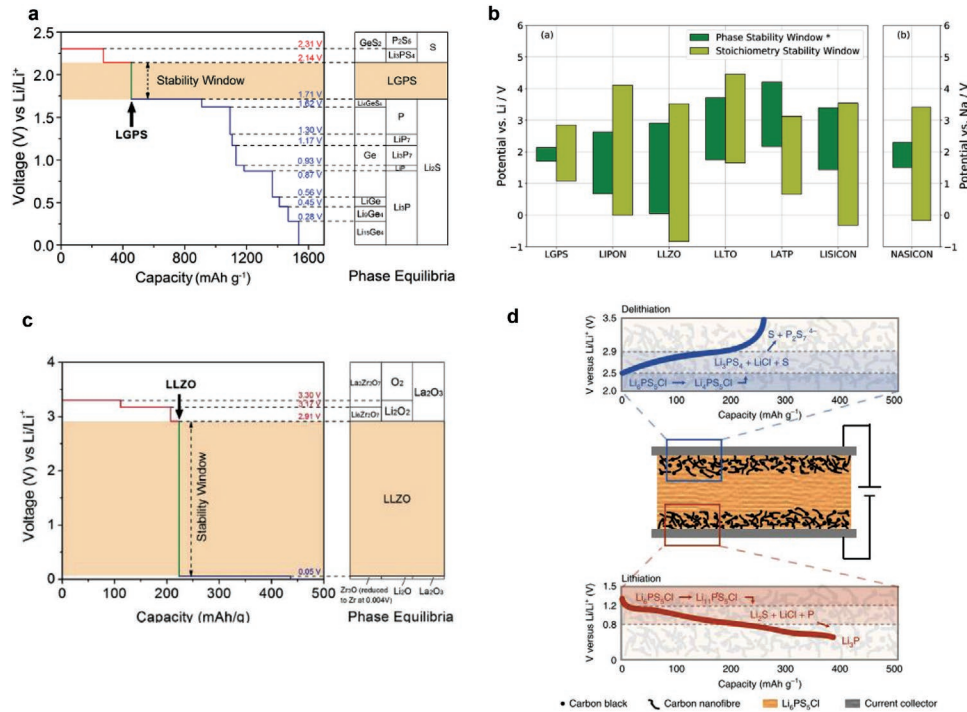


Figure 6. a) Electrochemical stability of $\text{Li}_{10}\text{GeP}_2\text{S}_{12}$. b) Stoichiometry stability windows and phase stability windows for various Li-SSE materials and NASICON. c) Electrochemical stability of $\text{Li}_{1-x}\text{Zr}_x\text{O}_3$ solid electrolytes. d) Schematic of the electrochemical activity of argyrodite LPSC on oxidation (delithiation) and reduction (lithiation). a,c) Reproduced with permission.^[76] Copyright 2016, Wiley-VCH, b) Reproduced with permission.^[303] Copyright 2020, the Royal Society of Chemistry. d) Reproduced with permission.^[308] Copyright 2020, the Nature Publishing Group.

3.3 V (Figure 6c). At voltages below 0.05 V, LLZO is reduced to Li_2O , La_2O_3 , and Zr_3O , which may be further reduced to Zr metal at ≈ 0 (0.004)V.^[76,308] X-ray photoelectron spectroscopy (XPS) analysis confirmed the reduction of Zr and oxidation of O in LLZO outside of its voltage stability window, indicated by the presence of thermodynamically-stable Zr_3O after discharge to 0 V.^[76] Similar to the case for sulfides, the experimentally improved electrochemical stability of LLZO is attributed to the surface passivation layer formed by the reduction and oxidation of the solid electrolyte at the anode and cathode sides, respectively, inhibiting further decomposition of the electrolyte.^[84,307] Unlike LGPS, the decomposition products of Li-garnet-type LLZO beyond its electrochemical stability window are not only electronically insulating but also ionically conducting (although poorly); thus, the use of a coating layer is not required but is recommended to increase the ionic conductivity and Li transport.^[76] Not all oxides are resilient to reduction, and perovskite-type LLTO, LISICON-type $\text{Li}_{3.5}\text{Zn}_{0.25}\text{GeO}_4$, and NASICON-type LATP and LAGP exhibit both theoretically^[59,82,303] and in most cases also experimentally^[309–313] a high reduction potential of ≈ 1.7 – 1.8 , 1.4 , ≈ 2.2 – 2.4 , and 2.7 V, respectively. The chemical composition, crystal structure,^[83] and inclusion of dopants^[315,314] have been observed to affect the electrochemical stability of lithium oxides.^[83,314] As a general rule, Ge^{4+} - and Ti^{4+} -containing oxide electrolytes (and possibly dopants such as Si, Sn, Al, and Zn)^[59] including NASICON-type LAGP ($\text{Li}_{1.5}\text{Al}_{0.5}\text{Ge}_{1.5}(\text{PO}_4)_3$), perovskite $\text{Li}_{3x}\text{La}_{2/3-x}\text{TiO}_3$ and $\text{Li}_{3.5}\text{Zn}_{0.25}\text{GeO}_4$ (LISICON) can be reduced and alloyed at low voltages to Li-Ge or Li-Ti, forming unfavorable electronically conducting interphases.^[59,312,315]

2.5.2. Sulfides

Generally, sulfide solid electrolytes exhibit poorer resistance to reduction and oxidation than oxides. Initially, the experimental electrochemical stability window determined via linear polarization of different types of sulfide electrolytes including $\text{Li}_{3.25}\text{Ge}_{0.25}\text{P}_{0.75}\text{S}_4$,^[165] $\text{Li}_{10}\text{GeP}_2\text{S}_{12}$,^[251] $\text{Li}_2\text{S}-\text{P}_2\text{S}_5-\text{LiI}$ ^[156] glass, and $\text{Li}_7\text{P}_2\text{S}_8\text{I}$ ^[316] was reported to be in the range of ≈ 0 – 5 / 10 V, excluding the Li plating/stripping process at ≈ 0 V. The wide experimental electrochemical stability window did not correspond to the limited electrochemical performance of sulfide-based solid-state batteries and was suggested to be associated with a passivation phenomenon resulting from the contribution of sulfide decomposition products.^[317,60] The use of the Li grand potential phase diagram to identify equilibria phases at different potentials and thermodynamically favorable reactions at specific potentials (assuming no kinetic limitations)^[76,172] revealed a significant narrowing of the LGPS experimental electrochemical stability window of ≈ 0 – 5 V,^[78] indicating the need for further research and clarification.^[317,60] A first-principles computation study indicated that the thermodynamically intrinsic stability voltage windows of sulfides, containing P^{5+} and high-valence ions such as Ge^{4+} , Sn^{4+} , and Si^{4+} , such as $\text{Li}_{10}\text{GeP}_2\text{S}_{12}$ (LGPS), $\text{Li}_{3.25}\text{Ge}_{0.25}\text{P}_{0.75}\text{S}_4$, Li_3PS_4 , LiGeS_4 , $\text{Li}_6\text{PS}_5\text{Cl}$, and $\text{Li}_7\text{P}_2\text{S}_8\text{I}$ are ≈ 1.6 – 1.7 and ≈ 2.1 – 2.3 V versus Li/Li^+ for the reduction of Ge^{4+} - or P^{5+} -containing sulfides and for the oxidation of S^{2-} , respectively.^[76,82,59,169] Recent DFT simulations, hypothesizing an indirect, kinetically favored decomposition route through (de) lithiation of argyrodite $\text{Li}_6\text{PS}_5\text{Cl}$, showed excellent agreement

to the stability window measured experimentally by galvanostatic investigation of ≈ 1.25 V ($\approx 1.25\text{--}2.5$ V), where oxidation and reduction were conducted on separate cells.^[308] It was suggested that the discrepancy observed until then between the theoretical and experimental stability window of common solid electrolytes, such as argyrodite $\text{Li}_6\text{PS}_5\text{Cl}$ (LPSC), garnet-LLZO, and NASICON-type LAGP, can be rationalized by considering an indirect decomposition of the solid electrolyte via lithiated and delithiated compositions instead of direct reaction to form final decomposition products.^[308] For the oxidation and reduction of argyrodite $\text{Li}_6\text{PS}_5\text{Cl}$, the compounds $\text{Li}_4\text{PS}_5\text{Cl}$ and $\text{Li}_{11}\text{PS}_5\text{Cl}$, respectively, were suggested to first form, followed by further decomposition into markedly more stable decomposition products, i.e., Li_3PS_4 , S, LiCl , and P, Li_2S , LiCl , respectively, as also previously indicated in other computational and experimental studies (Figure 6d).^[59,302,308,318] Here, the effective wider electrochemical stability window of argyrodite $\text{Li}_6\text{PS}_5\text{Cl}$ (LPSC) was attributed to not only kinetic stabilization via formation of indirect decomposition but also the electrolyte structure itself, which was suggested to contribute to the reversible capacity of the solid-state battery.^[308] The reversible decomposition reaction has perhaps contributed to the demonstration of a single-material-made battery (with the addition of conductive additive in the electrodes)^[304,308] but is also undesirable, causing volume changes, changes in the ionic conductivity, and an increase of the interfacial resistance upon cycling.^[260,318\text{--}321,76]

The combination of experimental and computational efforts supports the assumption that the experimentally determined electrochemical stability voltage window of $\approx 0\text{--}5$ V is not intrinsic to the material. The conflicting reports between the wide electrochemical stability window of 10 V associated with sulfides and the poor electrochemical performance of complete sulfide-based battery cells may be related to the experimental method used to determine the experimental stability window. It is possible that the relatively fast scanning rates and short dwelling time at high voltages do not fairly represent the sulfide stability and that high potentiostatic measurements at high voltages should be considered as a complementary investigation method to allow for subsequent chemical characterization of the solid electrolyte after prolong exposure to high voltages. Ceramic sulfides are an example of electrolytes with superb conductivities; however, reports of a narrow electrochemical stability window^[82,169,172] and interfacial reactions^[322,82,302] have caused their application in solid-state batteries to be questioned. The low oxidation and high reduction potentials of multiple sulfide electrolytes accompanied by the formation of an ion/electron insulating layer has led to the universal practice of electrode/electrolyte coating layers.^[323]

2.5.3. Food for Thought

The determination and identification of the intrinsic electrochemical stability window of solid electrolytes is of utmost importance to prevent the consumption and decomposition of the electrolyte during battery operation accompanied by ever-increasing interfacial resistance and deterioration of the electrochemical cell performance. According to computational studies, only a few solid electrolytes are thermodynamically stable

against metallic Li and against conventional cathode materials such as LiCoO_2 , LiMnO_2 , and LiFePO_4 (LCO, LMO, and LFP, respectively).^[59,82,135,302] Nonetheless, the thermodynamic stability window of the electrolyte does not need to extend beyond the voltages of the anode and cathode as kinetically limited passivation barrier layers constituted from decomposition products of the electrolyte can effectively widen the voltage stability window of the solid electrolyte and allow the stable operation of a battery cell.^[76] Moreover, it was recently proposed that the electrochemical stability window should be dictated by the oxidation and reduction potentials of the solid electrolytes (e.g., S and P for argyrodite, O and Zr for LLZO, and O and P for LAGP) and not by the most stable electrolyte decomposition products.^[308] The structural and chemical composition of the solid-electrolyte interphase layer passivate the interface, bridge/bring closer the chemical potential (in case of electronic insulation) between, for example, the Li metal and solid electrolyte, inhibiting further electrolyte decomposition and lowering the thermodynamic driving force for continuous decomposition of the electrolyte into the bulk.^[59,302,303] In liquid-based Li batteries, the formation of an insulating SEI is the key to the operation of the thermodynamically unstable Li metal in organic electrolytes and to the mitigation of continuous lithium consumption. In the solid-based systems, the formation of secondary interfacial phases with inferior Li ionic conductivity may be detrimental to the operation of solid-state batteries if the interfacial resistance gradually increases upon cell operation and battery cycling, which, in the case of electrical conduction, may ultimately lead to electrolyte consumption and short-circuit. Knowing the thermodynamic electrochemical window of a solid electrolyte is imperative to determining the operational voltage window of solid-state batteries with prolonged cycle life. Limited performance associated with gradually increasing interfacial resistance can at least partially be attributed to an overrated electrochemical operation window, which may lead to decomposition of the electrolyte and the formation of an interphase layer between the electrolyte and other components in the composite electrode and at the electrode/electrolyte interface. Greater attention should be placed on the investigation of the (de)lithiation redox potential (i.e., indirect decomposition mechanism) of the solid electrolytes to unfold their true potential and help better design electrolyte chemistries and interfaces.^[308] By coupling an appropriate electrode material with the solid electrolyte, decomposition of the electrolyte may be prevented or at least mitigated to some extent. One proposition is to couple a Li-In alloy anode (0.6 V) with a S cathode (2.3 V) to align with the electrochemical stability window of LLZO calculated as 0.05–2.91/3.5 V.^[76,308] However, such propositions are usually accompanied by lower voltage and capacity. Alternatively, coating layers^[324] can also be strategically applied to stabilize the electrode/electrolyte interface and reduce the interfacial resistance.

In the following sections, we will introduce acute challenges associated with the solid electrolyte/cathode and solid electrolyte/Li metal interfaces and discuss promising mitigation strategies. We start to discuss general cathode formation, origin of interfacial resistances and other strategies and approaches toward enhanced stability and performance including cathode coating, engineering microstructure and transport properties.

Then we turn to discuss Li-metal anode part, where we generally discuss the Li metal/solid electrolyte interfaces, both oxides and sulfides, focusing on chemical, mechanical and electrochemical instabilities including dendrite formation. Next, extensive evaluation of the interfacial resistance origins is presented alongside promising mitigation strategies. Lastly, we will finalize the review with a future perspective toward an ASSLBs highlighting promising approaches to resolve interfacial challenges and associated degradation phenomena.

3. Cathode: Toward True Solid

Interfacial impedance at the cathode side has been the main limiting factor in the overall performance even under a moderate charging/discharging rate. Sulfide- and oxide (garnet)-type solid electrolytes face serious interfacial issues during contact formation and battery operation.^[325] For example, the critical issue for sulfide-based cathode composites is the interfacial decomposition and chemical interdiffusion that simultaneously occur upon exposure to the high potential every charging step. As a result, insulating byproducts form at the interfaces and are the main source of the high interfacial impedance. Oxide-based cathode composites such as those based on Li-garnets mainly suffer from chemical compatibility issues during cathode preparation. Regardless of the class of solid electrolyte, interfaces between the active material and solid electrolyte often delaminate and suffer from contact loss during battery cycling because of the volume change of the active material during the Li intercalation and deintercalation process.^[200,326]

Needless to say, the solid-solid interfacial area in 3D cathodes for bulky and large-scale ASSLBs is much larger than, for example, that for planar-type microbatteries and typically use a single thin-film cathode (e.g., LiCoO₂, LCO).^[327] The use of a single cathode limits the cathode thickness to below $\approx 1\text{ }\mu\text{m}$ due to sluggish Li-ion conductivity, which in turn decreases the energy density and power performance.^[328–330] Conversely, a cathode for large-scale ASSLBs requires a thicker cathode, typically with a thickness of tens of micrometers or more, and can thus store a sufficient amount of energy.^[339] One way to ensure a thick cathode configuration without hampering performance is through the employment of a composite cathode arrangement with both the ionic conductor (solid electrolyte) and the active material strongly connected. It has been experimentally demonstrated that a 25 μm thick composite cathode consisting of LCO and LLZO (2:1 vol%) shows substantially higher cathode utilization (81% of its theoretical capacity) compared with a single LCO cathode (3%) with the same thickness and current density of 0.1 mA cm⁻² at 100 °C.^[331]

The multiparticle network of the composite cathode provides Li-ion percolation pathways for efficient redox reaction of the active material during battery operation. In contrast, in a conventional LIB, the aqueous organic electrolyte easily wets the entire surface of the active material, maximizing the contact area for reaction, the solid-solid contact in an ASSLB requires new chemistries and engineering strategies to efficiently provide high Li-ion transport percolation pathways while maintaining the chemical, mechanical, and electrochemical stability of the battery components. The geometric arrangement

and volume ratio of the two solid components in the cathode composite have been found to critically affect the battery performance,^[332–334] considering the electrochemical redox reactions are occurring at the cathode active material/solid electrolyte interfaces, i.e., at the active reaction sites. From a geometrical point of view, the cathode microstructure should be designed to minimize the charge-transfer/diffusion resistance during redox reactions by maximizing the active reaction sites as much as possible and increasing the number of reaction pathways. For example, an inhomogeneous distribution of active materials and/or discontinuity of the Li-ion transport pathway through solid electrolytes has led to high polarization resistance and low utilization of the active material.^[335] The aim of the design should be a well-distributed and continuous charge and mass transport network of each component. Finally, if the electronic conductivity in the cathode composite is limiting the performance of the composite cathode, the addition of a third component (i.e., carbon, oxide electronic conductors) must be considered. Unlike the solid electrolyte, the positive active material can induce concentration polarization, which may be alleviated to some extent if its conductivity increases and a more homogenous material utilization is achieved via the introduction of electronic conductors.^[336] Currently, the most studied active materials toward ASSLBs are layered cathodes (e.g., LCO or NMC), partially because of the high electronic conductivity, on the order of 10⁻⁴ S cm⁻¹ compared with that of other commonly used active materials (LiMn₂O₄ \approx 10⁻⁶ S cm⁻¹, LiFePO₄ \approx 10⁻⁹ S cm⁻¹),^[337] which also provides electronic transport pathways through the interconnected active material particles. Ultimately, high-density composite cathodes are required to improve the energy density while maintaining the aforementioned geometry criteria: (i) well-distributed and continuous network of each component for homogeneous reaction as well as Li-ion transport and (ii) a large number of active reaction sites of the active material and solid electrolyte.

The composite cathode processing strategy largely depends on the mechanical properties of the solid electrolyte and coassembly processing temperature of cathode and electrolyte constituent materials. Sulfide electrolytes can deform easily even at room temperature; thus, the composite cathode with desired microstructure can be fabricated by mechanically pressing the composite powder mixture. Thus, the microstructure with intimate contact in a sulfide-based composite cathode is readily achievable.^[150] In contrast, the preparation of an oxide-based cathode composite requires typically a sintering process at high-temperature, typically between 700 and 1050 °C, imposing new interfacial challenges by design and in processing. Without sintering, the interfacial area between the active materials and garnet electrolyte inside the composite cathode would be extremely limited and charge carriers involved in the redox reaction could only be transferred through very narrow interfaces that are made by point contacts, resulting in negligible reversible capacity.^[338] In addition, the thermal expansion coefficient between both materials should be matched during high-temperature processes to prevent mechanical delamination or cracking at the interface. Fabrication difficulties facing oxide-based composite cathodes have led to limited reports on the performance on the full-cell level, yielding less experimental demonstration of the superior properties of

oxide-based ASSLBs than those available for sulfide SEs.^[44] Given the limited reports, however, it is recently demonstrated that NASICON-type $\text{Li}_{1.5}\text{Al}_{0.5}\text{Ti}_{1.5}(\text{PO}_4)_3$ (LATP) oxide electrolyte as catholyte (the part of the electrolyte on the cathode side of an electrochemical cell) shows less degradation against oxidation and chemical interdiffusion during charge as directly compared to $\beta\text{-Li}_3\text{PS}_4$ (LPS).^[339] This result, the use of oxide as catholyte, shed light on the main degradation mechanism currently reported for state-of-the-art sulfide-based cathode composites. As soon as a fabrication strategy that satisfies intimate interfacial contacts and desired specific capacity based on active material loading is achieved, stable operation of oxide-based ASSLBs is anticipated.

In the following, we begin to discuss the origin of the interfacial impedance in solid-state cathodes followed by specific current issues at the interfaces for sulfide- and oxide-based electrolytes and active materials. Among the studies on oxide-based cathode composite, garnet electrolyte (LLZO) has been mostly investigated other than perovskite-type LLTO or NASICON-type LATP electrolyte due to the excellent compatibility of LLZO with metallic Li anode. Thus, we analyzed the literatures with special emphasis on garnet-based LLZO cathode composite. We discuss cathode coating as one of the important strategies to mitigate interfacial degradation followed by geometrical arrangement and conducting additives.

3.1. Origin of Interfacial Impedance and Current Pressing Issues at Cathode/Solid Electrolyte Interfaces

The interface between active materials and solid electrolyte can be defined as the bounding surface between and across the two components where a discontinuity in local structure, chemistry and their properties arise. In general, an interface is the region through which material parameters, such as the concentration of elements/charge carriers, crystal structure, electrical conductivity, defect density, elastic modulus, thermal expansion coefficient, etc., change from one side to the other. One or more of these changes may be involved at any given interface and can also show a gradient in case of interdiffusion at the phase boundary of the two constituent materials. The electrochemical performance of a composite cathode clearly depends on the combined property of the active materials, solid electrolyte, and their interfaces. The degree of discontinuity across the interface may be sharp or gradual depending on the interfacial mechanism.^[340] An example of a sharp interface may be the result of the wettability that can assist or impede adhesion at the interfaces. However, by definition, the wettability is the ability of a liquid to spread on a solid surface or represents the extent of intimate contact between a liquid and a solid; it does not necessarily mean a strong bond to the surface. In a perspective on ASSLBs, the formation of a solid electrolyte/Li metal interface is an excellent example as one of the simplest methods to assemble them is by melting Li metal on the surface of the solid electrolyte. A high interfacial impedance at the Li/solid electrolyte interface was reported because of the poor wettability of Li metal on LLZO electrolyte.^[80] Coating a thin metal or ceramic layer has been found to improve the wettability, lowering the interfacial resistance.^[194] Another example

is the role of the Li–B–O (Li_3BO_3 , LBO) compound during the formation of oxide-based cathode composites for ASSLBs, for which a high-temperature (>1000 °C) sintering process is often needed. Here, The LBO melts at ≈ 700 °C inside a cathode composite and forms an ionically conducting liquid phase to wet cathode compounds, providing intimate bonding between garnet solid electrolytes and cathode (e.g., LCO) particles, therefore lowering the interfacial resistance. Other types of interfacial joints for cathode composite constituents such as mechanical and physical bonding also create rather sharp interfaces for these. The degree of mechanical bonding is set by the contact area or length at the interfaces. For high mechanical bonding, one material must fill the hills and valleys on the surface of the other material. Surface roughness can contribute to mechanical bond strength depending on the void formation at the interface. Any bonding involving weak, secondary, or van der Waals forces; dipolar interactions; or hydrogen bonding can be classified as physical bonding. Thus far, the degree of physical bonding has not yet been explored, whereas the degree of mechanical bonding is reported to affect the interfacial formation. For instance, mechanical bonding may be considered the second important bonding mechanism at the Li/SE interface after wettability, and poor mechanical bonding can also increase interfacial resistance.^[341] At the cathode side, the formation of a sulfide-based cathode composite requires high pressure to create interfacial contact that is as mechanically sharp as possible.^[342]

Another type of interfacial bonding involves atomic, molecule, or electron transport, by diffusion processes, and chemical reactions (e.g., interdiffusion or decomposition), resulting in gradual interfacial bonding. This directly creates new phase in the interfacial zone, affecting the interfacial adhesion and electrochemical properties. The interfacial zone consists of near-surface layers of active materials and solid electrolytes and any layer(s) of material (interphase) existing between these surfaces. Regardless of the thickness of the interfacial zone, any type of interface properties can be largely affected by external conditions such as the processing temperature, difference in chemical potential, stress related to volume change of the active materials, etc. (Figure 7). Thermal treatment for intimate bonding (interfacial neck growth), applied potential during battery operation, and volume change of active materials upon lithiation/delithiation may lead to different modes of interfacial failure. Current issues in the formation of composite cathodes for ASSLB require careful attention for the design of electrochemically, chemically, and mechanically stable interfaces within components as well as a large number of active reaction sites to ensure sufficient kinetics for redox reaction. A number of interfacial issues leading to high impedances in composite cathodes have been identified over the last decade. These issues are subdivided into the four major categories below depending on two important external conditions (fabrication \approx processing temperature, operation \approx chemical potential difference in Li) (Table 1):

- A) chemical reaction during cell fabrication;
- B) electrochemical oxidation and chemical reaction during cycle;
- C) chemical reaction during cycle;
- D) chemomechanical degradation during cycle.

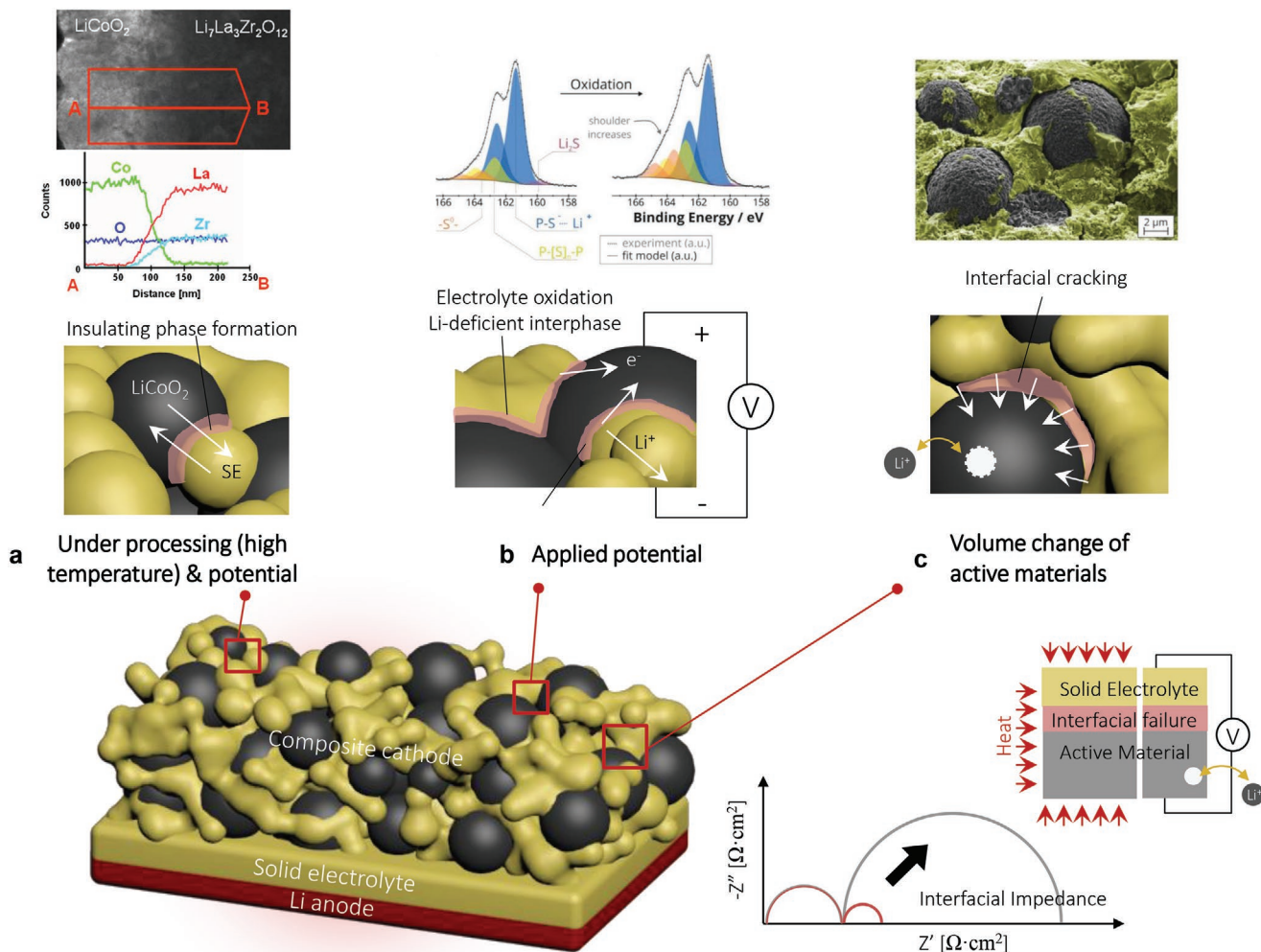


Figure 7. Common interfacial failure mechanism in all-solid-state Li metal batteries. a) Thermal treatment for intimate bonding (interfacial neck growth), a,b) applied potential during battery operation, and c) volume change of active materials upon lithiation/delithiation may lead to different modes of interfacial failures such as insulating phase formation due to a) interdiffusion, b) oxidation of the solid electrolyte, and c) interfacial cracking. a) Reproduced with permission.^[351] Copyright 2011, Elsevier. b) Reproduced with permission.^[320] Copyright 2017, Royal Society of Chemistry. c) Reproduced with permission.^[326] Copyright 2017, American Chemical Society. d) Reproduced with permission.^[509] Copyright 2020, Cell Press.

For this, various types of intrinsic interfacial stabilities have been accessed in both computational and experimental work. We begin to discuss the tendency of interfacial reaction and possible reaction products between the solid electrolyte (garnet, sulfide) and commonly used active materials such as LCO, $\text{LiNi}_x\text{Co}_y\text{Mn}_z\text{O}_2$ (NMC), $\text{LiNi}_x\text{Co}_y\text{Al}_z\text{O}_2$ (NCA), LiMn_2O_4 (LMO), and LiFePO_4 (LFPO) as well as high-voltage cathodes of $\text{LiNi}_{0.5}\text{Mn}_{1.5}\text{O}_4$, LiCoMnO_4 , and $\text{Li}_2\text{FeMn}_3\text{O}_8$. Then, we discuss how the interfacial instability affects performance as well as suggested strategies to realize high-performance solid-state cathode formation.

3.1.1. Interfacial Reaction during Cell Fabrication

Chemical reactions occur during cell fabrication (as well as cell operation) because of chemical mixing driving forces that typically exist at an interface. The high processing temperatures typically required to achieve intimate solid–solid contact

within oxide-based composite cathodes however accelerate chemical reaction kinetics and diffusion processes. The calculation of the thermodynamic reaction energy and possible reaction products using DFT has been critical to understanding experimental observations of the onset of reaction temperature, $T(rxt)$.^[61,82,135,302] A cathode composite system with several components can rarely be considered in thermodynamic equilibrium. More often than not, there will be a driving force for interfacial reaction between the two components, leading to a new state of thermodynamic equilibrium for the composite system. The reaction kinetics, the diffusivities of one constituent in another, etc. provide key information on the rate at which the system would tend to attain the equilibrium state. Because of this complex balance between thermodynamic driving forces and kinetically accessible mechanisms at the reaction temperature, most of this information cannot currently be quantified computationally. Instead, the computational methods have focused on capturing the maximal possible chemical driving force at an interface and the possible reaction

Table 1. List of reported interfacial degradation at sulfide and garnet electrolyte and oxide cathode materials.

Category	Solid Electrolyte	Active material (other components)	Measurement	Degradation	Ref.
A	Al–Li _{6.6} La ₃ Zr _{1.6} Ta _{0.4} O ₁₂	LiCoO ₂	XRD	Formation of LaCoO ₃ , LiCoO ₃ , Li ₂ CoZrO ₄ , and Li ₃ Zr _{0.18} Ta _{0.82} O ₄ at 1100 °C	[350]
A	Al–Li ₃ Zr ₂ O ₁₂	LiCoO ₂	XRD	Formation of t-LLZO at 700 °C	[338]
A	Li _{6.25} Al _{0.25} La ₃ Zr ₂ O ₁₂	LiCoO ₂	XRD	Stable up to 900 °C	[349]
A	Li _{6.25} Al _{0.25} La ₃ Zr ₂ O ₁₂	LiMn ₂ O ₄	XRD	Formation of Li ₂ MnO ₃ , La ₂ O ₃ , and La ₂ Zr ₂ O ₇ at 600 °C	[349]
A	Li _{6.25} Al _{0.25} La ₃ Zr ₂ O ₁₂	LiFePO ₄	XRD	Formation of Li ₃ PO ₄ , La ₂ Zr ₂ O ₇ , and Fe at 400 °C	[349]
A	Li _{6.6} La ₃ Zr _{1.6} Ta _{0.4} O ₁₂	LiNi _{0.5} Mn _{1.5} O ₄	XRD	Formation of Li ₂ MnO ₃ , La ₂ O ₃ , and La ₂ Zr ₂ O ₇ at 600 °C	[61]
A	Li _{6.6} La ₃ Zr _{1.6} Ta _{0.4} O ₁₂	LiCoMnO ₄	XRD	Formation of Li ₂ MnO ₃ at 600 °C	[61]
A	Li _{6.6} La ₃ Zr _{1.6} Ta _{0.4} O ₁₂	Li ₂ FeMn ₃ O ₈	XRD	Formation of Li ₂ MnO ₃ at 600 °C	[61]
A	Li _{6.75} La ₃ Zr _{1.75} Ta _{0.25} O ₁₂	LiCoO ₂	Raman XPS	Formation of LaCoO ₃ at 700 °C	[343]
A	Li _{6.75} La ₃ Zr _{1.75} Ta _{0.25} O ₁₂	LiNi _{1/3} Co _{1/3} Mn _{1/3} O ₂	Raman XPS	Formation of LaMO ₃ (M = Ni, Mn, Co) at 800 °C	[343]
A	Li _{6.75} La ₃ Zr _{1.75} Ta _{0.25} O ₁₂	LiMn ₂ O ₄	XRD	Formation of Li ₂ Mn ₂ O ₃ at 500 °C	[343]
A	Li _{6.75} La ₃ Zr _{1.75} Ta _{0.25} O ₁₂	LiFePO ₄	XRD	Formation of La _x Zr _{1-x} O _{2-2/x} , LaMO ₃ , Li ₃ PO ₄ and Fe at 500 °C	[343]
A	Li ₇ La ₃ Zr ₂ O ₁₂	LiCoO ₂	TEM	Formation of La ₂ CoO ₄ at 664 °C	[348]
A	Al–Li _{6.6} La ₃ Zr _{1.6} Ta _{0.4} O ₁₂	LiCoO ₂	Raman	Co diffusion into LLZO at 1050 °C	[200]
A	75Li ₂ S–25P ₂ S ₅ (glass ceramic)	LiNi _{1/3} Co _{1/3} Mn _{1/3} O ₂ (LiNbO ₃ coating)	XRD	Formation of CoNi ₂ S ₄ in air and Li ₄ P ₂ S ₆ under vacuum at 300 °C	[345]
B	Li _{6.75} La ₃ Zr _{1.75} Ta _{0.25} O ₁₂ (carbon-coated)	No active material (carbon, binder, liquid electrolyte)	CV	Clear cathodic current rises around 4.0 V Release of O ₂ when charged up to 4.5 V	[76]
B	Li _{6.625} La ₃ Zr _{1.625} Ta _{0.375} O ₁₂	No active material (carbon)	CV	Clear cathodic current rises at 3.7 V	[301]
B	Li ₃ PS ₄ glass	No active material (acetylene black)	XPS XANES	Formation of –S–S– bonds after cycle	[354]
B	β-Li ₃ PS ₄	No active material (carbon)	XPS	Formation of P-[S] _n -P and S ⁰ after 25 cycle (possible formation of Li ₂ P ₂ S ₆ , Li ₄ P ₂ S ₇ and Li ₄ P ₂ S ₈)	[320]
B	β-Li ₃ PS ₄	No active material (carbon)	XPS	Formation of –S–S– bond (Possible formation of S ₈ , P ₂ S ₅ , P ₂ S ₈ ⁴⁻ , P ₂ S ₇ ⁴⁻ , and P ₂ S ₆ ²⁻)	[355]
B	Li ₁₀ GeP ₂ S ₁₂	No active material (Pt)	CV	Clear cathodic current rises at 2.1 V	[76]
B	Li ₁₀ GeP ₂ S ₁₂	No active material (carbon, binder, liquid electrolyte)	CV XPS	Clear cathodic current rises at 2.7 V Formation of –S–S– bonds after charge	[304]
B	Li ₇ La ₃ Zr ₂ O ₁₂	–	DFT	Decomposed to Li ₂ O ₂ , La ₂ O ₃ , Li ₆ Zr ₂ O ₇ at 2.91 V	[59]
B	Li ₇ La ₃ Zr ₂ O ₁₂	LiCoO ₂	DFT	Decomposed to Zr, La ₂ O ₃ , Li ₈ ZrO ₆ at ≈3.1 V	[302]
B	Li ₃ PS ₄	–	DFT	Decomposed to S, P ₂ S ₅ at 2.31 V	[59]
B	Li ₃ PS ₄	LiCoO ₂	DFT	Decomposed to Li ₄ P ₂ S ₆ , Li ₂ S at ≈2.5 V	[302]
B	Li ₁₀ GeP ₂ S ₁₂	–	DFT	Decomposed to Li ₃ PS ₄ , GeS ₂ , S at 2.14 V	[59]
B	Li ₁₀ GeP ₂ S ₁₂	LiCoO ₂	DFT	Decomposed to Li ₄ GeS ₄ , Li ₄ P ₂ S ₆ , Li ₂ S at ≈2.3 V	[302]
B	Li ₆ PS ₅ Cl	–	DFT	Decomposed to Li ₃ PS ₄ , LiCl, S at 2.01 V	[59]
B	Li ₆ PS ₅ Cl	LiCoO ₂	DFT	Decomposed to LiCl, Li ₄ P ₂ S ₆ , Li ₂ S at ≈2.2 V	[302]
B, C	75Li ₂ S–25P ₂ S ₅ (Glass ceramic)	LiNi _{0.8} Co _{0.15} Al _{0.05} O ₂	TOF-SIMS	Formation of PO _{x-} and SO _{x-}	[364]
B, C	80Li ₂ S–20P ₂ S ₅ (glass ceramic)	LiCoO ₂	TEM	Interdiffusion of Co and S	[365]
B, C	β-Li ₃ PS ₄	LiNi _{0.8} Co _{0.1} Mn _{0.1} O ₂	XPS	The oxidized sulfur after 50th cycle	[339]
B, C	β-Li ₃ PS ₄	LiNi _{0.8} Co _{0.1} Mn _{0.1} O ₂	XPS	Formation of –S–S– bonds and PO _x after charge	[326]
B, C	Li ₁₀ GeP ₂ S ₁₂	LiNi _{0.5} Mn _{1.5} O ₄ (carbon)	XRD	Formation of secondary phase after cycle	[60]

Table 1. Continued.

Category	Solid Electrolyte	Active material (other components)	Measurement	Degradation	Ref.
B, C	Li ₁₀ GeP ₂ S ₁₂	LiCoO ₂ (LiNb _x Ta _{1-x} O ₃ coating, carbon)	XPS	Formation of —S—S— bonds after cycle 100th charge	[317]
B, C	Li ₁₀ GeP ₂ S ₁₂	LiCoO ₂ (LiNb _x Ta _{1-x} O ₃ coating)	XPS STEM, EELS	Formation of —S—S— bonds after 10 cycle Formation of Li depletion layer containing Co after cycle	[360]
B, C	Li ₆ PS ₅ Cl	NCM622	XPS TOF-SIMS	Formation of phosphate and sulfate after 100 cycle	[363]
B, C	Li ₆ PS ₅ Cl	LiCoO ₂ (carbon)	XPS	Formation of LiCl, P ₂ S ₅ , phosphates and —S—S— after 45 cycle	[361]
B, C	Li ₆ PS ₅ Cl	LiCoO ₂ (carbon)	XPS	Formation of S, Li ₂ S _n , P ₂ S _x , phosphates and LiCl after cycle	[362]
B, C	Li ₆ PS ₅ Cl	LiMn ₂ O ₄ (carbon)	XPS	Formation of S, Li ₂ S _n , P ₂ S _x , phosphates and LiCl after cycle	[362]
B, C	Li ₆ PS ₅ Cl	LiNi _{1/3} Co _{1/3} Mn _{1/3} O ₂ (carbon)	XPS	Formation of S, Li ₂ S _n , P ₂ S _x and phosphates after cycle	[362]
C	Li ₇ La ₃ Zr ₂ O ₁₂	LiCoO ₂	DFT	Formation of La ₂ Zr ₂ O ₇ , O ₂ , La ₂ O ₃	[302]
C	Li ₇ La ₃ Zr ₂ O ₁₂	Li _{0.5} CoO ₂	DFT	Formation of La ₂ O ₃ , La ₂ Zr ₂ O ₇ , Li ₇ Co ₅ O ₁₂ , O ₂	[82]
C	Li ₃ PS ₄	LiCoO ₂	DFT	Formation of Co(PO ₃) ₂ , CoS ₂ , S	[302]
C	Li ₃ PS ₄	Li _{0.5} CoO ₂	DFT	Formation of Co ₉ S ₈ , Li ₂ S, Li ₂ SO ₄ , Li ₃ PO ₄	[82]
C	Li ₁₀ GeP ₂ S ₁₂	LiCoO ₂	DFT	Formation of GeP ₂ O ₇ , S, CoS ₂	[302]
C	Li ₁₀ GeP ₂ S ₁₂	Li _{0.5} CoO ₂	DFT	Formation of Co ₉ S ₈ , Li ₂ S, Li ₂ SO ₄ , Li ₃ PO ₄ , Li ₄ GeO ₄	[82]
C	Li ₆ PS ₅ Cl	LiCoO ₂	DFT	Formation of CoS ₂ , S, CoP ₄ O ₁₁ , CoS ₂	[302]
D	Al-Li _{6.6} La ₃ Zr _{1.6} Ta _{0.4} O ₁₂	LiCoO ₂	Raman	Trans- and intergranular fracture after 100 cycles	[200]
D	β -Li ₃ PS ₄	LiNi _{0.8} Co _{0.1} Mn _{0.1} O ₂	XPS	Formation of pore at interface after charge	[326]

products.^[302] In the absence of thermodynamic and kinetic data, experimental studies would be necessary to determine the compatibility of the components.^[61,343] In all-solid-state cathode preparation, interfacial interactions are more frequent, which can cause changes in the constituent properties and/or interface structure. A schematic showing inter-diffusion phenomenon between Li₇La₃Zr₂O₁₂ and LiCoO₂, after resulting in solid solution as well as a layer of an intermediate phase, together with a real example, is presented in Figure 7a. The plateau region of the interfacial zone, which has a constant proportion of the two atomic species, is the region of interphase formation. The reaction products and reaction rates can vary, depending on the matrix composition and processing conditions such as the reaction temperature and time.

Sulfide solid electrolytes (LPSCl, LGPS, and LPS) are predicted to have a higher driving force for chemical reaction with the active materials than garnet solid electrolytes.^[302,344] This mainly originates from the strong tendency for the exchange of O and S between the sulfide solid electrolytes and oxide active materials to form PO₄³⁻ groups, which rationalizes why the sulfide solid electrolyte with LFPO interface exhibits the highest stability. For example, an onset reaction temperature of $T(rxt) \approx 300$ °C has been reported for the LPS/NMC interface ($E(rxt) = 422$ meV atom⁻¹).^[345] By considering high chemical reactivity from DFT calculation, little issue on chemical reaction during battery fabrication is reported because sulfide-based cathodes are mostly prepared at room temperature. Garnet-type solid electrolytes exhibit higher chemical compatibility with the active materials than sulfide solid electrolyte, which is

attributed to the difference in processing approaches derived from the difference in the mechanical properties of the solid electrolytes. The interfacial reactions that arise during fabrication can be found mostly at the garnet/cathode interface, whereas minor interfacial degradation occurs at the sulfide/cathode interfaces as most sulfide-based composite cathodes (and full cells) are typically processed by cold-pressing at room temperature.^[150,346] Garnet solid electrolytes generally exhibit higher mechanical strength than sulfide solid electrolytes, and high-temperature sintering is usually required to ensure good contact at the interface between garnet solid electrolytes and the cathode active material.^[61,137,347,348] As most cathode composite systems are nonequilibrium thermodynamic systems, a chemical potential gradient exists across the interface. Thus, given favorable kinetic conditions (which in practice means a high enough temperature or long enough time), chemical reactions will occur between the components. Therefore, most of chemical reaction during cell fabrication has been reported in garnet-based ASSLBs other than sulfide ones (Table 1).

LCO and Li(Ni_{1/3}Co_{1/3}Mn_{1/3})O₂ with a LLZO interface have a lower driving force (1 meV atom⁻¹) for chemical reaction than with LiMn₂O₄ (63 meV atom⁻¹) or LiFePO₄ (94 meV atom⁻¹) interfaces.^[82,344] The reaction tendency between LLZO and half-lithiated active material (LCO, NMC, NMO and LFP) is still the same but with increased reaction energy, indicating higher reactivity during charging. The reaction temperature $T(rxt)$ based on a pellet-type composite mixture (e.g., LLZO–LCO) was experimentally investigated by annealing at different temperatures (400–900 °C) and investigating the interfacial

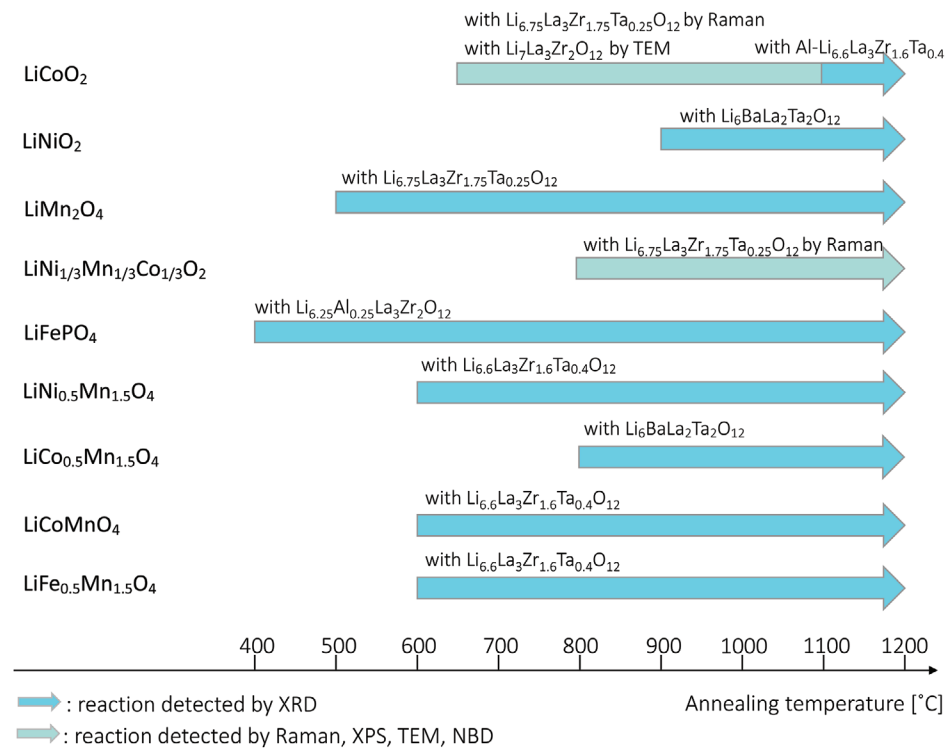


Figure 8. Chemical compatibility window of Li-garnet with oxide cathode active materials. Corresponding data are available in Table 1.

reaction products using Raman spectroscopy and X-ray diffraction (XRD). Encouragingly, the predicted tendency from DFT calculations has been quite consistent with experimental observations, indicating a lower interfacial reactivity of LLZO with LCO ($T(rxt)$: 700 °C) than with LMO or LFPO (both $T(rxt)$: 500 °C).^[343] Similar work has been performed using only XRD, showing the same tendency with different $T_{rxt} > 900$ °C for the LCO/LLZO interface, $T_{rxt} \approx 600$ °C for the LMO/LLZO interface, and $T(rxt) \approx 400$ °C for the LFPO/LLZO interface.^[349] In addition, the interfacial chemical stability showed $T(rxt) \approx 600$ °C between LLZO and high-voltage spinel-based active materials including Li₂NiMn₃O₈, LiCoMnO₄, and Li₂FeMn₃O₈.^[61] We summarize experimental observation for chemical stability of LLZO electrolyte with oxide cathode materials as function of annealing temperature (Figure 8). Comparing the results detected by XRD, oxide cathode active materials with rock salt layered-based (LCO, NMC, LNO)^[343,350,351] structure has apparently higher chemical stability against Li-garnet than ones with spinel-based (LiNi_{0.5}Mn_{1.5}O₄, LiCo_{0.5}Mn_{1.5}O₄, LiCoMnO₄, LiFe_{0.5}Mn_{1.5}O₄)^[61,351] and olivine-based (LFP)^[349] structure. In addition, it is shown that interfacial studies by Raman spectroscopy, XPS, TEM, or nanobeam electron diffraction (NBD) is more powerful tool than XRD to precisely identify the evidence of the reaction at lower temperature regime (rock-salt layered cathode against Li-garnet).^[343,348]

Thus far, LCO has been shown to form more stable interfacial stability with LLZO than other active materials. This has motivated numerous experimental efforts to achieve a deeper understanding between the interfacial impedance and performance of a full cell with LLZO–LCO cathode composite, implying that coassembly strategies of the composite cathode

other than LCO require to be investigated in the future. For example, in a recent study, differential scanning calorimetry (DSC) was used to investigate the reactivity of a LCO–LLZTO composite pellet, showing negligible reaction up to their sintering temperature ≈ 1050 °C except a minor reaction event at 700 °C.^[350] Subsequently, the same cathode preparation conditions were applied to ASSLB full-cell fabrication consisting of LCO–LLZTO as the cathode composite, LLZTO pellet as the solid electrolyte, and In–Li as the metallic anode, delivering a promising the first discharge capacity of 113 mA h g⁻¹ at a current density of 50 μA cm⁻² at 50 °C.^[200] To achieve intimate contact for the LCO/LLZO interface using a crystalline, micrometer-size LCO and LLZO powder, a sintering temperature over 1000 °C was required but with minor side reaction, which may be one of the reasons for the capacity being lower than the theoretical value.

To avoid potential reaction at high processing temperatures, LCO is often deposited at lower temperature (≤ 800 °C) either using a wet chemical method or physical vapor deposition. For instance, Li and Co acetate solution prepared by the sol-gel route was drop-coated on a LLZO pellet and then annealed at 800 °C, with no XRD evidence of interfacial reaction yet an interfacial resistance of several kΩ.^[352] Nonetheless, the reaction product of La₂Li_{0.5}Co_{0.5}O₄ was observed for a LCO/LLZO bilayer thin film fabricated via the sol-gel route at 800 °C.^[206] Likewise, a LCO thin film prepared on a LLZO pellet by pulsed laser deposition (PLD) and annealing at 664 °C resulted in an interfacial reaction product of La₂CoO₄, according to TEM–EDS and nanobeam diffraction analyses.^[348] Interestingly, another LCO thin film prepared by PLD at 600 °C on a LLZO pellet exhibited a relatively small interfacial resistance of 170 Ω cm²

at the cathode interface, and the full cell delivered a reversible charge/discharge capacity at a current density of $3.5 \mu\text{Acm}^{-2}$ for 100 cycles.^[353] Comparison of these low-temperature methods indicates that the LLZO/LCO interfaces formed at 800°C ^[352] and 664°C ^[348] produced more resistive interfaces than that formed at 600°C ,^[353] highlighting that a reduced processing temperature down to 600°C is beneficial for lowered chemical reaction and cathode impedance for the LCO/LLZO system. Collectively, the preparation of one of the composite components via a wet chemical process and low temperature may avoid high-temperature-driven interfacial reactions; however, the issues of low loadings and poor utilization of the active material remain unresolved, making these approaches impractical for high-energy-density ASSLB fabrication.

3.1.2. Electrochemical Oxidation and Chemical Reaction during Cycle

Interfacial degradation may occur not only during cell fabrication but also during battery operation, typically at the cathode side upon charging. Solid electrolytes adjacent to the electron source (active material) are subjected to electrochemical decomposition beyond their oxidation limit as well as to chemical reaction due to chemical mixing. A literature survey indicates that sulfide-based cathode composites are highly susceptible to degradation, primarily because of their lower oxidation limit and higher reactivity with active materials than garnet-based cathode composite (Table 1). The cathode interfacial degradation from electrochemical oxidation is apparent from the major capacity loss after the first charge and subsequent capacity fading upon cycling.^[60,320,326,354,355] Intensive experimental and computational efforts have been made to probe the chemical reaction or decomposed products at the interfaces.^[57,356] On the experimental side, substantial efforts have often been made using cyclic voltammetry (CV). XPS and TEM have emerged as a common approach for probing and identifying the element and composition present at the buried electrode/solid electrolyte interface. On the computational front, first-principles calculations have emerged as an important tool to predict interfacial reaction products.^[325,357] DFT grand potential phase diagrams at various chemical potential values have been used for similar purposes.^[358] The grand potential method represents the narrowest electrochemical stability due to the kinetic limitation, and the widest electrochemical stability window for solid electrolytes can be estimated using the topotactic stability method.^[169]

As mentioned, chemical reactions can be driven by applied voltage and resultant different degree of lithiation of oxide cathode during cell cycling affects the reactivity of solid electrolytes with oxide cathode materials even at room temperature (Figure 7a). This has been observed for sulfide-based cathode composites because of the strong reaction energy between the PS_4 groups and oxide cathodes, forming PO_4^{3-} groups and transition-metal sulfides under cycling condition.^[302] The effect of charging on the chemical reaction may be explained by the computed chemical reactivity between the charged or delithiated cathode and sulfide solid electrolytes being even more pronounced than that for discharged compounds.^[82] For example, DFT calculation predicted a high driving force for chemical reaction between sulfide solid electrolytes and charged LCO to

form Co_xS_y or PO_4^{3-} and SO_4^{2-} polyanions.^[344,357] Experimentally, a compatibility study of $\beta\text{-Li}_3\text{PS}_4$ and $\text{LiNi}_{0.8}\text{Mn}_{0.1}\text{Co}_{0.1}\text{O}_2$ showed no evidence of such products before cycling. After cycling, however, an interfacial reaction of the P-O_x species was observed as a result of chemical interdiffusion.^[326] Compared with those on sulfide solid electrolytes, there have been relatively fewer experimental studies on the chemical reaction of garnet solid electrolytes under room-temperature cycling because of the smaller reaction energy with common cathode materials (LCO, NCM, LMO, LFPO) at given battery operation condition.^[344] Knowledge of the chemical reaction at the interface is of importance. If there is an adverse effect on the interfacial resistance and electrochemical performance, alternative strategies must be considered to avoid or mitigate interfacial reactions. It is thus imperative to understand the thermodynamics and kinetics of reactions in order to control processing and achieve optimum properties.

Cathode interfaces are subjected to applied voltage during cell operation; thus, solid electrolytes adjacent to active materials can be decomposed outside their electrochemical window or beyond their oxidation limit. Although the electrochemical stability window is a bulk property of a solid electrolytes rather than a property of the interface with active material interface, it is still important to the interface stability as the electrochemical decomposition of the solid electrolyte typically occurs at the interface with an electron source from active materials or carbon; thus, the solid electrolyte in a cathode composite directly experiences the applied potential difference (Figure 7b).^[325] DFT calculation predicts that the electrochemical window for most solid electrolytes is below the redox potential of commonly used cathode active materials such as LCO (3.8 V), NMC (3.8 V), LMO (4.1 V), and LFP (3.5 V).^[359] As mentioned, calculation results show that the sulfide solid electrolytes based on thio-phosphates (i.e., LGPS or Li_3PS_4) are oxidized at ≈ 2.15 – 2.31 V, whereas garnet-based solid electrolytes (e.g., LLZO) are oxidized at 2.91 V.^[82] However, these calculated results contradicted some experimental results, where a wider oxidation limit of ≈ 5 V was reported for LGPS^[78] and LLZO^[84] solid electrolyte pellets sandwiched by Li and Au planar electrodes. Interestingly, a recent study using the same solid electrolytes showed that the oxidation current near the calculated potential could be clearly observed by replacing the planar Au electrode with a composite cathode type (LGPS/carbon or LLZO/carbon), therefore increasing the reaction area.^[76] For sulfide solid electrolyte, the decomposed materials have been computationally predicted to be S, P_2S_5 , $\text{Li}_4\text{P}_2\text{S}_6$, and Li_2S for Li_3PS_4 and Li_3PS_4 , GeS_2 , S, Li_4GeS_4 , $\text{Li}_4\text{P}_2\text{S}_6$, and Li_2S for LGPS at the onset of oxidation.^[59,302] The oxidized products with S–S bond for both $\beta\text{-Li}_3\text{PS}_4$ ^[320,326,355] and LGPS^[317,360] were experimentally confirmed in the composite cathode after cycling, which could affect cycle performance.

Experimentally, $\beta\text{-Li}_3\text{PS}_4$,^[59,320,326,339,354,355] $\text{Li}_{10}\text{GeP}_2\text{S}_{12}$ (LGPS),^[59,76,302,304] and $\text{Li}_6\text{PS}_5\text{Cl}$ ^[59,302,361–363] have been the most explored as components of cathode composites. XPS analysis was used to analyze the possible interfacial products from the increase of the oxidized species in the S 2p and P 2p signals in the spectra (Figure 7b). For example, the sulfide battery employing $\beta\text{-Li}_3\text{PS}_4$ and a cathode composite of $\text{LiNi}_{0.8}\text{Co}_{0.1}\text{Mn}_{0.1}\text{O}_2$ (NCM-811) and $\beta\text{-Li}_3\text{PS}_4$, increasing the

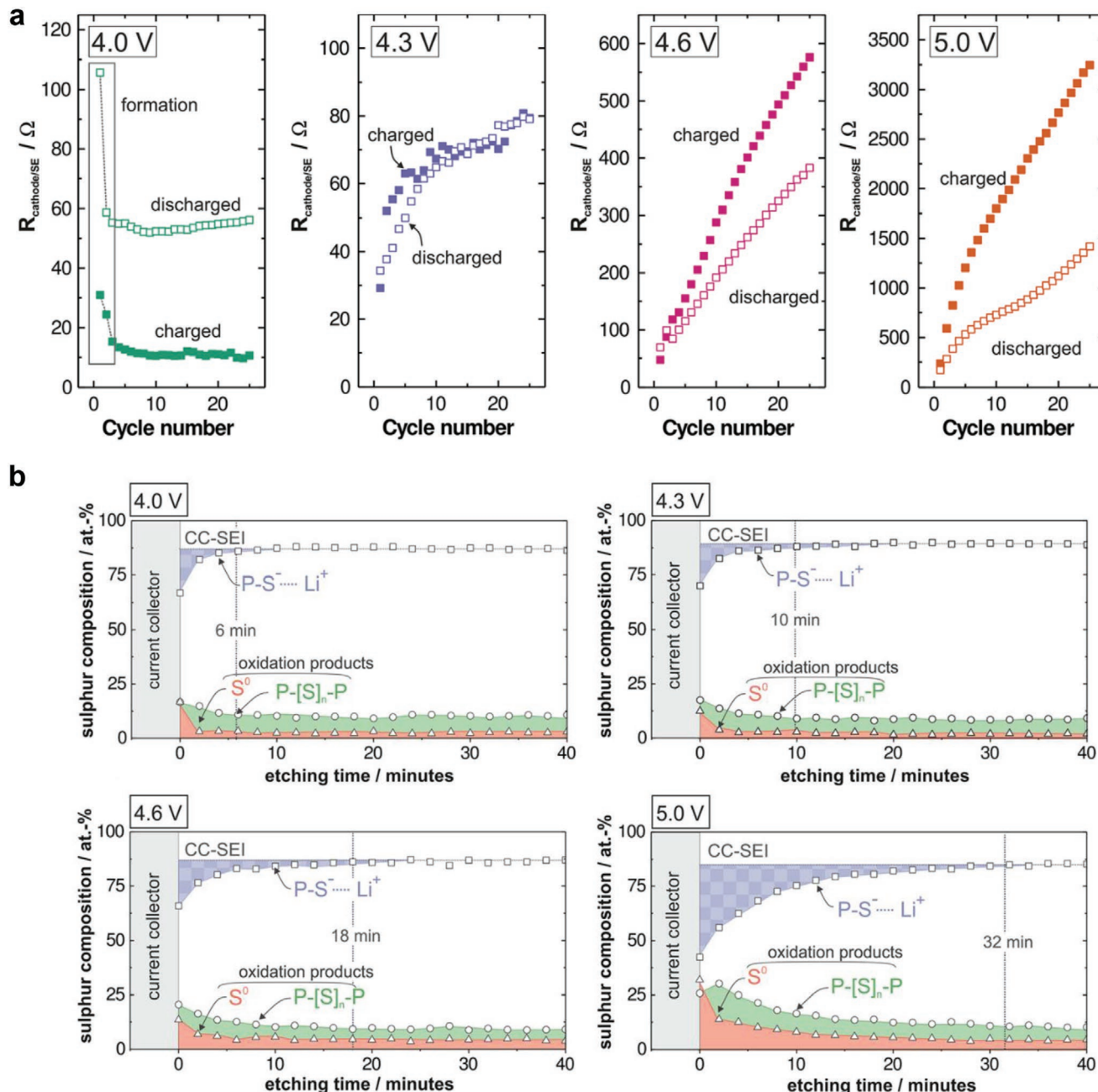


Figure 9. a) Evolution of interfacial resistance at cathode/sulfide electrolyte interface upon cycling for $\text{Li}-\text{In}||\beta-\text{Li}_3\text{PS}_4|\text{NCM-811} + \text{b}-\text{Li}_3\text{PS}_4$ batteries charged to different upper cut-off voltages between 4.0 and 5.0 V. b) Quantification of the cathode interface at the current collector from XPS S 2p spectra at different etching times and for different upper cut-off voltages ranging from 4.0 to 5.0 V. a,b) Reproduced with permission.^[320] Copyright 2019, Royal Society of Chemistry.

cathode interfacial impedance led to the formation of a passivating interphase upon charging above 3.8 V versus Li^+/Li and irreversible capacity loss after the first cycle at $214 \mu\text{A cm}^{-2}$ (0.1 C).^[326] These changes stemmed from the formation of P_2S_5 as the corresponding oxidized product. A similar interfacial product during charge was also reported when β - Li_3PS_4 was used as one of the cathode components in other studies.^[320,326,339,354,355] More specifically, the effect of different cut-off voltages from 4.0, 4.3, and 4.6–5.0 V on the interfacial

resistance of the β - Li_3PS_4 –NCM811 interface was investigated for a $\text{Li}-\text{In}||\beta-\text{Li}_3\text{PS}_4||\beta-\text{Li}_3\text{PS}_4$ –NCM811 cell (Figure 9a).^[320] Using electrochemical cycling experiments, electrochemical impedance spectroscopy (EIS), and ex situ/in situ XPS, significant interfacial resistance was shown to evolve, severely affecting the battery performance above charging voltages of 4.3 V. Furthermore, depth profiling of the forming interphase revealed that most of the decomposition occurred in direct contact with the current collector, explaining the local electric potential drop,

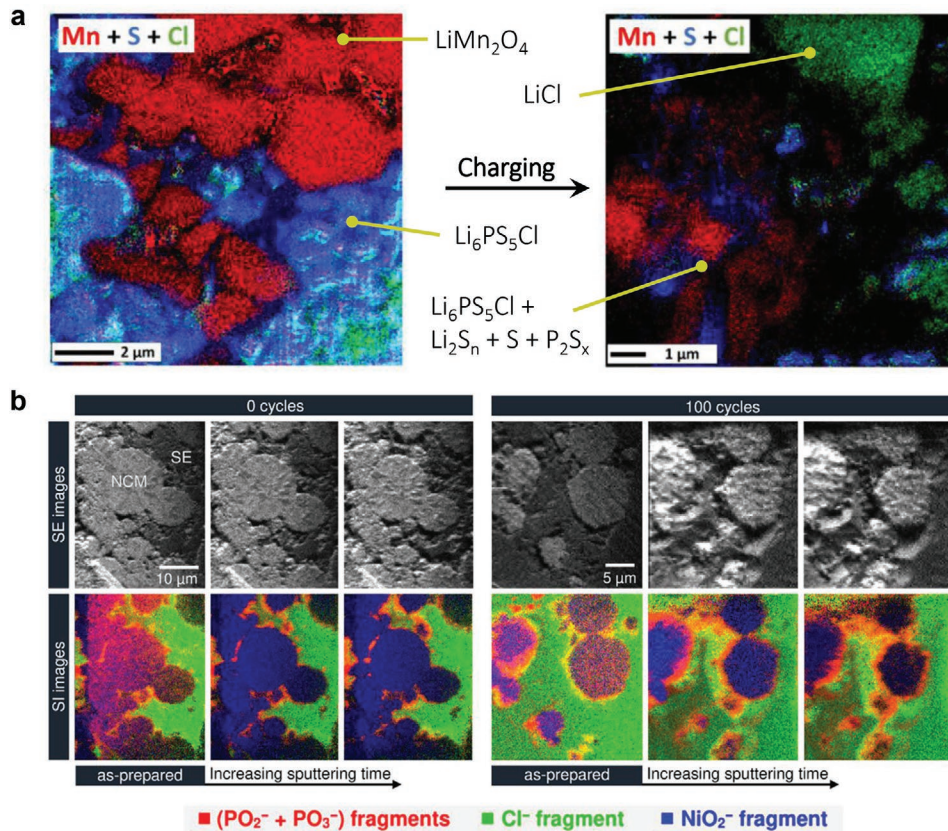


Figure 10. Elemental mapping of solid electrolyte interphase in sulfide based cathode composite. a) SAM mapping of Mn, S, and Cl elements from a cross section of the composite LiMn_2O_4 electrode of the $\text{LiMn}_2\text{O}_4/\text{Li}_6\text{PS}_5\text{Cl}/\text{Li}-\text{In}$ half-cell before and after charging. b) ToF-SIMS measurements on crater sidewalls for cathodes (NCM622/ $\text{Li}_6\text{PS}_5\text{Cl}$ interface) before and after cycling, showing a significant increase of PO_x^- - and SO_x^- -fragments due to battery cycling. a) Reproduced with permission.^[362] Copyright 2017, the American Chemical Society. b) Reproduced with permission.^[363] Copyright 2019, the American Chemical Society.

which is necessarily the highest at the current collector interface, as also shown by theoretical calculations (Figure 9b).^[320] The cut-off voltage and associated potential drop determined the thickness of the degradation layer, highlighting the need to protect the active material particles by such as coating and that the interface between the SE and current collector itself must be engineered.

With a LGPS SE, the theoretically predicted oxidation limit of 2.1 V (vs Li^+/Li) has been experimentally observed by CV investigation using a $\text{Li}|\text{LGPS}|\text{LGPS-Carbon}|\text{Pt}$ cell. Precise measurement was achieved by adding carbon to LGPS to increase the contact area between LGPS and an electron conductor for increased charge-transfer reaction, thus increasing the extent of the decomposition reaction.^[76] The oxidation of LGPS only started at 2.14 V into interfacial decomposition products of Li_3PS_4 , S, and GeS_2 , and the Li_3PS_4 was further oxidized into S and P_2S_5 above 2.31 V.^[59,76,304] The oxidation products at the interface, such as P_2S_5 , S, and GeS_2 , were neither electronic nor ionic conductive, increasing the cathode impedance.

The interfacial stability of the argyrodite-type $\text{Li}_6\text{PS}_5\text{Cl}$ (LPSC) solid electrolyte has been widely tested as a cathode composite with commonly used active materials of LCO, LiMn_2O_4 (LMO), and $\text{LiNi}_{1/3}\text{Co}_{1/3}\text{Mn}_{1/3}\text{O}_2$ (NMC).^[361–363] Regardless of the active materials used, LPSC was oxidized into typical decomposed

products (S, P_xS_y) but with a new phase of LiCl (Figure 10a).^[362] A scanning auger microscopy (SAM) image of the LMO-LPSC composite revealed clear phase separation between the LiCl particles and sulfur-containing particles after 22 cycles at current density of $66 \mu\text{A cm}^{-2}$. Before the cycle, a weak polysulfide signal from the XPS spectra was only detected on the surface of NMC and LMO, not in LCO. After the cycle, LMO contained a larger amount of oxidized sulfur species and polysulfide than LCO, whereas NMC contained less oxidation species than LMO. Overall, the degree of the decomposition reaction at the interface is proposed to follow the order LCO < NMC ≪ LMO. Interestingly, the oxidation processes of LPSC in the $\text{Li}-\text{In}|\text{LPSC}|\text{LPSC-NMC}$ cell did not hinder the cyclability over 300 cycles after a significant loss during the first 25 cycles. The partial reversibility (reversible formation of elemental sulfur and polysulfides) in the LPSC solid electrolyte may lead to the reversible capacity of the composite electrode.^[308]

Coming back to the differences in reactivity toward LPSC observed between the active materials, this is not only a result of the decomposition of the solid electrolyte (electrochemical reaction) but also the chemical reaction between the solid electrolyte and active materials during room-temperature cycling. Occasionally, chemical reaction is even reported in uncycled cathode composites, as mentioned above,^[362] and the growth of

the interfacial zone from both electrochemical decomposition and chemical reaction expands during charging and cycling. Importantly, the predicted interfacial compounds either from oxidation of the solid electrolyte or interdiffusion usually have different forms, assisting the interpretation of experimental observations.^[344] Typically, formation of the sulfate (SO_x^-) and phosphate (PO_x^-) provides direct evidence of chemical reaction because the oxygen from the active materials reacts with sulfur and phosphorous from the solid electrolyte.^[361,362,364] Recently, the XPS technique was expanded to 3D reconstructions of depth profiles and ToF-SIMS surface imaging of FIB crater sidewalls to obtain more detailed information on the composition of the SEI and visualization of its morphology.^[363] The SEI layer of LPSC-LiNi_{0.6}Co_{0.2}Mn_{0.2}O₂ (NMC622) composite cathodes mostly consists of phosphate- and sulfate-like species as well as polysulfides. The SEI layer of maximum 10 nm thickness was formed by an interfacial reaction between the NCM622 particles (oxygen source) and the solid electrolyte (phosphorus and sulfur source), resulting in a uniform shell around the NCM622 particles after 100 cycles at a current density of 214 μAcm^{-2} (0.1C) (Figure 10b). The interfacial products such as elemental sulfur, polysulfides, and phosphate- and sulfate-like species have mostly been reported. In addition to the exchange of P and O, cobalt sulfide compounds are also produced as a result of chemical interdiffusion after the 1st charge at the interface between LiCoO₂ and the Li₂S-P₂S₅ electrolyte. The cross-sectional scanning TEM (STEM) image and associated EDS line profile confirms that the interfacial layer contained Co, P, and S, with Co diffusing into Li₂S-P₂S₅ for over 50 nm after charging full cell (uncoated LCO|Li₂S-P₂S₅|In) under 0.13 mA cm⁻².^[365] Although the cobalt sulfide phase with lower Co²⁺ valence is known to be electronically conductive,^[366] it is clearly detrimental to the stability of the interfaces.^[59] Computational efforts (i.e., DFT calculation) mainly provide thermodynamic parameters such as the decomposition reaction products of the electrolytes at cathode chemical potentials, reaction energy, and chemical reaction products from the most favorable reactions at cathode/SSE interfaces, excluding kinetic information. Determining the interphase composition and thickness from careful experimentation will enable the development and characterization of protection concepts to alter the SEI formation and will provide a better understanding of the underlying mechanisms.

Compared to the interfaces in sulfide-based cathode composites, those in garnet-based cathode composites generally have higher thermodynamic stability against electrochemical decomposition and chemical reactions for room-temperature cycling. In addition, the difficulty of cell fabrication with garnet-based cathode composites, as discussed in previous section, has resulted in limited reports on the performance of full cells, yielding less experimental data on the electrochemical and chemical stability of garnet solid electrolyte under battery operating conditions than those available for sulfide solid electrolyte (Table 1). Most studies have either been based on computational work or CV investigation using a model cathode (e.g., Li|LLZO|LLZO-carbon|Pt cell) and not a full-cell-level investigation. These reports suggest that the onset of oxidation of LLZO in a cathode composite starts at \approx 3.7 V^[301] and \approx 4 V.^[76] Interestingly, the values from the precise measurement setup

were still higher than the DFT-predicted values (2.9 V^[76] and 3.2 V^[302] for LLZO), raising the question of why theoretical oxidation limit of LLZO is different than experimental observation. Obtaining precise information on the composition and thickness of the SEI as a function of voltage cut-off is critical to attain a better understanding of the stability of the SEI, which may assist future artificial SEI engineering. Regarding chemical reactions during cycling, only DFT calculation studies have reported interfacial products at the LLZO/LCO interface, suggesting products of La₂O₃, La₂Zr₂O₇, and Li₂CoO₄ at 3 V^[135] and La₂Zr₂O₇ and LaCoO₃ above 4 V.^[82] Unfortunately, all the reaction products above are likely to be poor ionic conductors; however, no clear experimental evidence has been obtained yet.

3.1.3. Chemomechanical Degradation during Cycling

Volume expansion and contraction of the active materials occurs because of the compositional change during charge/discharge, continuously generating stress at the established interfaces and leading to the formation of microgaps between the active material and solid electrolyte and thus contact loss (Figure 7c).^[200,260,326,367] Although maintaining the particle network in a cathode composite is important for Li-ion transport and the large contact is essential for charge transfer, redox reaction of the active materials leads to mechanical problems in the composite electrode. Principally, both the cathode and anode active materials undergo volume change during the charging/discharging process. The degree of the volume change depends on each cathode active material and is determined from the lattice parameter change of the active material upon redox reaction, as observed by XRD. Some active materials show a decrease and increase in volume corresponding to charging and discharging, respectively. For example, NMC111 undergoes volume contraction of roughly 2%, whereas NMC622 and NMC811 undergo larger volume contraction up to 6% because they are more affected by the large change of the Ni-ion radius upon transition-metal oxidation.^[368] Exceptionally, LCO exhibits the opposite volume change behavior.^[367] Accordingly, the volume change severely affects the sustainability of the composite electrode geometry. Liquid electrolytes can maintain the Li-ion networks as well as contacts with the active material because of their fluidity, whereas solid electrolytes have difficulty maintaining the geometry because the mechanical stress from the active material causes interfacial delamination or crack formation in the composite cathode, increasing the charge-transport resistances. Once mechanical failure progresses, high interfacial impedance and capacity decay are likely to occur because of the loss of active reaction sites.

Notably, this chemomechanical degradation usually occurs together with electrochemical and chemical degradation at the interfaces in the cathode composite, as can be directly observed by the irreversible impedance increase in a cathode composite after the first charge.^[326] Indeed, the mechanical debonding between NMC811 and β -Li₃PS₄ was directly observed by SEM before and after the 1st charge, and the resultant contact loss was maintained for 50 cycles under galvanostatic cycling at 214 $\mu\text{A cm}^{-2}$ (0.1 C) (Figure 7c). It was apparent that the significant contact loss occurred after the 1st charge when the

unit cell volume of NMC shrunk. Notably, the first charge and discharge capacities at 0.1C were 176 and 124 mAh g⁻¹, respectively, and the second charge and discharge capacities were ≈122 and ≈120 mAh g⁻¹, respectively (Coulombic efficiency $\eta = 70.5\%$, theoretical capacity of 200 mAh g⁻¹ of NMC811), indicating that mechanical degradation as well as electrochemical and chemical degradation mostly contributed to the reduction of the first discharge capacity. However, the mechanical degradation must continue as NCM repeatedly expands (during discharge) and shrinks (during charge) with cycling. Thus, one can expect that the degree of local connection and contact area constantly change, which could also affect the local propagation of interphase formation and the decomposition reaction. Based on the observation that the lattice volume of NMC811 decreases by roughly 1%, whereas that of LCO increases by roughly 2%, combining LCO with NCM has been found to balance the stresses from each active material. The cell employing stress mitigating composites was tested at 1–2.75 V (LTO anode) under the current density of 186 mA cm⁻², resulting in a decrease of the net stress and good preservation of the contact within the composite cathode (LCO–NCM– β -Li₃PS₄) after cycling.^[367] Very recently, Co-rich NCM (NCM361 and NCM271) was designed to have a minor volume change <1% for charging up to 4.4 V, which may be favorable to prevent gap formation between the solid electrolyte and active materials during operation.^[369] The quasi-zero-strain Co-rich NCM-based composite cathode appears to be a promising option for optimization of sulfide- and garnet-based ASSLBs with improved performance and cyclability by avoiding chemomechanical degradation.

In addition, electro-chemomechanical finite element method (FEM) simulations suggest that mechanical fracture would be prevented if the expansion of the electrode particles is less than 7.5%, the fracture energy of the solid electrolyte G_c is >4.0 J m⁻², and the Young's modulus in the order of $E_{SE} = 15$ GPa. It can be understood that a more compliant solid electrolyte such as sulfide ($E = 14$ –37.2 GPa)^[367] tends to deform more by stretching and shearing in response to the volume change of the active material and that the fracture typically develops in the regions where tensile stress forms in the SE matrix.^[262,370] A solid electrolyte with Young's modulus closer to that of the active material ($E_{LFP} = 117$,^[371] $E_{LCO} = 191$,^[372] $E_{LMO} = 194$,^[373] $E_{NMC} = 199$ GPa^[374]) tends to develop higher compressive stress but less tensile stress. Therefore, a rigid solid electrolyte like LLZO ($E = 150$ –162.6 GPa)^[137,180,256] and a cathode composite based on LLZO is anticipated to be more stable from the chemomechanical effect.

However, chemo-mechanical failure has been reported in the cathode composite of LLZO–LCO. The trans- and intergranular fractures within the cathode microstructure were hypothesized to be the degradation mechanism for the increased interfacial resistance (Figure 11a).^[200] A full-cell test of LCO–LLZO|LLZO|In–Li revealed that the first discharge capacity of 117 mAh g⁻¹ decreased to 36 mAh g⁻¹ after 100 cycles under a current density of 0.05 mA cm⁻¹ and 50 °C (theoretical capacity of 140 mAh g⁻¹).^[375] The total resistance of the cell was increased from 1138 Ω cm² in the first cycle to 5807 Ω cm² after 100 cycles, where only the polarization resistance degraded with cycling (Figure 11b). Assuming that the LLZO-based cathode composite has higher stability against electrochemical oxidation

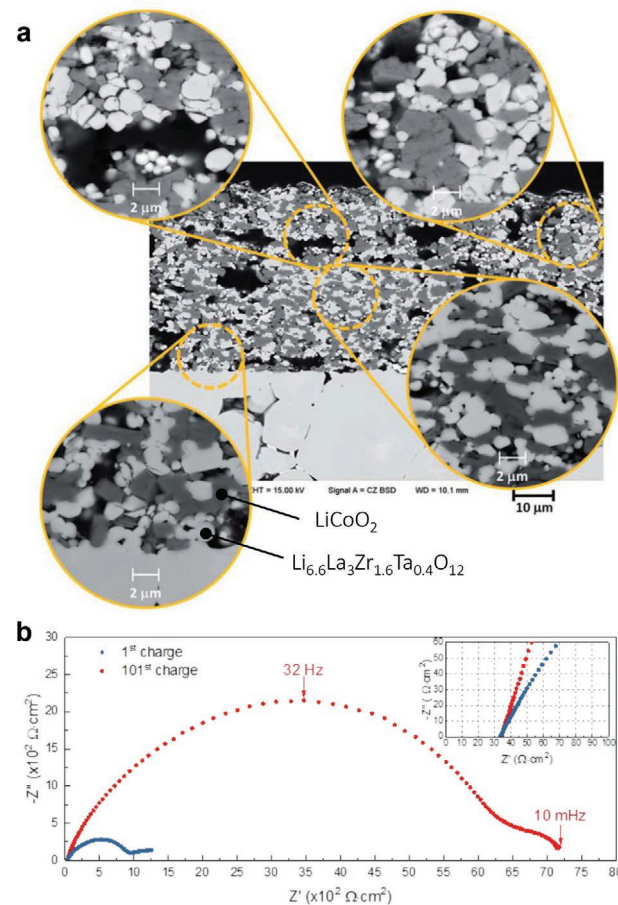


Figure 11. Mechanical degradation of garnet based cathode composite in Li_{6.6}La₃Zr_{1.6}Ta_{0.4}O₁₂–LiCoO₂/Li_{6.6}La₃Zr_{1.6}Ta_{0.4}O₁₂/In–Li cell. a) SEM cross-section images of a composite cathode of Li_{6.6}La₃Zr_{1.6}Ta_{0.4}O₁₂–LiCoO₂ that underwent 100 charge–discharge cycles at 50 °C. b) Electrochemical impedance spectra before and after 100 cycling. a,b) Reproduced with permission.^[200] Copyright 2019, Royal Society of Chemistry.

and chemical reaction during room-temperature cycling than sulfide-based cathode composites, the observed microcracks in the LLZO–LCO composite cathode from the repetitive expansion and contraction of LCO is thought to be the main origin of the capacity degradation.

To mitigate the interfacial degradation from the interfacial contact issues in the solid–solid interface system, hybrid-type cathodes on LLZO solid electrolytes have often been tested by adding small amounts of a liquid or polymer electrolyte in the composite electrode.^[376–378] However, in this case, we lose the benefits of the solid electrolyte, e.g., safety and wide temperature ranges for operation.

3.2. Strategies and Approaches toward Enhanced Stability and Performance

3.2.1. Cathode Coating

The high interfacial impedances originate from electrochemical decomposition, chemical reaction, and chemo-mechanical

degradation between the active material and sulfide and garnet electrolytes. A major task facing sulfide-based cathode composites is to avoid oxidation products observed during the charge cycle, e.g. P_2S_5 , S, that are electronic or ionic insulators. LLZO-based cathode composites face serious chemical reaction during cathode fabrication. In addition, regardless of the solid electrolyte selected, the active materials undergo significant volume changes during lithium (de)intercalation, which leads to detrimental contact loss within the composite cathode. All of these issues lead to the formation of adverse interfacial products, which directly cause deterioration of the interfacial resistance, capacity, cyclability, and battery life.

Given the conventional understanding, the engineering of sulfide- and garnet-based cathode composites is recommended. By far, applying an artificial SEI layer, namely, a cathode coating, on the active material surface has been the predominant approach for enhanced battery performance since the cathode coating has already been widely used in conventional liquid-electrolyte-based LIBs. However, the different criteria for liquid and solid systems and other fundamental considerations have recently been reviewed by.^[325,357,379] Briefly, the implicit requirements for coating materials for solid state cathodes can be summarized as follows:

- a) high electrochemical decomposition voltage (>4.5 V vs Li) with negligible electronic conductivity to avoid oxidation;
- b) chemically stable with the both active materials and solid electrolyte;
- c) uniform coverage and/or morphology to maintain percolation;
- d) mechanically “plastic” and deformable to accommodate volume change;
- e) environmental benign, nonhydroscopic, low cost, and offers ease of preparation;
- f) diffusion barrier characteristics to block mutual interdiffusion during high-temperature processing.

Both sulfide- and garnet-based cathode composites must meet criteria *a–e* over the entire employed range of lithium activity and operation temperature. For *f*, it is particularly necessary for the processing of garnet-based cathode composites. Based on the literature survey, most of the cathode coatings have been applied for sulfide-based cathode composites, with only one study on a garnet-based cathode composite (**Table 2**). More precisely, there are limited examples of electrochemical, chemical, and chemo-mechanical issues related to garnet-based cathode composites because of the fabrication difficulty.

A summary of the effective coatings for sulfide- and garnet-based solid state batteries shows that primarily ternary oxides of $LiNbO_3$, $Li_4Ti_5O_{12}$, and Li_4SiO_4 (Li_2O-SiO_2) have been applied to layered cathodes (LCO, NMC, and NCA). $LiNbO_3$ coating has been shown to be particularly effective for both sulfide- and garnet-based cathode composites, improving the interfacial resistance, capacity, cyclability, and rate capability.^[324,380,381] The application of $Li_4Ti_5O_{12}$ coatings on LCO,^[382] NMC,^[383] and NCA^[384] has also been demonstrated to be effective in enhancing capacity, rate performance, and interfacial resistance. In general, a thickness of $Li_4Ti_5O_{12}$ between 5 and 150 nm has

been investigated to show the best performance under various experimental conditions. However, high temperature of 600 °C is required to prepare $Li_4Ti_5O_{12}$ with a high conduction state, leading to Co diffusion from LCO to $Li_4Ti_5O_{12}$ and an increase of electronic conduction. In contrast, $LiTaO_3$ or $LiNbO_3$ can be prepared to have higher ionic conductivity at a lower temperature ≈400 °C for the amorphous state and perform better in terms of interfacial resistance than $Li_4Ti_5O_{12}$ coating.^[323]

Of the Li–Si–O coating materials used on LCO, the Li-containing ternary oxide (Li_2SiO_3) has been demonstrated to outperform the binary oxide (SiO_2).^[365,385–390] Further, Li_2SiO_3 coating can effectively prevent chemical reaction by blocking Co diffusion during charge in the interfacial zone between LCO and $Li_2S-P_2S_5$ (80:20 mol%) glass–ceramics.^[365] In fact, the effectiveness of Li_3PO_4 coating has been found to exceed that of Li_4SiO_4 with respect to room-temperature ionic conductivity and interfacial resistance.^[390] In several reports, 5–8 nm thick Li_2O-ZrO_2 (LZO) has been applied as an effective coating material for NCA and NMC cathodes and an amorphous LPS solid electrolyte up to the very high potential of 4.82 V.^[391,392] Other oxide coatings including amorphous $Li_{3-x}La_{2/3-x}TiO_3$,^[393] Li_2CO_3 ,^[394] Li_2MoO_4 ,^[395] $Li_{3-x}B_{1-x}C_xO_3$,^[396] and $LiInO_2-LiI$ ^[397] have resulted in improved capacity as protective coatings for sulfide-based cathode composites. Among them, the most successful case was a LZO-coated NMC cathode composite used in a 600 mAh pouch-type full cell consisting of NMC– $Li_6PS_5Cl|Li_6PS_5Cl|Ag-C$, demonstrating unprecedented performance with a coulombic efficiency (CE) greater than 99.8% for 1000 cycles at a charging rate of 0.1 C (0.68 mA cm⁻²) and at a discharging rate of 0.2 C (1.36 mA cm⁻²) (**Figure 12a**).^[346]

The experimental validation of promising coating materials for garnet-based cathode composites has not yet been reported except for one model experiment in which a 10 nm thick Nb coating was introduced by RF-sputtering between a LLZO electrolyte pellet and thin-film LCO. Full cell of $LiCoO_2(Nb)||LLZO||Li$ was tested at a current density of 1 mA cm⁻² with and without Nb addition. The interface coated with the amorphous Li–Nb–O layer was found to effectively mitigate second-phase formation of La–Co–O, reduced the interfacial resistance from 2600 to 150 Ω cm² after charging at 4.0 V, and improve the overall performance.^[382] Despite the improvement, the first discharge capacity achieved of 80 mAh g⁻¹ is still below the expected discharge capacity (140 mAh g⁻¹), meaning that still there is the resistive interphase between LCO and LLZO, limiting the Li-ion motion at the interface thereby decrease the cell's efficiency toward full utilization of LCO cathode. Further optimization or novel effective coating materials for garnet/cathode interface are required.

Based on first-principles calculation, the commonly used ternary oxides of $LiNbO_3$, $Li_4Ti_5O_{12}$, Li_4SiO_4 , Li_3PO_4 , and Li_2ZrO_3 offer higher oxidation limits than sulfide and garnet electrolytes but still lower than the cut-off voltage, for example, of LCO (4.2 V), implying that oxidation is still occurring.^[82,302] However, slow oxidation kinetics help to protect solid electrolytes from oxidation. Very recently, polyanionic materials such as borate and phosphate were found to offer higher oxidation limits (>4.5 V) and excellent chemical compatibility compared with those of oxide coating materials because of the strong covalent bonds (such as P–O and B–O) and sharing

Table 2. List of reported coating materials for sulfide and garnet based cathode composite.

Coating	Methods for coating (conditions)	Cathode	Solid electrolyte	R_{in} for cathode (conditions) [Ohm cm ²]	Ref.
Carbon	Spark plasma sintering (500 °C)	LiCoO ₂	0.01Li ₃ PO ₄ -0.63Li ₂ S-0.36SiS ₂	n/a	[510]
Carbon	CVD (250 °C)	LiNi _{0.8} Co _{0.15} Al _{0.05} O ₂	75Li ₂ S-25P ₂ S ₅	≈100 (25 °C, 4.0 V vs Li/Li ⁺)	[364]
Nb	RF magnetron sputtering (RT, Ar)	LiCoO ₂	Li ₇ La ₃ Zr ₂ O ₁₂	150 (RT, 4.0 V vs Li/Li ⁺)	[398]
Ta	RF magnetron sputtering (RT, Ar)	LiCoO ₂	Li ₇ Ta ₂ Zr ₂ O ₁₂	500 (RT, 4.0 V vs Li/Li ⁺)	[398]
Ti solid solution	Liquid phase synthesis (700 °C)	LiNi _{0.8} Co _{0.15} Al _{0.05} O ₂	Li ₁₀ GeP ₂ S ₁₂	253 (RT, 4.32 V vs Li/Li ⁺)	[511]
TiO ₂	Liquid phase synthesis (350 °C)	LiCoO ₂	80Li ₂ S-20P ₂ S ₅	157 (RT, 4.2 V vs Li/Li ⁺)	[512]
TaO ₃	Liquid phase synthesis and UV light irradiation	LiCoO ₂	Li _{3.25} Ge _{0.25} P _{0.75} S ₄	4000 (25 °C, 3.92 V vs Li/Li ⁺)	[513]
SiO ₂	Liquid phase synthesis (350 °C)	LiCoO ₂	80Li ₂ S-20P ₂ S ₅	173 (RT, 4.2 V vs Li/Li ⁺)	[385]
SiO ₂	Liquid phase synthesis (350 °C)	LiCoO ₂	80Li ₂ S-20P ₂ S ₅	707 (RT, 4.6 V vs Li/Li ⁺)	[387]
SiO ₂	Liquid phase synthesis (350 °C)	LiCoO ₂	80Li ₂ S-20P ₂ S ₅	173 (RT, 4.2 V vs Li/Li ⁺)	[388]
Al ₂ O ₃	ALD (300 °C)	LiCoO ₂	Li _{3.25} Ge _{0.25} P _{0.75} S ₄	≈200 (30 °C, 4.3 V vs Li/Li ⁺)	[514]
Al ₂ O ₃	Liquid phase synthesis (350 °C, O ₂)	LiNi _{1/3} Mn _{1/3} Co _{1/3} O ₂	a-Li ₃ PS ₄	≈300 (25 °C, 4.3 V vs Li/Li ⁺)	[552]
ZrO ₂	Liquid phase synthesis (750 °C, O ₂)	LiNi _{1/3} Mn _{1/3} Co _{1/3} O ₂	a-Li ₃ PS ₄	250 (25 °C, 4.3 V vs Li/Li ⁺)	[516]
Li ₂ CO ₃	Liquid phase synthesis (300 °C, air)	LiNi _{0.6} Co _{0.2} Mn _{0.2} O ₂	β-Li ₃ PS ₄	≈50 (25 °C, 2.9 V vs Li/Li ⁺ , after 100 cycles discharge)	[517]
Li ₂ CO ₃	Liquid phase synthesis (400 °C, CO ₂)	LiCoO ₂	78Li ₂ S-22P ₂ S ₅	294 (RT, 4.25 V vs Li/Li ⁺)	[394]
Li ₄ Ti ₅ O ₁₂	Liquid phase synthesis (400 °C in O ₂)	LiCoO ₂	Li _{3.25} Ge _{0.25} P _{0.75} S ₄	35 (RT, 4.2 V vs Li/Li ⁺)	[382]
Li ₄ Ti ₅ O ₁₂	Liquid phase synthesis (350 °C)	LiNi _{1/3} Mn _{1/3} Co _{1/3} O ₂	80Li ₂ S-19P ₂ S ₅ -1P ₂ O ₅	79 (25 °C, 4.4 V vs Li/Li ⁺)	[383]
Li ₄ Ti ₅ O ₁₂	Liquid phase synthesis (300 °C, air)	LiNi _{0.8} Co _{0.15} Al _{0.05} O ₂	70Li ₂ S-30P ₂ S ₅	≈25 (RT, 4.2 V vs Li/Li ⁺)	[384]
Li ₄ Ti ₅ O ₁₂	Liquid phase synthesis (350 °C)	LiMn ₂ O ₄	80Li ₂ S-20P ₂ S ₅	n/a	[525]
Li ₂ Ti ₂ O ₅	Liquid phase synthesis (350 °C)	LiCoO ₂	80Li ₂ S-20P ₂ S ₅	110 (RT, 4.2 V vs Li/Li ⁺)	[512]
LiNbO ₃	Liquid phase synthesis (400 °C, O ₂)	LiNi _{0.8} Co _{0.1} Mn _{0.1} O ₂	Li ₁₀ GeP ₂ S ₁₂	126 (35 °C, 4.4 V vs Li/Li ⁺)	[381]
LiNbO ₃	Liquid phase synthesis (400 °C, O ₂)	LiCoO ₂	Li _{3.25} Ge _{0.25} P _{0.75} S ₄	n/a	[324]
LiNbO ₃	Liquid phase synthesis (400 °C, O ₂)	LiMn ₂ O ₄	Li _{3.25} Ge _{0.25} P _{0.75} S ₄	≈160 (RT, 4.3 V vs Li/Li ⁺)	[380]
LiTaO ₃	Liquid phase synthesis (400 °C, O ₂)	LiCoO ₂	Li _{3.25} Ge _{0.25} P _{0.75} S ₄	n/a	[323]
Li ₃ PO ₄	PLD (RT, Ar)	LiCoO ₂	80Li ₂ S-20P ₂ S ₅	≈400 (25 °C, 4.4 V vs Li/Li ⁺)	[526]
Li ₃ PO ₄	PLD (RT, Ar)	LiNi _{0.5} Mn _{1.5} O ₄	80Li ₂ S-20P ₂ S ₅	275 (25 °C, 4.8 V vs Li/Li ⁺)	[527]
Li ₃ PO ₄	PLD (RT, Ar)	LiCoO ₂	80Li ₂ S-20P ₂ S ₅	≈62 (25 °C, 4.2 V vs Li/Li ⁺)	[390]
Li ₄ SiO ₄	PLD (RT, Ar)	LiCoO ₂	80Li ₂ S-20P ₂ S ₅	≈130 (25 °C, 4.2 V vs Li/Li ⁺)	[390]
Li ₂ SiO ₃	Liquid phase synthesis (350 °C)	LiCoO ₂	80Li ₂ S-20P ₂ S ₅	126 (RT, 4.2 V vs Li/Li ⁺)	[385]
Li ₂ SiO ₃	Liquid phase synthesis (350 °C)	LiCoO ₂	80Li ₂ S-20P ₂ S ₅	589 (RT, 4.6 V vs Li/Li ⁺)	[387]
Li ₂ SiO ₃	Liquid phase synthesis (350 °C)	LiCoO ₂	80Li ₂ S-20P ₂ S ₅	102 (RT, 4.2 V vs Li/Li ⁺)	[388]
Li ₂ SiO ₃	Liquid phase synthesis (350 °C)	LiCoO ₂	80Li ₂ S-20P ₂ S ₅	≈110 (RT, 4.2 V vs Li/Li ⁺)	[365]
Li ₂ SiO ₃	Liquid phase synthesis	LiCoO ₂	80Li ₂ S-20P ₂ S ₅	≈125 (RT, 4.2 V vs Li/Li ⁺)	[512]
LiAlO ₂	Liquid phase synthesis (350 °C, O ₂)	LiNi _{1/3} Mn _{1/3} Co _{1/3} O ₂	a-Li ₃ PS ₄	300 (25 °C, 4.3 V vs Li/Li ⁺)	[515]
Li ₂ O-ZrO ₂	Liquid phase synthesis (350 °C, air)	LiNi _{0.8} Co _{0.15} Al _{0.05} O ₂	80Li ₂ S-20P ₂ S ₅	117 (25 °C, 4.0 V vs Li/Li ⁺)	[391]
Li ₂ ZrO ₃	Liquid phase synthesis (650 °C, air)	LiNi _{0.6} Co _{0.2} Mn _{0.2} O ₂	I-doped Li ₂ P ₃ S ₁₁	20 (RT, 4.82 V vs Li/Li ⁺)	[528]
Li ₄ GeO ₄	PLD (RT, Ar)	LiCoO ₂	80Li ₂ S-20P ₂ S ₅	≈140 (25 °C, 4.2 V vs Li/Li ⁺)	[390]
L ₃ BO ₃	Liquid phase synthesis (600 °C, air)	LiCoO ₂	Li ₆ PS ₅ Cl	20 (30 °C, 3.9 V vs Li/Li ⁺ , after discharge)	[396]
Li ₂ MoO ₄	Liquid phase synthesis (600 °C)	LiNi _{0.8} Co _{0.15} Al _{0.05} O ₂	75Li ₂ S-22P ₂ S ₅ -3Li ₂ SO ₄	n/a	[395]
LiInO ₂	Liquid phase synthesis (650 °C, air)	LiNi _{0.8} Co _{0.15} Al _{0.05} O ₂	75Li ₂ S-22P ₂ S ₅ -3Li ₂ SO ₄	n/a	[397]
LiNb _{0.5} Ta _{0.5} O ₃	Liquid phase synthesis (450 °C)	LiCoO ₂	Li ₁₀ GeP ₂ S ₁₂	15 (–, 4.2 V vs Li/Li ⁺)	[317]
LiNb _{0.5} Ta _{0.5} O ₃	Liquid phase synthesis (450 °C)	LiCoO ₂	Li ₁₀ GeP ₂ S ₁₂	19 (–, 4.2 V vs Li/Li ⁺)	[360]
50Li ₄ SiO ₄ – 50Li ₃ PO ₄	PLD (RT, Ar)	LiCoO ₂	80Li ₂ S-20P ₂ S ₅	38 (RT, 4.2 V vs Li/Li ⁺)	[389]
Li _{3.5} SiO ₅ P _{0.5} O ₄	PLD (RT, Ar)	LiCoO ₂	80Li ₂ S-20P ₂ S ₅	≈38 (25 °C, 4.2 V vs Li/Li ⁺)	[390]

Table 2. Continued.

Coating	Methods for coating (conditions)	Cathode	Solid electrolyte	R_{in} for cathode (conditions) [Ohm cm ²]	Ref.
Li _{3.5} Ge _{0.5} P _{0.5} O ₄	PLD (RT, Ar)	LiCoO ₂	80Li ₂ S–20P ₂ S ₅	≈65 (25 °C, 4.2 V vs Li/Li ⁺)	[390]
Li _{3-x} B _{1-x} C _x O ₃	Liquid phase synthesis (600 °C, air)	LiCoO ₂	Li ₆ PS ₃ Cl	12 (30 °C, 3.9 V vs Li/Li ⁺ , after discharge)	[396]
Li ₂ CO ₃ –LiNbO ₃	Liquid phase synthesis (300 °C, air)	LiNi _{0.6} Co _{0.2} Mn _{0.2} O ₂	β -Li ₃ PS ₄	20 (25 °C, 2.9 V vs Li/Li ⁺ , after 100 cycles discharge)	[517]
Li _{0.33} La _{0.56} TiO ₃	Liquid phase synthesis (700 °C)	LiCoO ₂	78Li ₂ S–22P ₂ S ₅	1000 (RT, 4.3 V vs Li/Li ⁺)	[529]
Li _{0.5} La _{0.5} TiO ₃	Liquid phase synthesis (700 °C)	LiCoO ₂	78Li ₂ S–22P ₂ S ₅	935 (RT, 4.3 V vs Li/Li ⁺)	[529]
Li _{0.75} La _{0.42} TiO ₃	Liquid phase synthesis (700 °C)	LiCoO ₂	78Li ₂ S–22P ₂ S ₅	640 (RT, 4.3 V vs Li/Li ⁺)	[529]
LiInO ₂ –LiI	Liquid phase synthesis (650 °C, air)	LiNi _{0.8} Co _{0.15} Al _{0.05} O ₂	75Li ₂ S–22P ₂ S ₅ –3Li ₂ SO ₄	n/a	[397]
NiS	Liquid phase synthesis (400 °C, N ₂)	LiCoO ₂	80Li ₂ S–20P ₂ S ₅	47 (RT, at Li _{0.6} CoO ₂)	[530]
CoS	Liquid phase synthesis (400 °C, N ₂)	LiCoO ₂	80Li ₂ S–20P ₂ S ₅	102 (RT, at Li _{0.6} CoO ₂)	[530]
80Li ₂ S–20P ₂ S ₅	PLD (RT, Ar)	LiCoO ₂	80Li ₂ S–20P ₂ S ₅	26 (RT, 4.2 V vs Li/Li ⁺)	[524]

of the same ions with oxides and sulfides.^[344] In any case, understanding of the oxidation kinetics of SEs and the suppression of the interfacial degradation during room-tempera-

ture cycling and/or high-temperature cofiring is key to determining the lifetime of a coating layer; therefore, we need verify how these coating materials work through experiments. In

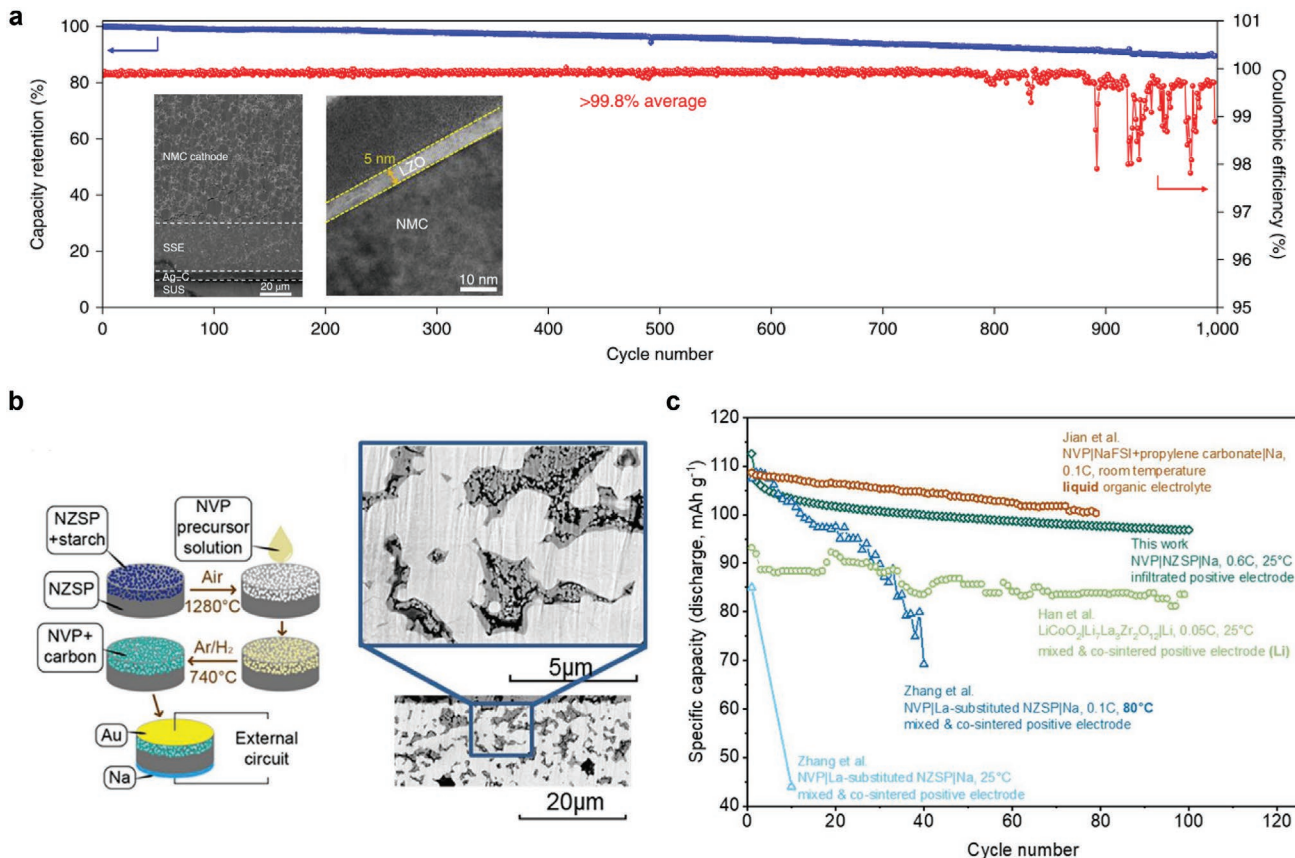


Figure 12. Electrochemical performance of all-solid-state batteries. a) Cycling performance and Coulombic efficiency of the Ag–C|Li₆PS₅Cl||LiNi_{0.90}Co_{0.05}Mn_{0.05}O₂ (NMC) prototype pouch cell (0.6 Ah) are plotted against the cycle numbers. A charge/discharge rate of 0.5 C/0.5 C was applied (voltage window, 2.5–4.25 V vs Li⁺/Li at 60 °C). The areal capacity loading of the NMC cathode was 6.8 mAh cm⁻² (1.0 C = 6.8 mA cm⁻²). Inset shows TEM image of an LZO-coated NMC particle. b) Design and fabrication of infiltrated all-solid-state sodium batteries. Manufacturing steps (left) for an Na₃V₂P₃O₁₂ (NVP)-Na_{3.4}Zr₂Si_{2.4}P_{0.6}O₁₂ (NZSP)-Na battery using the chemical infiltration method through porous NZSP scaffold for increased effective reaction area. SEM images (right) of a cross-sectional NVP (dark contrast)-infiltrated NZSP (bright contrast) pellet. c) Discharge capacity degradation of different all-solid-state lithium and sodium battery with liquid electrolyte. a) Reproduced with permission.^[346] Copyright 2016, the Nature Publishing Group. b,c) Reproduced with permission.^[409] Copyright 2017, Elsevier.

particular, developing new coating materials and novel coating strategies (processing) for garnet-based cathode preparation is urgent next task. Probing the local chemistry and phase evolution over cycles at the grain boundaries will be an important to optimize cathode coating toward ASSLB with high energy and long cycles.

3.2.2. Geometric Arrangement Concerns toward Maximizing Reaction Sites

When designing composites in general, one must consider their unique characteristics as follow. First, composite materials are inherently heterogeneous at the microstructural level, as they consist of two or three components with different strengths, different expansion properties upon bias, etc. Even after selecting the component characteristics and interface characteristics, one can obtain a range of electrochemical performance depending upon the geometric arrangement of the cathode composite. Physical properties such as the mechanical and electrical conductivity of the composite cathode can be controlled by the transport property of the active materials and solid electrolytes, their volume/size ratio, the number of interfaces (reaction sites), and characteristics of the interface region. In particular, the connection network and charge-transport properties of the ionic and electronic phases must be optimized for composite cathodes. It is expected that the particle size and ratio between the active material and solid electrolyte also significantly affect the charge-transport network and resistance in a cathode composite.^[334,335,399–401] Very recently, it was shown that high volume fractions of LZO-coated NMC can be fully utilized in a cathode composite if the smaller particles of LPS are used rather than those of NMC. For example, a cold-pressed solid-state cathode composite with liquid-cell-level cathode volume loading (≈ 50 vol% or 80 wt%) is achievable by using large cathode particles (≈ 12 μm) and small SE particles (≈ 1.5 μm) without sacrificing specific capacity at a current density of 0.05 mA cm^{-2} ,^[333] encouraging to be tested for long cycles.

For oxide-based ASSLBs, there has been little success in applying similar research for microstructure optimization because of the processing challenges. Rather, the more prominent issue is how to create chemically and mechanically stable interfaces between the active materials and solid electrolytes as well as between solid electrolytes. Unlike sulfide solid electrolytes, garnet solid electrolytes require processing temperatures higher than 1000 $^{\circ}\text{C}$ to develop strong necks with another LLZO and LCO to form a dense cathode composite.^[126,131,138,402] At this temperature, most of the active materials will be decomposed or reacted with LLZO.^[61,343] Lowering the cofiring temperature down to 700 $^{\circ}\text{C}$ is possible with promising performance but requires 12–34 wt%^[45,403] of inactive phases of sintering aids such as Li–B–O oxides, which currently requires sacrificing of a portion of the cathode loading. Additionally, it is not ideal to add such large quantities because of the poor ionic conductivity (10^{-6} S cm^{-1}) of Li–B–O oxides.^[404] Another approach is to first prepare a porous-electrolyte network at high temperature and then introduce active materials by infiltration.^[405–409]

Although it has been challenging to achieve the theoretical capacity of active materials in many of these reports, mainly because of the high interfacial resistance, in a very recent work,^[409] quite impressive performance for all-solid-state sodium batteries was demonstrated. The $\text{Na}_3\text{V}_2\text{P}_3\text{O}_{12}$ (NVP) active material of $1.7\text{--}3$ mg cm^{-2} was introduced by chemical infiltration through a porous $\text{Na}_{3.4}\text{Zr}_2\text{Si}_{2.4}\text{P}_{0.6}\text{O}_{12}$ (NZSP) electrolyte scaffold and sintering at 740 $^{\circ}\text{C}$ (Figure 12b), with good specific capacity of the active positive electrode material (>95 mAh g^{-1}) and high coulombic efficiency ($>99\%$) for 100 cycles at a current density of $35\text{--}127.6$ $\mu\text{A cm}^{-2}$. Comparison of specific capacity with cycle number among the all-oxide Na and Li metal batteries indicates that infiltrated NVP–NZSP composite cathode outperforms state-of-art LBO–LLZO–LCO composite cathode (Figure 12c). For processing of oxide-based SEs, many techniques have been developed to attain good cathode interfaces with low interfacial resistance. Based on the knowledge gained from prior art (additive approach, infiltration approach), the design of more practical solid-state cathodes through microstructure optimization, as shown in refs. [332,333], is suggested.

3.2.3. Conductive Additives in Solid-State Cathode

The electronic conductivity in cathode composites is another important parameter to improve the utilization of the active material. Typically, ASSLB cathode composites consist of a mixture of the active material and SE without conductive additives. In sulfide solid electrolytes, the additives cause severe degradation (decomposition of the solid electrolytes) upon cycling and should thus preferably be avoided.^[60,317,320,326,354] In some cases, the active material has a relatively high electronic conductivity and electronic transport pathways are provided only through interconnected active materials. For example, the carbon-free solid-state cathode composite based on $\text{NCM}622\text{--}\beta\text{-Li}_3\text{PS}_4$ ^[335] (at 0.1 C) and LCO–LLZO^[200] (at 20 $\mu\text{A cm}^{-2}$) can deliver theoretical charge capacity but with noticeable capacity decay, meaning that there are limited ion or/and electron transport in state-of-cathode composite toward achieving full utilization of active material. During oxide-based cathode composite preparation, carbon additives have been mostly excluded because the cathode processing temperature are above the carbon-burnout temperature (≈ 500 $^{\circ}\text{C}$). Controlling sintering gas from the oxidizing to reducing atmosphere can be considered; however, the electrolyte and active materials must be stable without decomposition under such conditions.^[409] Alternatively, inorganic electronic conductive materials, such as indium tin oxide ($\text{In}_{2(1-x)}\text{Sn}_{2x}\text{O}_3$) powders, can be used as oxide electronic conductive agents.^[199] Nevertheless, an understanding of the rate-limiting step among the multiple transport steps inside the as-prepared cathode composite is critical. For example, the total conductivity and the partial electronic and ionic conductivity of the cathode composite can be characterized using the DC polarization technique with an ion- or electronic-blocking electrode.^[335,410] These transport properties are strongly affected by the choice of active materials and solid electrolyte as well as their particle size/volume ratio and geometric arrangement, providing a concrete direction toward improved solid-state cathode performance.

4. Anode: Adopting Lithium Metal in the Solid

Replacing the conventional carbonaceous anode (LiC_6) in Li batteries with a Li metal anode can yield a 50% increase in the practical energy density (3860 vs 372 mAh g⁻¹) and is considered one of the most promising approaches to realize high-energy-density batteries.^[19] The US DOE targets a high per-cycle utilization (at least 80%) of Li metal present, a cumulative capacity plated before cell short circuiting $> 10 \text{ mAh cm}^{-2}$, a plating current density $> 3 \text{ mA cm}^{-2}$, and a high per-cycle areal capacity of $> 3 \text{ mAh cm}^{-2}$ at the device level.^[19,32] Ideally, a limited Li source (15–30 μm or 3–6 mA h cm⁻²) and the complete stripping of Li metal during discharge are needed in Li-metal batteries to minimize “soft” shorts and support high-energy-density batteries.^[19] Nonetheless, the preparation of ultrathin Li (<30 μm) by extrusion and subsequent calendaring (“rolling”) is challenging because of the adhesiveness and reactivity of Li metal.^[411] Spreading molten Li metal directly onto a metal current collector (or solid electrolyte) is a promising alternative strategy toward cost-effective and scalable ultrathin Li processing but is contingent upon tuning the surface energy ('wettability') of molten Li metal to facilitate its homogenous spreading on various lithiophobic substrates, namely the metal current collector and ceramic solid electrolyte (e.g., Cu, Ni, LLZO, carbon).^[412] Another major predicament accompanying the use of a limited Li source is the 100% volume change of Li metal during discharge/charge (stripping/plating) that necessitates an excess lithium metal reservoir of 20%–300%,^[413] which in turn reduces the volumetric energy density, induces stresses and shape change, destabilizes interfaces, and results in limited cycle life. Strategies to use layered reduced graphene sheets,^[414] a polyimide-ZnO core–shell structure,^[415] mixed ionic-electronic conductor tubular 3D host,^[416] or carbon spheres^[417] as rigid and stable Li hosts to store Li metal to reduce volume change are still immature and prevent making full use of the alkali metal. Thus, the adoption of Li metal remains one of the most promising and challenging approaches to achieve safer high-energy-density batteries, especially in applications favoring ceramic or polymer solid electrolytes. There are other foreseen challenges associated with the morphological changes associated with the electrochemical deposition and dissolution of Li metal, especially during cycling at high current densities ($> 1 \text{ mA cm}^{-2}$), such as Li dendrite nucleation and propagation, interface delamination, and pore formation.

Oxide and sulfide solid electrolytes can offer high total ionic conductivities of up to $\approx 1 \text{ mS cm}^{-1}$, with some solid electrolytes providing high chemical stability against Li metal (e.g., LLZO, LiPON). Nevertheless, the nature of mass transport at both intrinsic interfaces (between grains, defects, etc.) and extrinsic interfaces (Li metal/electrolyte) remains a major hurdle that can lead to large kinetic and charge-transfer polarizations and cell failure (capacity fading, short circuiting).^[258] This is especially true when considering that unstable electrode/electrolyte interfaces over multiple discharge/charge cycles are one of the main sources of battery failure, both with liquid and solid electrolytes.^[418] The inherent chemical properties ('wettability', chemical stability in air and upon contact with Li metal, SEI properties and stability), electrochemical properties (redox potentials), and mechanical properties (Young's modulus, shear

modulus, formability and fracture toughness) of the solid electrolyte determine the nature of the physical contact that may be feasible with Li metal. Poor contact typically facilitates: *i*) high interfacial resistance (hundreds of $\text{ohm}\cdot\text{cm}^2$),^[419] *ii*) inhomogeneous current distributions leading to the propagation of Li dendrites at high current density, *iii*) a gradual increase of the interfacial resistance during cycling due to unstable interphase formation and loss of contact, *iv*) relatively low CCD ($\approx 0.3\text{--}0.4 \text{ mA cm}^{-2}$),^[65] and *v*) unstable Li stripping/plating test (at $0.05\text{--}0.5 \text{ mA cm}^{-2}$)^[65] with poor electrochemical performance of a full ASSLB cell, unless a surface modification strategy is undertaken. As such, special attention should be paid to the reducing nature of Li metal^[420] and its chemical compatibility with the solid electrolyte^[59] in addition to maintaining a low interfacial resistance while suppressing mossy/dendritic Li growth, particularly at high current densities ($> 1 \text{ mA cm}^{-2}$).^[70,76,179,280,283\text{--}287] These precautions are necessary to improve the safety^[421] as well as the poor cycling stability, capacity fading,^[422] and low coulombic efficiency associated with the operation of Li-metal-based batteries^[422] and overcome the rate-capability limitation originating from the restricted diffusion of Li vacancies, which can potentially lead to interfacial voids and loss of contact between the Li metal and solid electrolyte.^[423]

In the following section, a detailed discussion of the Li metal/solid electrolyte interfaces, both for oxides and sulfides, focusing on chemical and electrochemical instabilities through the effects on dendrite formation and battery performance is presented alongside promising mitigation strategies. Then the origin of the high interfacial resistance between Li metal and the most promising solid electrolyte of the oxides (i.e., LLZO) and sulfide-ion-conducting families will be presented, alongside promising mitigation strategies to secure long-term stable interfaces toward a solid-state Li battery with improved safety and rate capabilities.

4.1. Li/Solid-Electrolyte Interface: Chemical, Electrochemical, and Mechanical Considerations, including Mitigation Strategies

The coupling of Li metal with a solid electrolyte necessities an interface that is chemically, electrochemically, and mechanically stable with sufficiently fast charge-transfer kinetics to support the fast Li stripping/plating during battery operation. Electrochemical compatibility (i.e., redox stability) between the Li metal and solid electrolyte is essential to prevent reduction of the electrolyte by the Li metal, meaning that the electrochemical potential of Li metal must be higher than the lowest occupied molecular orbital (LUMO) of the electrolyte, unless a stable passivation layer (i.e., an interphase layer) is formed. Broadly, Li solid electrolytes, except for Li binary compounds such as Li_3N , Li_2S , and Li_3P , are thermodynamically unstable against Li metal and decompose at low potentials, leading to the formation of an interphase layer (Table 3).^[59,82,303,309,310] The ideal interphase is a nanometrically thin good ionic conductor and an electronic insulator (Figure 13a). The electronically insulating character of the interphase reduces the Li chemical potential (sum of the electrochemical potential of the electronic and ionic carriers) to be within the electrochemical window of

Table 3. List of stable and unstable passivation layer between solid electrolyte and Li metal.

SEs		Reduction potential against Li [V]	Decomposition product	Detecting method	Ref.
Stable passivation layer	LiPON $\text{Li}_{1.4}\text{PO}_{2.2}\text{N}_{0.7}$	0	Li_3PO_4 , Li_3P , Li_3N , and Li_2O Li_3P , Li_3N , Li_2O	XPS	[424]
	LLZO	0.05	Li_2O , La_2O_3 , Zr_3O , and Zr metal at ≈ 0 V Contact with Li, tetragonal LLZO	First-principles thermodynamic calculations First-principles computations In situ scanning transmission electron microscope (STEM)	[82] [76,308] [420]
	Crystalline $\text{Li}_7\text{P}_3\text{S}_{11}$	2.3	Contact with Li, Li_2S , Li_3P , and additional reduced phosphate species such as LiP , LiP_5 , or LiP_7	XPS and time-dependent impedance spectroscopy analysis	[425]
	$\beta\text{-Li}_3\text{PS}_4$	1.7	Li_2S and Li_3P $\text{P}_2\text{S}_6^{4-}$ and Li_2S	First-principles thermodynamic calculations In situ Raman and XPS analysis	[59,82] [496]
	$\text{Li}_6\text{PS}_5\text{X}$ ($\text{X} = \text{Cl}, \text{Br}, \text{I}$)	1.7	Contact with Li, Li_3P , Li_2S , and LiX	In situ XPS combined with time-resolved impedance spectroscopy	[318]
	$\text{Li}_{0.33}\text{La}_{0.56}\text{TiO}_3$ LLTO	1.75	Contact with Li, Reduction of Ti^{4+} to Ti^{3+} , oxidized Li^+ inserting into $\text{La}^{3+}/\text{Li}^{+}$ -site vacancies Ti_6O , La_2O_3 , and Li_2O at 0 V	SIMS, XPS	[428]
Unstable passivation layer	$\text{Li}_{10}\text{GeP}_2\text{S}_{12}$ (LGPS)	1.71	Contact with Li Li_3P , Li_2S , and Li-Ge alloy Li_3P , Li_2S , and $\text{Li}_{15}\text{Ge}_4$ at 0 V	In situ XPS, time-resolved impedance spectroscopy	[427]
	$\text{Li}_{1.3}\text{Al}_{0.3}\text{Ti}_{1.7}(\text{PO}_4)_3$ (LATP, LATTP)	2.17	Observed Li_2S $\text{Ti}^{4+} \rightarrow \text{Ti}^{3+}$ Formation of a new mixed ionic-electronic thin conductive layer	XRD XPS	[59,82] [312]
	$\text{Li}_{1.5}\text{Al}_{0.5}\text{Ge}_{1.5}(\text{PO}_4)_3$ (LAGP, LATGP)	2.7	Ti_3P , TiAl , Li_3P , Li_2O at 0 V $\text{Ge}^{4+} \rightarrow \text{Gex}^+$, $\text{Ti}^{4+} \rightarrow \text{Ti}^{3+}$ Formation of a new mixed ionic-electronic thin conductive layer	First-principles thermodynamic calculations XPS	[59,82] [312]
			Li_9Al_4 , $\text{Li}_{15}\text{Ge}_4$, Li_3P , Li_2O at 0 V	First-principles thermodynamic calculations	[59,82]

the solid electrolyte, inhibiting further electrode decomposition and stabilizing the Li/electrolyte interface. The high experimental electrochemical stability window, occasionally observed between thermodynamically unstable solid electrolytes when in contact with Li metal, originates from a kinetically stabilizing, self-limited, passivation interphase layer at the Li/electrolyte interface, facilitated by the electronic insulating and ion-conducting nature of the interphase,^[59] as observed for several solid electrolytes including LLZO, LiPON, and $\text{Li}_7\text{P}_3\text{S}_{11}$.^[424–426] However, for solid electrolytes such as LGPS, LAGP, and LATP, which contain cations such as Ti^{4+} , Ge^{4+} , Al^{3+} , and Zn^{2+} , the reduction of the cations at low potentials and the evolution of metallic states leads to high electronic conduction, continuous electrochemical reduction of the solid electrolyte, and interphase layer growth during cycling, which ultimately leads to the short circuit of the cell (Figure 13b).^[312,425] The last factor typically negates their use as electrolytes in ASSLBs unless an electron-blocking and Li^{+} -ion-conducting interlayer is used.^[312,427] For example, NASICON-type LATP exhibits excellent resistance to oxidation with a high theoretical oxidation potential (based on Li grand potential phase diagram) of 4.21 V versus Li^+/Li but

has a relatively high theoretical reduction potential of 2.17 V versus Li^+/Li because of the reduction of Ti from Ti^{4+} to Ti^{3+} (similar to LLTO and Ge in LAGP), leading to an ionic and electronic mixed conduction, which negatively affects the stability against Li metal.^[59] XPS analysis has also confirmed that Li-conducting glass ceramics containing Ti^{4+} , Ta^{5+} , and Ge^{4+} , such as LATP and LAGP, readily react with Li metal with the formation of a new mixed ionic-electronic thin conductive layer that leads to a continuous increase in the electrolyte impedance with time.^[312] A troublesome issue for Li oxides with high reduction potentials is the anode material being unable to react at potentials higher than its reduction potential, e.g., 1.7 V versus Li^+/Li for perovskite-type $\text{Li}_{3x}\text{La}_{2/3-x}\text{TiO}_3$. Indeed, coupling $\text{Li}_{3x}\text{La}_{2/3-x}\text{TiO}_3$ and Li metal involves the insertion of Li^+ ions into $\text{La}^{3+}/\text{Li}^{+}$ -site vacancies in $\text{Li}_{3x}\text{La}_{2/3-x}\text{TiO}_3$ accompanied by the reduction of Ti^{4+} to Ti^{3+} and an increase in electronic conductivity because of the existence of mixed $\text{Ti}^{3+}/\text{Ti}^{4+}$ states.^[428] The unstable interphase layer formed at the Li/electrolyte interface, where continuous “thickening” (growth) could effectively terminate Li dendrite propagation^[283] but also inhibit further Li^{+} -ion transport, would in turn increase the cell

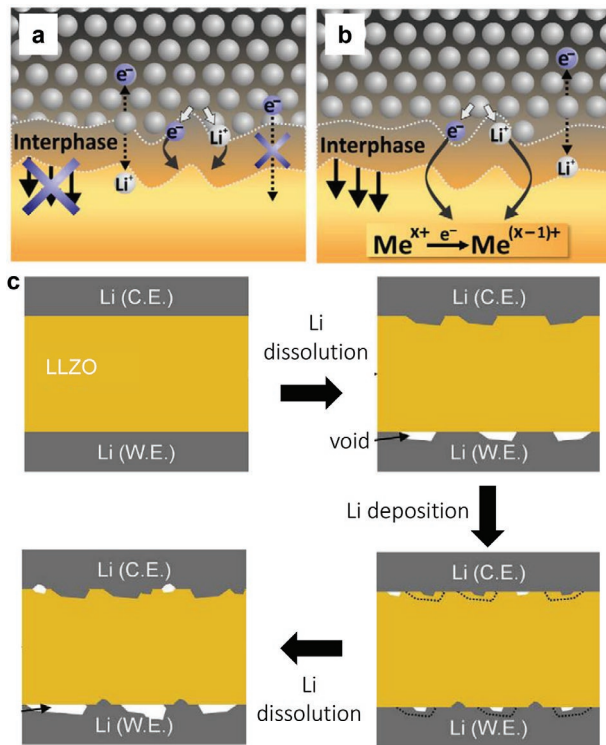


Figure 13. Formation mechanism of solid electrolyte interphase (SEI) between solid electrolyte and Li metal anode. a) Reactive and metastable solid–electrolyte interphase (SEI). b) Reactive and mixed conducting interphase. c) Schematic illustration of the dynamic changes at the Li/LLZO interface during repeated Li dissolution/deposition cycles. a,b) Reproduced with permission.^[315] Copyright 2015, Elsevier. c) Reproduced with permission.^[433] Copyright 2018, Elsevier.

impedance (manifesting in large polarization) and limit cycle life.^[283,312] When solid electrolytes are not stable in the presence of Li metal (i.e., they possess high reduction potentials) or have an unstable interphase layer, the need for an artificial protective film is sparked; Polyplus^[429] is one example of a coating layer introduced to protect LATP against Li metal.

In contrast to LATP, LiPON and LLZO are Li conductors with excellent compatibility against Li metal (reduction potential of 0.69 V vs Li⁺/Li for LATP and LiPON and 0.05 V for LLZO vs Li⁺/Li) because of the passivation mechanism.^[59] The low thermodynamic driving force for LLZO reduction at 0 V (-0.02 eV per atom) and the electrochemical stability window experimentally determined by CV experiments^[84,307,311] indicate that kinetic stabilization stemming from the formation of an interphase may result in an effectively wider stability window, suggesting its possible pairing with Li metal despite the thermodynamic instability. In a first-principles calculation study based on the evaluation of the intercalation voltages for various garnet-type materials $\text{Li}_x\text{La}_3\text{M}_2\text{O}_{12}$ ($\text{M} = \text{Zr}^{4+}, \text{Ti}^{4+}, \text{Nb}^{5+}, \text{Ta}^{5+}, \text{Sb}^{5+}, \text{Bi}^{5+}$, etc.) and Li atoms, the redox potential of the lithium garnet-type structure was observed to be strongly related to the effective nuclear charge experienced by the valence electron of the cation M at octahedral sites.^[83] Garnets with smaller effective nuclear charge cations such as Zr⁴⁺ or Ta⁵⁺ at the octahedral sites are thermodynamically nonreactive

with Li metal because of the lower covalent-bonding character of the octahedral metal than Ta⁵⁺ in the perovskite $\text{La}_{1/3}\text{TaO}_3$.^[83] Nonetheless, computational analysis based on the grand canonical phase diagram revealed the instabilities of LLZO against Li metal having a low reduction potential of 0.05 V,^[76,82] leading to possible cation reduction at low potentials with the subsequent evolution of metallic states at the Li/LLZO interface.^[76] This last finding was also confirmed experimentally, with the coloration observed upon the immersion of LLZO in molten Li attributed to the reduction of Zr and/or Al in LLZO^[76,430] and Zr⁴⁺ reduction of Zr-3d by Li metal for a cycled Li/LLZO/Li symmetrical cell confirmed by XPS depth profile analysis.^[65] Li₃PS₄ and LiPON are excellent examples of electrolytes that are expected to be unstable against Li metal due to the rather high theoretical reduction potentials of ≈ 1.7 – 2.1 and ≈ 0.7 V, respectively, according to first-principles computation based on the Li grand potential phase diagram.^[59,302,303] However, a barrier layer with decomposition products of extended reduction stability toward Li metal forms at the interface including Li₂S (0–2.2 V) and Li₃P for Li₃PS₄ and Li₂O (0–3.1 V), Li₃P, Li₃PO₄ (0.7–4.2 V), Li₄P₂O₇, and Li₃N (0–0.6 V) for LiPON.^[59,302,424,431] Importantly, the decomposition products at the interface such as Li₃N and Li₃P exhibit adequate Li ionic conductivity to the base solid state electrolyte material, and are hypothesized to thereby contribute to high stability but also the excellent cyclability of thousands of cycles reported for LiPON-based thin-film solid-state batteries.^[42,432]

The potentially high chemical reactivity between Li metal and solid electrolytes (especially for LATP, LAGP, and LGPS), poor solid–solid contact (especially for Li metal with LLZO), and significant volume changes during Li stripping and plating are predicted to cause continuous deterioration of the integrity of the Li/electrolyte interface. Even for a stable solid-electrolyte interphase (e.g., Li/LLZO, Li/LiPON), to realize an ASSLB with improved cycle life and longevity, the good chemical stability between the Li metal and solid electrolyte must be accompanied with excellent adhesion and “wettability” between the two components to ensure good interfacial contact. Nonetheless, maintaining good interfacial contact, improving the interface kinetics, and securing morphological stability between Li metal and the solid electrolyte under current load is considered a herculean task when considering the foreseen large volume changes and morphological instabilities (e.g., poor “wettability,” pore formation, delamination, dendrites), and ultimately contact loss, associated with plating and stripping of the Li metal during cycling.^[81] Volume changes may lead to pressure oscillations, where evolution of localized stresses at the Li/solid electrolyte interfaces may result in mechanical failure of the solid electrolyte (cracking, bending, etc.), contact loss, leading to low coulombic efficiency during cycling and limiting the safe practical applicability of high-energy-density ASSLBs.^[367] Although the (electro)chemo-mechanics coupling at the Li/solid electrolyte has yet to be fully characterized and resolved, partially because of the buried nature of the interfaces, the morphological instabilities (namely pore/voids formation) at the Li metal/solid electrolyte interface have already been proven to cause contact loss during anodic loading.^[81] A reference electrode was strategically placed in a three-electrode Li/LLZO/Li cell, and the dynamic changes in the charge-transfer resistance

at the Li/LLZO interfaces during dissolution and deposition of Li metal were successfully decoupled, confirming that the deterioration of the interfacial resistance was in fact mainly due to Li dissolution (rather than deposition) and the formation of voids at the Li/LLZO interface (Figure 13c).^[433] In general, Li-metal dissolution (striping) at the Li/solid electrolyte interface is followed by the diffusion of Li ions across the interface to an available vacant site (or interstitial site) in the solid electrolyte, accompanied by the formation of a Li vacant site and an electron at the Li-metal surface.^[81] The Li stripping rate (i.e., the discharge rate) is thus kinetically limited by the diffusion rate of Li vacant sites created at the Li metal, which for a high discharge rate ($> 0.2 \text{ mA cm}^{-2}$) may supersaturate and accumulate into voids near the interface, leading to morphological instabilities (pores) and loss of physical contact at the Li metal/electrolyte interface.^[423] Insufficient contact (in terms of shape and size of the contact area) between Li metal and the solid electrolyte due to anodic dissolution (void formation) may lead to bending of the current lines at discrete contact spot near the interface (constriction/spreading resistance)^[434] and to the high interfacial resistance typically observed at Li/electrolyte interfaces, such as for Li/LLZO.^[81,435] The mechanical properties and intrinsic limitation of the vacancy diffusion coefficient play a key role in the interface dynamics and electrode kinetics of the Li metal^[81] and may require the use of Li-alloy interlayers, where higher diffusion coefficient compared with pure Li metal can be achieved, thereby alleviating the accumulation of vacancies, formation of pores, and loss of contact at high discharge rates ($> 0.2 \text{ mA cm}^{-2}$). The aforementioned loss of contact between Li metal and the solid electrolyte is detrimental to the battery operation.

Dendrite formation and propagation have been highlighted as major failure mechanisms for chemically stable interfaces (Li/LLZO, Li/Li₃PS₄); in contrast, mechanically driven failure due to interphase growth may be the major deterioration mechanism for Li/electrolyte interfaces with poor chemical stability. Damaged, nonhomogeneous interfaces may instigate nonuniform Li-ion flux, preferable Li plating, and large mechanical stresses, further increasing the cell impedance and leading to inhomogeneous local potentials that may affect Li stripping/plating.^[436] The nonuniform current density distributions can also lead to the formation and propagation of Li dendrites, possibly but not necessarily^[287] accelerated through grain boundaries and voids, where Li-ion conduction is more prevalent, leading to the mechanical failure of the solid electrolyte, degradation of the interfaces, and deterioration of cell performance.^[70,285,437] Namely, the contact between Li metal and the solid electrolyte and the formation of an unstable static interphase may instigate continuous growth of the interphase and massive volume changes (in a constrained interface) in addition to compositional, morphological, and structural change at the Li/solid electrolyte interface. The interphase cannot withstand mechanical deformation without mechanical degradation (e.g., cracks), which can further enhance the Li-ion flux and instigate Li dendrite growth and continuous growth of the interphase layer (and further consumption of the Li metal). Further interfacial deterioration may persist during the dynamic stripping and plating of Li metal upon battery cycling, where a nonuniform interface morphology may create stress concentrations

that lead to the premature fracture of the solid electrolyte, as recently observed for Li/LAGP, and overall electrochemical degradation of the cell.^[438–440] For an unstable, mixed-conducting interphase layer, as observed at the interphases of Li/LAGP, the continuous growth of the interphase and volume expansion exerts a tensile stress on the LAGP electrolyte, ultimately causing its fracture.^[438–440]

The intrinsic morphological instabilities of metal electrodes cannot be prevented but can be at least partially accounted for when applying external pressure by considering the cell assembly strategy in processing. Applying pressure during i) cell fabrication to ensure good physical contact during Li/electrolyte interface formation and ii) cell operation to ease loss of contact and lower interfacial resistance can have a significant effect on the interface kinetics and thus affect the overall cycling performance degradation associated with volume changes and “wettability.”^[81] Moreover, it has been shown that maintaining low interfacial resistance (minimizing pore formation and growth by, for example, applying external load) during Li stripping is highly important to prevent short circuiting due to Li propagation through the solid electrolyte.^[81] The magnitude of applied pressure will be dominated by the mechanical properties of the Li metal (plastic deformation, creep behavior, etc.). At high external pressure, the area of the contact spots between Li metal and the solid electrolyte will increase owing to plastic deformation of the soft Li metal.^[81] When Li-metal stripping was conducted under an applied pressure of 35 MPa, no contact loss and/or interfacial resistance change were observed (Figure 14a).^[81] Applying a high external pressure of several hundreds of MPa to the Li/LLZO interface has proven effective in lowering the interfacial resistance to negligibly small values. Without external pressure, stripping experiment shows serious contact loss after $\approx 12 \text{ h}$ (1.2 mA h cm^{-2}) (Figure 14b).

The charge-transfer resistance at the Li/electrolyte interface will be affected by both the applied external pressure and the mechanical properties of Li metal in addition to the ionic conductivity of the solid electrolyte (according to the constriction resistance theory) and the mechanical properties of the Li/solid electrolyte contact points.^[81] Thus, compositional tuning (e.g., multiple elemental doping) of the solid electrolyte to improve its ionic conductivity can be considered as a valid strategy toward reducing the Li metal/electrolyte interfacial resistance, improving the Li electrode kinetics and easing Li dendrite propagation.^[58,441,442] The application of external pressure to improve physical contact and reduce the interfacial resistance to negligible small values has been reported for both LLZO^[81,442,443] and Li₃PS₄^[215,444] but has limited applicability, as it may lead to mechanical failure because of the brittle nature and low fracture toughness of most thin solid electrolytes. Another strategy to mitigate the intrinsic challenges associated with utilizing a pure Li metal as the anode material, i.e., morphological interface instabilities, significant volume changes, and dendrite formation and propagation, is through the use of a 3D solid-electrolyte framework as a host for the plating and subsequent stripping of the Li metal (Figure 14c).^[445] Generally speaking, current density plays a key role in the formation of Li dendrites. Thus, increasing the surface area of Li metal (for instance, by using Li powder or surface patterning of Li-metal foil^[446] or by infiltrating Li metal into a porous framework)^[447]

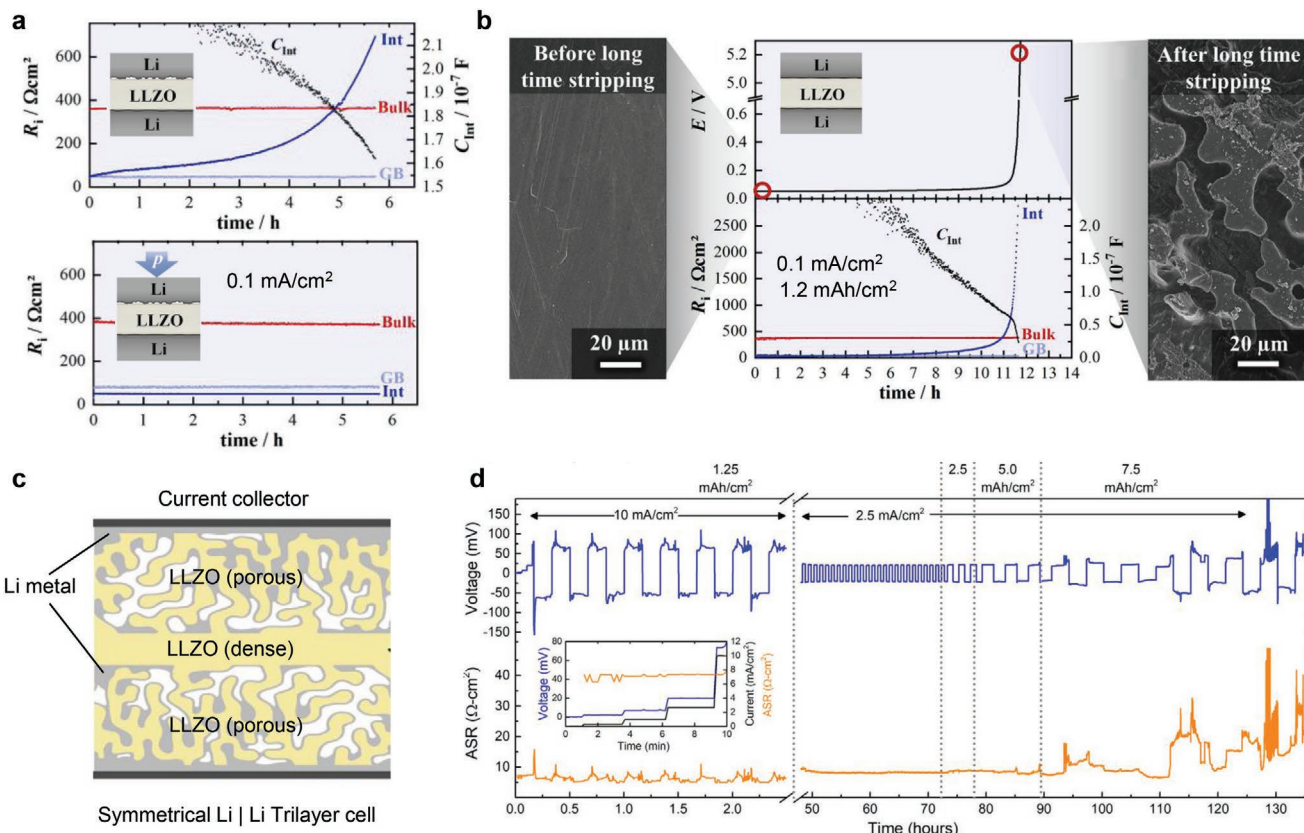


Figure 14. a) Effect of pressure on interfacial resistance in Li|Li symmetrical LLZO cell. Results of long-time lithium stripping experiments at 0.1 mA cm^{-2} without externally applied pressure (top) and $\approx 35 \text{ MPa}$ external applied pressure perpendicular to the interface (down). By applying external pressure, pore formation that leads to contact loss is fully prevented. b) Microstructure of Li metal contact with LLZO electrolyte before and after stripping at current density of 0.1 mA cm^{-2} for 12 h (1.2 mAh cm^{-2}). c,d) 3D solid electrolyte framework as a host for the plating and subsequent stripping of the Li metal; trilayer LLZO electrolyte with infiltrated Li metal anode shows cumulative areal capacity plated of 7.5 mAh cm^{-2} under two different current densities of 2.5 and 10 mA cm^{-2} . a,b) Reproduced with permission.^[81] Copyright 2019, the American Chemical Society. c,d) Reproduced with permission.^[198] Copyright 2019, Elsevier.

and decreasing the effective current density may delay, to some extent, the formation of dendrites. When cycled for 7.5 mAh cm^{-2} at 10 and 2.5 mA cm^{-2} for 100 h, Li metal grew in the pores of a garnet host (one side coated with Al_2O_3 to improve wettability with molten Li) with an interfacial resistance around $10 \Omega \text{ cm}^2$ (Figure 14d).^[445]

Substantial work is still needed to obtain a better understanding of the (electro)chemical and mechanical interrelation during the operation of a solid-state Li-metal battery at both stable and unstable interfaces (e.g., Li/LLZO and Li/LAGP, respectively) to better direct interface engineering efforts.^[448]

4.2. Li Dendrite Formation and Propagation in Solid Electrolytes: Challenges and Strategies

Inorganic ceramic solid electrolytes have often been regarded as a key component in achieving the goals of suppressing Li dendrite propagation, preventing short-circuit events, increasing the CCD (the maximum current before Li dendrite formation), and improving the overall battery cell safety. Although Li dendrites have been shown to grow in most types of considered

battery electrolytes, including liquids^[283] and polymers,^[449] solid-state inorganic ceramics were expected to be impervious to Li-dendrite propagation owing to their high Li transference number (close to unity, Figure 3)^[449] and unique mechanical properties, including a high shear modulus on the order of tens to hundreds of GPa^[279,450] and low fracture toughness (K_{IC}) (Figure 3).^[179] The unfavorable mechanical properties of sulfides (e.g., low fracture toughness, low shear moduli, approximately only twice that of Li metal)^[179] position them at higher risk of Li dendrite formation;^[58,259] Oxide solid electrolytes possess significantly higher shear moduli on the order of tens of GPa, up to 1 order of magnitude higher than that of Li metal.^[256,257] Nonetheless, it has been suggested that lithium dendrites penetrate preferably the solid electrolyte through or along grain boundaries,^[451] interconnected pores, and surface defects,^[58,287] challenging the general consensus of the battery operation regime of solid electrolytes.^[282,451–454] In particular, the growth of Li dendrites has been observed in polycrystalline^[70,76,179,280,283–287] and single-crystal garnet-type LLZO,^[287] NASICON-type $\text{Li}_2\text{O}-\text{Al}_2\text{O}_3-\text{P}_2\text{O}_5-\text{TiO}_2-\text{GeO}_2$ (LATP)^[283] as also in $\text{Li}_{1.5}\text{Al}_{0.5}\text{Ge}_{1.5}(\text{PO}_4)_3$ (LAGP),^[281] glassy (amorphous) $\text{Li}_2\text{S}-\text{P}_2\text{S}_5$ (LPS),^[280,282,287] glass-ceramic $\text{Li}_7\text{P}_3\text{S}_{11}$,^[455] and

polycrystalline $\text{Li}_{10}\text{GeP}_2\text{S}_{12}$ (LGPS)^[76] and $\beta\text{-Li}_3\text{PS}_4$,^[287] to name a few. In dense LLZO (> 99%)^[70] and glass–ceramic sulfide solid electrolytes (e.g., 80Li₂S·20P₂S₅, 75Li₂S·25P₂S₅),^[451,456] Li dendrites were observed to propagate along grain boundaries at CCDs above ≈ 0.6 and 1 mA cm⁻², respectively, setting the upper limit of operation and charging rates before failure.^[19,285,451,456] To put in context, stable Li metal stripping/plating of a LIB with a fluoroethylene-carbonate-based electrolyte solution was observed at 2 mA cm⁻² with an areal capacity of 3.3 mAh cm⁻² for more than 1100 cycles.^[457] The nucleation and growth of the soft and ductile Li metal dendrites in various solid electrolytes under diverse cycling conditions, for instance in the hard and dense oxide garnet LLZO electrolyte^[70] with a shear modulus of 58–60 GPa,^[256,257] has proven that the purely mechanical criterion (shear modulus > 6.8 GPa)^[279,458] is unreliable for ceramic Li solid electrolytes because of volume changes of the electrode material, structure fragmentation, and deterioration of interfacial contact during battery operation. Needless to say, the shear modulus is not the sole parameter controlling dendritic growth, and parameters such as the electrolyte microstructure (e.g., pores, grain orientation, grain boundaries, dislocations),^[80,179,459,460] surface/interfacial chemistry,^[80] inhomogeneous Li/electrolyte contact,^[70] Li wettability,^[80] ionic conductivity at the grain boundaries,^[58] interfacial resistance^[80,285] and even proximity to current collectors,^[459] in addition to the mechanical considerations all contribute to different degrees to Li-metal propagation through the electrolyte and still remain under investigation.

The microstructure of the solid electrolyte, including pre-existing surface defects (e.g., pores, surface cracks, grains, gain boundaries, defects), can affect the local Li-ion concentration and transport properties, instigating dendrite formation, inducing crack opening, and affecting the Li/solid electrolyte interface mechanical integrity.^[258,287,459] Generally speaking, the slower self-diffusion of Li metal compared with that of Li⁺ ions in LLZO electrolyte was hypothesized to create a greater flux of Li⁺ ions toward the interface relative to that of metallic lithium away from the interface, leading to Li metal build-up and “hot-spots”.^[285] Similarly, as Li-ion migration cannot occur through voids and pores in the solid electrolyte, which in turn lowers the Li-ion flux, creating a nonuniform ionic charge distribution profile. A strong Li-ion flux gradient in the solid electrolyte may lead to high local concentration polarization and drive degradation mechanisms by creating “hot spots” and leading to Li deposition within those defected areas.^[258] Once the flaws are filled with Li, mechanical stress is built within both Li metal and the solid electrolyte and is expected to continuously rise upon further Li plating/propagation, extending the surface defects and inducing crack opening, even in case of a low-shear-modulus metal such as Li.^[287] Furthermore, the interfacial stress and electrical potential were combined to describe the local chemical potential of Li metal at the solid electrolyte interface and to further analyze the nucleation and growth of Li dendrites at grain boundaries.^[58] Both the ionic conductivity and the mechanical properties (fracture stress, ability to resist fracture) of the solid electrolyte in addition to the interfacial stresses were observed to be critical parameters affecting the CCD leading to dendrite formation.^[58] Low ionic conductivity at the grain boundaries, high electronic conductivity and/or

physical irregularities in the shape of the Li/solid electrolyte interface may lead to a (electro)chemo-mechanical potential of Li that will provide a driving force for the nucleation of Li dendrites.^[58] Moreover, as the specific grain boundary resistance is up to 2 order of magnitude larger with higher electronic conduction, compared to the grain lattice contribution, the transport of Li ion may be blocked at the grain boundary zones and thus becoming more susceptible for Li metal precipitation and propagation, which necessitates increasing the ionic conductivity or decreasing the electronic conductivity of the grain boundaries in order to suppress Li dendrite growth. In case of the low electronic conductivity LIPON (10^{-15} – 10^{-12} S cm⁻¹),^[461,462] metallic Li formation was alleviated because of the lack of surface states that could trap excess electrons. The excess electrons would in turn migrated to the bulk of LIPON, which has a low Li nucleation tendency and thus effectively suppressing the formation of Li dendrites.^[460] It was hypothesized that the reduction of LLZO at very high overpotentials and the formation of metallic states may facilitate Li-metal nucleation along grain boundaries,^[58] pore surfaces, and Li/LLZO interfaces for sufficient electronic conduction therein.^[76,280,460] The ability of pore surfaces to trap excess electrons, localized around La³⁺, thermodynamically favoring the reduction of Li⁺ atoms, provides possible electron pathways for metallic lithium formation in LLZO.^[460] Additionally, theoretical calculations^[460] have also predicted that the formation of a stable 6 nm thick interfacial tetragonal LLZO phase at the cubic LLZO/Li metal interface^[420] will not prevent metallic Li formation due to trapping of excess electrons, essential to Li nucleation.^[460] Thus, microstructural and grain boundary tuning are an important engineering tool toward achieving higher CCD for the stripping and plating of Li metal.

Although some efforts have been focused on eliminating grain boundaries (via single crystal, amorphous phases), the observation of lithium dendrites in single-crystal LLZO^[459,463] suggests that although lithium metal preferably propagates intergranularly in LLZO, grain boundaries are not a prerequisite for the evolution of Li filaments alone. Poor adhesion^[70] and poor Li wettability,^[80] surface contamination (LiOH and Li₂CO₃),^[80] may also have adverse effects on the Li/electrolyte interfacial resistance,^[80,285] leading to localized high-current-density “hot-spots” and electrochemically driven mechanical stresses. As a general guideline, solid electrolytes should have a moderate elastic modulus (\approx tens of GPa) to be able to, on the one hand, suppress dendrite formation and, on the other hand, prevent stress evolution at the interface through elastic deformation.^[150] Nevertheless, a high modulus is a fly in the ointment as, unlike liquid electrolytes, when Li metal recedes (several micrometers) during discharge, the adhesion between the Li metal and solid electrolyte cannot be maintained for electrolytes with moduli higher than a few MPa,^[450] leading to poor electrode–electrolyte adhesion, higher interfacial resistance, and nonuniform current densities, which may lead to dendrite growth.^[57,285] Strategies to suppress dendrite propagation while promoting fast charging rates with high lithium passage per cycle are needed.^[464] One possible strategy involves reduction of the high Li/electrolyte interfacial resistance (by 1–2 orders of magnitude) by improving the physical contact between the two materials by applying pressure, mechanical polishing, or

applying heat treatment in an inert environment^[285,437,465] and by improving the Li metal wettability on the electrolyte by adding a thin coating or buffer layers of Al₂O₃,^[466] ZnO,^[452] amorphous LPO,^[65] Au,^[70,459] or Si.^[467] Improved interfacial contact can be also achieved through organic–inorganic hybridization, where a polymer electrolyte (elastic modulus <0.1 GPa) is sandwiched between the Li metal and ceramic electrolyte. Another strategy involves the addition of a Li-alloying interlayer^[459] to reduce the energetic barrier for Li plating (overpotential), smooth the voltage drop between the electrolyte and electrode,^[57] and delay Li penetration and propagation. An ultralow Li/LLZO interfacial resistance on the order of 2 Ω cm² was achieved through a simple coating-free process of wet polishing followed by heat treatment (500 °C) in an inert atmosphere,^[80,285] with a CCD of 1 mA cm⁻² (**Table 4**).^[285] With a similar interfacial resistance of 2–10 Ω cm², however, trilayer (porous–dense–porous) LLZO^[198] electrolyte showed stable cycling (yet only 7) with the highest CCD of 10 mA cm⁻² at room temperature, achieving areal capacity up to 1.25 mAh cm⁻² for 2.5 hour. Continuous DC cycling leading to the stable cycling up to 5 mAh cm⁻² under 2.5 mA cm⁻² is demonstrated. Given the similar interfacial resistances, the results could be understood by the increased contact area (the number of active reaction sites) of Li/LLZO interfaces and thus lower current density in the porous LLZO as compare to flat LLZO, suggesting that the use of a porous scaffold or a host structure would be a beneficial strategy for stable cycling for solid/Li metal interfaces as well as accommodating volume changes of Li metal during cycles. Very recently, the effect of 5–10 μm thick nanoporous buffer-layer was investigated as the host and seed layer for sulfide-based ASSLBs without the use of excess Li metal anode. Unusually large capacity of 600 mAh-sized cell consists of argyrodite (Li₆PS₅Cl) as solid electrolyte, LiNi_{0.90}Co_{0.05}Mn_{0.05}O₂ (NMC) as cathode and Ag–C buffer layer anode, showed a reversible cycling (CE > 99.8%) for 1000 cycles at a C-rate of 0.1–0.2 C (1.36–0.68 mA cm⁻²).^[346] The nanoporous Ag–C allows initial formation of Li–Ag alloy inside the buffer layer seeds homogenous lithium deposition and minimizes dendrite growth for long cycling.^[468] Continuous attention and investigation using the buffer layer approach (porous scaffold, host structure) should be encouraged for further development of ASSLB technologies that show high dendrite resistance (C-rate > 1C) for long cycles through engineering strategies. Overall we see that there are important developments currently proceeding, which we see as strong hope to further improve on active strategies to mitigate Li-dendrites. Nevertheless, Li dendrite propagation along grain boundaries^[459] makes the microstructure (grain size), electronic transport at the surface and bulk, and ionic diffusion kinetics at the grain boundaries important parameters.^[179] A strategy involving the compositional tuning of the solid electrolyte (e.g., O substitution for S in sulfides, Li halides, doping in LLZO)^[281,282,455,469,470] to tailor its electro-chemo-mechanics properties and alter the solid-electrolyte interphase composition and transport properties and thus manipulate the nature of the interface between the solid electrolyte and Li metal was largely explored.^[62] For sulfide solid electrolytes, optimization of the processing conditions of the glass–ceramic sulfides and encouraging precipitation of high-conductivity phases in addition to improving adhesion between the electrolyte particles has been

utilized as a strategy to mitigate Li dendrite propagation.^[456] Based on the understanding that the Li/electrolyte interface stability and nature (chemical, mechanical, microstructure, etc.) of the interphase layer largely affect Li dendrite formation and ultimately the battery rate and cycle performance, another strategy, similar to that used in LIBs where electrolyte fluorinated additives have been employed, has been suggested to tailor a stable and efficient interphase layer and suppress dendrite growth.^[457] Another strategy involving the addition of a liquid additive to the solid electrolyte has also been explored as a tool to mitigate Li dendrite propagation by reacting (e.g., to form LiF) and consuming Li dendrites and thus suppressing their growth.^[455]

Pathways toward dendrite-free all-solid-state Li-based battery cells include but are not limited to suppressing Li dendrites and increasing the CCD by increasing the ionic conductivity or lowering the electronic conductivity at grain boundaries, introducing dendrite-free LIPON or Li₃PO₄^[470] thin layers between the electrolyte and Li metal, reducing the concentration of defects and flaws and the overall interfacial resistance, increasing solid electrolyte/Li reaction sites, and modifying the Li nucleation tendency through defect generation or doping (e.g., to affect the La atoms on the surface of LLZO). Other approaches include engineering of the current collector. A negative electrode Au- or Ni-coated porous, instead of a planar, current collector with micro-sized pores was utilized to instigate the preferable plating and stripping of Li metal in the pores and mitigate Li dendrite propagation through the solid electrolyte (**Figure 15a**).^[471] Another strategy involved the relief of compressive stresses during Li electroplating on Cu current, which is a major driving force for Li dendrite growth, through a surface-wrinkling-induced stress-relaxation mechanism enabled when the current collector was supported by a soft substrate (Polydimethylsiloxane-PDMS) (**Figure 15b**).^[436]

4.3. Li/LLZO Interface: Instabilities and Mitigation Strategies

4.3.1. Interfacial Instabilities

The chemical compatibility between Li metal and LLZO electrolyte was initially studied in an *in-situ* STEM investigation, where the formation of a 6 nm thick interfacial layer was confirmed, resulting from the localized phase transition from cubic to tetragonal LLZO when in contact with Li metal.^[420] In a greatly simplified experiment, a LLZO pellet exposed to molten Li at room temperature for 24 h did not show any signs of discoloration,^[83] unlike perovskite LLTO^[83] or LLZO at elevated temperature (300 °C), where intergranular cracking of LLZO was observed.^[430] First-principles computational analysis (Li grand potential phase diagram) revealed decomposition of the solid electrolyte at voltages lower than 0.05 V with reduction products including Li₂O, La₂O₃, Zr₃O, and Zr metal at \sim 0 (0.004)V,^[76,308] which was confirmed experimentally by XPS analysis.^[76] The experimentally improved electrochemical stability of LLZO (determined by CV experiments) was attributed to the surface passivation layer formed by the reduction and oxidation of the solid electrolyte at the anode and cathode sides, respectively, inhibiting further decomposition of the electrolyte.^[84,307] Despite these findings, substantial endeavors are required to realize the

Table 4. List of reported treatment for the interface between Li metal and sulfide or garnet electrolyte.

Treatment	Composition of SE	Resistance of Li/SE without → with treatment (temp.) [ohm cm ²]	Cycle number showing unstable behavior in plating/stripping tests without → with treatment (areal capacity per cycle, current density, temp.)	1st discharge capacity in full cell tests without → with treatment (cathode configuration, current density, temp.) [mAh g ⁻¹]	Ref.
Si coating	Li _{6.85} La _{2.9} Ca _{0.1} Zr _{1.75} Nb _{0.25} O ₁₂	925 → 127 (RT)	n.a. → over 75th (0.017 mAh cm ⁻² , 0.2 mA cm ⁻² , RT)	n.a.	[467]
Sn coating	Li _{6.375} La ₃ Zr _{1.375} Nb _{0.625} O ₁₂	758 → 47 (RT)	1st → over 500th (0.25 mAh cm ⁻² , 0.5 mA cm ⁻² , RT)	126.4 → 151.7 (LiFePO ₄ + carbon + binder + LE, 0.1C, RT)	[203]
Au coating	Li _{6.6} La ₃ Zr _{1.6} Ta _{0.4} O ₁₂	1055 → 168 on one side 1871 → 117 on the other side (25 °C)	1st → over 1st (0.4 mAh cm ⁻² , 0.8 mA cm ⁻² , 50 °C)	n.a.	[70]
Ge coating	Li _{6.85} La _{2.9} Ca _{0.1} Zr _{1.75} Nb _{0.25} O ₁₂	925 → 115 (RT)	n.a. → over 43rd (0.008 mAh cm ⁻² , 0.1 mA cm ⁻² , RT)	≈120 → 138 (Gel/LiFePO ₄ + carbon + binder + LE, 0.1C, RT)	[483]
Al coating	Li ₇ La _{2.75} Ca _{0.25} Zr _{1.75} Nb _{0.25} O ₁₂	950 → 75 (20 °C)	4th → over 36th (0.008 > 0.017 mAh cm ⁻² , 0.05 > 0.2 mA cm ⁻² , 20 °C)	n.a. → 132 (LiFePO ₄ + carbon + binder + LE, 0.1 mA cm ⁻² , 20 °C)	[69]
ZnO coating	Li _{6.75} La _{2.75} Ca _{0.25} Zr _{1.75} Nb _{0.25} O ₁₂	1900 → 20 (n.a.)	n.a. → over 135th (0.017 mAh cm ⁻² , 0.1 mA cm ⁻² , n.a.)	n.a.	[452]
Al ₂ O ₃ coating	Li ₇ La _{2.75} Ca _{0.25} Zr _{1.75} Nb _{0.25} O ₁₂	1716 → 34 (RT)	1st → over 7th (0.05 mAh cm ⁻² , 0.1 mA cm ⁻² , RT)	n.a. → 103 (Li ₂ FeMn ₃ O ₈ + carbon + binder + LE, 0.1C, RT)	[466]
Li ₂ SiO ₃ coating	Li _{6.75} La _{2.75} Ca _{0.25} Zr _{1.5} Ta _{0.5} O ₁₂	1772 → 187 (25 °C)	1st → over 300th (0.1 mAh cm ⁻² , 0.1 mA cm ⁻² , 25 °C)	n.a. → 151 (LiNi _{1/3} Co _{1/3} Mn _{1/3} O ₂ + carbon + binder + LE, 0.18C, 25 °C)	[482]
Li ₃ PO ₄ Coating	Li _{6.5} La ₃ Zr _{1.5} Ta _{0.5} O ₁₂	6 ^{a)} → ≈1 ^{a)} (RT)	1st → over 35th (0.5 mAh cm ⁻² , 0.2 mA cm ⁻² , 25 °C)	n.a. → 143 (LiFePO ₄ + carbon + binder + LE, 0.3C, 25 °C)	[65]
PVDF-HFP+LE coating	Li ₇ La _{2.75} Ca _{0.25} Zr _{1.75} Nb _{0.25} O ₁₂	1400 → 222 (RT)	n.a. → over 45th (0.021 mAh cm ⁻² , 0.125 mA cm ⁻² , RT)	n.a. → ≈145 (Gel/LiFePO ₄ + carbon + binder + LE, 1C, RT)	[67]
Acid treatment	Li _{6.4} La ₃ Zr _{1.4} Ta _{0.6} O ₁₂	940 → 26 (30 °C)	1st → over 700 th (0.05 > 0.1 mAh cm ⁻² , 0.1 > 0.2 mA cm ⁻² , 30 °C)	135.7 → 142.7 (LFP + carbon + LE, 0.1C, 30 °C)	[478]
Au coating	75Li ₂ S–25P ₂ S ₅	n.a.	2nd → over 5th (≈0.26 mAh cm ⁻² , 0.064 mA cm ⁻² , 25 °C)	n.a.	[64]
Si coating	Li ₂ S–P ₂ S ₅	n.a.	n.a.	n.a. → 450 ^{b)} (LNiO ₃ /LiCoO ₂ , 0.1 mA cm ⁻² , RT)	[489]
Li ₁ coating	Li ₇ P ₃ S ₁₁	127 → 66 (RT)	54th → 116 th (0.1 mAh cm ⁻² , 0.5 mA cm ⁻² , RT)	106.4 → ≈115 (LiNbO ₃ –LiCoO ₂ , 0.1 mA cm ⁻² , RT)	[455]
LiF coating	Li ₇ P ₃ S ₁₁	127 → 48 (RT)	54th → over 200th (0.1 mAh cm ⁻² , 0.5 mA cm ⁻² , RT)	106.4 → 118.9 (Li ₇ P ₃ S ₁₁ /LiNbO ₃ –LiCoO ₂ , 0.1 mA cm ⁻² , RT)	[455]

^{a)}After precycle; ^{b)}Unit is μAh cm⁻².

full potential of an ASSLB with LLZO solid electrolyte, namely the investigation of adhesion issues originating from poor “wettability” and point contacts between Li metal and the lithiophobic LLZO solid electrolyte.^[412] When LLZO is employed as an electrolyte in an ASSLB, the low Li-ion conductivity across the Li/LLZO interface (rather than the Li-ion conductivity in the bulk LLZO) has proven to be a pressing issue stemming from the poor and discrete point contact between Li metal and the rigid LLZO oxide. The integrity of the interfacial bonding between Li metal and solid electrolytes may lead to high interfacial resistance^[230,441,465] and inhomogeneous current density distribution at the interface, resulting in nucleation and growth

of Li metal dendrites,^[70] which could impede further development of LLZO as a solid electrolyte toward ASSLBs unless adequate study, engineering strategies, and out-of-the-box thinking are implemented.^[80,247,248,376,452,466,467] Both the morphology and surface chemistry (including contamination) of LLZO affects the interfacial bonding between Li metal and the solid electrolyte.^[80,472] The challenge is twofold as Li metal must adhere not only to the solid electrolyte but also to the metal current collector (commonly Cu or Ni). Both components are typically lithiophobic, requiring an additional surface modification step to alter the surface energy of either Li metal, the solid electrolyte, or the current collector and to preferentially form a stable,

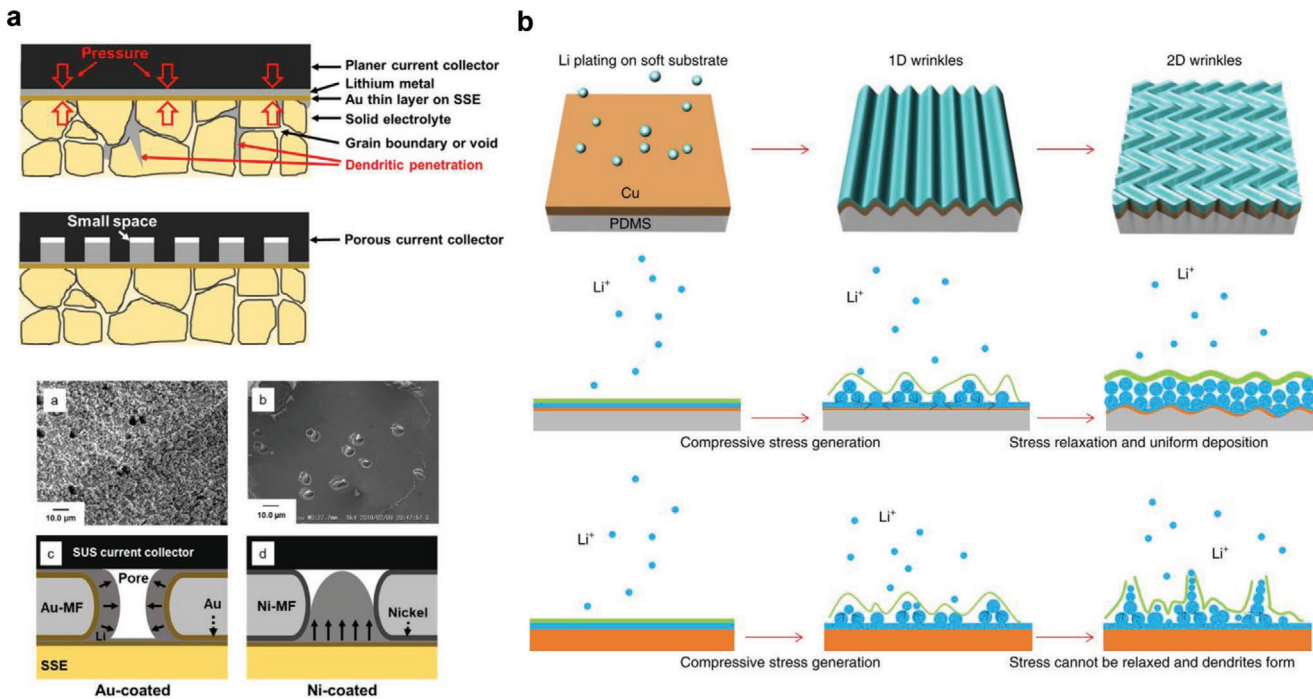


Figure 15. Strategies to mitigate Li dendrite formation by a) porous current collector (Au and Ni) b) soft PDMS substrate to accommodate compressive stress generated during Li plating. a) Reproduced with permission.^[471] Copyright 2020, the American Chemical Society. b) Reproduced with permission.^[436] Copyright 2018, the Nature Publishing Group.

self-limited interphase layer. For instance, a rapid and low-cost chemical strategy to tune the surface energy of Li metal and facilitate its spread on Cu substrates was recently reported.^[412] A \approx 500 nm organic abietic resin ($-COOH$ functional group) was cast on Cu substrates followed by heat treatment for 5 s at 250 °C, which facilitated the spread of molten Li and generation of a relatively compact ultrathin Li layer of 10–20 μm .^[412]

Quantifying the “wettability” between solid Li metal and LLZO electrolyte is not straightforward because determining the contact angle using the typical sessile drop method only provides information about the liquid/solid interface and not the solid/solid interface.^[80] The poor wettability of molten Li on top of a LLZO^[69,80,473] surface and Cu current collector,^[412] represented by an obtuse contact angle because of the higher surface energy of Li metal compared with the substrate, has been a topic of interest because of its dramatic effect on the interfacial ASR and, consequently, on the CCD and long-term stable cycling with Li metal. When sufficient and uniform “wettability” cannot be achieved between Li metal and the solid electrolyte, even for a chemically stable electrolyte such as LLZO, Li^+ ions will be plated preferentially on the solid-electrolyte grain boundaries, where the Li^+ -ion flux is locally enhanced under higher electric field.^[68,474] The adhesion strength, determined by surface chemistry, has been suggested as a metric to quantify the wettability of solid Li metal on LLZO (solid/solid interface).^[472] The electrochemical and mechanical properties of the Li/LLZO interface have been correlated, with a relation between high interfacial (adhesion) strength and low interfacial resistance observed.^[472] When a Li ionic insulator contamination layer, namely Li_2CO_3 , is formed on the LLZO surface, a high interfacial resistance is observed because of the drastic decrease in the Li/LLZO

adhesive strength, which is governed by the surface chemistry and Li “wettability”.^[472] Achieving lower interfacial resistance at the Li/solid electrolyte interface is of paramount importance as it plays a key role in minimizing Li dendrite nucleation and growth, which is one of the main contributors to poor Li stripping/plating stability, coulombic efficiency, and cycle life.^[70,80,230] In principle, the Li/LLZO interfacial ASR should be compatible with interfacial resistances in conventional LIBs, i.e., lower than several tens of $\text{ohm}\cdot\text{cm}^2$. Moreover, it has been suggested that an interfacial charge-transfer resistance greater than 14 $\text{ohm}\cdot\text{cm}^2$ may lead to protuberance growth at the lithium interface because of the concentration of current density.^[58] The high interface ASR observed at Li/LLZO interfaces, typically on the order of several hundred up to thousands of $\text{ohm}\cdot\text{cm}^2$,^[126,419] is generally attributed to the formation of the Li carbonate passivation layer (Li_2CO_3)^[230,465,475] and poor chemical and/or physical contact, resulting in microscopic gaps and low contact points at the Li/LLZO interface^[69,230,472] in addition to the formation and propagation of Li dendrites.^[70]

LLZO has a strong thermodynamic preference to form Li_2CO_3 layer when exposed to H_2O and CO_2 in air.^[230] The energetic preference has proven to be strongly correlated to the surface microstructure of the solid electrolyte and more highly pronounced in large-grained (\approx 150 μm) LLZO samples than in small-grained (\approx 20 μm) samples with multiple grain boundaries.^[465] According to experimental and theoretical analysis, the lower interfacial resistance (37 vs 130 $\text{ohm}\cdot\text{cm}^2$) and improved cycling performance observed in small-grained LLZO samples can be attributed to its improved air stability and lower carbonate layer content.^[476] In addition to contributing to the high interfacial resistance when LLZO is coupled with Li metal, the

Li_2CO_3 contamination layer hinders the Li “wettability” with the solid electrolyte, leading to discrete solid–solid point contacts and high ASR. Unlike the bulk resistance of the solid electrolyte, the interfacial resistance cannot be simply reduced by minimizing the electrolyte thickness; an increase of the effective surface area for reaction and/or mitigation of resistive layers such as Li_2CO_3 in the case of a Li/LLZO interface are necessary.^[80,441] The surface contamination layer (Li_2CO_3) and poor interfacial contact have been suggested as major contributors leading to the high charge-transfer resistance typically observed at Li/LLZO interfaces.^[80,230,465,472,475,477] Nonetheless, it has been proven both theoretically^[79] and experimentally^[80,81] that the intrinsic ASR in the specific case of Li/LLZO is negligibly low ($\approx 0.01\text{--}2 \text{ ohm cm}^2$)^[79\text{--}81] if no contamination layer is present and high external loads ($\approx 400 \text{ MPa}$) are applied (followed by their complete relaxation) during/after cell fabrication to maintain intimate contact.^[81] Moreover, measurements of the pressure-dependent electrode kinetics of the Li metal revealed that the interfacial charge-transfer process at the Li/LLZO interface is only marginally more energy demanding than the bulk hopping process; thus, it was concluded that high ASR at the Li/LLZO interface is not the limiting factor toward the development of a solid-state Li battery.^[81]

4.3.2. Mitigation Strategies to Reduce Interfacial Resistance at the Li/LLZO Interface

The interface ASR resulting from the Li_2CO_3 layer formed upon LLZO exposure to H_2O and CO_2 can be significantly reduced to tens of $\text{ohm}\cdot\text{cm}^2$ by simple physical polishing under an inert environment.^[230] Introducing heating while i) applying relatively low pressure (at 175°C)^[419] or ii) removing Li_2CO_3 and glass-phase contamination layers through calcination with carbon (at 700°C)^[475] or iii) as a part of a recycling procedure (at 100°C)^[437] has proven beneficial in reducing the interfacial ASR down to $25 \text{ ohm}\cdot\text{cm}^2$ (at 25°C), improving the cycling stability, and improving the CCD by a factor of $3\text{--}0.36 \text{ mA cm}^{-2}$.^[419] In addition, adopting a wet-polishing procedure followed by heat treatment (at 400°C – 500°C) resulted in an interfacial ASR as low as $2 \text{ ohm}\cdot\text{cm}^2$ due to the removal of the carbonate layer (see Section 2.3), a CCD of 0.3 mA cm^{-2} , and stable galvanostatic cycling (0.2 mA cm^{-2} for 100 cycles) of a Li/LLZO/Li symmetric cell.^[80] Although the polishing procedure may introduce contaminants to the electrolyte surface, the moderate- and high-temperature procedures are time consuming and may instigate Li loss. Alternatively, chemical^[478] and electrochemical^[65,473] pretreatments including rapid acid pretreatment to remove the surface Li_2CO_3 layer and precycling at lower rates to improve contact during cycling, respectively, have also been marginally explored. A low interfacial resistance of $26 \text{ }\Omega\cdot\text{cm}^2$ against Li metal was achieved with stable Li stripping/plating tests at 0.2 mA cm^{-2} for over 700 h; in comparison, a Li/LLZO/Li symmetric cell without the acid treatment merely operated for 5 cycles under 0.1 mA cm^{-2} before short circuiting.^[478] Additionally, increasing the temperature slightly above the melting point of lithium metal ($\approx 180^\circ\text{C}$) to promote Li infusion into the LLZO rough surface is somewhat beneficial for reducing the interfacial resistance as it improves the physical

contact between the two components. However, the microscopic voids, interfacial flaws, and poor wettability intrinsically stemming from the chemical nature of Li metal and the rigid LLZO oxide ceramic necessitate the exploration of additional engineering routes other than early pressure–temperature–surface treatments (chemical and mechanical polishing) conducted to reduce the interfacial ASR by removing contamination layers and improving physical contact.^[80]

Whereas initial strategies were focused on the removal of the already formed surface contamination layer, current strategies involve tuning of the chemical composition and microstructure of the electrolyte^[247,248,258,441,465] and grain-boundary engineering^[465,480] to prevent or minimize the formation of the contamination layer by improving the air stability of LLZO. For instance, the Li/LLZO interface microstructure, namely multiple surface layer grain boundaries (observed in small-grained samples), was observed to play a critical role in achieving low interfacial ASR and long-term stable cycling with Li metal.^[465] The small-grained LLZO samples are linked to lower susceptibility to air and higher interface roughness, resulting in more contact points and a larger contact area between Li metal and LLZO and thus reducing the interfacial resistance.^[69,480] Controlling the surface chemistry by introducing additives (e.g., LiF, Li_3BO_3) in the processing of the solid electrolyte has also been successful in improving the air stability and lowering the resistance at the Li/LLZO interface.^[247,248] For LiF, a small amount (2 wt%) added to LLZO has been shown to decrease the interfacial resistance between Li metal and LLZO from 1260 to $345 \text{ }\Omega\text{ cm}^2$, attributed to the reduced amount of lithium carbonate formed during air exposure.^[247] Increasing the relative density of LLZO (to 93.7%) and improving the grain-boundary conductivity by ≈ 1 order of magnitude via the addition of Al_2O_3 (0.5 wt%) to LLZO was observed to be effective in lowering the interfacial resistance of the Li/LLZO/Li cell to $95 \text{ }\Omega\text{ cm}^2$.^[437] Additional high-ASR-mitigation strategies involve the use of physical-vapor-deposition-based coatings to improve the adhesion between the rigid solid electrolyte and soft Li metal^[69,70,203,452,466,416,479] and surface-energy tuning of Li metal through the introduction of alloying elements and graphite-based components.^[473,480,481]

Interlayers Deposited on the Solid Electrolytes mainly via Physical Vapor Deposition: One of the key promising strategies to tune the Li metal/LLZO interface chemistry and combat the high interfacial resistance, large polarization, and inhomogeneous ion flow across the interface,^[70] which originate from poor “wettability”, is through interface engineering by depositing thin-film layers on top of the solid electrolyte. These intermediary layers, desirably soft and amorphous, adhere to both materials and preferentially create a spontaneous and stable lithiated contact with excellent Li ionic conductivity and homogeneous current density distribution to effectively suppress to nucleation and growth of Li dendrites.^[376,452,466,467] These layers can be made of non-, poorly, or highly electronically conductive amorphous or crystalline materials deposited via various methods on top of LLZO pellets. Typically, following the deposition process, a Li metal foil is pressed onto the lithophilic, surface-modified LLZO pellet during a heating procedure between 175°C and 300°C . The heat treatment easily melts the Li metal, which then fills surface defects, forming a well-connected interface, facilitating the formation of a Li-rich phase

and improving the physical contact between Li metal and the solid electrolyte. DFT calculation based on Li grand potential diagram analysis validated the improved interface stability of various coating materials/Li compared with Li/LLZO, enabling low interfacial resistance at the anode side.^[65,466,482] Whereas in the former, reductive potential conditions formed Li-containing compounds, the later DFT analysis predicted non Li-containing compounds, such as Zr₄O, Zr₃O, and La₂O₃, which are elastically stiff with a higher Li diffusion barrier.^[482] This approach has been realized with amorphous Si^[467] deposited via plasma-enhanced chemical vapor deposition (PECVD), an amorphous lithium silicate (Li₂SiO₃) layer deposited by a liquid-phase process,^[482] and with graphite, simply drawn with a pencil on top of an LLZO pellet.^[376] The deposition of a thin metal coating (\approx 10–20 nm), such as Al,^[69] Ge,^[483] and Au,^[70] Sn^[203] deposited via e-beam evaporation and magnetron sputtering, respectively, can promote closer contact at the rigid Li/LLZO interface and a self-assembled “Li⁺ ion-breathing” interface due to

the alloying reaction between molten Li metal and another metal (Figure 16a–b; Table 4). The formation of a Li-rich solid solution makes the lithiophobic^[480] LLZO electrolyte lithophilic, which improves the “wettability” and interfacial contact between the solidified Li metal and LLZO.^[69,466,416,479] Most techniques reduce the Li/LLZO interfacial ASR by roughly 1 order of magnitude to tens of ohm·cm² with a stable (flat) voltage plateau and low overpotential (\approx 30–70 mV) during galvanostatic Li stripping and plating tests (at \approx 0.08–0.5 mA cm⁻²) conducted in symmetric Li/LLZO/Li cells.^[69,70,203] A Li/Ge-modified-LLZO/LFP cell at 1C delivered a capacity of 140 mA h g⁻¹ up to 100 cycles, comparable to a full cell using liquid electrolyte, with a slightly better coulombic efficiency (\approx 100%) (Figure 16c).^[483] As previously mentioned, Li alloys can offer higher diffusion coefficients than pure Li metal with higher reduction potential, thus serving as a viable solution to maintain high stability upon contact with the solid electrolyte.^[81] Nonetheless, the reduced nucleation barrier for Li plating for Li

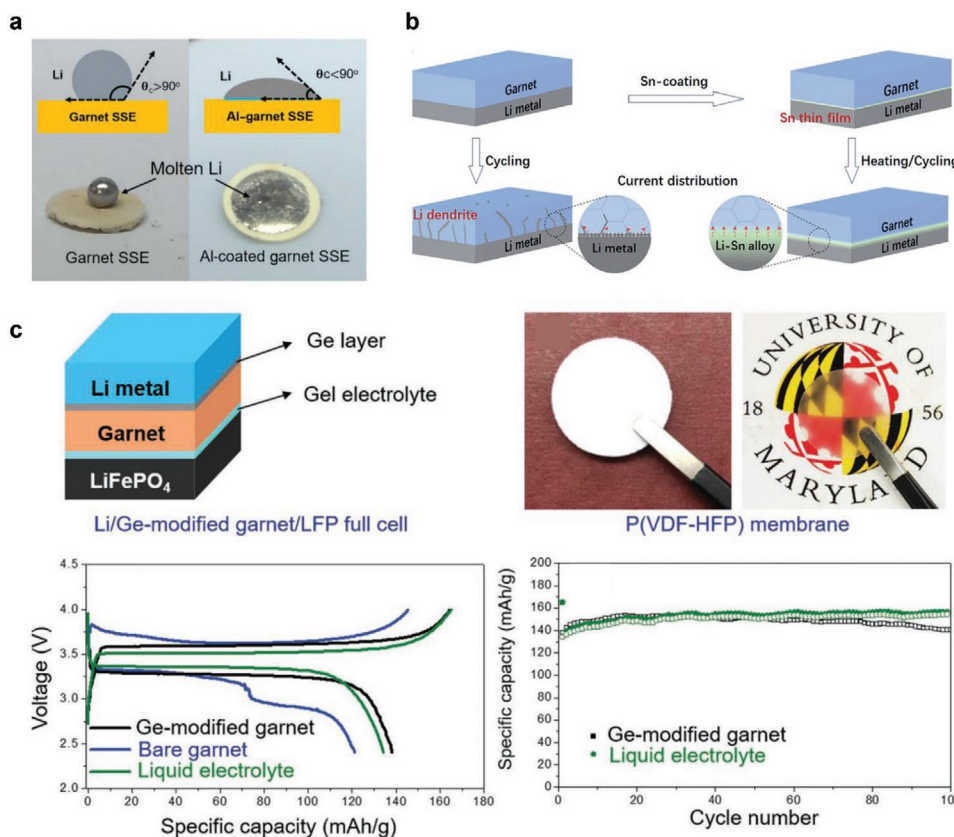


Figure 16. a) Effect of interfacial modification by introducing thin-metal coating between Li metal and LLZO. Improved Li wettability is demonstrated by Al coating. b) A schematic of the garnet–lithium interface performance achieved using LLZO electrolyte with or without surface modification. Without surface modification, LLZO/Li interface suffers poor contact and large interfacial resistance, leading to an uneven lithium flux and thus the formation of lithium dendrites. With the Sn thin-film modification, a self-limited intermediate layer of Li-Sn alloy appears and then bridges the garnet and the lithium, fulfilling excellent contact and wetting between LLZO electrolyte and Li metal and homogenizing the current distribution and lithium flux. c) Electrochemical performance of full cells paired with LiFePO₄ cathodes. Schematic of the full cell structure, where a gel membrane was used between garnet and LFP cathode. Photographs of the P(VDF-HFP)-based gel membrane before and after being soaked in liquid electrolyte. After soaking in liquid electrolyte, the P(VDF-HFP) membrane turned transparent (from left to right). First charge–discharge curve comparison of the Li/LLZO/LFP cell, the Li/Ge-modified-LLZO/LFP cell and Li/liquid-electrolyte/LFP cell tested at 1C between voltage window of 2.4–4.0 V. Cycling performance of the Li/Ge-modified-garnet/LFP cell and Li/liquid-electrolyte/LFP cell at 1C. a) Reproduced with permission.^[69] Copyright 2017, American Association for the Advancement of Science. b) Reproduced with permission.^[203] Copyright 2018, the Royal Society of Chemistry. c) Reproduced with permission.^[483] Copyright 2016, Wiley-VCH.

alloys compared with pure Li metal was not able to prevent Li dendrite growth through the solid electrolyte (LLZO). Moreover, lithium plating was observed to occur between the Li–Au layer and LLZO, indicating that the effect of the Li-alloying interlayer (higher contact area) may be limited (cannot withstand high current densities and is contingent on the Li transport characteristics in the alloy).^[459] In fact, a small Li metal reservoir at the anode side was suggested to be sufficient to prevent low coulombic efficiency due to Li loss by lowering the overpotential for nucleation and decreasing the driving force for Li metal nucleation and propagation through the solid electrolyte via grain boundaries and pores.^[459] Nevertheless, Li plating below a pre-existing dense Li layer will eventually drive Li dendrite nucleation and growth when current densities are increased above a critical value (typically 0.5 mA cm^{-2} in the case of Li/LLZO/Li).^[459] Aside from Li alloying, an additional efficient interlayer between Li metal and LLZO can be achieved through conversion reaction. Conformal metal-oxide coating layers deposited via atomic layer deposition (ALD), such as ultrathin ALD-Al₂O₃^[466] and ZnO,^[452] have exhibited low interfacial resistance (1 and 20 ohm cm², respectively). The successful operation of a complete high-voltage LFMO cathode/LLZO/Li cell was also reported using the ALD-Al₂O₃ coating, attributed to the improved wettability and possibly prevention of LLZO decomposition at the Li-metal interface.

Driven by the success of solid-state Li metal thin-film batteries with LiPON electrolyte, the promising interface

engineering and grain-boundary modification strategy, involving the infusion of amorphous Li₃PO₄ (LPO) onto LLZO was strategically suggested to mitigate both interfacial resistance and Li dendrite propagation.^[65,66] The air-stable LPO can be introduced during the sintering step of LLZO ($\approx 1150^\circ\text{C}$), where it tends to melt and form an amorphous phase near grain boundaries due to its low melting temperature of 837°C .^[66] Recently, a 10 nm LPO solid electrolyte deposited via ALD and further annealed at 600°C on top of a LLZO pellet underwent stable Li stripping/plating at 1 mA cm^{-2} for 180 h with an areal capacity of 0.5 mAh cm^{-2} , the highest reported to date (Figure 17a–c; Table 4).^[65] The LPO-infused LLZO exhibited low interfacial resistance (≈ 17 and $1 \text{ ohm}\cdot\text{cm}^2$ after precycling at 0.05 mA cm^{-2} , most likely due to improved contact during cycling) and endured a CCD up to $\approx 2 \text{ mA cm}^{-2}$ measured in a Li/LLZO/Li symmetrical cell. The highest reported CCD and the multiple Li stripping/plating cycles at 1 mA cm^{-2} (25°C), enabled by the presence of the coated and infused LPO layer between the Li metal and LLZO electrolyte, were attributed to i) the improved mechanical strength and ionic conductivity of the grain boundaries, ii) the homogeneous Li deposition/dissolution, and iii) the formation of a stable solid electrolyte interphase comprised of Li₃PO, Li₂O, Li₃P, etc.,^[65,66] which was formed by the reduction (oxidation) of LPO at potentials lower (higher) than 0.7 (4.21) V versus Li⁺/Li (Figure 17d).^[65] The ionically conducting, electronically insulating, and self-limiting interphase layer resulted in improved interfacial stability. The

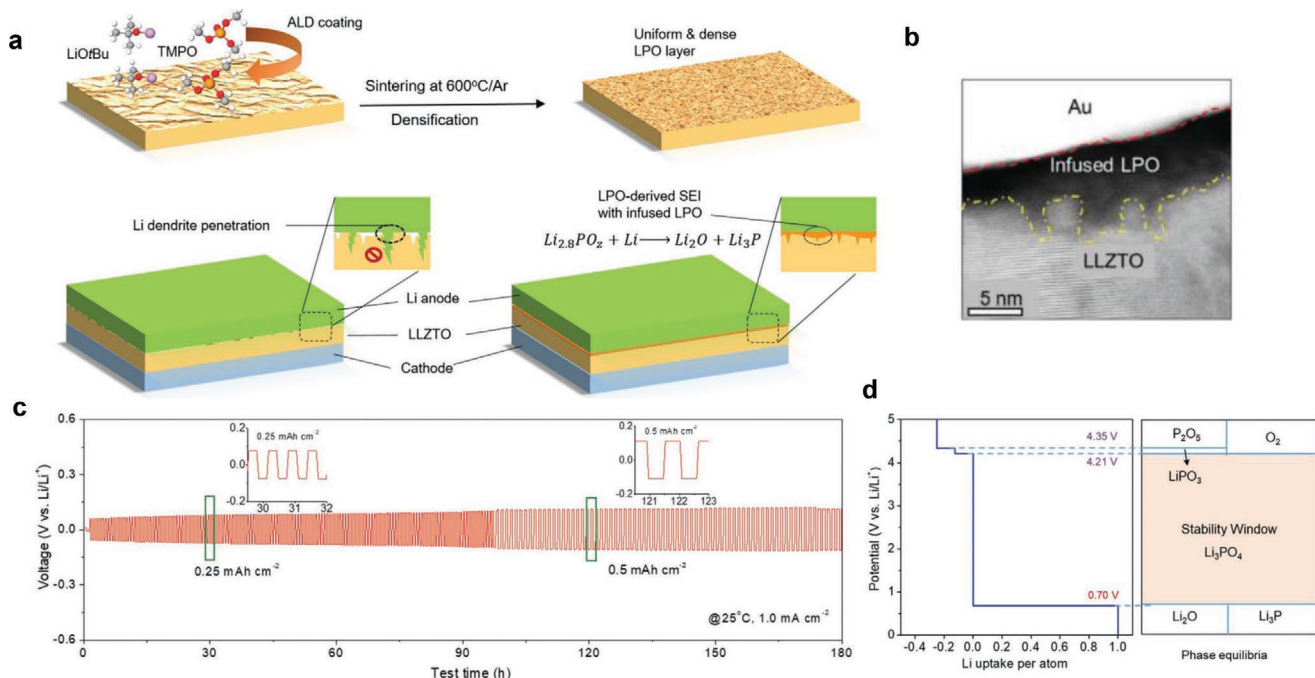


Figure 17. Effect of interfacial modification by introducing Li₃PO₄ between Li metal and LLZO on electrochemical performance. a) Illustration of the interface design of ionic conductive but electronic insulating SEI using atomic layer deposition (ALD). Formation of amorphous Li₃PO₄ (LPO, $\approx 10 \text{ nm}$) layer on polished LLZO pellet via decomposition of LiOtBu and TMPO. The pellet presents rough surface with a large amount of cracks and pores due to surface inhomogeneity during sintering. Surface densification under high temperature, which helps form uniform and dense LPO interphase (brown). Lithium dendrite penetration into the garnet electrolyte, resulting from unstable and weak interface chemistry during cycling with Li anode. The top LPO layer stabilizes the Li/LLZO interface by forming a stable and dense SEI with Li₂O, Li₃P chemicals (orange). b) Galvanostatic cycling of Li/LPO/LLZO/Li cell with a current density of 1.0 mA cm^{-2} ; the cell was precycled at 0.05 mA cm^{-2} . c) Typical dark-field cross-section TEM image at the interface of LPO/LLZTO with the Au coating layer d) Electrochemical stability window of Li₃PO₄. Reproduced with permission.^[65] Copyright 2020, Wiley-VCH.

suppression of Li dendrite propagation was attributed to the coverage of surface defects and cracks by the amorphous LPO layer and to the internal expansion and/or diffusion of LPO into grain boundaries, as confirmed by high-angle annular dark-field scanning transmission electron microscopy (HAADF-STEM).^[65] Moreover, the LPO modification lowered the electronic conductivity of LLZO by ≈ 1 order of magnitude from 10^{-8} to $\approx 10^{-9}$ S cm $^{-1}$, which has been suggested to be mostly responsible for the phenomenon of Li dendrite nucleation and growth.^[280]

Polymer Layers: Soft, flexible, pin-hole-free polymer interlayers that can easily self-adapt to the morphological changes of Li metal and provide smart interface regulation capabilities have been suggested as an innovative strategy for using Li metal anodes in LIBs by homogenizing the local current density and effectively controlling the Li deposition morphology.^[484–486] Although knowledge on polymer coatings can be transferred from liquid to solid-state batteries, limited success is anticipated as the adaptive properties of the polymer, largely responsible for the battery performance improvement, cannot be fully exploited when constrained between two solid components. Nonetheless, polymer interfacial layers (interlayers) can offer improved “wettability” between Li metal and the rigid oxide electrolyte, increase the Li $^{+}$ transference number, and homogenize the Li $^{+}$ -ion flux across the interfaces and thus potentially suppress dendrite formation.^[67,68] A gel polymer electrolyte (PVDF-HFP; 40 μ m thickness), known for its soft and flexible structure, high ionic conductivity, and excellent wettability, was incorporated as an interlayer between the solid electrolyte and electrodes (Li metal and LiFePO₄ cathode) to improve the interfacial contact and decrease the interfacial resistance.^[67] Although a 1- and 2-orders of magnitude decrease in the interfacial layer resistance was observed in the Li/electrolyte (214 ohm·cm 2) and cathode/electrolyte (248 ohm cm 2) half-cells (Table 4), respectively, stable cycling of a complete LFP/Hybrid LLZO/Li cell was demonstrated at room temperature with a capacity of 140 mAh g $^{-1}$ at 1C for 70 cycles.^[67] A different approach included the use of a sandwiched electrolyte configuration of polymer/LATP/polymer with higher resistance than the single polymer electrolyte but twice the number of cycles of a full Li/LiFePO₄ cell (\approx 700 cycles at 0.2C–0.6C) with improved coulombic efficiency.^[68] By blocking the polymer membranes with the LATP solid electrolyte and immobilizing the polymer salt anion at the polymer/ceramic interface, the magnitude of the electric field across the interfaces was reduced, further stabilizing the Li/polymer interfaces against interfacial chemical degradation reaction.^[68]

4.4. Li/Sulfide Interface: Instabilities and Mitigation Strategies

4.4.1. Interfacial Instabilities

Sulfide solid electrolytes not only possess high ionic conductivity with low grain-boundary resistance; their mechanical properties (e.g., ductility) enable low-temperature processing, which should in principle aid in achieving favorable interfaces when coupled with the electrode material. Nonetheless, achieving chemical compatibility and electrochemical stability between

the ultimate anode material, namely the highly reducing Li metal, and sulfide solid electrolytes is of paramount importance toward the feasibility of a cost-effective long-term stable ASSLB with sulfide solid electrolyte. Although cyclic voltammetry, which measured an overestimated electrochemical stability window of \approx 7 V, may not be the most appropriate method for Li/sulfide interphase stability investigation, extensive interfacial analysis including *in situ* and *ex situ* XPS,^[318,425,427] Raman,^[487] and SEM^[451] combined with electrochemical investigation of Li stripping/plating tests and time-resolved electrochemical impedance spectroscopy,^[62,318,425,427] corroborate the formation of a passivation interphase layer due to the poor chemical stability between Li metal and the majority of sulfide solid electrolytes.^[318,425,427,487] The poor chemical stability, resulting from the thermodynamic favorable tendency to react with Li metal, leads to a reaction between sulfide solid electrolytes and Li metal, which can degrade the interface, contingent upon its electronic characteristics, lead to growth and “thickening” of the interphase layer to more than a few nanometers, increase the interfacial ASR, and impair the rate and cycle performance of the cell. Tailoring the interphase composition (and thus the chemical and mechanical properties) via composition tuning of the solid electrolytes^[62,63,251,488] and/or coating layers^[64,455,489] and additives^[455] are promising strategies for enhancing the long-term chemical stability of the Li/electrolyte interface.

Generally, sulfides exhibit exceedingly high decomposition energy at low potentials (\approx 1 eV atom $^{-1}$ at 0 V), signifying reduction reactions of the solid electrolyte.^[59] The stability of different sulfide-based solid electrolytes at \approx 0 V determined by CV (e.g., Li₁₀GeP₂S₁₂,^[304,490] Li_{9.54}Si_{1.74}P_{1.44}S_{11.7}Cl_{0.3},^[305] β -Li₃PS₄,^[63,215] Li₇P₂S₈I,^[316] Li₆PS₅X (X = Cl, Br, I),^[306] and Li₇P₃S₁₁^[217]), completely contrasts with the narrow thermodynamic stability window and high reduction potentials of \approx 1.7 V versus Li $^{+}$ /Li for LGPS, Li₃PS₄, Li₆PS₅Cl, and Li_{3.25}Ge_{0.25}P_{0.75}S₄ and \approx 2.3 V versus Li $^{+}$ /Li for Li₇P₃S₁₁, as predicted by first-principles calculations based on Li grand potential diagrams.^[59,76,82,302] Indeed, most high-ion-conducting sulfide solid electrolytes, namely Li₁₀GeP₂S₁₂, Li_{9.54}Si_{1.74}P_{1.44}S_{11.7}Cl_{0.3}, and Li₇P₃S₁₁, which exhibit ionic conductivities on the order of 10 $^{-2}$ S cm $^{-1}$, are unstable against Li metal, requiring the use of Li alloys to mitigate interfacial decomposition reactions to secure, at least, modest cycling performance.^[365,427,491,492] According to first-principles thermodynamic calculations, at voltages lower than \approx 1.7 V versus Li $^{+}$ /Li, the reduction and lithiation of Li₃PS₄ starts with the formation of P and Li₂S, with the formation of Li₃P at lower voltages (\approx 0 V). The electronically insulating reduction decomposition products, namely Li₂S, a poor ionic conductor (\approx 10 $^{-9}$ S cm $^{-1}$),^[59,82,172,425,493] and Li₃P (\approx 10 $^{-4}$ S cm $^{-1}$),^[494] should in principle form a passivating interphase layer between the Li metal and sulfide solid electrolyte, which should inhibit further decomposition. Indeed, a kinetically stabilized interphase layer of a few nanometers has been reported to form between several phosphorous-based sulfide solid electrolytes and Li metal. Nonetheless, the composition of the interphase layer and the compositional change under current load, and even at idle conditions, may lead to a resistive interphase layer of a few tens or hundreds of ohm·cm 2 ,^[318,425] which are unpractical values for high-rate, long-term operative ASSLBs. Among the different sulfide-based electrolytes, β -Li₃PS₄ (75Li₂S·25P₂S₅ glass

or glass-ceramic), the most air-stable phase of the $\text{Li}_2\text{S} \cdot \text{P}_2\text{S}_5$ binary system, is a good candidate to serve as a high ionic conducting ($>10^{-4}$ S cm $^{-1}$) solid electrolyte that can also offer favorable interfaces but still limited cell performance.^[63,214] Based on in situ Raman and XPS analysis, it was suggested that during Li^+ reduction and plating (on gold electrode), the oxidation of Li metal is accompanied by a quasi-reversible conversion of PS_4^{3-} to form $\text{P}_2\text{S}_6^{4-}$ and Li_2S (4-electron transfer process) at the electrode/electrolyte interface.^[487] Nonetheless, after only 3 cycles, a drop in the open-circuit voltage was evident, indicating further increase in the cell impedance and interface compositional change.^[487] In case of a nanostructured $\beta\text{-Li}_3\text{PS}_4$ with an ionic conductivity of $\approx 10^{-4}$ S cm $^{-1}$, a 5 V electrochemical stability window was reported with high stability against Li metal manifested in ≈ 40 mV overpotential at a current density of 0.1 mA cm $^{-2}$ for over 20 cycles (≈ 80 h).^[215] A computer modeling simulation indicated that the $\text{Li}_3\text{PS}_4/\text{Li}$ interfaces are not stable compared with $\text{Li}_3\text{PO}_4/\text{Li}$ interfaces and instigate decomposition of the electrolyte and the breaking of P-S bonds into a thin protective buffer layer on the Li_3PS_4 surface comprised of Li_2S , which stabilizes the $\text{Li}_3\text{PS}_4/\text{Li}$ interface by serving as a kinetic barrier.^[495]

The reduction of sulfides during Li stripping/plating, i.e., at low voltages of ≈ 0 V, accompanied by the formation of a solid interphase layer, may improve the “wettability” between Li metal and the sulfide solid electrolyte. Nonetheless, the reduction decomposition products of sulfides and thiophosphates (e.g., $\text{Li}_{10}\text{GeP}_2\text{S}_{12}$ (LGPS), $\text{Li}_{13.25}\text{Ge}_{0.25}\text{P}_{0.75}\text{S}_4$, Li_3PS_3 , Li_4GeS_4 , $\text{Li}_6\text{PS}_5\text{Cl}$, and $\text{Li}_7\text{P}_2\text{S}_8\text{I}$) at the Li metal side are expected to exhibit poor Li-ion conductivity compared with the solid electrolyte, leading to high interfacial resistance.^[494,496] Still, the major concern is the possible ionic-electronic mixed conduction species and continuous “thickening” of the interphase layer. The formation of a decomposition layer consisting of Li-metal alloys (e.g., Li-Ge alloys) may form a mixed ionic-electronic conducting layer, requiring a form of passivating protection layers to stabilize the Li/electrolyte interface, observed in Li halide additives, such as LiI , LiF , LiBr , and LiCl .^[72,469,497] LGPS is an excellent example of a crystalline sulfide-based solid electrolyte that fulfills the necessary prerequisite for a solid electrolyte and exhibits a high ionic conductivity (1.2×10^{-2} S cm $^{-1}$ 27 °C) and low electronic conductivity ($\approx 10^{-9}$ S cm $^{-1}$) at room temperature.^[78] Nonetheless, although LGPS was initially suggested to exhibit a chemical stability window of $\approx 0\text{--}5$ V versus Li^+/Li determined via cyclic voltammetry,^[78] theoretical consideration predicted structural instabilities^[498] in addition to it being a metastable phase that is not stable against Li metal (reduction by Li at low voltages and extraction of Li at high voltages),^[172] questioning its potential role in solid-state Li-metal batteries.^[427,318,487] According to first-principles thermodynamic calculations, $\text{Li}_{10}\text{GeP}_2\text{S}_{12}$ ^[172] starts with the reduction and lithiation of LGPS at voltages lower than ≈ 1.7 V versus Li^+/Li and with the formation of Li_4GeS_4 , P, and Li_2S and Li-P and Li-Ge-based compounds at lower voltages (≈ 0 V), including $\text{Li}_{15}\text{Ge}_4$, Li_3P , and Li_2S , as also demonstrated by XPS.^[76,82,169,172] The high reduction potential indicates that the aforementioned sulfide is unlikely to be stable against Li metal with the formation of Li_2S , as also confirmed experimentally at the Li/LGPS interface using XRD.^[60] It has become evident that LGPS

possesses poor interfacial stability and chemical compatibility with Li metal, forming a diffusion-limited interphase layer composed of Li_3P , Li_2S , and Ge or Li-Ge alloys (e.g., $\text{Li}_{15}\text{Ge}_4$) as determined by in situ XPS combined with time-resolved impedance spectroscopy,^[427] aligning with theoretical predictions.^[59,82,302] The interfacial decomposition of LGPS with Li metal was implied by the fast interfacial resistance increase, ≈ 10 times higher compared with $\text{Li}_7\text{P}_3\text{S}_{11}$,^[425] and the deterioration of the charge-transfer kinetics,^[427] which are attributed to the continuous reduction of Ge^{4+} resulting in an electronic conducting interphase layer.^[318,427] After long-term contact between Li and LGPS (≈ 3 mm thick pellet), an ≈ 20 nm thick interphase with a resistance of ≈ 250 ohm · cm 2 was determined, ≈ 1 order of magnitude higher than the bulk resistance of LGPS electrolyte, jeopardizing the use of LGPS as a practical solid electrolyte for ASSLBs because of the interfacial resistances originating from the poor interface stability between Li metal and LGPS^[427] (also applicable for $\text{Li}_7\text{P}_3\text{S}_{11}$).^[318,425] Moreover, in situ Raman analysis conducted under applied potential (1 to -0.5 V) suggests that LGPS is not stable and exhibits irreversible interfacial chemical changes, especially below 0.1 V.^[487] The implementation of Li halides either as a buffer layer between Li metal and the solid electrolyte or incorporated into the sulfide electrolyte has been suggested based on their sufficient solubility in sulfides and their low melting point ($\approx 450\text{--}850$ °C), which allows them to also function as a possible binder and wetting agent with Li metal.^[469] The high reduction potential of Li halides compared with Li metal and their stability at higher potentials could in principle improve the electrochemical stability of the solid electrolyte and enable the coupling of sulfide electrolytes with high-voltage cathodes.^[469] Compositional tuning of LGPS by incorporating Li-Br to obtain a LiBr-LGPS composite electrolyte, where the highly conducting $\text{Li}_6\text{PS}_5\text{Br}$ phase and $\text{Li}_{10}\text{GeP}_2\text{S}_{12}$ coexist and the partial substitution of Br^- (with larger ionic radius) with S^{2-} in LGPS, which could broaden the conduction pathways of Li ions, was used to improve the interfacial conduction kinetics and electrochemical stability with Li metal.^[469] Nonetheless, the LiBr-LGPS composite only showed limited improvement during Li stripping/plating, requiring the use of a Li-In anode material to achieve long-term cycling stability.^[469]

Unlike LGPS, highly crystalline form $\text{Li}_7\text{P}_3\text{S}_{11}$ (without a residual glassy phase) was shown to exhibit a kinetically stabilized interphase with a significantly lower thickness of only ≈ 2 nm upon contact with Li metal, as determined by time-dependent impedance spectroscopy analysis.^[425] Further XPS analysis determined that the main component of the interphase was Li_2S accompanied by Li_3P (and some additional reduced phosphate species such as LiP , LiP_5 , or LiP_7) according to the following reaction: $\text{Li}_7\text{P}_3\text{S}_{11} + 24\text{Li} \rightarrow 11\text{Li}_2\text{S} + 3\text{Li}_3\text{P}$, degrading the interfacial properties of the Li/ $\text{Li}_7\text{P}_3\text{S}_{11}$ interface and necessitating interface modification for ASSLB applications.^[425] Electrochemical analysis indicated the bulk resistance of $\text{Li}_7\text{P}_3\text{S}_{11}$ (1 mm thickness) was ≈ 80 Ω cm 2 ; however, the Li/ $\text{Li}_7\text{P}_3\text{S}_{11}$ interfacial resistance was evaluated to be 50% higher at ≈ 125 Ω cm 2 . DFT analysis was used to calculate the interface energy of $\text{Li}_7\text{P}_3\text{S}_{11}$ as a function of the number of Li, and it was concluded that the electrolyte is unstable against Li metal, supporting the introduction of buffer Li-binary buffer layers, such as LiF and

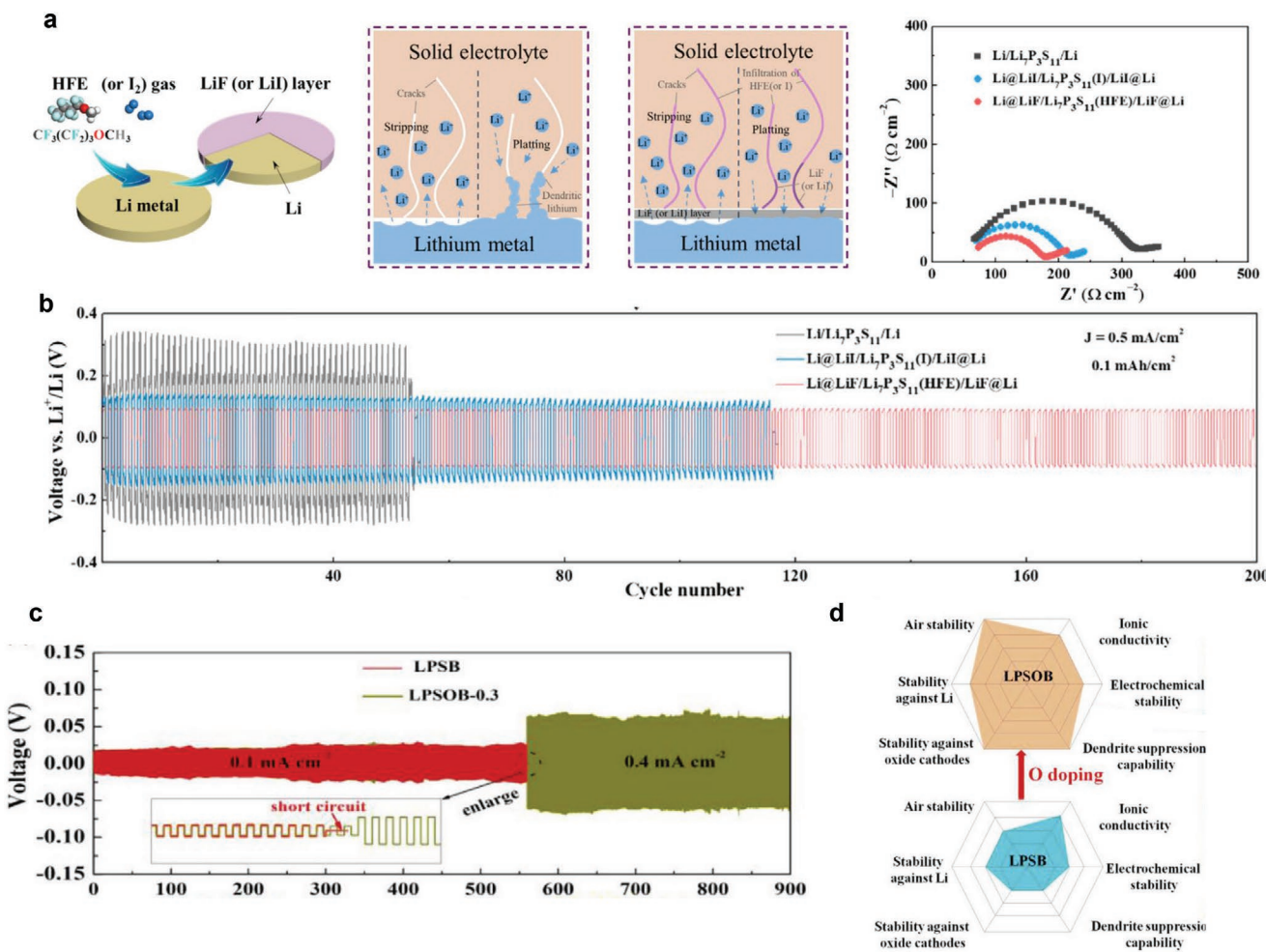


Figure 18. a) Effect of interfacial modification by introducing LiF and LiI between Li metal and Li₂P₃S₁₁. On interfacial resistance, symmetrical cell performance, and full cell performance. Schematic diagrams of the processes for the surface coating of LiF (or LiI) layer on the Li metal surface (left). Schematic diagrams of lithium stripping/plating behavior of bare Li with untreated solid electrolyte and LiF (or LiI) coated Li metal with HFE (or I) infiltrated electrolyte (center). Nyquist plots of Li/LPS/Li, Li@LiI/LPS(I)/LiI@Li, and Li@LiF/LPS(HFE)/LiF@Li symmetrical cells (right). Galvanostatic b) Galvanostatic discharge/charge voltage profiles of Li/Li₂P₃S₁₁/Li (black), Li@LiI/Li₂P₃S₁₁(I)/LiI@Li (blue), and Li@LiF/Li₂P₃S₁₁(HFE)/LiF@Li (red) symmetrical cells at current densities of 0.5 mA cm⁻² with a fixed stripping/plating capacity of 0.1 mAh cm⁻² at room temperature. c) Galvanostatic cycling of the Li/Li₆PS₅Br and Li/Li₆PS_{4.7}O_{0.3}Br symmetric cells at constant current densities of 0.1 and 0.4 mA cm⁻², d) Schematic illustration depicting the superiority of O-doped electrolyte and its application on all-solid-state battery. a,b) Reproduced with permission.^[455] Copyright 2018, Elsevier. c,d) Reproduced with permission.^[62] Copyright 2018, Elsevier.

LiI, to increase the interface energy and improve Li diffusion across the interface, relieve interface stress, and promote uniform Li deposition (**Figure 18a–b**, Table 4).^[455] Upon introducing LiF (and LiI) coating layers between the Li metal and solid electrolyte, the resistance was reduced to ~50 (and 65) Ω cm², respectively, attributed to the suppression of side reactions and a more stable interphase layer.^[455] In addition, a 100% decrease in the overpotential for Li stripping/plating to 12 mV was achieved during 200 cycles at 0.5 mA cm⁻².^[455]

The stability of argyrodite solid electrolyte against Li metal was also investigated using in situ XPS combined with time-resolved impedance spectroscopy. It was observed that when Li₆PS₅X (X = Cl, Br, I) argyrodite comes in contact with Li metal, it decomposes into an interphase layer composed of Li₃P, Li₂S, and LiX with increasing interfacial resistance growth, especially for Li₆PS₅I.^[318] In situ XPS was used to

evaluate the stability of Li₆PS₅X against Li metal, and the formation of a diffusion-controlled SEI layer with a thickness of a few nanometers comprised of Li₂S, Li₃P, and minor reduced phosphorous species was confirmed, according to the following reaction: Li₆PS₅X + 8Li → 5Li₂S + Li₃P + LiX.^[318] The interphase mainly consisted of the low-conducting Li₂S phase, which has low ionic and electronic conductivities, and partially of the ion-conducting compounds Li₃P and LiX, leading to a resistive SEI. Even under idle conditions (without current load), both for Li₆PS₅X (X = Cl, Br)^[318] and Li₇P₃S₁₁^[425,318] the interfacial resistance between the solid electrolyte and Li metal increased over time, amounting to a few tens of Ω cm² (and hundreds of Ω cm² when simulated to continuously grow for over 10 years), which is two orders of magnitude higher compared than that for a liquid LIB and is unacceptable considering the solid electrolyte (~20 μm) is estimated to exhibit a resistance of 0.2 Ω cm²

for a total ionic conductivity of 1 mS cm^{-1} .^[499,500] $\text{Li}_6\text{PS}_5\text{I}$ and $\text{Li}_{10}\text{GeP}_2\text{S}_{12}$ exhibited even higher interfacial resistance with fast SEI growth of up to hundreds of $\text{k}\Omega \text{ cm}^2$.^[318] The substitution of O for S in $\text{Li}_6\text{PS}_5\text{Br}$ via the addition of Li_2O has been employed to chemically and mechanically tune the properties of the solid electrolyte and, more importantly, of the SEI. The O doping led to the introduction of oxide-based compounds, namely Li_3OBr , into the interphase layer, improved the chemical stability against Li metal, and led to the formation of a kinetically stabilized interphase, similar to that of $\text{Li}_7\text{P}_3\text{S}_{11}$,^[425] which lowered the Li/electrolyte interfacial resistance by 50% and increased the CCD by a factor of 2.^[62]

4.4.2. Mitigation Strategies to Reduce Interfacial Resistance at the Li/Sulfide Interface

One strategy to stabilize the Li/sulfide solid electrolyte interface and improve the Li stripping/plating capabilities through the solid electrolytes is through substitution or doping of elements.^[63,62] O substitution for S in sulfides is a powerful and simple approach to significantly change the mechanical, chemical, and electrochemical properties of the solid electrolyte. Moreover, the interface nature between the solid electrolyte and Li metal can be highly improved and Li dendrites can be suppressed.^[62] O doping in $\text{Li}_6\text{PS}_5\text{Br}$, namely $\text{Li}_6\text{PS}_{4.7}\text{O}_{0.3}\text{Br}$, where O atoms substitute S atoms at available S^{2-} sites, rather than at the PS_4 tetrahedra sites, has been recently suggested as a strategy to improve the chemical and electrochemical stability of the solid electrolyte against Li metal and high-voltage cathodes and to suppress Li dendrites.^[62] The CCD increased from 0.45 to 0.89 mA cm^{-2} and stable cycle performance was achieved at 0.4 mA cm^{-2} for 900 cycles ($\approx 900 \text{ h}$) (Figure 18c). The improvement of all the chemical and electrochemical performance aspects was attributed to the improvement in mechanical properties, especially strengthening of the shear modulus, and the O-containing compounds in the interphase layer (Figure 18d). For instance, the presence of the superionic conductor Li_3OBr on Li metal, confirmed by XRD, improved the Li ionic conductivity across the Li/electrolyte interface.^[62] Interphase layers comprised of oxide-based compounds with high Young's modulus, such as Li_3PO_4 , have been proven successful in restraining Li dendrite growth in organic electrolytes.^[470] In view of this point, the reduction of Li dendrite propagation through $\text{Li}_6\text{PS}_{4.7}\text{O}_{0.3}\text{Br}$ was attributed to the formation of Li_3OBr at the interface.^[62] The addition of 1 mol% P_2O_5 to the electrolyte, namely $75\text{Li}_2\text{S} \cdot 24\text{P}_2\text{S}_5 \cdot 1\text{P}_2\text{O}_5$, has also been proven successful in increasing the ionic conductivity of the solid electrolyte by 56% to $8 \times 10^{-4} \text{ S cm}^{-1}$, lowering the overpotential for Li electrodeposition by 20% to $\approx 30 \text{ mV}$ for 100 plating/stripping cycles ($\approx 100 \text{ h}$).^[63] Moreover, a Li/ $75\text{Li}_2\text{S} \cdot 24\text{P}_2\text{S}_5 \cdot 1\text{P}_2\text{O}_5$ /LCO cell cycled at 0.1C exhibited slightly improved cycling performance with a discharge capacity of 109 mAh g^{-1} and a $\approx 10\%$ improvement in capacity retention after 30 cycles.^[63] The effect of introducing O atom dopants into $\beta\text{-Li}_3\text{PS}_4$ ^[488] and LGPS^[251] to stabilize the crystal structure, increase the ionic conductivity, and improve the interface stability against Li metal has already been reported.^[251,488] As O is more electronegative than S (the P–O bond is stronger than the P–S bond), free space

between two successive O dopants through which Li ions can travel is created, driving the transport behavior from 2D to 3D in the $\beta\text{-Li}_3\text{PS}_4$ structure.^[488] The calculation also reveals that the O atom doping also mitigates decomposition reactions at the interface through the formation of a Li_2S -like buffer layer.^[488] Ba-substituted $\text{Li}_{10}\text{GeP}_2\text{S}_{12}$, namely, $\text{Li}_{9.4}\text{Ba}_{0.3}\text{GeP}_2\text{S}_{12}$, was also synthesized to achieve a high ionic conductivity of $\approx 7 \times 10^{-4} \text{ S cm}^{-1}$ with improved electrochemical stability toward Li metal.^[490] The improved electrochemical stability toward Li metal, indicated by the 20 cycles (40 h) of Li stripping/plating at 0.1 mA with an overpotential of 100–200 mV (50% lower than that for unsubstituted LGPS), was attributed to the structural stability resulting from the stable interactions between Ba^{2+} and S^{2-} in the $\text{Li}_{9.4}\text{Ba}_{0.3}\text{GeP}_2\text{S}_{12}$ structure.^[490]

Tailoring the Li/sulfide electrolyte (glass, glass–ceramic $\text{Li}_2\text{S} \cdot \text{P}_2\text{S}_5$, and crystalline) interphase composition can be achieved relatively easy via compositional tuning of the sulfide electrolyte^[282] through the introduction of soluble, high-ionic-conductivity compounds with low electronic conductivity (e.g., LiI , $\text{LiF-Li}_3\text{N}$, LiBr).^[281,282,455,469] An addition of 30% mole of LiI (band gap of 6.4 eV), to improve the ion conductivity and lower the electronic conductivity of the SEI, to the glass $75\text{Li}_2\text{S} \cdot 25\text{P}_2\text{S}_5$ solid electrolyte resulted in an increase of the CCD from 0.4 to 1 mA cm^{-2} for 60 h at room temperature; however, long-term stable Li stripping/plating performance (200 h; 70 mV overpotential) was achieved at higher temperatures (60–100 °C) at 1.5 mA cm^{-2} .^[282] In a different case, the doping of $\beta\text{-Li}_3\text{PS}_4$ with LiI , viz. the $\text{Li}_7\text{P}_2\text{S}_8\text{I}$ phase, resulted in stable Li stripping/plating performance with an overpotential of $\approx 10 \text{ mV}$ when cycled at 0.2 mA cm^{-2} for $\approx 80 \text{ h}$, attributed to the enhanced interfacial kinetics and ionic conductivity and highly dense electrolyte network.^[316] The use of other Li halides, such as LiF , LiCl , and LiBr , in $\text{Li}_2\text{S} \cdot \text{P}_2\text{S}_5$ systems has also been reported; however, their limited success (lower CCD) was attributed to their potentially lower solubilities in the sulfide solid electrolyte compared with LiI .^[282] Nonetheless, when a liquid additive was used to form a coating layer on top of Li metal (by spontaneously reacting at 150 °C) and also used to infiltrate the pores in the solid electrolyte, the layer formed was a dense LiF layer (compared with the rough and porous LiI layer) that resulted in improved suppression of Li dendrite penetration through the solid electrolyte due to the consumption of Li dendrites by the liquid additive.^[455] That is, in addition to initially forming the LiF layer, the sole purpose of the liquid additive was to efficiently react with and consume Li dendrites and suppress their growth. The addition of the additive allowed for stable Li stripping/plating cycles at 0.5 mA cm^{-2} for 200 cycles with a low average overpotential of 12 mV (0.1 mA cm^{-2}).^[455] As shown above, modifying bulk composition in particular of sulfide solid-electrolyte has been shown significant improvement on interfacial charge-transport between the solid electrolyte and Li metal. The modified composition would create different class of SEI layer or the kinetically stabilized interphase with Li metal anode, especially strengthening the shortcomings of original composition; chemical compatibility, ionic transport and mechanical properties. Lowered interfacial resistance or overpotential for Li deposition, increased CCDs and ability to operate under higher (C-rate >1C) with high CE are the ideal outcome of such modification. Nonetheless, the modification has no real value when materials' (original) superior properties

become weakened. For example, sulfide electrolyte necessitates widening their electrochemical stability window and air stability whereas processability of sulfide electrolyte should be preserved. In this regard, introduction of thin artificial SEI layer would be better choice as discussed below.

Although less suited for practical large-scale applications, to improve the interfacial stability and unify the interface, vacuum evaporation of the Li metal can be adopted instead of the attachment of Li foil.^[64] Li evaporation directly on a sulfide electrolyte resulted in better interfacial contact than mechanically pressing and improved the stripping/plating cycling.^[64,454] In addition, the physical vapor deposition of a thin gold (60 nm)^[64] or Si (20 nm)^[489] layer at the interface between Li metal and the solid electrolyte has been suggested to stabilize Li plating and stripping in full cells. The deposition of a thin gold layer (60 nm) on both sides of a glass Li₃PS₄ (75Li₂S·25P₂S₅) electrolyte pellet followed by vacuum evaporation of a thin Li-metal layer in a symmetric cell, namely Li/Au/Li₃PS₄/Au/Li, resulted in more uniform deposition of Li metal with higher Li utilization through longer cycling; however, the average ≈30% utilization of Li metal was retained for merely 5 cycles.^[64] The most lithiated phase Li₁₅Au₄ alloy was observed after Li deposition and was suggested to lower the interfacial resistance by filling all the voids and interfacial flaws at the solid-electrolyte interface.

The aforementioned strategies have shown limited success, and the intrinsic poor interface stability between sulfide solid electrolytes (mainly LGPS and Li₆PS₅X) and Li metal, including the poor Li plating/stripping performance,^[454,492] have urged the replacement of Li metal mainly by Li-In (indium)^[365,491,492] but also by other Li alloys such as Li-Al,^[501,502,492] Li-Sn,^[503] and Li-Si.^[503,489] Upon replacing the highly reducing Li metal with Li-metal alloys with a higher reduction potential (~0.6 V vs Li⁺/Li),^[365] the chemical stability of the interface improved, which was attributed to a more stable interphase, and lower interfacial resistance with stable cycle life was reported, especially for the Li-In system.^[492] Nonetheless, in addition to the use of indium lowering the battery voltage and capacity, thus reducing the energy density, indium is also considered costly compared with Li metal and may increase the cell cost even further. Using a rather thick (0.1 mm) Al metal foil sandwiched between Li metal and LGPS solid electrolyte, a self-assembled “Li⁺ ion-breathing” interface with the ability to transport Li⁺ ions was achieved due to the alloying of Al with molten Li metal.^[501] Nonetheless, the reported cycle life and rate performance are still unsatisfactory, and a thorough investigation of the SEI components to gain a fundamental understanding of the origin of the improved performance has yet to be conducted.

5. Outlook and Perspective

Solid-state Li metal batteries employing inorganic solid electrolytes are shedding light on a safer and more efficient next generation of rechargeable batteries. Although solid-state batteries can offer high gravimetric and volumetric energy of 250 Wh kg⁻¹ and 700 Wh L⁻¹, respectively, the slow kinetics can impair the fast discharge and charge performance. This roadmap for the development of successful ASSLBs focuses on five parameters:

energy density, power density, long-term stability, processing, and safety.^[10] Although solid electrolytes may offer the ultimate solution toward a safe high-energy-density battery, reduced at low potentials (by Li metal) and oxidized at intermediate potentials, the performance of ASSLBs still falls short of that of batteries using liquid electrolytes and requires attention. Safety will not automatically be enhanced in battery applications through the use of solid electrolytes, especially with the use of Li metal. Improving the safety of ASSLBs relies on mindful interface tailored solutions and engineering strategies in order to secure good passivation layers and stabilized interfaces over a wide temperature range and under diverse battery operating conditions.^[34,504] Depending on the processing technique and preparation conditions, the electrode/electrolyte interface may become the bottleneck dictating the power density of the ASSLB.

Battery scientists have achieved several important material discoveries and engineering breakthroughs in recent years: namely, the discovery of new solid electrolytes (e.g., Li_{9.54}Si_{1.74}P_{1.44}S_{11.7}Cl_{0.3}^[40] LiTa₂PO₈^[85,86]) exhibiting ionic conductivity in a solid state that is competitive with that of organic liquid electrolytes, performance improvements enabled by interfacial coatings or buffer layers, and microstructure engineering solutions at the electrode/electrolyte interfaces. Very recently, Ah-class pouch cells with a high energy density (>900 Wh L⁻¹) and superior cycle life (>1000 times) based on an ASSLB cell using an argyrodite (Li₆PS₅Cl) solid electrolyte were reported, which is an important breakthrough in Li-metal battery technology, with the potential for future development of EV batteries with high energy density and safety.^[346] These performance results suggest that an EV will be able to travel up to 800 km on a single charge, featuring a cycle life of over 1000 charges. Although several proof-of-concepts and important seed technologies for ASSLBs have been reported, their commercialization requires continuous development and refinement from the single-cell to the multistack level. We highlight our perspective on the challenges and promising mitigation strategies associated with oxide and sulfide solid electrolytes and their interfaces with Li-metal anodes and oxide-based cathodes toward the realization of high-energy-density ASSLBs.

Solid electrolytes are intended to replace both the separator and liquid electrolyte in conventional LIBs.^[411] To mature in commercial applications further, ASSLBs require technologies that will enable their cost-effective integration into existing Li-ion battery manufacturing lines, which is strongly driven by the processing and solid battery assembly strategies. A decrease in the processing cost of thin Li metal and/or technological breakthroughs and low-temperature solid electrolyte processing, and good coassembly strategies targeting low temperatures for electrode/electrolyte assemblies are greatly needed. Specifically, there is an urgent need for the development of low-cost, scalable synthesis routes that can support the formation of ~20 μm thick dense, highly conducting solid electrolytes and cost-effective ultrathin Li metal films alongside low-temperature and cost-effective processing to realize stable and intimate cathode/solid electrolyte contact, which have been recently outlined in ref. [43]. Critical issues related to the pairing of solid electrolytes with cathode materials (i.e., the active material, conductive additive, and polymer binder) such as physical contact and chemical and electrochemical stability,

including the high interfacial resistance often observed for sulfide electrolytes (despite their favorable mechanical properties), need to be addressed to secure long-term battery operation. Although bulk polarization is not an issue associated with solid electrolytes, ASSLBs have not been usually capable of satisfactory cycling at current densities $> 0.6 \text{ mA cm}^{-2}$ because of i) the penetration of Li dendrites through solid electrolytes, ii) the poor (electro)chemical interface stability, and iii) the poor maintenance of physical contact (leading to the propagation of cracks and delamination of interfaces). The decomposition of the solid electrolyte when in contact with cathode and/or Li metal anode materials and the evolution of interphases can lead to stress/strain evolution, crack formation and propagation, delamination of interfaces, and poor overall physical connectivity between particles and components.^[57] Compositional tuning and surface or microstructure engineering of the solid electrolyte may, in principle, be used to tune the (electro) chemomechanics properties of the solid electrolyte but, more importantly, will enable easy manipulation of the electrode/electrolyte long-term stability by spontaneously forming a self-limited, high ion-conducting, low electronic-conducting solid interphase layer with favorable mechanical properties.

On the anode side, the use of a Li-metal anode imposes challenges associated with Li dendrite growth and instabilities of the SEI at the Li/electrolyte interface in addition to possible “wettability” issues. The importance of adhesion with the Li-metal anode was illustrated by the improved mechanical strength and reduced resistance for Li⁺-ion transport at the interface achieved by improving the “wettability” of Li metal on a LLZO electrolyte through simple surface treatment.^[466] Transitioning from a liquid to a solid electrolyte toward an ASSLB introduces new interfacial challenges arising from i) poor solid–solid contacts between the Li metal and the rigid oxide solid electrolyte or ii) poor chemical stability between the Li metal and sulfide solid electrolytes and thus the continuous growth of the SEI. Despite much progress in addressing this topic, cycling at high current densities ($> 3 \text{ mA h cm}^{-2}$) remains a major challenge that demands innovative approaches. Considering i) adhesion to both Li and the solid electrolyte, ii) chemical compatibility, and iii) electrochemical compatibility in addition to iv) sufficient ionic and negligible electronic conductivity, more attention should be placed on Li binary compounds (Li₃N, LiF, Li₂O, etc.) as intermediate coating materials,^[59] in addition to coating layers with reduced electronic conductivities (e.g., LiPON, Li₃PO₄) at the Li/electrolyte interface to improve the coulombic efficiency and suppress dendrite growth. The appropriate pairing of the electrode material with a solid electrolyte to minimize mutual decomposition suggests the use of Li alloy and/or sulfur cathodes, particularly for sulfides. The use of Li alloys could be a compromise, especially for sulfide solid electrolytes, which are unstable against Li metal and require an additional coating layer. Increasing the interfacial area by incorporating Li metal into a highly porous electrolyte improves the critical current density for garnets. Nonetheless, cost and energy considerations are still needed to prove the superiority of such systems over typical LIBs. An approach where an anode-less cell with only a current collector is utilized and the cathode is the only source for Li metal plating, without any need for Li excess, may not only reduce the costs associated with the processing

of ultrathin Li metal films but also suppress dendrite growth and enable the use of high-conducting sulfide solid electrolytes owing to the lack of direct contact between the Li metal and solid electrolyte.^[346] Currently, anode-less solid-state batteries cells with high energy density show great potential; however, cost-effective alternatives to precious metals are needed.

On the cathode side, when the electrolyte is placed in contact with a conductive additive such as carbon or the current collector, decomposition can occur, necessitating an expansion of coating strategies to additives and current collectors.^[320,322] Tailored interfaces with excellent adhesion between electrodes are mandatory to stabilize the electrode/electrolyte interfaces, resist delamination, and decrease interfacial resistance to achieve acceptable performance (thousands of cycles, $> 1 \text{ mA cm}^{-2}$, $> 1\text{C}$).^[504] Despite the excellent chemical, mechanical, and electrochemical properties of any type of solid electrolyte, low bulk, grain-boundary, and interfacial resistance between the electrode and electrolyte are prerequisites for their widespread commercial adoption. Interfacial failure processes originating from poor chemical stability, electrochemical oxidation, and chemo-mechanical degradation during cell fabrication or operation (cycling) are of prime concern and typically result in a continuous increase of the interfacial resistance between the active materials and solid electrolyte in a cathode composite. Chemomechanical issues (i.e., interfacial cracking during cycling) from state-of-the-art sulfide-based ASSLBs highlight the necessity of applied pressure during cycling,^[10] which will add another unpredictable variable to battery processing later in the commercialization step. Compared with the chemo-mechanical issues for sulfide-based cathodes, those for garnet solid electrolytes have not been widely reported. Considering the different major bonding mechanisms, oxide-based cathode composites are expected to exhibit stronger bonding driven by elevated-temperature sintering because both mechanical bonding and chemically induced bonding are involved. As soon as a processing method to produce more stable oxide interfaces is established, it could potentially provide opportunities to avoid interfacial cracking and the need for applied pressure by accommodating the stress level created during volume change of active materials.^[262,370] Overall, the formation of a mechanically and chemically stable SEI with high ionic conductivity but low electronic conductivity is a key condition for long-term battery operation. Regardless of the solid electrolyte selected, artificial protection on the cathode surface by introducing coating layers such as Li₄Ti₅O₁₂, LiTaO₃, LiNbO₃, Li₂SiO₃, or Li₃PO₄ has been shown to reduce the resistance at the cathode/electrolyte interface.

To conclude, the development of ASSLBs is very promising but remains in its infancy. Reports on the performance of full solid-state Li-based batteries involving garnet-type LLZO and sulfide-type Li₁₀GeP₂S₁₂ mainly with layered oxides (LCO, NMC) because of their excellent capacity, compatibility, and electronic conductivity, are growing; however, the full-cell performance requires further attention as it is currently representing only tens or hundreds cycles and at low rates $< 1\text{C}$. SSBs employing oxides such as LLZO often exhibit strong charging polarization because of the cathode/electrolyte interface and interfaces within the composite cathode,^[505] whereas SSBs employing sulfides often exhibit low first-cycle efficiency and capacity fading of 1–2% per charging cycle because of the growth of a highly

resistive interfacial layer on the cathode formed by oxidation of the solid electrolyte during charging.^[60,326] Even when coatings layers (or other strategies) are employed for sulfide-based SSBs, a Li alloy (typically Li-In) with higher reduction potential than Li metal is used once a full cell is tested. Recent sulfide-based ASSLBs based on Li₂O-ZrO₂-coated NMC exhibited impressive performance for 1000 cycles; however, a thorough understanding of the role of the coating materials remains lacking,^[506] and the state-of-the-art performance of oxide-based ASSLBs is far behind in the race, limited to an irreversible capacity up to 70^[331] or 100 cycles.^[45] Suitable coating strategy (composition, processing, thickness) combined with precise interfacial characterization of the buried interfaces should be further established and explored in a full SSB cell, preferably in a three-electrode cell configuration, which, although challenging in terms of fabrication, will better resolve the battery failure modes and clarify their potential feasibility if and when they are put into practical use.

Supporting Information

Supporting Information is available from the Wiley Online Library or from the author.

Acknowledgements

This work was supported in parts by NGK Inc. and the National Science Foundation MRSEC Program (grant no. DMR-1419807). M.B. acknowledges financial support from the US-Israel Fulbright Program, the Zuckerman Israeli Postdoctoral Scholar Program, and the MIT-Technion Postdoctoral Fellowship. L.K. acknowledges financial support from Xi'an Jiaotong University and the office of the Chinese Postdoctoral Council. J.L.M.R. thanks the Thomas Lord Foundation for financial support.

Conflict of Interest

The authors declare no conflict of interest.

Author Contributions

K.J.K and M.B contributed equally to this work. K.J.K and M.B initiated the concept of the paper, contributed equally to the research, figure preparation, discussion of data, writing, editing, and proofreading of the manuscript. M.W contributed to parts in the "Cathode: toward true solid" section and to figures and tables preparation. L.K contributed to parts in the "Introduction" section and to figures and tables preparation. J.L.M.R. discussed, edited, and revised the manuscript in all parts. This article is intended to become a chapter in the upcoming book "Nanda, Augustyn, Transition Metal Oxides for Electrochemical Energy Storage, Wiley-VCH, Weinheim, 2021, ISBN 978-3-527-34493-2.

Keywords

interfacial resistance, Li metal, oxide-based cathodes, solid state batteries

Received: August 20, 2020
Revised: September 22, 2020
Published online:

- [1] B. Scrosati, *J. Solid State Electrochem.* **2011**, *15*, 1623.
- [2] T. Placke, R. Kloepsch, S. Dühnen, M. Winter, *J. Solid State Electrochem.* **2017**, *21*, 1939.
- [3] P. Balaya, C. S. Sijnandana, *J. Phys. Chem. Solids* **1994**, *55*, 39.
- [4] Z. P. Cano, D. Banham, S. Ye, A. Hintennach, J. Lu, M. Fowler, Z. Chen, *Nat. Energy* **2018**, *3*, 279.
- [5] D. Mukai, K. Kobayashi, T. Kurahashi, N. Matsueda, *Mitsubishi Heavy Ind. Tech. Rev.* **2012**, *49*, 6.
- [6] J. Daly, Japan looks at recycling vehicle batteries for renewable power, <http://oilprice.com/Alternative-Energy/Renewable-Energy/Japan-Looks-at-Recycling-Vehicle-Batteries-for-Renewable-Power.html> (accessed: February 2014).
- [7] T. Chen, Y. Jin, H. Lv, A. Yang, M. Liu, B. Chen, Y. Xie, Q. Chen, *Trans. Tianjin Univ.* **2020**, *26*, 208.
- [8] B. Dunn, H. Kamath, J. M. Tarascon, *Science* **2011**, *334*, 928.
- [9] L. Trahey, F. R. Brushett, N. P. Balsara, G. Ceder, L. Cheng, Y. M. Chiang, N. T. Hahn, B. J. Ingram, S. D. Minteer, J. S. Moore, K. T. Mueller, L. F. Nazar, K. A. Persson, D. J. Siegel, K. Xu, K. R. Zavadil, V. Srinivasan, G. W. Crabtree, *Proc. Natl. Acad. Sci. USA* **2020**, *117*, 12550.
- [10] J. Janek, W. G. Zeier, *Nat. Energy* **2016**, *1*, 16141.
- [11] A. Manthiram, X. Yu, S. Wang, *Nat. Rev. Mater.* **2017**, *2*, 16103.
- [12] M. M. Thackeray, C. Wolverton, E. D. Isaacs, *Energy Environ. Sci.* **2012**, *5*, 7854.
- [13] M. Salama, R. A. Rosy, R. Yemini, Y. Gofer, D. Aurbach, M. Noked, *ACS Energy Lett.* **2019**, *4*, 436.
- [14] M. Balaish, A. Kraytsberg, Y. Ein-Eli, *Phys. Chem. Chem. Phys.* **2014**, *16*, 2801.
- [15] M. Balaish, J. W. Jung, I. D. Kim, Y. Ein-Eli, *Adv. Funct. Mater.* **2020**, *30*, 1808303.
- [16] M. Li, J. Lu, Z. Chen, K. Amine, *Adv. Mater.* **2018**, *30*, 1800561.
- [17] D. Andre, S. J. Kim, P. Lamp, S. F. Lux, F. Maglia, O. Paschos, B. Stiasny, *J. Mater. Chem. A* **2015**, *3*, 6709.
- [18] J. W. Choi, D. Aurbach, *Nat. Rev. Mater.* **2016**, *1*, 16013.
- [19] P. Albertus, S. Babinec, S. Litzelman, A. Newman, *Nat. Energy* **2018**, *3*, 16.
- [20] United States Council for Automotive Reseacg (USABC) LLC, USABC Goals for Advanced High-Performance Batteries for Electric Vehicle (EV) Applications **2019**, p. 1.
- [21] U.S. Department of Energy, Batteries.
- [22] W. Li, X. Liu, H. Celio, P. Smith, A. Dolocan, M. Chi, A. Manthiram, *Adv. Energy Mater.* **2018**, *8*, 1703154.
- [23] L. O. Valonen, J. N. Reimers, *J. Electrochem. Soc.* **2005**, *152*, A882.
- [24] V. Etacheri, R. Marom, R. Elazari, G. Salitra, D. Aurbach, *Energy Environ. Sci.* **2011**, *4*, 3243.
- [25] <https://news.samsung.com/global/samsung-presents-ground-breaking-all-solid-state-battery-technology-to-nature-energy> (accessed: March 2020).
- [26] K. Liu, Y. Liu, D. Lin, A. Pei, Y. Cui, *Sci. Adv.* **2018**, *4*, 9820.
- [27] J. Duan, X. Tang, H. Dai, Y. Yang, W. Wu, X. Wei, Y. Huang, *Electrochim. Energy Rev.* **2020**, *3*, 1.
- [28] P. G. Balakrishnan, R. Ramesh, T. Prem Kumar, *J. Power Sources* **2006**, *155*, 401.
- [29] E. Peled, *J. Electrochem. Soc.* **1979**, *126*, 2047.
- [30] E. Peled, D. Golodnitsky, G. Ardel, *J. Electrochem. Soc.* **1997**, *144*, L208.
- [31] S. Menkin, D. Golodnitsky, E. Peled, *Electrochim. Commun.* **2009**, *11*, 1789.
- [32] P. Albertus, Integration and Optimization of Novel Ion-conducting Solids (IONICS) **2016**.
- [33] M. D. Tikekar, S. Choudhury, Z. Tu, L. A. Archer, *Nat. Publ. Gr.* **2016**, *1*, 1.
- [34] D. Aurbach, Y. Talyosef, B. Markovsky, E. Markevich, E. Zinigrad, L. Asraf, J. S. Gnanaraj, H. J. Kim, *Electrochim. Acta* **2004**, *50*, 247.
- [35] J. Pires, A. Castets, L. Timperman, J. Santos-Peña, E. Dumont, S. Levasseur, C. Tessier, R. Dedryvère, M. Anouti, *J. Power Sources* **2015**, *296*, 413.

- [36] L. Xia, Y. Xia, Z. Liu, *J. Power Sources* **2015**, 278, 190.
- [37] D. Aurbach, K. Garnolsky, B. Markovsky, Y. Gofer, M. Schmidt, U. Heider, *Electrochim. Acta* **2002**, 47, 1423.
- [38] R. McMillan, H. Slegir, Z. X. Shu, W. Wang, *J. Power Sources* **1999**, 81–82, 20.
- [39] X. Judez, G. G. Eshetu, C. Li, L. M. Rodriguez-Martinez, H. Zhang, M. Armand, *Joule* **2018**, 2, 2208.
- [40] Y. Kato, S. Hori, T. Saito, K. Suzuki, M. Hirayama, A. Mitsui, M. Yonemura, H. Iba, R. Kanno, *Nat. Energy* **2016**, 1, 16030.
- [41] M. Nagao, A. Hayashi, M. Tatsumisago, *J. Mater. Chem.* **2012**, 22, 10015.
- [42] J. Li, C. Ma, M. Chi, C. Liang, N. J. Dudney, *Adv. Energy Mater.* **2015**, 5, 1401408.
- [43] J. L. M. R. Moran Balaish, J. C. Gonzalez-Rosillo, K. J. Kim, Y. Zhu, Z. D. Hood, *Nat. Energy* **2020**.
- [44] S. Randau, D. A. Weber, O. Kötz, R. Koerver, P. Braun, A. Weber, E. Ivers-Tiffée, T. Adermann, J. Kulisch, W. G. Zeier, F. H. Richter, J. Janek, *Nat. Energy* **2020**, 5, 259.
- [45] F. Han, J. Yue, C. Chen, N. Zhao, X. Fan, Z. Ma, T. Gao, F. Wang, X. Guo, C. Wang, *Joule* **2018**, 2, 497.
- [46] I. A. J. Gordon, S. Grangeon, H. Takenouti, B. Tribollet, M. Armand, C. Davoisne, A. Débart, S. Laruelle, *Electrochim. Acta* **2017**, 223, 63.
- [47] D. Aurbach, *J. Power Sources* **2000**, 89, 206.
- [48] J. Ma, C. Wang, S. Wroblewski, *J. Power Sources* **2007**, 164, 849.
- [49] C. Wang, J. Hong, *Electrochim. Solid-State Lett.* **2007**, 10.
- [50] M. Winter, R. J. Brodd, *Chem. Rev.* **2004**, 104, 4245.
- [51] Y. Gao, A. M. Nolan, P. Du, Y. Wu, C. Yang, Q. Chen, Y. Mo, S. H. Bo, *Chem. Rev.* **2020**, 120, 5954.
- [52] J. Maier, *Physical Chemistry of Ionic Materials: Ions and Electrons in Solids*, John Wiley & Sons, New York **2004**.
- [53] E. Gileadi, *Physical Electrochemistry: Fundamentals, Techniques, and Applications*, Wiley-VCH Verlag GmbH & Co. KGaA, Weinheim **2011**.
- [54] S. Gantenbein, M. Weiss, E. Ivers-Tiffée, *J. Power Sources* **2018**, 379, 317.
- [55] J. Illig, M. Ender, T. Chrobak, J. P. Schmidt, D. Klotz, E. Ivers-Tiffée, *J. Electrochem. Soc.* **2012**, 159, A952.
- [56] D. Andre, M. Meiler, K. Steiner, H. Walz, T. Soczka-Guth, D. U. Sauer, *J. Power Sources* **2011**, 196, 5349.
- [57] T. Famprakis, P. Canepa, J. A. Dawson, M. S. Islam, C. Masquelier, *Nat. Mater.* **2019**, 18, 1278.
- [58] R. Raj, J. Wolfenstein, *J. Power Sources* **2017**, 343, 119.
- [59] Y. Zhu, X. He, Y. Mo, *ACS Appl. Mater. Interfaces* **2015**, 7, 23685.
- [60] G. Oh, M. Hirayama, O. Kwon, K. Suzuki, R. Kanno, *Chem. Mater.* **2016**, 28, 2634.
- [61] L. Miara, A. Windmüller, C. L. Tsai, W. D. Richards, Q. Ma, S. Uhlenbruck, O. Guillon, G. Ceder, *ACS Appl. Mater. Interfaces* **2016**, 8, 26842.
- [62] Z. Zhang, L. Zhang, X. Yan, H. Wang, Y. Liu, C. Yu, X. Cao, L. van Eijck, B. Wen, *J. Power Sources* **2019**, 410–411, 162.
- [63] Y. Tao, S. Chen, D. Liu, G. Peng, X. Yao, X. Xu, *J. Electrochim. Soc.* **2016**, 163, A96.
- [64] A. Kato, A. Hayashi, M. Tatsumisago, *J. Power Sources* **2016**, 309, 27.
- [65] T. Deng, X. Ji, Y. Zhao, L. Cao, S. Li, S. Hwang, C. Luo, P. Wang, H. Jia, X. Fan, X. Lu, D. Su, X. Sun, C. Wang, J. G. Zhang, *Adv. Mater.* **2020**, 32, e2000030.
- [66] B. Xu, W. Li, H. Duan, H. Wang, Y. Guo, H. Li, H. Liu, *J. Power Sources* **2017**, 354, 68.
- [67] B. Liu, Y. Gong, K. Fu, X. Han, Y. Yao, G. Pastel, C. Yang, H. Xie, E. D. Wachsman, L. Hu, *ACS Appl. Mater. Interfaces* **2017**, 9, 18809.
- [68] W. Zhou, S. Wang, Y. Li, S. Xin, A. Manthiram, J. B. Goodenough, *J. Am. Chem. Soc.* **2016**, 138, 9385.
- [69] K. K. Fu, Y. Gong, B. Liu, Y. Zhu, S. Xu, Y. Yao, W. Luo, C. Wang, S. D. Lacey, J. Dai, Y. Chen, Y. Mo, E. Wachsman, L. Hu, *Sci. Adv.* **2017**, 3, e1601659.
- [70] C. L. Tsai, V. Roddatis, C. V. Chandran, Q. Ma, S. Uhlenbruck, M. Brann, P. Heitjans, O. Guillon, *ACS Appl. Mater. Interfaces* **2016**, 8, 10617.
- [71] H. Kwak, K. H. Park, D. Han, K. W. Nam, H. Kim, Y. S. Jung, *J. Power Sources* **2020**, 446, 227338.
- [72] G. Sahu, E. Rangasamy, J. Li, Y. Chen, K. An, N. Dudney, C. Liang, *J. Mater. Chem. A* **2014**, 2, 10396.
- [73] G. Sahu, Z. Lin, J. Li, Z. Liu, N. Dudney, C. Liang, *Energy Environ. Sci.* **2014**, 7, 1053.
- [74] R. Kanno, T. Hata, Y. Kawamoto, M. Irie, *Solid State Ionics* **2000**, 130, 97.
- [75] M. A. Kraft, S. P. Culver, M. Calderon, F. Böcher, T. Krauskopf, A. Senyshyn, C. Dietrich, A. Zevalkink, J. Janek, W. G. Zeier, *J. Am. Chem. Soc.* **2017**, 139, 10909.
- [76] F. Han, Y. Zhu, X. He, Y. Mo, C. Wang, *Adv. Energy Mater.* **2016**, 6, 1501590.
- [77] Z. Q. Wang, M. S. Wu, G. Liu, X. L. Lei, B. Xu, C. Y. Ouyang, *Int. J. Electrochem. Sci.* **2014**, 9, 562.
- [78] N. Kamaya, K. Homma, Y. Yamakawa, M. Hirayama, R. Kanno, M. Yonemura, T. Kamiyama, Y. Kato, S. Hama, K. Kawamoto, A. Mitsui, *Nat. Mater.* **2011**, 10, 682.
- [79] J. Gao, X. X. Guo, Y. Li, Z. Ma, X. X. Guo, H. Li, Y. Zhu, W. Zhou, *Adv. Theory Simul.* **2019**, 2, 1900028.
- [80] A. Sharafi, E. Kazyak, A. L. Davis, S. Yu, T. Thompson, D. J. Siegel, N. P. Dasgupta, J. Sakamoto, *Chem. Mater.* **2017**, 29, 7961.
- [81] T. Krauskopf, H. Hartmann, W. G. Zeier, J. Janek, *ACS Appl. Mater. Interfaces* **2019**, 11, 14463.
- [82] Y. Zhu, X. He, Y. Mo, *J. Mater. Chem. A* **2016**, 4, 3253.
- [83] M. Nakayama, M. Kotobuki, H. Munakata, M. Nogami, K. Kanamura, *Phys. Chem. Chem. Phys.* **2012**, 14, 10008.
- [84] S. Ohta, T. Kobayashi, T. Asaoka, *J. Power Sources* **2011**, 196, 3342.
- [85] N. Ishigaki, K. Kataoka, D. Morikawa, M. Terauchi, K. Hayamizu, J. Akimoto, *Solid State Ionics* **2020**, 351, 115314.
- [86] J. Kim, J. Kim, M. Avdeev, H. Yun, S. J. Kim, *J. Mater. Chem. A* **2018**, 6, 22478.
- [87] J. C. Bachman, S. Muy, A. Grimaud, H. H. Chang, N. Pour, S. F. Lux, O. Paschos, F. Maglia, S. Lupart, P. Lamp, L. Giordano, Y. Shao-Horn, *Chem. Rev.* **2016**, 116, 140.
- [88] R. D. Shannon, *Acta Crystallogr., Sect. A: Found. Crystallogr.* **1976**, 32, 751.
- [89] Y. Inaguma, C. Liquan, M. Itoh, T. Nakamura, T. Uchida, H. Ikuta, M. Wakihara, *Solid State Commun.* **1993**, 86, 689.
- [90] S. Stramare, V. Thangadurai, W. Weppner, *Chem. Mater.* **2003**, 15, 3974.
- [91] A. Morata-Orrantia, S. García-Martín, M. Á. Alario-Franco, *Chem. Mater.* **2003**, 15, 363.
- [92] Y. Harada, T. Ishigaki, H. Kawai, J. Kuwano, *Solid State Ionics* **1998**, 108, 407.
- [93] Y. Harada, Y. Hirakoso, H. Kawai, J. Kuwano, *Solid State Ionics* **1999**, 121, 245.
- [94] A. Mei, X. L. Wang, J. Le Lan, Y. C. Feng, H. X. Geng, Y. H. Lin, C. W. Nan, *Electrochim. Acta* **2010**, 55, 2958.
- [95] H. Geng, J. Lan, A. Mei, Y. Lin, C. W. Nan, *Electrochim. Acta* **2011**, 56, 3406.
- [96] C. W. Ban, G. M. Choi, *Solid State Ionics* **2001**, 140, 285.
- [97] W. J. Kwon, H. Kim, K. N. Jung, W. Cho, S. H. Kim, J. W. Lee, M. S. Park, *J. Mater. Chem. A* **2017**, 5, 6257.
- [98] Y. Dong, Z. Zhang, A. Alvarez, I. W. Chen, *Acta Materialia* **2020**, 199, 264.
- [99] J. F. Wu, X. Guo, *Phys. Chem. Chem. Phys.* **2017**, 19, 5880.
- [100] C. Ma, K. Chen, C. Liang, C. W. Nan, R. Ishikawa, K. More, M. Chi, *Energy Environ. Sci.* **2014**, 7, 1638.
- [101] H. Aono, E. Sugimoto, Y. Sadaoka, N. Imanaka, G. Adachi, T. Katsumata, Y. Matsui, Y. Inaguma, M. Itoh, *Solid State J. Electro-Chem. Soc.* **1990**, 137, 1023.

- [102] G. F. Ortiz, M. C. López, P. Lavela, C. Vidal-Abarca, J. L. Tirado, *Solid State Ionics* **2014**, 262, 573.
- [103] M. A. Subramanian, R. Subramanian, A. Clearfield, *Solid State Ionics* **1986**, 18–19, 562.
- [104] A. Kubanska, L. Castro, L. Tortet, O. Schäf, M. Dollé, R. Bouchet, *Solid State Ionics* **2014**, 266, 44.
- [105] V. Thangadurai, A. K. Shukla, J. Gopalakrishnan, *J. Mater. Chem.* **1999**, 9, 739.
- [106] N. Anantharamulu, K. Koteswara Rao, G. Rambabu, B. Vijaya Kumar, V. Radha, M. Vithal, *J. Mater. Sci.* **2011**, 46, 2821.
- [107] H. Y. P. Hong, *Mater. Res. Bull.* **1976**, 11, 176.
- [108] Z. Jian, Y. S. Hu, X. Ji, W. Chen, *Adv. Mater.* **2017**, 19, 1601925.
- [109] H. Aono, E. Sugimoto, E. Sugimoto, Y. Sadaoka, N. Imanaka, G. J. Adachi, *Electrochem. Soc.* **1989**, 136, 590.
- [110] S. c. Li, J. y. Cai, Z. x. Lin, *Solid State Ionics* **1988**, 28, 1265.
- [111] E. C. Bucharsky, K. G. Schell, A. Hintennach, M. J. Hoffmann, *Solid State Ionics* **2015**, 274, 77.
- [112] M. Illbeigi, A. Fazlali, M. Kazazi, A. H. Mohammadi, *Solid State Ionics* **2016**, 289, 180.
- [113] C. A. Geiger, E. Alekseev, B. Lazic, M. Fisch, T. Armbruster, R. Langner, M. Fechtelkord, N. Kim, T. Pettke, W. Weppner, *Inorg. Chem.* **2011**, 50, 1089.
- [114] N. Bernstein, M. D. Johannes, K. Hoang, *Phys. Rev. Lett.* **2012**, 109, 205702.
- [115] J. Awaka, A. Takashima, K. Kataoka, N. Kijima, Y. Idemoto, J. Akimoto, *Chem. Lett.* **2011**, 40, 60.
- [116] Y. Chen, E. Rangasamy, C. Liang, K. An, *Chem. Mater.* **2015**, 27, 5491.
- [117] D. Wang, Q. Sun, J. Luo, J. Liang, Y. Sun, R. Li, K. Adair, L. Zhang, R. Yang, S. Lu, H. Huang, X. Sun, *ACS Appl. Mater. Interfaces* **2019**, 11, 4954.
- [118] H. Xie, J. A. Alonso, Y. Li, M. T. Fernández-Díaz, J. B. Goodenough, *Chem. Mater.* **2011**.
- [119] J. F. Nonemacher, C. Hüter, H. Zheng, J. Malzbender, M. Krüger, R. Spatschek, M. Finsterbusch, *Solid State Ionics* **2018**, 321, 126.
- [120] E. Rangasamy, J. Wolfenstine, J. Sakamoto, *Solid State Ionics* **2012**, 206, 28.
- [121] A. Kuhn, J. Y. Choi, L. Robben, F. Tietz, M. Wilkening, P. Heitjans, *Z. Phys. Chem.* **2012**, 226, 525.
- [122] Y. Wang, A. Huq, W. Lai, *Solid State Ionics* **2014**, 255, 39.
- [123] T. Thompson, J. Wolfenstine, J. L. Allen, M. Johannes, A. Huq, I. N. David, J. Sakamoto, *J. Mater. Chem. A* **2014**, 2, 13431.
- [124] M. Matsui, K. Takahashi, K. Sakamoto, A. Hirano, Y. Takeda, O. Yamamoto, N. Imanishi, *Dalton Trans.* **2014**, 43, 1019.
- [125] H. Buschmann, J. Dölle, S. Berendts, A. Kuhn, P. Bottke, M. Wilkening, P. Heitjans, A. Senyshyn, H. Ehrenberg, A. Lotnyk, V. Duppel, L. Kienle, J. Janek, *Phys. Chem. Chem. Phys.* **2011**, 13, 19378.
- [126] H. El Shinawi, J. Janek, *J. Power Sources* **2013**, 225, 13.
- [127] D. Rettenwander, C. A. Geiger, G. Amthauer, *Inorg. Chem.* **2013**, 52, 8005.
- [128] R. Jalem, M. J. D. Rushton, W. Manalastas, M. Nakayama, T. Kasuga, J. A. Kilner, R. W. Grimes, *Chem. Mater.* **2015**, 27, 2821.
- [129] X. Tong, V. Thangadurai, E. D. Wachsman, *Inorg. Chem.* **2015**, 54, 3600.
- [130] D. Rettenwander, C. A. Geiger, M. Tribus, P. Tropper, G. Amthauer, *Inorg. Chem.* **2014**, 53, 6264.
- [131] R. Murugan, V. Thangadurai, W. Weppner, *Angew. Chem., Int. Ed.* **2007**, 46, 7778.
- [132] R. Wagner, G. J. Redhammer, D. Rettenwander, G. Tippelt, A. Welzl, S. Taibl, J. Fleig, A. Franz, W. Lottermoser, G. Amthauer, *Chem. Mater.* **2016**.
- [133] D. Rettenwander, G. Redhammer, F. Preishuber-Pflügl, L. Cheng, L. Miara, R. Wagner, A. Welzl, E. Suard, M. M. Doeff, M. Wilkening, J. Fleig, G. Amthauer, *Chem. Mater.* **2016**, 28, 2384.
- [134] S. Mukhopadhyay, T. Thompson, J. Sakamoto, A. Huq, J. Wolfenstine, J. L. Allen, N. Bernstein, D. A. Stewart, M. D. Johannes, *Chem. Mater.* **2015**, 27, 3658.
- [135] L. J. Miara, W. D. Richards, Y. E. Wang, G. Ceder, *Chem. Mater.* **2015**, 27, 4040.
- [136] W. Xia, B. Xu, H. Duan, Y. Guo, H. Kang, H. Li, H. Liu, *ACS Appl. Mater. Interfaces* **2016**, 8, 5335.
- [137] S. Yu, R. D. Schmidt, R. Garcia-Mendez, E. Herbert, N. J. Dudney, J. B. Wolfenstine, J. Sakamoto, D. J. Siegel, *Chem. Mater.* **2016**, 28, 197.
- [138] Y. Li, J. T. Han, C. A. Wang, H. Xie, J. B. Goodenough, *J. Mater. Chem.* **2012**, 22, 15357.
- [139] M. Huang, A. Dumon, C. W. Nan, *Electrochem. Commun.* **2012**, 21, 62.
- [140] R. Murugan, S. Ramakumar, N. Janani, *Electrochem. Commun.* **2011**, 13, 1373.
- [141] S. Kumazaki, Y. Iriyama, K. H. Kim, R. Murugan, K. Tanabe, K. Yamamoto, T. Hirayama, Z. Ogumi, *Electrochem. Commun.* **2011**, 13, 509.
- [142] C. Deviannapoorani, L. Dhivya, S. Ramakumar, R. Murugan, *J. Power Sources* **2013**, 240, 18.
- [143] J. L. Allen, J. Wolfenstine, E. Rangasamy, J. Sakamoto, *J. Power Sources* **2012**, 206, 315.
- [144] S. Qin, X. Zhu, Y. Jiang, M. Ling, Z. Hu, J. Zhu, *Appl. Phys. Lett.* **2018**, 112, 113901.
- [145] Y. Ren, K. Chen, R. Chen, T. Liu, Y. Zhang, C. W. Nan, *J. Am. Ceram. Soc.* **2015**, 98, 3606.
- [146] C. Cao, Z. Bin Li, X. L. Wang, X. B. Zhao, W. Q. Han, *Front. Energy Res.* **2014**, 2, 1.
- [147] C. Wang, K. Fu, S. P. Kammampata, D. W. Mcowen, A. J. Samson, L. Zhang, G. T. Hitz, A. M. Nolan, E. D. Wachsman, Y. Mo, V. Thangadurai, *Chem. Rev.* **2020**.
- [148] J. W. Fergus, *J. Power Sources* **2010**, 195, 4554.
- [149] A. Hayashi, M. Tatsumisago, *J. Ceram. Soc. Jpn.* **2018**, 126, 214.
- [150] A. Sakuda, A. Hayashi, M. Tatsumisago, *Sci. Rep.* **2013**, 3, 2.
- [151] A. Sakuda, A. Hayashi, Y. Takigawa, K. Higashi, M. Tatsumisago, *J. Ceram. Soc. Jpn.* **2013**, 121, 946.
- [152] V. Lacivita, A. S. Westover, A. Kercher, N. D. Phillip, G. Yang, G. Veith, G. Ceder, N. J. Dudney, *J. Am. Chem. Soc.* **2018**, 140, 11029.
- [153] Y. Kim, J. Saienga, S. W. Martin, *J. Phys. Chem. B* **2006**, 110, 16318.
- [154] K. Hirai, M. Tatsumisago, *Solid State Ionics* **1995**, 78, 269.
- [155] A. Kato, M. Yamamoto, A. Sakuda, A. Hayashi, M. Tatsumisago, *ACS Appl. Energy Mater.* **2018**, 1, 1002.
- [156] S. Ujiie, A. Hayashi, M. Tatsumisago, *Solid State Ionics* **2012**, 211, 42.
- [157] B. Fahys, G. Robert, *Solid State Ionics* **1981**, 5, 663.
- [158] F. Mizuno, A. Hayashi, K. Tadanaga, M. Tatsumisago, *Solid State Ionics* **2006**, 177, 2721.
- [159] K. Minami, A. Hayashi, M. Tatsumisago, *J. Ceram. Soc. Jpn.* **2010**, 118, 305.
- [160] T. Minami, A. Hayashi, M. Tatsumisago, *Solid State Ionics* **2006**, 177, 2715.
- [161] Y. Onodera, K. Mori, T. Otomo, A. C. Hannon, S. Kohara, K. Itoh, M. Sugiyama, T. Fukunaga, *J. Phys. Soc. Jpn.* **2010**, 79, 87.
- [162] Y. Onodera, K. Mori, T. Otomo, M. Sugiyama, T. Fukunaga, *J. Phys. Soc. Jpn.* **2012**, 81, 044802.
- [163] Y. Seino, T. Ota, K. Takada, A. Hayashi, M. Tatsumisago, *Energy Environ. Sci.* **2014**, 7, 627.
- [164] H. J. Deiseroth, S. T. Kong, H. Eckert, J. Vannahme, C. Reiner, T. Zaif, M. Schlosser, *Angew. Chem., Int. Ed.* **2008**, 47, 755.
- [165] R. Kanno, M. Murayama, *J. Electrochem. Soc.* **2001**, 148, A742.
- [166] M. Murayama, N. Sonoyama, A. Yamada, R. Kanno, *Solid State Ionics* **2004**, 170, 173.
- [167] H. Y. P. Hong, *Mater. Res. Bull.* **1978**, 13, 117.
- [168] Y. Wang, W. D. Richards, S. P. Ong, L. J. Miara, J. C. Kim, Y. Mo, G. Ceder, *Nat. Mater.* **2015**, 14, 1026.

- [169] S. P. Ong, Y. Mo, W. D. Richards, L. Miara, H. S. Lee, G. Ceder, *Energy Environ. Sci.* **2013**, *6*, 148.
- [170] J. Bhattacharya, C. Wolverton, *Carbon – Sci. Technol.* **2016**, *8*, 92.
- [171] D. A. Weber, A. Senyshyn, K. S. Weldert, S. Wenzel, W. Zhang, R. Kaiser, S. Berendts, J. Janek, W. G. Zeier, *Chem. Mater.* **2016**, *28*, 5905.
- [172] Y. Mo, S. P. Ong, G. Ceder, *Chem. Mater.* **2012**, *24*, 15.
- [173] A. Kuhn, J. Köhler, B. V. Lotsch, *Phys. Chem. Chem. Phys.* **2013**, *15*, 11620.
- [174] R. Malik, D. Burch, M. Bazant, G. Ceder, *Nano Lett.* **2010**, *10*, 4123.
- [175] S. Ohta, M. Kawakami, H. Nozaki, C. Yada, T. Saito, H. Iba, *J. Mater. Chem. A* **2020**, *8*, 8989.
- [176] L. Cheng, J. S. Park, H. Hou, V. Zorba, G. Chen, T. Richardson, J. Cabana, R. Russo, M. Doeff, *J. Mater. Chem. A* **2014**, *2*, 172.
- [177] M. Huang, T. Liu, Y. Deng, H. Geng, Y. Shen, Y. Lin, C. W. Nan, *Solid State Ionics* **2011**, *204*, 41.
- [178] Y. Kim, H. Jo, J. L. Allen, H. Choe, J. Wolfenstine, J. Sakamoto, *J. Am. Ceram. Soc.* **2016**, *99*, 1367.
- [179] A. Sharafi, C. G. Haslam, R. D. Kerns, J. Wolfenstine, J. Sakamoto, *J. Mater. Chem. A* **2017**, *5*, 21491.
- [180] J. Wolfenstine, H. Jo, Y. H. Cho, I. N. David, P. Askeland, E. D. Case, H. Kim, H. Choe, J. Sakamoto, *Mater. Lett.* **2013**, *96*, 117.
- [181] A. N. Wang, J. F. Nonemacher, G. Yan, M. Finsterbusch, J. Malzbender, M. Krüger, *J. Eur. Ceram. Soc.* **2018**, *38*, 3201.
- [182] Y. Zhang, F. Chen, R. Tu, Q. Shen, L. Zhang, *J. Power Sources* **2014**, *268*, 960.
- [183] S. W. Baek, J. M. Lee, T. Y. Kim, M. S. Song, Y. Park, *J. Power Sources* **2014**, *249*, 197.
- [184] P. Shi, G. Qu, S. Cai, Y. Kang, T. Fa, C. Xu, *J. Am. Ceram. Soc.* **2018**, *101*, 4076.
- [185] T. Clemenceau, N. Andriamady, P. Kumar M. K., A. Badran, V. Avila, K. Dahl, M. Hopkins, X. Vendrell, D. Marshall, R. Raj, *Scr. Mater.* **2019**, *172*, 1.
- [186] E. C. Bucharsky, K. G. Schell, T. Hupfer, M. J. Hoffmann, M. Rohde, H. J. Seifert, *Ionics* **2016**, *22*, 1043.
- [187] A. M. Laptev, H. Zheng, M. Bram, M. Finsterbusch, O. Guillon, *Mater. Lett.* **2019**, *247*, 155.
- [188] Y. Liu, Q. Sun, D. Wang, K. Adair, J. Liang, X. Sun, *J. Power Sources* **2018**, *393*, 193.
- [189] H. Guo, T. J. M. Bayer, J. Guo, A. Baker, C. A. Randall, *J. Eur. Ceram. Soc.* **2017**, *37*, 2303.
- [190] W. Lee, C. K. Lyon, J. H. Seo, R. Lopez-Hallman, Y. Leng, C. Y. Wang, M. A. Hickner, C. A. Randall, E. D. Gomez, *Adv. Funct. Mater.* **2019**, *29*, 1.
- [191] F. He, W. Zheng, L. Liang, B. Gu, *J. Eur. Ceram. Soc.* **2020**, *40*, 6241.
- [192] J. H. Seo, K. Verlinde, R. Rajagopalan, E. D. Gomez, T. E. Mallouk, C. A. Randall, *Mater. Sci. Eng., B* **2019**, *250*, 114435.
- [193] J. H. Seo, K. Verlinde, J. Guo, D. S. B. Heidary, R. Rajagopalan, T. E. Mallouk, C. A. Randall, *Scr. Mater.* **2018**, *146*, 267.
- [194] B. J. Smith, G. M. Phillip, M. E. Sweeney, *Environ. Sci. 2019*.
- [195] E. Yi, W. Wang, J. Kieffer, R. M. Laine, *J. Power Sources* **2017**, *352*, 156.
- [196] H. Shen, E. Yi, M. Amores, L. Cheng, N. Tamura, D. Y. Parkinson, G. Chen, K. Chen, M. Doeff, *J. Mater. Chem. A* **2019**, *7*, 20861.
- [197] E. Yi, H. Shen, S. Heywood, J. Alvarado, D. Y. Parkinson, G. Chen, S. W. Sofie, M. M. Doeff, *ACS Appl. Energy Mater.* **2020**, *3*, 170.
- [198] G. T. Hitz, D. W. McOwen, L. Zhang, Z. Ma, Z. Fu, Y. Wen, Y. Gong, J. Dai, T. R. Hamann, L. Hu, E. D. Wachsman, S. Information, G. T. Hitz, D. W. McOwen, L. Zhang, Z. Ma, Z. Fu, Y. Wen, Y. Gong, J. Dai, T. R. Hamann, L. Hu, E. D. Wachsman, *Mater. Today* **2019**, *22*, 50.
- [199] T. Liu, Y. Zhang, X. Zhang, L. Wang, S. X. Zhao, Y. H. Lin, Y. Shen, J. Luo, L. Li, C. W. Nan, *J. Mater. Chem. A* **2018**, *6*, 4649.
- [200] C. L. Tsai, Q. Ma, C. Dellen, S. Lobe, F. Vondahlen, A. Windmüller, D. Grüner, H. Zheng, S. Uhlenbruck, M. Finsterbusch, F. Tietz, D. Fattakhova-Rohlfing, H. P. Buchkremer, O. Guillon, *Sustainable Energy Fuels* **2019**, *3*, 280.
- [201] C. Loho, R. Djedjadic, M. Bruns, O. Clemens, H. Hahn, *J. Electrochem. Soc.* **2017**, *164*, A6131.
- [202] J. F. Wu, E. Y. Chen, Y. Yu, L. Liu, Y. Wu, W. K. Pang, V. K. Peterson, X. Guo, *ACS Appl. Mater. Interfaces* **2017**, *9*, 1542.
- [203] M. He, Z. Cui, C. Chen, Y. Li, X. Guo, *J. Mater. Chem. A* **2018**, *6*, 11463.
- [204] R. Pfenninger, M. Struzik, I. Garbayo, E. Stilp, J. L. M. Rupp, *Nat. Energy* **2019**, *4*, 475.
- [205] D. J. Kalita, S. H. Lee, K. S. Lee, D. H. Ko, Y. S. Yoon, *Solid State Ionics* **2012**, *229*, 14.
- [206] M. Bitzer, T. Van Gestel, S. Uhlenbruck, *Thin Solid Films* **2016**, *615*, 128.
- [207] N. Janani, S. Ramakumar, L. Dhivya, C. Deviannapoorani, K. Saranya, R. Murugan, *Ionics* **2011**, *17*, 575.
- [208] R. J. Chen, M. Huang, W. Z. Huang, Y. Shen, Y. H. Lin, C. W. Nan, *J. Mater. Chem. A* **2014**.
- [209] R. Djedjadic, M. Botros, C. Benel, O. Clemens, S. Indris, A. Choudhary, T. Bergfeldt, H. Hahn, *Solid State Ionics* **2014**, *263*, 49.
- [210] S. Iwasaki, T. Hamanaka, T. Yamakawa, W. C. West, K. Yamamoto, M. Motoyama, T. Hirayama, Y. Iriyama, *J. Power Sources* **2014**, *272*, 1086.
- [211] Y. Iriyama, M. Wadaguchi, K. Yoshida, Y. Yamamoto, M. Motoyama, T. Yamamoto, *J. Power Sources* **2018**, *385*, 55.
- [212] D. Popovici, H. Nagai, S. Fujishima, J. Akedo, *J. Am. Ceram. Soc.* **2011**, *94*, 3847.
- [213] M. Tatsumisago, A. Hayashi, *Int. J. Appl. Glass Sci.* **2014**, *5*, 226.
- [214] H. Muramatsu, A. Hayashi, T. Ohtomo, S. Hama, M. Tatsumisago, *Solid State Ionics* **2011**, *182*, 116.
- [215] Z. Liu, W. Fu, E. A. Payzant, X. Yu, Z. Wu, N. J. Dudney, J. Kiggans, K. Hong, A. J. Rondinone, C. Liang, *J. Am. Chem. Soc.* **2013**, *135*, 975.
- [216] S. Ito, M. Nakakita, Y. Aihara, T. Uehara, N. Machida, *J. Power Sources* **2014**, *271*, 342.
- [217] R. C. Xu, X. H. Xia, Z. J. Yao, X. L. Wang, C. D. Gu, J. P. Tu, *Electrochim. Acta* **2016**, *219*, 235.
- [218] J. A. Brant, D. M. Massi, N. A. W. Holzwarth, J. H. Macneil, A. P. Douvalis, T. Bakas, S. W. Martin, M. D. Gross, J. A. Aitken, *Chem. Mater.* **2015**, *27*, 189.
- [219] M. Tachez, J. P. Malugani, R. Mercier, G. Robert, *Solid State Ionics* **1984**, *14*, 181.
- [220] Z. D. Hood, C. Kates, M. Kirkham, S. Adhikari, C. Liang, N. A. W. Holzwarth, *Solid State Ionics* **2016**, *284*, 61.
- [221] I. H. Chu, H. Nguyen, S. Hy, Y. C. Lin, Z. Wang, Z. Xu, Z. Deng, Y. S. Meng, S. P. Ong, *ACS Appl. Mater. Interfaces* **2016**, *8*, 7843.
- [222] K. Homma, M. Yonemura, T. Kobayashi, M. Nagao, M. Hirayama, R. Kanno, *Solid State Ionics* **2011**, *182*, 53.
- [223] M. Cengiz, H. Oh, S.-H. Lee, *J. Electrochem. Soc.* **2019**, *166*, A3997.
- [224] Ö. U. Kudu, T. Famprakis, B. Fleutot, M. D. Braida, T. Le Mercier, M. S. Islam, C. Masquelier, *J. Power Sources* **2018**, *407*, 31.
- [225] M. Tatsumisago, S. Hama, A. Hayashi, H. Morimoto, T. Minami, *Solid State Ionics* **2002**, *154–155*, 635.
- [226] H. Tsukasaki, S. Mori, S. Shiotani, H. Yamamura, *Solid State Ionics* **2018**, *317*, 122.
- [227] J. Trevey, J. Jum Suk, J. Yoon Seok, C. R. Stoldt, L. Se-Hee, J. S. Jang, Y. S. Jung, C. R. Stoldt, S.-H. Lee, *Electrochim. Commun.* **2009**, *11*, 1830.
- [228] K. H. Park, Q. Bai, D. H. Kim, D. Y. Oh, Y. Zhu, Y. Mo, Y. S. Jung, *Adv. Energy Mater.* **2018**, *8*, 1800035.
- [229] A. Sharafi, S. Yu, M. Naguib, M. Lee, C. Ma, H. M. Meyer, J. Nanda, M. Chi, D. J. Siegel, J. Sakamoto, *J. Mater. Chem. A* **2017**, *5*, 13475.

- [230] L. Cheng, E. J. Crumlin, W. Chen, R. Qiao, H. Hou, S. Franz Lux, V. Zorba, R. Russo, R. Kostecki, Z. Liu, K. Persson, W. Yang, J. Cabana, T. Richardson, G. Chen, M. Doeff, *Phys. Chem. Chem. Phys.* **2014**, *16*, 18294.
- [231] L. Cheng, C. H. H. Wu, A. Jarry, W. Chen, Y. Ye, J. Zhu, R. Kostecki, K. Persson, J. Guo, M. Salmeron, G. Chen, M. Doeff, A.-S. Li, L. Cheng, C. Hao Wu, A. Jarry, W. Chen, Y. Ye, J. Zhu, R. Kostecki, K. Persson, J. Guo, M. Salmeron, G. Chen, M. Doeff, C. H. H. Wu, A. Jarry, W. Chen, Y. Ye, J. Zhu, R. Kostecki, K. Persson, J. Guo, M. Salmeron, G. Chen, M. Doeff, *ACS Appl. Mater. Interfaces* **2015**, *7*, 17649.
- [232] W. Xia, B. Xu, H. Duan, X. Tang, Y. Guo, H. Kang, H. Li, H. Liu, *2017*.
- [233] S. Kobi, A. Mukhopadhyay, *J. Eur. Ceram. Soc.* **2018**, *38*, 4707.
- [234] Y. Jin, P. J. McGinn, *J. Power Sources* **2013**, *239*, 326.
- [235] W. Xia, B. Xu, H. Duan, X. Tang, Y. Guo, H. Kang, H. Li, H. Liu, *J. Am. Ceram. Soc.* **2017**, *100*, 2832.
- [236] O. Familoni, Y. Zhou, H. Duan, *Solid Electrolytes for Advanced Applications*, Vol. 12, Springer International Publishing, Berlin **2019**.
- [237] G. Larraz, A. Orera, M. L. Sanjuán, *J. Mater. Chem. A* **2013**, *1*, 11419.
- [238] S. G. Kang, D. S. Sholl, *J. Phys. Chem. C* **2014**, *118*, 17402.
- [239] M. Nyman, T. M. Alam, S. K. McIntyre, G. C. Bleier, D. Ingersoll, *Chem. Mater.* **2010**, *22*, 5401.
- [240] C. Liu, K. Rui, C. Shen, M. E. Badding, G. Zhang, Z. Wen, *J. Power Sources* **2015**, *282*, 286.
- [241] L. Truong, V. Thangadurai, *Chem. Mater.* **2011**, *23*, 3970.
- [242] C. Galven, J. L. Fourquet, M. P. Crosnier-Lopez, F. Le Berre, *Chem. Mater.* **2011**, *23*, 1892.
- [243] C. Galven, J. Dittmer, E. Suard, F. Le Berre, M. P. Crosnier-Lopez, *Chem. Mater.* **2012**, *24*, 3335.
- [244] X. Zeng, A. J. Martinolich, K. A. See, K. T. Faber, *J. Energy Storage* **2020**, *27*, 101128.
- [245] T. Zhang, Y. Liu, T. D. Christopher, S. Huang, T. Söhnle, X. Song, W. Gao, P. Cao, *Ceram. Int.* **2020**, *46*, 3889.
- [246] J. Gai, E. Zhao, F. Ma, D. Sun, X. Ma, Y. Jin, Q. Wu, Y. Cui, *J. Eur. Ceram. Soc.* **2018**, *38*, 1673.
- [247] Y. Li, B. Xu, H. Xu, H. Duan, X. Lü, S. Xin, W. Zhou, L. Xue, G. Fu, A. Manthiram, J. B. Goodenough, *Angew. Chem., Int. Ed.* **2017**, *56*, 753.
- [248] L. C. Zhang, J. F. Yang, Y. X. Gao, X. P. Wang, Q. F. Fang, C. H. Chen, *J. Power Sources* **2017**, *355*, 69.
- [249] Y. Kim, J. Saienga, S. W. Martin, *J. Non-Cryst. Solids* **2005**, *351*, 3716.
- [250] J. Saienga, S. W. Martin, *J. Non-Cryst. Solids* **2008**, *354*, 1475.
- [251] Y. Sun, K. Suzuki, K. Hara, S. Hori, T. A. Yano, M. Hara, M. Hirayama, R. Kanno, *J. Power Sources* **2016**, *324*, 798.
- [252] K. Kanazawa, S. Yubuchi, C. Hotehama, M. Otoyama, S. Shimono, H. Ishibashi, Y. Kubota, A. Sakuda, A. Hayashi, M. Tatsumisago, *Inorg. Chem.* **2018**, *57*, 9925.
- [253] K. H. Park, D. Y. Oh, Y. E. Choi, Y. J. Nam, L. Han, J. Y. Kim, H. Xin, F. Lin, S. M. Oh, Y. S. Jung, *Adv. Mater.* **2016**, *28*, 1874.
- [254] A. Hayashi, H. Muramatsu, T. Ohtomo, S. Hama, M. Tatsumisago, *J. Mater. Chem. A* **2013**, *1*, 6320.
- [255] H. Fang, P. Jena, *Proc. Natl. Acad. Sci. USA* **2017**, *114*, 11046.
- [256] J. E. Ni, E. D. Case, J. S. Sakamoto, E. Rangasamy, J. B. Wolfenstein, *J. Mater. Sci.* **2012**, *47*, 7978.
- [257] J. Wolfenstein, J. L. Allen, J. Sakamoto, D. J. Siegel, H. Choe, *Ionics* **2018**, *24*, 1271.
- [258] M. B. Dixit, M. Regala, F. Shen, X. Xiao, K. B. Hatzell, *ACS Appl. Mater. Interfaces* **2019**, *11*, 2022.
- [259] F. P. McGrohan, T. Swamy, S. R. Bishop, E. Eggleton, L. Porz, X. Chen, Y. M. Chiang, K. J. Van Vliet, *Adv. Energy Mater.* **2017**, *7*, 1602011.
- [260] W. Zhang, D. Schröder, T. Arlt, I. Manke, R. Koerver, R. Pinedo, D. A. Weber, J. Sann, W. G. Zeier, J. Janek, *J. Mater. Chem. A* **2017**, *5*, 9929.
- [261] W. Fitzhugh, F. Wu, L. Ye, H. Su, X. Li, *Small* **2019**, *15*, 1901470.
- [262] G. Bucci, T. Swamy, Y. M. Chiang, W. C. Carter, *J. Mater. Chem. A* **2017**, *5*, 19422.
- [263] L. Y. Beaulieu, K. W. Eberman, R. L. Turner, L. J. Krause, J. R. Dahn, *Electrochem. Solid-State Lett.* **2001**, *4*, A137.
- [264] H. Tavassol, E. M. C. Jones, N. R. Sottos, A. A. Gewirth, *Nat. Mater.* **2016**, *15*, 1182.
- [265] A. F. Bower, P. R. Guduru, V. A. Sethuraman, *J. Mech. Phys. Solids* **2011**, *59*, 804.
- [266] A. Hayashi, A. Sakuda, M. Tatsumisago, *Front. Energy Res.* **2016**, *4*, 1.
- [267] S. F. Pugh, *London, Edinburgh, Dublin Philos. Mag. J. Sci.* **1954**, *45*, 823.
- [268] Y. H. Cho, J. Wolfenstein, E. Rangasamy, H. Kim, H. Choe, J. Sakamoto, *J. Mater. Sci.* **2012**, *47*, 5970.
- [269] C. Cooper, A. C. Sutorik, J. Wright, E. A. Luoto, G. Gilde, J. Wolfenstein, *Adv. Eng. Mater.* **2014**, *16*, 755.
- [270] K. G. Schell, F. Lemke, E. C. Bucharsky, A. Hintennach, M. J. Hoffmann, *J. Mater. Sci.* **2017**, *52*, 2232.
- [271] S. D. Jackman, R. A. Cutler, *J. Power Sources* **2012**, *218*, 65.
- [272] E. G. Herbert, W. E. Tenhaeff, N. J. Dudney, G. M. Pharr, *Thin Solid Films* **2011**, *520*, 413.
- [273] Z. Deng, Z. Wang, I.-H. Chu, J. Luo, S. P. Ong, *J. Electrochem. Soc.* **2016**, *163*, A67.
- [274] R. Chaim, M. Hefetz, *J. Mater. Sci.* **2004**, *39*, 3057.
- [275] D. P. Miannay, *Fracture Mechanics*, 1st ed., Elsevier, Amsterdam **1998**.
- [276] M. Barsoum, *Fundamentals of Ceramics*, Taylor and Francis, London **2003**.
- [277] T. Clyne, D. Hull, *An Introduction to Composite Materials*, 3rd ed., Cambridge University Press, Cambridge **2019**.
- [278] R. D. Schmidt, J. Sakamoto, *J. Power Sources* **2016**, *324*, 126.
- [279] C. Monroe, J. Newman, *J. Electrochem. Soc.* **2005**, *152*, A396.
- [280] F. Han, A. S. Westover, J. Yue, X. Fan, F. Wang, M. Chi, D. N. Leonard, N. J. Dudney, H. Wang, C. Wang, *Nat. Energy* **2019**, *4*, 187.
- [281] G. Hou, X. Ma, Q. Sun, Q. Ai, X. Xu, L. Chen, D. Li, J. Chen, H. Zhong, Y. Li, Z. Xu, P. Si, J. Feng, L. Zhang, F. Ding, L. Ci, *ACS Appl. Mater. Interfaces* **2018**, *10*, 18610.
- [282] F. Han, J. Yue, X. Zhu, C. Wang, *Adv. Energy Mater.* **2018**, *8*, 6.
- [283] B. Wu, S. Wang, J. Lochala, D. Desrochers, B. Liu, W. Zhang, J. Yang, J. Xiao, *Energy Environ. Sci.* **2018**, *11*, 1803.
- [284] W. Manalastas, J. Rikarte, R. J. Chater, R. Brugge, A. Aguadero, L. Buannic, A. Llordés, F. Aguesse, J. Kilner, *J. Power Sources* **2019**, *412*, 287.
- [285] M. Wang, J. B. Wolfenstein, J. Sakamoto, *Electrochim. Acta* **2019**, *296*, 842.
- [286] E. J. Cheng, A. Sharafi, J. Sakamoto, *Electrochim. Acta* **2017**, *223*, 85.
- [287] L. Porz, T. Swamy, B. W. Sheldon, D. Rettenwander, T. Frömling, H. L. Thaman, S. Berendts, R. Uecker, W. C. Carter, Y. M. Chiang, *Adv. Energy Mater.* **2017**, *7*, 1701003.
- [288] L. Viswanathan, Y. Ikuma, A. V. Virkar, *J. Mater. Sci.* **1983**, *18*, 109.
- [289] R. Sakanoi, T. Shimazaki, J. Xu, Y. Higuchi, N. Ozawa, K. Sato, T. Hashida, M. Kubo, *J. Chem. Phys.* **2014**, *140*, 121102.
- [290] R. W. Rice, *J. Mater. Sci.* **1996**, *31*, 1969.
- [291] R. K. Nanstad, D. P. Edmonds, *Pressure Vessel Piping Technol.* **1985**, *84*, 507.
- [292] J. Wolfenstein, J. L. Allen, J. Read, J. Sakamoto, G. Gonzalez-Doncel, *J. Power Sources* **2010**, *195*, 4124.
- [293] D. B. Sirdeshmukh, L. Sirdeshmukh, K. G. Subhadra, K. K. Rao, S. B. Laxman, *Bull. Mater. Sci.* **2001**, *24*, 469.
- [294] Theoretical and Applied Mechanics, *Phys. Today* **1962**, *15*, 82.
- [295] A. Makishima, J. D. Mackenzie, *J. Non. Cryst. Solids* **1973**, *12*, 35.
- [296] A. Kato, M. Nagao, A. Sakuda, A. Hayashi, M. Tatsumisago, *J. Ceram. Soc. Jpn.* **2014**, *122*, 552.
- [297] Z. Zhang, J. H. Kennedy, *Solid State Ionics* **1990**, *38*, 217.

- [298] J. G. Swallow, W. H. Woodford, F. P. McGrogan, N. Ferralis, Y.-M. Chiang, K. J. Van Vliet, *J. Electrochem. Soc.* **2014**, 161, F3084.
- [299] F. Wu, W. Fitzhugh, L. Ye, J. Ning, X. Li, *Nat. Commun.* **2018**, 9, 4037.
- [300] H. L. Tuller, *Solid State Batteries: Materials Design and Optimization*, The Kluwer International Series in Engineering and Computer Science Series Editor, Springer, New York **1994**.
- [301] R. Jalem, Y. Morishita, T. Okajima, H. Takeda, Y. Kondo, M. Nakayama, T. Kasuga, *J. Mater. Chem. A* **2016**, 4, 14371.
- [302] W. D. Richards, L. J. Miara, Y. Wang, J. C. Kim, G. Ceder, *Chem. Mater.* **2016**, 28, 266.
- [303] T. Binninger, A. Marcolongo, M. Mottet, V. Weber, T. Laino, *J. Mater. Chem. A* **2020**, 8, 1347.
- [304] F. Han, T. Gao, Y. Zhu, K. J. Gaskell, C. Wang, *Adv. Mater.* **2015**, 27, 3473.
- [305] R. Xu, Z. Wu, S. Zhang, X. Wang, Y. Xia, X. Xia, X. Huang, J. Tu, *Chem. - Eur. J.* **2017**, 23, 13950.
- [306] S. Boulineau, M. Courty, J. M. Tarascon, V. Viallet, *Solid State Ionics* **2012**, 221, 1.
- [307] T. Thompson, S. Yu, L. Williams, R. D. Schmidt, R. Garcia-Mendez, J. Wolfenstine, J. L. Allen, E. Kioupakis, D. J. Siegel, J. Sakamoto, *ACS Energy Lett.* **2017**, 2, 462.
- [308] T. K. Schwietert, V. A. Arselewska, C. Wang, C. Yu, A. Vasileiadis, N. J. J. de Klerk, J. Hageman, T. Hupfer, I. Kerkamm, Y. Xu, E. van der Maas, E. M. Kelder, S. Ganapathy, M. Wagemaker, *Nat. Mater.* **2020**, 19, 428.
- [309] X. Xu, Z. Wen, X. Yang, J. Zhang, Z. Gu, *Solid State Ionics* **2006**, 177, 2611.
- [310] C. H. Chen, K. Amine, *Solid State Ionics* **2001**, 144, 51.
- [311] E. A. Il, K. V. Druzhinin, N. S. Saetova, B. D. Antonov, V. I. Pryakhina, *Electrochim. Acta* **2018**, 285, 326.
- [312] P. Hartmann, T. Leichtweiss, M. R. Busche, M. Schneider, M. Reich, J. Sann, P. Adelhelm, J. Janek, *J. Phys. Chem. C* **2013**, 117, 21064.
- [313] X. Xu, Z. Wen, X. Wu, X. Yang, Z. Gu, *J. Am. Ceram. Soc.* **2007**, 90, 2802.
- [314] H. Nemori, Y. Matsuda, S. Mitsuoka, M. Matsui, O. Yamamoto, Y. Takeda, N. Imanishi, *Solid State Ionics* **2015**, 282, 7.
- [315] S. Wenzel, T. Leichtweiss, D. Krüger, J. Sann, J. Janek, *Solid State Ionics* **2015**, 278, 98.
- [316] E. Rangasamy, Z. Liu, M. Gobet, K. Pilar, G. Sahu, W. Zhou, H. Wu, S. Greenbaum, C. Liang, *J. Am. Chem. Soc.* **2015**, 137, 1384.
- [317] W. Zhang, T. Leichtweiss, S. P. Culver, R. Koerver, D. Das, D. A. Weber, W. G. Zeier, J. Janek, *ACS Appl. Mater. Interfaces* **2017**, 9, 35888.
- [318] S. Wenzel, S. J. Sedlmaier, C. Dietrich, W. G. Zeier, J. Janek, *Solid State Ionics* **2018**, 318, 102.
- [319] C. Yu, S. Ganapathy, E. R. H. V. Eck, H. Wang, S. Basak, Z. Li, M. Wagemaker, *Nat. Commun.* **2017**, 8, 1.
- [320] R. Koerver, F. Walther, I. Aygün, J. Sann, C. Dietrich, W. G. Zeier, J. Janek, J. Auvergniot, A. Cassel, D. Foix, V. Viallet, V. Seznec, R. Dedryvère, R. Koerver, F. Walther, I. Aygün, J. Sann, C. Dietrich, W. G. Zeier, J. Janek, *J. Mater. Chem. A* **2017**, 5, 22750.
- [321] D. H. S. Tan, E. A. Wu, H. Nguyen, Z. Chen, M. A. T. Marple, J. M. Doux, X. Wang, H. Yang, A. Banerjee, Y. S. Meng, *ACS Energy Lett.* **2019**, 4, 2418.
- [322] Y. Tian, T. Shi, W. D. Richards, J. Li, J. C. Kim, S. H. Bo, G. Ceder, *Energy Environ. Sci.* **2017**, 10, 1150.
- [323] K. Takada, N. Ohta, L. Zhang, K. Fukuda, I. Sakaguchi, R. Ma, M. Osada, T. Sasaki, *Solid State Ionics* **2008**, 179, 1333.
- [324] N. Ohta, K. Takada, I. Sakaguchi, L. Zhang, R. Ma, K. Fukuda, M. Osada, T. Sasaki, *Electrochim. Commun.* **2007**, 9, 1486.
- [325] Y. Xiao, Y. Wang, S. H. Bo, J. C. Kim, L. J. Miara, G. Ceder, *Nat. Rev. Mater.* **2020**, 5, 105.
- [326] R. Koerver, I. Aygün, T. Leichtweiss, C. Dietrich, W. Zhang, J. O. Binder, P. Hartmann, W. G. Zeier, J. Janek, *Chem. Mater.* **2017**, 29, 5574.
- [327] C. M. Julien, A. Mauger, *Coatings* **2019**, 9, 386.
- [328] A. A. Talin, D. Ruzmetov, A. Kolmakov, K. McKelvey, N. Ware, F. El Gabaly, B. Dunn, H. S. White, *ACS Appl. Mater. Interfaces* **2016**, 8, 32385.
- [329] Y. Matsuda, N. Kuwata, J. Kawamura, *Solid State Ionics* **2018**, 320, 38.
- [330] N. J. Dudney, Y. Il Jang, *J. Power Sources* **2003**, 119–121, 300.
- [331] M. Finsterbusch, *ACS Appl. Mater. Interfaces* **2018**, 10, 22329.
- [332] W. Zhang, D. A. Weber, H. Weigand, T. Arlt, I. Manke, D. Schröder, R. Koerver, T. Leichtweiss, P. Hartmann, W. G. Zeier, J. Janek, *ACS Appl. Mater. Interfaces* **2017**, 9, 17835.
- [333] T. Shi, Q. Tu, Y. Tian, Y. Xiao, L. J. Miara, O. Kononova, G. Ceder, *Adv. Energy Mater.* **2019**, 1902881.
- [334] A. Bielefeld, D. A. Weber, J. Janek, *J. Phys. Chem. C* **2019**, 123, 1626.
- [335] F. Strauss, T. Bartsch, L. De Biasi, A. Y. Kim, J. Janek, P. Hartmann, T. Brezesinski, *ACS Energy Lett.* **2018**, 3, 992.
- [336] *Handbook of Solid State Batteries*, 2nd ed. (Ed: R. Wahap), World Scientific, Singapore **2016**.
- [337] M. Park, X. Zhang, M. Chung, G. B. Less, A. M. Sastry, *J. Power Sources* **2010**, 195, 7904.
- [338] K. Park, B. C. Yu, J. W. Jung, Y. Li, W. Zhou, H. Gao, S. Son, J. B. Goodenough, *Chem. Mater.* **2016**, 28, 8051.
- [339] T. Yoshinari, R. Koerver, P. Hofmann, Y. Uchimoto, W. G. Zeier, J. Janek, *ACS Appl. Mater. Interfaces* **2019**, 11, 23244.
- [340] K. K. Chawla, *Composite Materials Science and Engineering*, Springer, New York **2003**, p. 20.
- [341] J. Kasemchainan, S. Zekoll, D. Spencer Jolly, Z. Ning, G. O. Hartley, J. Marrow, P. G. Bruce, *Nat. Mater.* **2019**, 18, 1105.
- [342] F. Hao, F. Han, Y. Liang, C. Wang, Y. Yao, *MRS Bull.* **2018**, 43, 746.
- [343] Y. Ren, T. Liu, Y. Shen, Y. Lin, C. W. Nan, *J. Mater.* **2016**, 2, 256.
- [344] Y. Xiao, L. J. Miara, Y. Wang, G. Ceder, *Joule* **2019**, 3, 1252.
- [345] H. Tsukasaki, T. Uchiyama, K. Yamamoto, S. Mori, Y. Uchimoto, H. Kowada, A. Hayashi, M. Tatsumisago, *J. Power Sources* **2019**, 434, 226714.
- [346] Y. G. Lee, S. Fujiki, C. Jung, N. Suzuki, N. Yashiro, R. Omoda, D. S. Ko, T. Shiratsuchi, T. Sugimoto, S. Ryu, J. H. Ku, T. Watanabe, Y. Park, Y. Aihara, D. Im, I. T. Han, *Nat. Energy* **2020**, 5, 299.
- [347] M. Zarabian, M. Bartolini, P. Pereira-Almao, V. Thangadurai, *J. Electrochem. Soc.* **2017**, 164, A1133.
- [348] K. H. Kim, Y. Iriyama, K. Yamamoto, S. Kumazaki, T. Asaka, K. Tanabe, C. A. J. Fisher, T. Hirayama, R. Murugan, Z. Ogumi, *J. Power Sources* **2011**, 196, 764.
- [349] J. Wakasugi, H. Munakata, K. Kanamura, *Electrochemistry* **2017**, 85, 77.
- [350] B. Gotzen, J. Dornseiffer, C.-L. L. Tsai, O. Guillot, C. Dellen, M. Finsterbusch, S. Lobe, S. Uhlenbruck, D. Sebold, J. Dornseiffer, S. Lobe, C. Dellen, C.-L. L. Tsai, B. Gotzen, D. Sebold, M. Finsterbusch, O. Guillot, *J. Electroceram.* **2017**, 38, 197.
- [351] V. Thangadurai, W. Weppner, *J. Power Sources* **2005**, 142, 339.
- [352] M. Kotobuki, H. Munakata, K. Kanamura, Y. Sato, T. Yoshida, *J. Electrochem. Soc.* **2010**, 157, A1076.
- [353] S. Ohta, T. Kobayashi, J. Seki, T. Asaoka, *J. Power Sources* **2012**, 202, 332.
- [354] T. Hakari, M. Deguchi, K. Mitsuhashira, T. Ohta, K. Saito, Y. Oriksa, Y. Uchimoto, Y. Kowada, A. Hayashi, M. Tatsumisago, *Chem. Mater.* **2017**, 29, 4768.
- [355] T. Swamy, X. Chen, Y. M. Chiang, *Chem. Mater.* **2019**, 31, 707.
- [356] D. H. S. S. Tan, A. Banerjee, Z. Chen, Y. S. Meng, *Nat. Nanotechnol.* **2020**, 15, 170.
- [357] A. M. Nolan, Y. Zhu, X. He, Q. Bai, Y. Mo, *Joule* **2018**, 2, 2016.
- [358] H. Tang, Z. Deng, Z. Lin, Z. Wang, I. H. Chu, C. Chen, Z. Zhu, C. Zheng, S. P. Ong, *Chem. Mater.* **2018**, 30, 163.
- [359] B. L. Ellis, K. T. Lee, L. F. Nazar, *Chem. Mater.* **2010**, 22, 691.

- [360] W. Zhang, F. H. Richter, S. P. Culver, T. Leichtweiss, J. G. Lozano, C. Dietrich, P. G. Bruce, W. G. Zeier, J. Janek, *ACS Appl. Mater. Interfaces* **2018**, *10*, 22226.
- [361] J. Auvergniot, A. Cassel, D. Foix, V. Viallet, V. Seznec, R. Dedryvère, *Solid State Ionics* **2017**, *300*, 78.
- [362] J. Auvergniot, A. Cassel, J. B. Ledeuil, V. Viallet, V. Seznec, R. Dedryvère, *Chem. Mater.* **2017**, *29*, 3883.
- [363] F. Walther, R. Koerver, T. Fuchs, S. Ohno, J. Sann, M. Rohnke, W. G. Zeier, J. Janek, *Chem. Mater.* **2019**.
- [364] H. Visbal, Y. Aihara, S. Ito, T. Watanabe, Y. Park, S. Doo, *J. Power Sources* **2016**, *314*, 85.
- [365] A. Sakuda, A. Hayashi, M. Tatsumisago, *Chem. Mater.* **2010**, *22*, 949.
- [366] R. Ramachandran, M. Saranya, C. Santhosh, V. Velmurugan, B. P. C. Raghupathy, S. K. Jeong, A. N. Grace, *RSC Adv.* **2014**, *4*, 21151.
- [367] R. Koerver, W. Zhang, L. De Biasi, S. Schweidler, A. O. Kondrakov, S. Kolling, T. Brezesinski, P. Hartmann, W. G. Zeier, J. Janek, *Energy Environ. Sci.* **2018**, *11*, 2142.
- [368] K. Ishidzu, Y. Oka, T. Nakamura, *Solid State Ionics* **2016**, *288*, 176.
- [369] F. Strauss, L. de Biasi, A.-Y. Kim, J. Hertle, S. Schweidler, J. Janek, P. Hartmann, T. Brezesinski, *ACS Mater. Lett.* **2020**, *2*, 84.
- [370] G. Bucci, B. Talamini, A. Renuka Balakrishna, Y. M. Chiang, W. C. Carter, *Phys. Rev. Mater.* **2018**, *2*, 105407.
- [371] T. Maxisch, G. Ceder, *Phys. Rev. B: Condens. Matter Mater. Phys.* **2006**, *73*, 1.
- [372] E. J. Cheng, N. J. Taylor, J. Wolfenstine, J. Sakamoto, *J. Asian Ceram. Soc.* **2017**, *5*, 113.
- [373] Y. Qi, L. G. Hector, C. James, K. J. Kim, *J. Electrochem. Soc.* **2014**, *161*, F3010.
- [374] E. J. Cheng, K. Hong, N. J. Taylor, H. Choe, J. Wolfenstine, J. Sakamoto, *J. Eur. Ceram. Soc.* **2017**, *37*, 3213.
- [375] A. Manthiram, *Nat. Commun.* **2020**, *11*, 1550.
- [376] Y. Shao, H. Wang, Z. Gong, D. Wang, B. Zheng, J. Zhu, Y. Lu, Y. S. Hu, X. Guo, H. Li, X. Huang, Y. Yang, C. W. Nan, L. Chen, *ACS Energy Lett.* **2018**, *3*, 1212.
- [377] K. Fu, Y. Gong, G. T. Hitz, D. W. McOwen, Y. Li, S. Xu, Y. Wen, L. Zhang, C. Wang, G. Pastel, J. Dai, B. Liu, H. Xie, Y. Yao, E. D. Wachsman, L. Hu, *Energy Environ. Sci.* **2017**, *10*, 1568.
- [378] X. Tao, Y. Liu, W. Liu, G. Zhou, J. Zhao, D. Lin, C. Zu, O. Sheng, W. Zhang, H. W. Lee, Y. Cui, *Nano Lett.* **2017**, *17*, 2967.
- [379] S. P. Culver, R. Koerver, W. G. Zeier, J. Janek, *Adv. Energy Mater.* **2019**, *9*, 1900626.
- [380] K. Takada, N. Ohta, L. Zhang, X. Xu, B. T. Hang, T. Ohnishi, M. Osada, T. Sasaki, *Solid State Ionics* **2012**, *225*, 594.
- [381] X. Li, L. Jin, D. Song, H. Zhang, X. Shi, Z. Wang, L. Zhang, L. Zhu, *J. Energy Chem.* **2020**, *40*, 39.
- [382] N. Ohta, K. Takada, L. Zhang, R. Ma, M. Osada, T. Sasaki, *Adv. Mater.* **2006**, *18*, 2226.
- [383] H. Kitaura, A. Hayashi, K. Tadanaga, M. Tatsumisago, *Electrochim. Acta* **2010**, *55*, 8821.
- [384] Y. Seino, T. Ota, K. Takada, *J. Power Sources* **2011**, *196*, 6488.
- [385] A. Sakuda, H. Kitaura, A. Hayashi, K. Tadanaga, M. Tatsumisago, *Electrochim. Solid-State Lett.* **2008**, *11*, A1.
- [386] M. Tatsumisago, A. Hayashi, *Funct. Mater. Lett.* **2008**, *01*, 31.
- [387] A. Sakuda, H. Kitaura, A. Hayashi, K. Tadanaga, M. Tatsumisago, *J. Power Sources* **2009**, *189*, 527.
- [388] A. Sakuda, H. Kitaura, A. Hayashi, K. Tadanaga, M. Tatsumisago, *J. Electrochem. Soc.* **2009**, *156*, A27.
- [389] Y. Sakurai, A. Sakuda, A. Hayashi, M. Tatsumisago, *Solid State Ionics* **2011**, *182*, 59.
- [390] Y. Ito, Y. Sakurai, S. Yubuchi, A. Sakuda, A. Hayashi, M. Tatsumisago, *J. Electrochim. Soc.* **2015**, *162*, A1610.
- [391] S. Ito, S. Fujiki, T. Yamada, Y. Aihara, Y. Park, T. Y. Kim, S. W. Baek, J. M. Lee, S. Doo, N. Machida, *J. Power Sources* **2014**, *248*, 943.
- [392] Y.-J. Kim, R. Rajesh, K.-S. Ryu, *Sci. Adv. Mater.* **2020**, *12*, 412.
- [393] D. S. Sungwoo Noh, J. Kim, M. Eom, *J. Ind. Eng. Chem.* **2015**, *86*.
- [394] J. Kim, M. Kim, S. Noh, G. Lee, D. Shin, *Ceram. Int.* **2016**, *42*, 2140.
- [395] H. W. Kwak, Y. J. Park, *Thin Solid Films* **2018**, *660*, 625.
- [396] S. H. Jung, K. Oh, Y. J. Nam, D. Y. Oh, P. Brüner, K. Kang, Y. S. Jung, *Chem. Mater.* **2018**, *30*, 8190.
- [397] H. W. Kwak, Y. J. Park, *Sci. Rep.* **2019**, *9*, 8099.
- [398] T. Kato, T. Hamanaka, K. Yamamoto, T. Hirayama, F. Sagane, M. Motoyama, Y. Iriyama, *J. Power Sources* **2014**, *260*, 292.
- [399] A. Sakuda, T. Takeuchi, H. Kobayashi, *Solid State Ionics* **2016**, *285*, 112.
- [400] M. Calpa, N. C. Rosero-Navarro, A. Miura, K. Tadanaga, *Electrochim. Acta* **2019**, *296*, 473.
- [401] H. Wan, J. P. Mwizerwa, X. Qi, X. Xu, H. Li, Q. Zhang, L. Cai, Y. S. Hu, X. Yao, *ACS Appl. Mater. Interfaces* **2018**, *10*, 12300.
- [402] M. Kotobuki, K. Kanamura, Y. Sato, T. Yoshida, *J. Power Sources* **2011**, *196*, 7750.
- [403] S. Ohta, J. Seki, Y. Yagi, Y. Kihira, T. Tani, T. Asaoka, *J. Power Sources* **2014**, *265*, 40.
- [404] M. Tatsumisago, N. Machida, T. Minami, *Yogyo Kyokai Shi/J. Ceram. Soc. Jpn.* **1987**, *95*, 197.
- [405] M. Kotobuki, H. Munakata, K. Kanamura, *J. Power Sources* **2011**, *196*, 6947.
- [406] M. Kotobuki, Y. Suzuki, K. Kanamura, Y. Sato, K. Yamamoto, T. Yoshida, *J. Power Sources* **2011**, *196*, 9815.
- [407] J. van den Broek, S. Afyon, J. L. M. Rupp, *Adv. Energy Mater.* **2016**, *6*, 1600736.
- [408] Y. Ren, T. Liu, Y. Shen, Y. Lin, C. W. Nan, *Ionics* **2017**, *23*, 2521.
- [409] T. Lan, C. L. Tsai, F. Tietz, X. K. Wei, M. Heggen, R. E. Dunin-Borkowski, R. Wang, Y. Xiao, Q. Ma, O. Guillou, *Nano Energy* **2019**, *65*, 104040.
- [410] B. J. Neudecker, *J. Electrochim. Soc.* **1996**, *143*, 2198.
- [411] J. Schnell, H. Knörzer, A. J. Imbsweiler, G. Reinhart, *Energy Technol.* **2020**, *8*, 1901237.
- [412] S. H. Wang, J. Yue, W. Dong, T. T. Zuo, J. Y. Li, X. Liu, X. D. Zhang, L. Liu, J. L. Shi, Y. X. Yin, Y. G. Guo, *Nat. Commun.* **2019**, *10*, 4930.
- [413] R. Schmuck, R. Wagner, G. Hörpel, T. Placke, M. Winter, *Nat. Energy* **2018**, *3*, 267.
- [414] D. Lin, Y. Liu, Z. Liang, H. W. Lee, J. Sun, H. Wang, K. Yan, J. Xie, Y. Cui, *Nat. Nanotechnol.* **2016**, *11*, 626.
- [415] Y. Liu, D. Lin, Z. Liang, J. Zhao, K. Yan, Y. Cui, *Nat. Commun.* **2016**, *7*, 10992.
- [416] Y. Chen, Z. Wang, X. Li, X. Yao, C. Wang, Y. Li, W. Xue, D. Yu, S. Y. Kim, F. Yang, A. Kushima, G. Zhang, H. Huang, N. Wu, Y.-W. Mai, J. B. Goodenough, J. Li, *Nature* **2020**, *578*, 251.
- [417] K. Yan, Z. Lu, H. W. Lee, F. Xiong, P. C. Hsu, Y. Li, J. Zhao, S. Chu, Y. Cui, *Nat. Energy* **2016**, *1*, 16010.
- [418] R. Xu, X. B. Cheng, C. Yan, X. Q. Zhang, Y. Xiao, C. Z. Zhao, J. Q. Huang, Q. Zhang, *Matter* **2019**, *1*, 317.
- [419] R. Inada, S. Yasuda, H. Hosokawa, M. Saito, T. Tojo, Y. Sakurai, *Batteries* **2018**, *4*, 26.
- [420] C. Ma, Y. Cheng, K. Yin, J. Luo, A. Sharafi, J. Sakamoto, J. Li, K. L. More, N. J. Dudney, M. Chi, *Nano Lett.* **2016**, *16*, 7030.
- [421] D. Ren, X. Feng, L. Lu, M. Ouyang, S. Zheng, J. Li, X. He, *J. Power Sources* **2017**, *364*, 328.
- [422] K. H. Chen, K. N. Wood, E. Kazyak, W. S. Lepage, A. L. Davis, A. J. Sanchez, N. P. Dasgupta, *J. Mater. Chem. A* **2017**, *5*, 11671.
- [423] T. R. Jow, *J. Electrochim. Soc.* **1983**, *130*, 737.
- [424] A. Schwöbel, R. Hausbrand, W. Jaegermann, *Solid State Ionics* **2015**, *273*, 51.
- [425] S. Wenzel, D. A. Weber, T. Leichtweiss, M. R. Busche, J. Sann, J. Janek, *Solid State Ionics* **2016**, *286*, 24.
- [426] Z. Wang, D. Santhanagopalan, W. Zhang, F. Wang, H. L. Xin, K. He, J. Li, N. Dudney, Y. S. Meng, *Nano Lett.* **2016**, *16*, 3760.

- [427] S. Wenzel, S. Randau, T. Leichtweic, D. A. Weber, J. Sann, W. G. Zeier, J. Janek, *Chem. Mater.* **2016**, *28*, 2400.
- [428] K. Y. Yang, I. C. Leu, K. Z. Fung, M. H. Hon, M. C. Hsu, Y. J. Hsiao, M. C. Wang, *J. Mater. Res.* **2008**, *23*, 1813.
- [429] S. J. Visco, V. Y. Nimon, A. Petrov, K. Pridatko, N. Goncharenko, E. Nimon, L. De Jonghe, Y. M. Volkovich, D. A. Bograchev, *J. Solid State Electrochem.* **2014**, *18*, 1443.
- [430] J. Wolfenstine, J. L. Allen, J. Read, J. Sakamoto, *J. Mater. Sci.* **2013**, *48*, 5846.
- [431] A. Kato, H. Kowada, M. Deguchi, C. Hotehama, A. Hayashi, M. Tatsumisago, *Solid State Ionics* **2018**, *322*, 1.
- [432] J. B. Bates, N. J. Dudney, B. Neudecker, A. Ueda, C. D. Evans, *Solid State Ionics* **2000**, *135*, 33.
- [433] H. Koshikawa, S. Matsuda, K. Kamiya, M. Miyayama, Y. Kubo, K. Uosaki, K. Hashimoto, S. Nakanishi, *J. Power Sources* **2018**, *376*, 147.
- [434] M. Meyer, H. Rickert, U. Schwitzer, *Solid State Ionics* **1983**, *9–10*, 689.
- [435] S. Edition, *Electrical*.
- [436] X. Wang, W. Zeng, L. Hong, W. Xu, H. Yang, F. Wang, H. Duan, M. Tang, H. Jiang, *Nat. Energy* **2018**, *3*, 227.
- [437] R. Sudo, Y. Nakata, K. Ishiguro, M. Matsui, A. Hirano, Y. Takeda, O. Yamamoto, N. Imanishi, *Solid State Ionics* **2014**, *262*, 151.
- [438] J. A. Lewis, F. J. Q. Cortes, M. G. Boebinger, J. Tippens, T. S. Marchese, N. Kondekar, X. Liu, M. Chi, M. T. McDowell, *ACS Energy Lett.* **2019**, *4*, 591.
- [439] J. Tippens, J. C. Miers, A. Afshar, J. A. Lewis, F. J. Q. Cortes, H. Qiao, T. S. Marchese, C. V. Di Leo, C. Saldana, M. T. McDowell, *ACS Energy Lett.* **2019**, *4*, 1475.
- [440] H. Chung, B. Kang, *Chem. Mater.* **2017**, *29*, 8611.
- [441] H. Buschmann, S. Berendts, B. Mogwitz, J. Janek, *J. Power Sources* **2012**, *206*, 236.
- [442] K. Ishiguro, Y. Nakata, M. Matsui, I. Uechi, Y. Takeda, O. Yamamoto, N. Imanishi, *J. Electrochem. Soc.* **2013**, *160*, A1690.
- [443] K. Ishiguro, H. Nemori, S. Sunahiro, Y. Nakata, R. Sudo, M. Matsui, Y. Takeda, O. Yamamoto, N. Imanishi, *J. Electrochem. Soc.* **2014**, *161*, A668.
- [444] E. Rangasamy, G. Sahu, J. K. Keum, A. J. Rondinone, N. J. Dudney, C. Liang, *J. Mater. Chem. A* **2014**, *2*, 4111.
- [445] G. T. Hitz, D. W. McOwen, L. Zhang, Z. Ma, Z. Fu, Y. Wen, Y. Gong, J. Dai, T. R. Hamann, L. Hu, E. D. Wachsman, *Mater. Today* **2019**, *22*, 50.
- [446] M. H. Ryou, Y. M. Lee, Y. Lee, M. Winter, P. Bieker, *Adv. Funct. Mater.* **2015**, *25*, 834.
- [447] C. Yang, L. Zhang, B. Liu, S. Xu, T. Hamann, D. McOwen, J. Dai, W. Luo, Y. Gong, E. D. Wachsman, L. Hu, *Proc. Natl. Acad. Sci. USA* **2018**, *115*, 3770.
- [448] J. A. Lewis, J. Tippens, F. Javier, Q. Cortes, M. T. McDowell, **2019**.
- [449] Y. Métivier, G. Richomme, *Lect. Notes Comput. Sci.* **1994**, *775*, 341.
- [450] G. M. Stone, S. A. Mullin, A. A. Teran, D. T. Hallinan, A. M. Minor, A. Hexemer, N. P. Balsara, *J. Electrochem. Soc.* **2012**, *159*, A222.
- [451] M. Nagao, A. Hayashi, M. Tatsumisago, T. Kanetsuku, T. Tsuda, S. Kuwabata, *Phys. Chem. Chem. Phys.* **2013**, *15*, 18600.
- [452] J. A. Lewis, J. Tippens, F. J. Q. Cortes, M. T. McDowell, *Trends Chem.* **2019**, *1*, 845.
- [453] T. Yamada, *J. Electrochem. Soc.* **2015**, *162*.
- [454] M. Nagao, A. Hayashi, M. Tatsumisago, *Electrochem. Commun.* **2012**, *22*, 177.
- [455] R. Xu, F. Han, X. Ji, X. Fan, J. Tu, C. Wang, *Nano Energy* **2018**, *53*, 958.
- [456] R. Garcia-Mendez, F. Mizuno, R. Zhang, T. S. Arthur, J. Sakamoto, *Electrochim. Acta* **2017**, *237*, 144.
- [457] E. Markevich, G. Salitra, F. Chesneau, M. Schmidt, D. Aurbach, *ACS Energy Lett.* **2017**, *2*, 1321.
- [458] A. Masias, N. Felten, R. Garcia-Mendez, J. Wolfenstine, J. Sakamoto, *J. Mater. Sci.* **2019**, *54*, 2585.
- [459] T. Krauskopf, R. Dippel, H. Hartmann, K. Peppler, B. Mogwitz, F. H. Richter, W. G. Zeier, J. Janek, *Joule* **2019**, *3*, 2030.
- [460] H. K. Tian, B. Xu, Y. Qi, *J. Power Sources* **2018**, *392*, 79.
- [461] J. Li, N. J. Dudney, J. Nanda, C. Liang, *ACS Appl. Mater. Interfaces* **2014**, *6*, 10083.
- [462] Y. Su, J. Falgenhauer, A. Polity, T. Leichtweiss, A. Kronenberger, J. Obel, S. Zhou, D. Schlettwein, J. Janek, B. K. Meyer, *Solid State Ionics* **2015**, *282*, 63.
- [463] T. Swamy, Y.-M. Chiang, **2011**, *9*, 2.
- [464] Y. Cao, M. Li, J. Lu, J. Liu, K. Amine, *Nat. Nanotechnol.* **2019**, *14*, 200.
- [465] L. Cheng, W. Chen, M. Kunz, K. Persson, N. Tamura, G. Chen, M. Doeff, *ACS Appl. Mater. Interfaces* **2015**, *7*, 2073.
- [466] X. Han, Y. Gong, K. Fu, X. He, G. T. Hitz, J. Dai, A. Pearse, B. Liu, H. Wang, G. Rubloff, Y. Mo, V. Thangadurai, E. D. Wachsman, L. Hu, *Nat. Mater.* **2017**, *16*, 572.
- [467] W. Luo, Y. Gong, Y. Zhu, K. K. Fu, J. Dai, S. D. Lacey, C. Wang, B. Liu, X. Han, Y. Mo, E. D. Wachsman, L. Hu, *J. Am. Chem. Soc.* **2016**, *138*, 12258.
- [468] K. J. Kim, J. J. Hinricher, J. L. M. Rupp, *Nat. Energy* **2020**, *5*, 278.
- [469] H. Zhang, X. Li, S. Hao, X. Zhang, J. Lin, *Electrochim. Acta* **2019**, *325*, 134943.
- [470] N. W. Li, Y. X. Yin, C. P. Yang, Y. G. Guo, *Adv. Mater.* **2016**, *28*, 1853.
- [471] S. Shinzo, E. Higuchi, M. Chiku, A. Hayashi, H. Inoue, *ACS Appl. Mater. Interfaces* **2020**.
- [472] M. Wang, J. Sakamoto, *J. Power Sources* **2018**, *377*, 7.
- [473] Y. Huang, B. Chen, J. Duan, F. Yang, T. Wang, Z. Wang, W. Yang, C. Hu, W. Luo, Y. Huang, *Angew. Chem., Int. Ed.* **2020**, *59*, 3699.
- [474] Y. Ren, Y. Shen, Y. Lin, C. W. Nan, *Electrochim. Commun.* **2015**, *57*, 27.
- [475] Y. Li, X. Chen, A. Dolocan, Z. Cui, S. Xin, L. Xue, H. Xu, K. Park, J. B. Goodenough, *J. Am. Chem. Soc.* **2018**, *140*, 6448.
- [476] A.-S. Li, L. Cheng, C. Hao Wu, A. Jarry, W. Chen, Y. Ye, J. Zhu, R. Kostecki, K. Persson, J. Guo, M. Salmeron, G. Chen, M. Doeff, **2015**.
- [477] R. H. Basappa, T. Ito, H. Yamada, *J. Electrochem. Soc.* **2017**, *164*, A666.
- [478] H. Huo, Y. Chen, N. Zhao, X. Lin, J. Luo, X. Yang, Y. Liu, X. Guo, X. Sun, *Nano Energy* **2019**, *61*, 119.
- [479] T. Deng, X. Ji, Y. Zhao, L. Cao, S. Li, S. Hwang, C. Luo, P. Wang, H. Jia, X. Fan, X. Lu, D. Su, X. Sun, C. Wang, J. Zhang, *Adv. Mater.* **2020**, *32*, 2000030.
- [480] L. Cheng, C. H. Wu, A. Jarry, W. Chen, Y. Ye, J. Zhu, R. Kostecki, K. Persson, J. Guo, M. Salmeron, G. Chen, *ACS Applied Materials & Interfaces* **2015**, *7*, 17649.
- [481] C. Wang, H. Xie, L. Zhang, Y. Gong, G. Pastel, J. Dai, B. Liu, E. D. Wachsman, L. Hu, W. Chengwei, X. Hua, Z. Lei, G. Yunhui, G. Pastel, D. Jiaqi, L. Boyang, E. D. Wachsman, H. Liangbing, *Adv. Energy Mater.* **2018**, *8*, 1701963.
- [482] N. C. Rosero-navarro, R. Kajiwara, Y. Tateyama, A. Miura, K. Tadanaga, *Appl. Energy Mater.* **2020**, *3*, 5533.
- [483] W. Luo, Y. Gong, Y. Zhu, Y. Li, Y. Yao, Y. Zhang, K. K. Fu, G. Pastel, C. F. Lin, Y. Mo, E. D. Wachsman, L. Hu, *Adv. Mater.* **2017**, *29*, 1606042.
- [484] G. Zheng, C. Wang, A. Pei, J. Lopez, F. Shi, Z. Chen, A. D. Sendek, H. W. Lee, Z. Lu, H. Schneider, M. M. Safont-Sempere, S. Chu, Z. Bao, Y. Cui, *ACS Energy Lett.* **2016**, *1*, 1247.
- [485] N. W. Li, Y. Shi, Y. X. Yin, X. X. Zeng, J. Y. Li, C. J. Li, L. J. Wan, R. Wen, Y. G. Guo, *Angew. Chem., Int. Ed.* **2018**, *57*, 1505.
- [486] Y. Gao, Y. Zhao, Y. C. Li, Q. Huang, T. E. Mallouk, D. Wang, *J. Am. Chem. Soc.* **2017**, *139*, 15288.
- [487] L. Sang, R. T. Haasch, A. A. Gewirth, R. G. Nuzzo, *Chem. Mater.* **2017**, *29*, 3029.
- [488] X. Wang, R. Xiao, H. Li, L. Chen, *Phys. Chem. Chem. Phys.* **2016**, *18*, 21269.
- [489] M. Ogawa, R. Kanda, K. Yoshida, T. Uemura, K. Harada, *J. Power Sources* **2012**, *205*, 487.

- [490] Y. Sun, W. Yan, L. An, B. Wu, K. Zhong, R. Yang, *Solid State Ionics* **2017**, 301, 59.
- [491] M. Nagao, A. Hayashi, M. Tatsumisago, *Electrochemistry* **2012**, 80, 734.
- [492] C. Yu, L. van Eijck, S. Ganapathy, M. Wagemaker, *Electrochim. Acta* **2016**, 215, 93.
- [493] F. Altörfer, W. Bührer, I. Anderson, O. Schärfel, H. Bill, P. L. Carron, H. G. Smith, *Phys. B: Phys. Condens. Matter* **1992**, 180–181, 795.
- [494] G. Nazri, *Solid State Ionics* **1989**, 34, 97.
- [495] N. D. Lepley, N. A. W. Holzwarth, Y. A. Du, *Phys. Rev. B* **2013**, 88, 104103.
- [496] F. Mizuno, A. Hayashi, K. Tadanaga, M. Tatsumisago, *Adv. Mater.* **2005**, 17, 918.
- [497] N. Sata, K. Eberman, K. Eberl, J. Maier, *Nature* **2000**, 408, 946.
- [498] S. Adams, R. Prasada Rao, *J. Mater. Chem.* **2012**, 22, 7687.
- [499] K. Xu, *Chem. Rev.* **2004**.
- [500] D. R. Rajagopalan Kannan, P. K. Terala, P. L. Moss, M. H. Weatherspoon, *Int. J. Electrochem.* **2018**, 2018, 7.
- [501] R. Kanno, M. Murayama, T. Inada, T. Kobayashi, K. Sakamoto, N. Sonoyama, A. Yamada, S. Kondo, *Electrochim. Solid-State Lett.* **2004**, 7, A455.
- [502] T. Kobayashi, A. Yamada, R. Kanno, *Electrochim. Acta* **2008**, 53, 5045.
- [503] M. Sakuma, K. Suzuki, M. Hirayama, R. Kanno, *Solid State Ionics* **2016**, 285, 101.
- [504] A. C. Luntz, J. Voss, K. Reuter, *J. Phys. Chem. Lett.* **2015**, 6, 4599.
- [505] T. Liu, Y. Ren, Y. Shen, S. X. Zhao, Y. Lin, C. W. Nan, *J. Power Sources* **2016**, 324, 349.
- [506] Y. Q. Zhang, Y. Tian, Y. Xiao, L. J. Miara, Y. Aihara, T. Tsujimura, T. Shi, M. C. Scott, G. Ceder, *Adv. Energy Mater.* **2020**, 1903778.
- [507] Y. Zhu, J. C. Gonzalez-rosillo, M. Balaish, Z. D. Hood, K. Joong, J. L. M. Rupp, *Nat. Rev. Mater.*, <https://doi.org/10.1038/s41578-020-00261-0>
- [508] W. Xia, B. Xu, | Huanan, D. | Xiaoyi Tang, Y. Guo, H. Kang, H. Li, | H. Liu, H. Liu, H. Duan, X. Tang, Y. Guo, H. Kang, H. Li, H. Liu, *J. Am. Ceram. Soc.* **2017**, 100, 2832.
- [509] E. Kazyak, R. Garcia-Mendez, W. S. LePage, A. Sharafi, A. L. Davis, A. J. Sanchez, K.-H. Chen, C. Haslam, J. Sakamoto, N. P. Dasgupta, *Matter* **2020**, 2, 1025.
- [510] H. Takahara, T. Takeuchi, M. Tabuchi, H. Kageyama, Y. Kobayashi, Y. Kurisu, S. Kondo, R. Kanno, *J. Electrochem. Soc.* **2004**, 151, A1539.
- [511] J. Yang, B. Huang, J. Yin, X. Yao, G. Peng, J. Zhou, X. Xu, *J. Electrochem. Soc.* **2016**, 163, A1530.
- [512] A. Sakuda, A. Hayashi, M. Tatsumisago, *J. Power Sources* **2010**, 195, 599.
- [513] X. Xu, K. Takada, K. Fukuda, T. Ohnishi, K. Akatsuka, M. Osada, B. T. Hang, K. Kumagai, T. Sekiguchi, T. Sasaki, *Energy Environ. Sci.* **2011**, 4, 3509.
- [514] J. H. Woo, J. J. Travis, S. M. George, S.-H. Lee, *J. Electrochem. Soc.* **2015**, 162, A344.
- [515] K. Okada, N. Machida, M. Naito, T. Shigematsu, S. Ito, S. Fujiki, M. Nakano, Y. Aihara, *Solid State Ionics* **2014**, 255, 120.
- [516] N. MacHida, J. Kashiwagi, M. Naito, T. Shigematsu, *Solid State Ionics* **2012**, 225, 354.
- [517] A. Y. Kim, F. Strauss, T. Bartsch, J. H. Teo, T. Hatsukade, A. Mazilkin, J. Janek, P. Hartmann, T. Brezesinski, *Chem. Mater.* **2019**, 31, 9664.
- [518] H. Kitaura, A. Hayashi, K. Tadanaga, M. Tatsumisago, *Solid State Ionics* **2011**, 192, 304.
- [519] K. Chen, K. Yamamoto, Y. Orikasa, T. Uchiyama, Y. Ito, S. Yubuchi, A. Hayashi, M. Tatsumisago, K. Nitta, T. Uruga, **2018**, 327, 150.
- [520] S. Yubuchi, Y. Ito, T. Matsuyama, A. Hayashi, M. Tatsumisago, *Solid State Ionics* **2016**, 285, 79.
- [521] Study of $\text{LiNi}_{0.6}\text{Co}_{0.2}\text{Mn}_{0.2}\text{O}_2$ Coated with Li_2ZrO_3 Nanolayers in All-Solid-State Lithium Ion Batteries.pdf.
- [522] S. Noh, J. Kim, M. Eom, D. Shin, *Ceram. Int.* **2013**, 39, 8453.
- [523] A. Sakuda, N. Nakamoto, H. Kitaura, A. Hayashi, K. Tadanaga, M. Tatsumisago, *J. Mater. Chem.* **2012**, 22, 15247.
- [524] A. Sakuda, A. Hayashi, T. Ohtomo, S. Hama, M. Tatsumisago, *J. Power Sources* **2011**, 196, 6735.



Kun Joong Kim is a postdoctoral researcher in the Electrochemical Materials Laboratory at Massachusetts Institute of Technology (MIT) under the supervision of Prof. Jennifer Rupp. He earned his Ph.D. in Materials Science & Engineering from the Pohang University of Science and Technology (POSTECH). His research is focused on inorganic material science and engineering for electrochemical energy conversion and storage device. He enjoys understanding electroceramic materials as well as discovering new functionality. He likes to design and process ceramic architectures and their interfaces for novel solid-state fuel cells, sensors and batteries, not limited to inception, but performance demonstration to the scaled fabrication. He particularly excited to work in the period when battery technology is transitioning from liquid to solid technology toward safer battery systems.



Moran Balaish is a Fulbright postdoctoral fellow in the Electrochemical Materials Laboratory headed by Prof. Jennifer Rupp at Massachusetts Institute of Technology (MIT). Balaish is a materials scientist and chemist, holding a Ph.D. in Energy Engineering (Technion-Israel Institute of Technology). Her research is focused on the fundamental study of structure-property-performance of solid-state Lithium-ion conductors for neuromorphic computing, energy storage, and chemical sensing applications. Her wider scientific interests span over electrochemical analysis and surface chemistry of oxides and polymers, non-aqueous electrochemistry, materials and device fabrication for green energy applications, and beyond.



Jennifer L. M. Rupp is the Thomas Lord Associate Professor of Electro-chemical Materials at the Department of Materials Science and Engineering and the Department of Electrical Engineering and Computer Science at MIT. She earned her Ph.D. in Materials Science and Engineering from ETH Zurich. Rupp is an advocate for green tech, which shapes her research and engineering program in strong collaboration with industry, inventions, and her increasing role as an activist. Her research is in designing and engineering ceramic materials and their properties for device functions in energy, sensing, and neuromorphic computation. Considering techno-economics in processing of energy storage, as well as drafting more exotically cyber physical and high throughput production of ceramics in the 4th industrial revolution currently, excite her. Rupp founded the LILA-mentoring program to support engineers and scientists of color, females, and LGBTIQ to become leaders in the solid-state material and chemistry communities.